ÉCOLE DOCTORALE
Énergie - Matériaux - Sciences de la Terre et de l'Univers
Institut des Sciences de la Terre d'Orléans / School of Earth Sciences and Engineering, Nanjing university

THÈSE EN COTUTELLE INTERNATIONALE présentée par :

Xinghua NI

soutenue le : 19 décembre 2024

pour obtenir le grade de :
Docteur de Université d'Orléans
et de l'Université de Nanjing

Discipline/ Spécialité : Sciences de l'Univers

Late Paleozoic - Early Mesozoic tectonic evolution of the southwestern Central Asian Orogenic Belt: Structural, metamorphic and magmatic evidence from the eastern Tianshan

THÈSE dirigée par :

CHEN Yan	Professeur, Université d'Orléans
WANG Bo	Professeur, Nanjing University

RAPPORTEURS :

CLUZEL Dominique	Professeur, Université de la Nouvelle-Calédonie
LI Pengfei	Directeur de recherche, Guangzhou Institute of Geochemistry

---

JURY :

JIANG Yingde	Directeur de recherche, State Key Laboratory of Isotope Geochemistry, Président du jury
CAI Keda	Professeur, China University of Geosciences
CHEN Yan	Professeur, Université d'Orléans
CLUZEL Dominique	Professeur, Université de la Nouvelle-Calédonie
FAURE Michel	Professeur, Université d'Orléans
LI Pengfei	Directeur de recherche, Guangzhou Institute of Geochemistry
WANG Bo	Professeur, Nanjing University
ZHU Wenbin	Professeur, Nanjing University

INVITE :

SORET Mathieu	Docteur, Ecole Normale Supérieure de Paris

ACKNOWLEDGEMENTS

From 2020 to 2024, although it was not a happy start due to the pandemic, I have finally reached the end of this incredible journey of becoming a doctor. Born in a small and underdeveloped village in southeastern China, I never imagined that one day I would earn a doctorate in a country so far away from home. I feel incredibly fortunate to reflect on how much I have grown, not only professionally but also personally, during this endeavor. This achievement would not have been possible without the help, support, and encouragement of many people. In the following, I will do my best to express my heartfelt gratitude to everyone who has been part of this journey.

首先，我要向我的导师**陈岩**教授与**王博**教授表达最深的谢意。他们不仅是我学术研究和科研道路上的明灯，更是我人生旅途中的重要导师。我仍然清晰地记得，第一次坐飞机便是跟随王博教授前往新疆进行野外考察，而第一次与外国人接触，则是在野外工作中与陈岩老师以及 Michel Faure 与 Stéphane Scaillet 教授共事。虽然当时我的英语水平还不足以让我流利交流，但那次经历极大地拓宽了我的视野，也成为了我科研生涯的起点。在随后的岁月里，无论是在生活上还是工作上，他们都给予了我无微不至的关怀与大量的帮助。我由衷地向他们表示感谢！

其次，我要衷心感谢给予我巨大帮助的老师们。**Dominique Cluzel** 教授在野外考察与论文写作方面提供了很多细致的指导和帮助，**Mathieu Soret** 博士指导我开展了系统的变质岩岩石学研究，**Michel Faure** 教授为我在科学问题和数据解读上提出了许多富有建设性的建议，**Stéphane Scaillet** 教授协助我圆满完成了完成了 ^{40}Ar-^{39}Ar 测年研究，**Ida Di Carlo** 在电子探针测试方面给予了我大力支持，**胡欢**老师在 U-Pb 测年方面为我提供了重要的帮助。**李鹏飞**老师、**蒋映德**老师、**朱文斌**老师、**蔡克大**老师在论文评阅和答辩环节也给予了诸多宝贵建议与建设性的意见。在此向各位老师表示最诚挚的感谢！

此外，我衷心感谢**中国国家留学基金委**。正是得益于国家留学基金委提供的公派留学奖学金，我才得以顺利完成在法国的学业与生活。这份资助不仅给予了我经

济上的支持，更是我追梦路上的坚实后盾。我深感荣幸与感激！

我还要衷心感谢我的朋友们，正是他们的鼎力相助，让我能够勇敢面对挑战，顺利完成工作。已经毕业的**刘洪升**、**钟凌林**、**朱鑫**和**何智远**博士，为我提供了许多宝贵的工作和人生建议。**刘珈硕**、**李盈莹**、**曹婷婷**、**宋芳**、**陈一逸**、**孙雨欣**、**何筱珂**在野外考察、实验测试以及日常生活的点点滴滴中，都给予了我无私的帮助和关怀。**刘欣宇**、**刘丹阳**、**江勇**等好友给了我很多鼓励与支持。同时，我要感谢**南大拳击社**的各位朋友，让我不仅找到了自己的爱好，还结识了一群志同道合的小伙伴。

我要感谢我深爱的家人们。爷爷**倪邦林与**已经过世的奶奶**陈丙兰**，是他们从小照看我长大，始终如一地鼓励我勇往直前。母亲**陈秀琼和**父亲**倪占全**为我提供了巨大的经济支持，正是他们的无私付出，才使我得以顺利完成学业。堂姐**倪丹**与表姐**王兰**陪伴我度过了童年与少年的欢乐时光，她们的支持与陪伴对我而言意义非凡。衷心感谢我的家人们，是你们让我感受到了无尽的温暖与力量。

最后，我要感谢我自己。这一路走来并不容易，犹记得儿时天还未亮就要独自走五里山路去上学。山路蹒跚且阴森，尤其是遇到下雨天更是泥泞湿滑，难以前行。偶尔饭盒水漏了中午还只能挨饿，或者依靠同学们的善意“救济”。在初中时便离家住宿学校，不得不学会独立，身材矮小的我总是占不到“便宜”。这些经历虽艰辛，却也铸就了我坚韧的性格，让我能够克服重重困难走到今日。所以为了对得起曾经吃过的苦，更要好好走未来的路。

天高地阔，大有可为！人海苍苍，顺遂无忧！

Rien n’est impossible à celui qui rêve, ose, persévère et refuse d’abandonner.

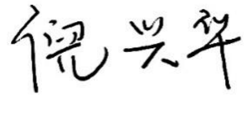

2024 年 12 月 24 日

于南京

Contents

Résumé étendu de la thèse en français

Les orogènes d'accrétion, formés le long de marges convergentes, se caractérisent par une longue évolution et sont les principaux sites de croissance continentale sur la Terre. La convergence lithosphérique met en œuvre des processus tectoniques complexes, tels que l'avancée ou le retrait de la zone de subduction, l'accrétion arc/arc ou arc/continent, la collision de blocs et l'extension post-collision. De plus, les processus en œuvre dans les ceintures orogéniques anciennes sont compliqués à appréhender en raison de l'importante érosion, supprimant l'enregistrement sédimentaire et une bonne part des structures tectoniques superficielles. Leur compréhension nécessite par conséquent une analyse approfondie des déformations de la croûte moyenne, du métamorphisme et du magmatisme.

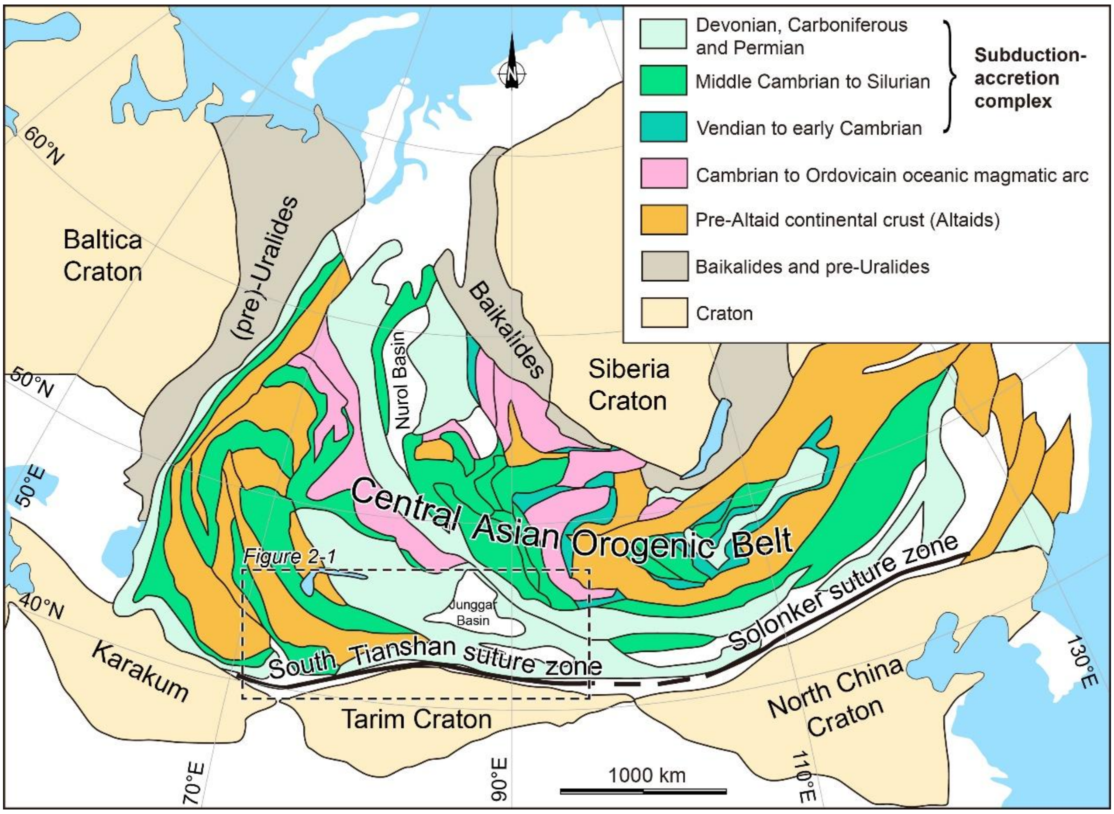

Figure 1. Aperçu du cadre tectonique et des principales divisions de la Ceinture Orogénique d'Asie Centrale (CAOB en anglais) et des cratons adjacents.

La Ceinture Orogénique d'Asie Centrale (CAOB en anglais) est un vaste système orogénique d'accrétion au sein de l'Eurasie, formé par la subduction de l'Océan Paléo-Asiatique (PAO en anglais) et la convergence des cratons de Sibérie, Tarim - Chine du Nord, et Baltique (Europe de l'Est) pendant le Néoprotérozoïque et le Paléozoïque supérieur. Elle est considérée comme le plus grand orogène d'accrétion du Phanérozoïque, à l'origine de la constitution d'un volume significatif de croute continentale juvénile et offre un laboratoire naturel pour examiner la croissance continentale et les processus d'orogénèse. Le Tianshan oriental, situé au Sud-Ouest de la CAOB, détient des enregistrements cruciaux de subduction, d'accrétion arc/arc et arc/continent et d'évolution post-collision, fournissant des aperçus sur la tectonique orogénique. Cependant, l'accord est loin d'être acquis sur l'interprétation de son évolution géodynamique, et des débats subsistent sur des questions liées à la nature des socles continentaux mis en jeu, aux processus tectoniques, à la chronologie de l'amalgamation finale, et à l'interprétation du magmatisme.

Tout d'abord, la nature du socle des régions du Tianshan Nord et de Junggar reste controversée. Certains auteurs ont proposé que ces régions comportent un ancien socle continental d'âge Archéen à Paléoprotérozoïque. Cependant, de nombreux autres suggèrent que ce socle pourrait être composé d'une croûte continentale juvénile comprenant principalement des systèmes orogéniques paléozoïques, y compris des arcs océaniques, des complexes d'accrétion et même de la croûte océanique. La raison principale de ce débat est que, contrairement aux blocs du Tianshan central et de Yili, aucun élément de socle précambrien n'y a été identifié in situ. De plus, la formation des bassins de Junggar et de Turfan-Hami, recouverts de sédiments cénozoïques, a conduit à des spéculations sur la présence d'un ancien socle continental sous-jacent. Dans de tels cas, les compositions isotopiques de Nd et de Hf de zircon de roches magmatiques issues de la croûte profonde sont susceptibles de fournir des informations sur la nature de cette croûte non exposée.

Les processus tectoniques en jeu dans la convergence du Tianshan oriental, en particulier pendant le Paléozoïque supérieur où la transition tectonique a pu se produire, restent mal définis dans le détail. Des études antérieures ont suggéré que l'évolution du Tianshan oriental au Paléozoïque supérieur impliquait probablement des retraits et avancées épisodiques des zones de subduction, des collisions arc-arc avec le Junggar oriental, ainsi qu'une extension post-collision. Cependant, ces suggestions sont principalement basées sur des études provenant de sites dispersés. En outre, le manque de preuves concernant les modèles de déformation et les états thermiques, en particulier les structures d'extension, rend le modèle tectonique mal assuré.

La chronologie de l’amalgamation (suture finale) du Tianshan oriental fait débat depuis longtemps avec deux hypothèses en présence : (1) du Carbonifère supérieur au Permien inférieur, et (2) du Permien supérieur au Trias. L’une des principales raisons de cette controverse réside dans les différentes interprétations du magmatisme et des structures régionales. Il est donc nécessaire de mener des études sur les variations spatiales et temporelles du magmatisme, ainsi que la déformation régionale de la croûte.

Enfin, des roches magmatiques du Paléozoïque supérieur au Trias inférieur sont réparties dans tout le Tianshan oriental. Cependant, l’origine et la signification géodynamique de ces roches, en particulier celles du Trias, restent controversées. Plusieurs modèles ont été proposés pour le contexte géodynamique du magmatisme triasique : (1) l’extension intracontinentale ; (2) la transition tectonique de la compression syn-collision vers l'extension post-collision ; (3) la transition tectonique de l'accrétion supra-subduction vers la collision ; et (4) la subduction continentale induite par les effets lointains de la subduction de la Téthys. Des études complètes et détaillées sur le magmatisme triasique sont donc essentielles pour clarifier le contexte géodynamique du Mésozoïque inférieur du Tianshan oriental. Dans cette thèse, l’histoire tectono-métamorphique du Complexe Métamorphique de Xiaopu (XMC) dans l’Est du Tianshan du Nord sera abordée en premier avec des analyses structurale, métamorphique et géochronologique détaillées. Deuxièmement, des contraintes spatiales et temporelles sur l’évolution tectono-magmatique du Paléozoïque supérieur du Tianshan oriental et du Junggar oriental ont été établies sur la base des données géochronologiques, géochimiques et isotopiques de la littérature et nos propres données. Enfin, l'évolution magmatique du Trias a été reconstituée à partir d'études pétrographiques, géochronologiques, géochimiques et isotopiques des granitoïdes triasiques récemment identifiés dans la région de Bogda, ainsi que des données publiées provenant du Tianshan oriental.

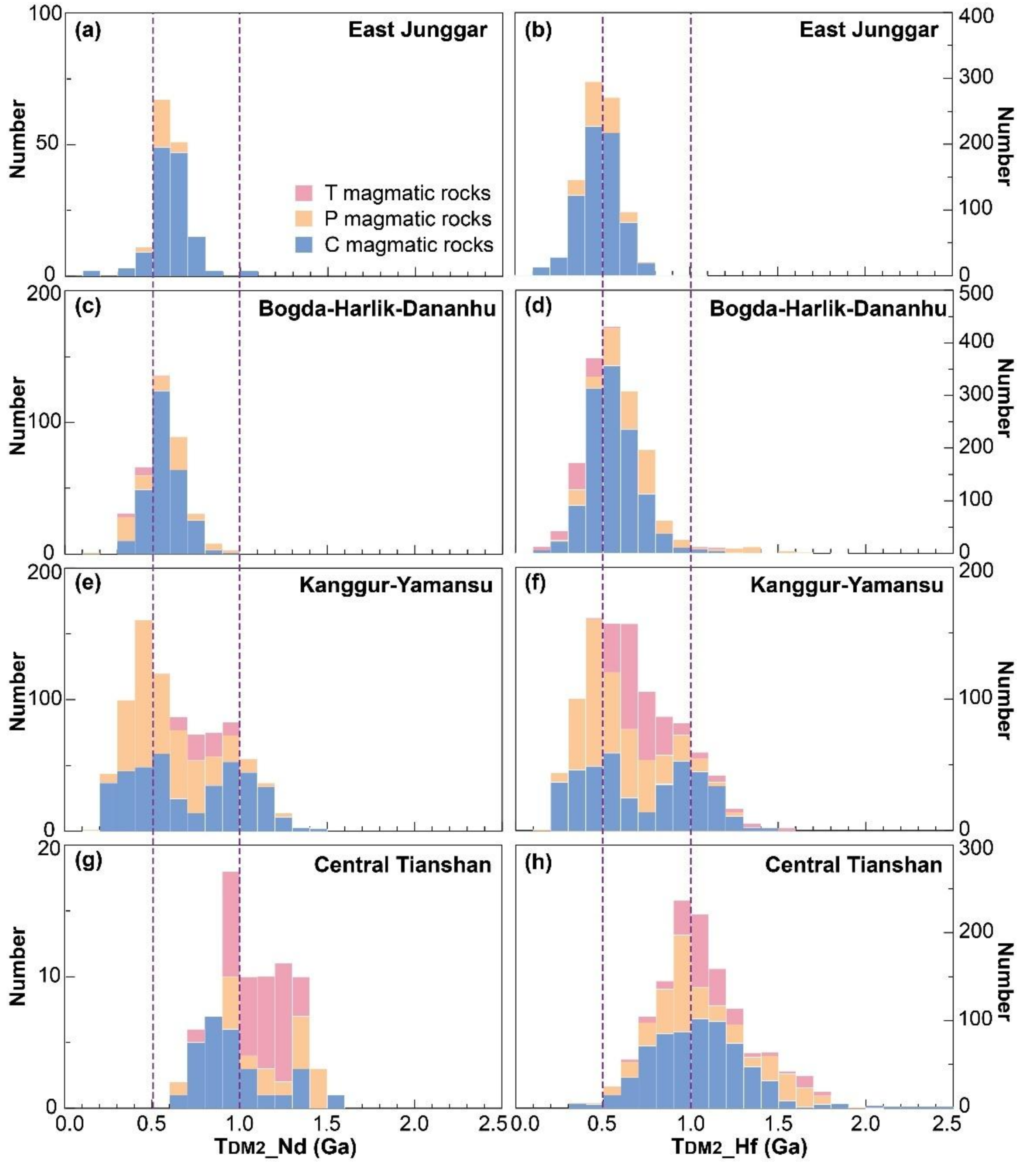

Figure 2. Statistiques des âges modèles en deux étapes (modèle à deux phases T_{DM2}) du Nd et du zircon Hf des régions de Junggar oriental, Bogda-Harlik-Dananhu, Kanggur-Yamansu et Tianshan central.

En intégrant les données disponibles de anciennes études, les principaux résultats conduisent aux synthèses et conclusions suivantes :

(1) La nature du socle crustal dans les régions orientales de Tianshan et de Junggar oriental

La nouvelle base de données de roches magmatiques du Carbonifère au Trias montre des âges modèles en deux étapes pour le Nd et le Hf des zircons (T_{DM2}) dans les régions de Junggar Est et de Bogda-Harlik-Dananhu sont similaires et compris entre 0,3 et 0,8 Ga avec des pics autour de 0,5 Ga (figures 2 et 3). Ceci est significativement différent du bloc du Tianshan central, où les roches magmatiques présentent des âges TDM2 de 0,7 à 1,5 Ga, avec un pic à environ 1,0 Ga (figures 2 et 3). Par conséquent, le socle des orogènes de Junggar oriental et de Bogda-Harlik-Dananhu ne comporte probablement pas de croûte continentale ancienne comme celle du bloc de Tianshan Central, mais il est plutôt constitué d'une croûte juvénile formée pendant le Néoprotérozoïque et le Paléozoïque.

Dans la région de Kanggur-Yamansu de l'Est Tianshan, les roches magmatiques du Paléozoïque supérieur, en particulier du Carbonifère, présentent deux populations d'âges T_{DM2}. Une population d'âge s'étend de 0,2 à 0,7 Ga, avec un pic vers 0,5 Ga, et l'autre, allant de 0,8 à 1,2 Ga, montre un pic vers 1,0 Ga. La première est comparable aux composantes juvéniles des orogènes de Junggar oriental et de Bogda-Harlik-Dananhu, tandis que la seconde est similaire à la croûte continentale du bloc de Tianshan central. D'après les variations spatiales des données isotopiques Nd de roche totale et Hf de zircon (Figure 3), la partie occidentale de l'orogène de Kanggur-Yamansu présente généralement de compositions isotopiques Nd et Hf plus enrichies que sa partie orientale. Par conséquent, le socle de l'orogène de Kanggur-Yamansu comprend une ancienne croûte continentale à l'Ouest et seulement une croûte juvénile à l'Est.

L'épaisseur estimée de la croûte des orogènes de Junggar Est et de Dananhu-Harlik pendant le Paléozoïque supérieur varie de 30 à 60 km. Si cette estimation est fiable, le volume de croûte juvénile dans le socle du CAOB serait substantiel. La formation et la préservation d'un tel volume de croûte juvénile indiquent une croissance continentale significative pendant le Néoprotérozoïque et le Paléozoïque au Sud-Ouest de la CAOB.

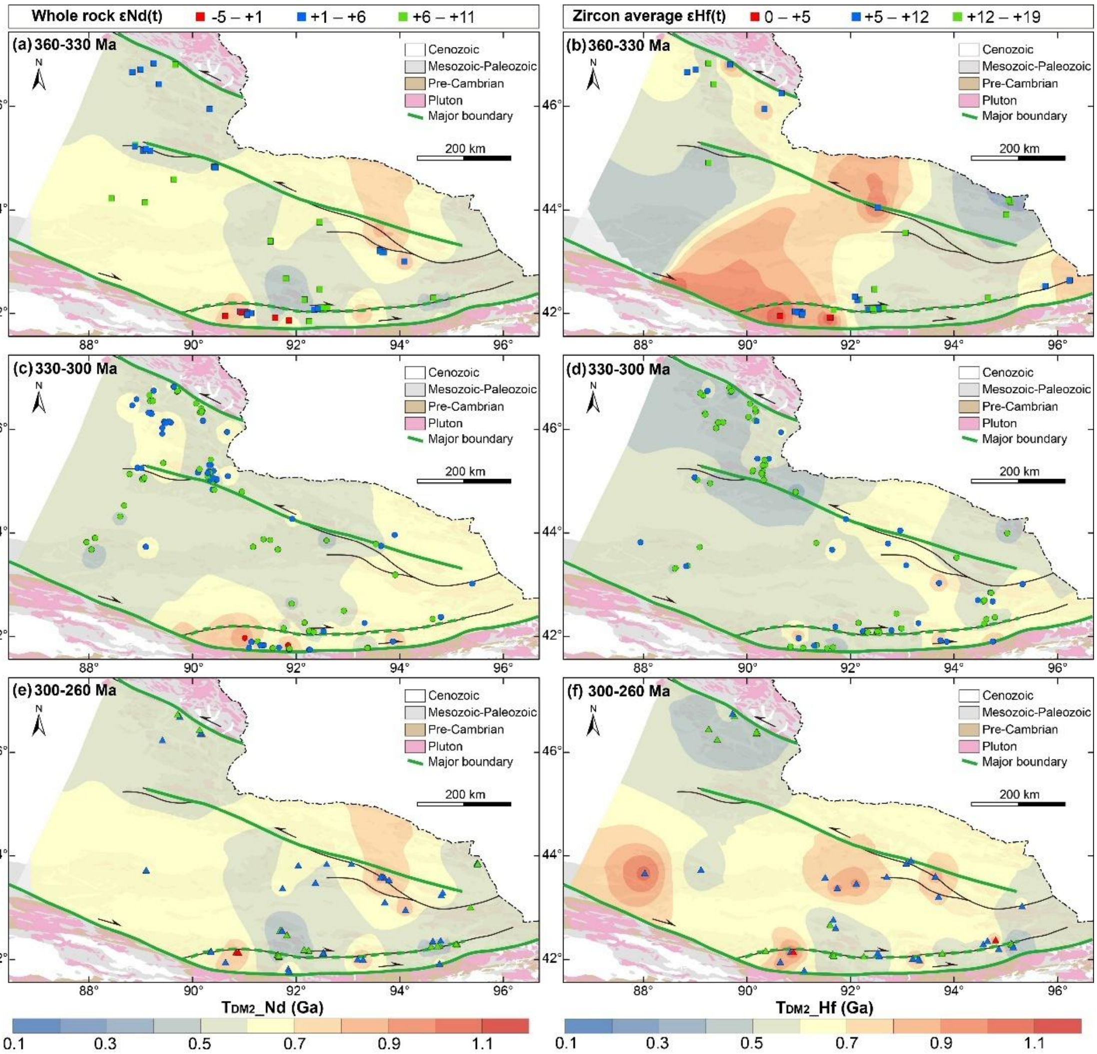

Figure 3. Figure 3. Cartes montrant les valeurs εNd(t) de roche totale et les moyennes de εHf(t) de zircon des roches magmatiques d'âge du Paléozoïque inférieur. Les symboles verts, bleus et rouges représentent respectivement les valeurs εNd(t) ou εHf(t) élevées, intermédiaires et faibles.

(2) Processus tectoniques impliqués dans la convergence du Tianshan oriental pendant le Carbonifère

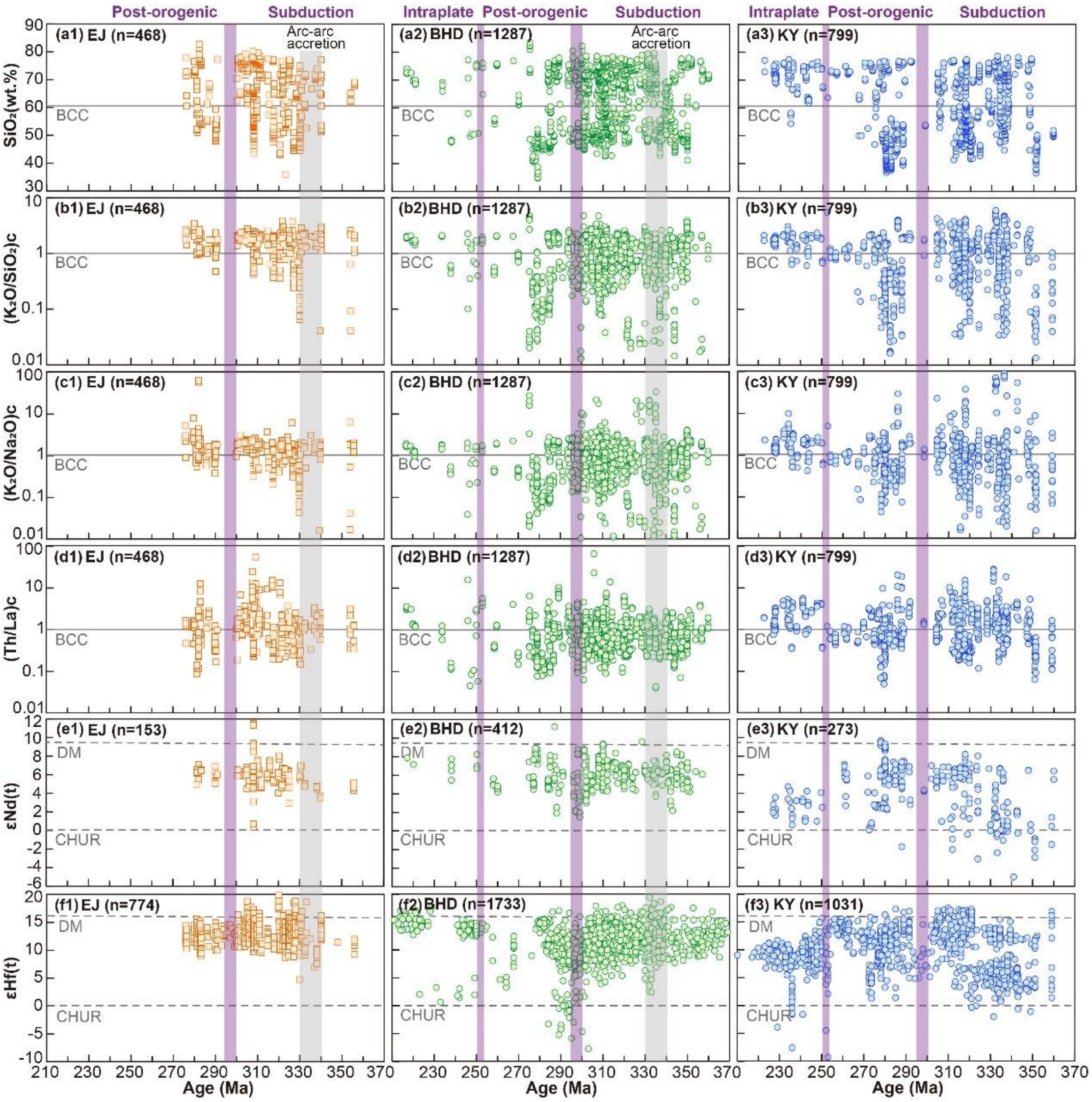

Figure 4. Évolution des compositions géochimiques et isotopiques des roches magmatiques des régions de Junggar Est (EJ), Bogda-Harlik-Dananhu (BHD) et Kanggur-Yamansu (KY). Les rapports K_2O/SiO_2, K_2O/Na_2O et Th/La sont normalisés par la croûte continentale globale (BCC).

Dans la région de Harlik, on suppose qu'il existe au Carbonifère inférieur un stade de compression NE-SW à partir de plissement et de chevauchement des strates crustales. La croûte des régions de Junggar Est et de Bogda-Harlik-Dananhu a subi un épaississement notable vers 340-330 Ma, accompagné de la formation de roches présentant des compositions isotopiques de Nd et Hf relativement enrichies (Figure 4). Par conséquent, il a été proposé que l'accrétion des arcs de Bogda-Harlik-Dananhu au

Junggar oriental, suite à la fermeture de l'océan Kalamaili, se serait produite vers 340-330 Ma. Ceci est cohérent avec les âges de la ceinture ophiolitique de Kalamaili (~420 à 330 Ma) et la discordance régionale du Carbonifère sur les roches plus anciennes.

Entre 330 et 310 Ma, une transtension senestre guidée par des accidents orientés NW-SE s'est produite dans la région de Harlik, immédiatement suivie par la mise en place de plutons granitiques et la formation d'un complexe métamorphique de HT-LP inversé (Figure 5).

Entre-temps, la croûte de la région de Bogda-Harlik-Dananhu s'est considérablement amincie, par comparaison à la croûte plus épaisse observée dans les régions de Dananhu et du Junggar Est. De plus, un magmatisme mafique de type arc et des granitoïdes « chauds » ont été observés dans les régions de Bogda-Harlik et du sud de Junggar Est, tandis que des granitoïdes « froids » ont été trouvés dans la région de Dananhu. Ces éléments de preuves suggèrent une extension d'arrière arc ou intra-arc pendant le Carbonifère moyen et inférieur, attribuée au retrait de la plaque océanique subductée de Kanggur dans l'est du Tianshan du Nord (Figure 5).

(3) L'amalgamation finale du Tianshan oriental vers 300 Ma

Une quiescence magmatique se produit dans les régions de Junggar Est et de Kanggur-Yamansu vers 300 Ma, couplée à une réduction soudaine des roches magmatiques intermédiaires dans la région de Bogda-Harlik-Dananhu (Figure 4). En même temps, les régions de Bogda-Harlik-Dananhu et de Kanggur-Yamansu ont connu un épaississement important de la croûte continentale. Les valeurs εNd(t) de roche totale et εHf(t) de zircon ont également diminué pendant cette période, avec des signatures isotopiques Nd et Hf plus enrichies trouvées dans certains échantillons de la région de Bogda-Harlik-Dananhu (Figure 4). Combiné à une diminution significative des valeurs de δ11B de roche totale et des valeurs de δ18O de zircon et à la transition d'un environnement marin vers un environnement terrestre vers 300 Ma, ainsi qu'à un mouvement latitudinal relatif négligeable entre le bloc Yili, le bassin de Turpan-Hami et l'orogène de Yamansu depuis le Carbonifère supérieur, comme proposé par des études antérieures, nous en déduisons que la fermeture de l'océan Kanggur et l’amalgamation finale du Tianshan oriental se sont produites vers 300 Ma.

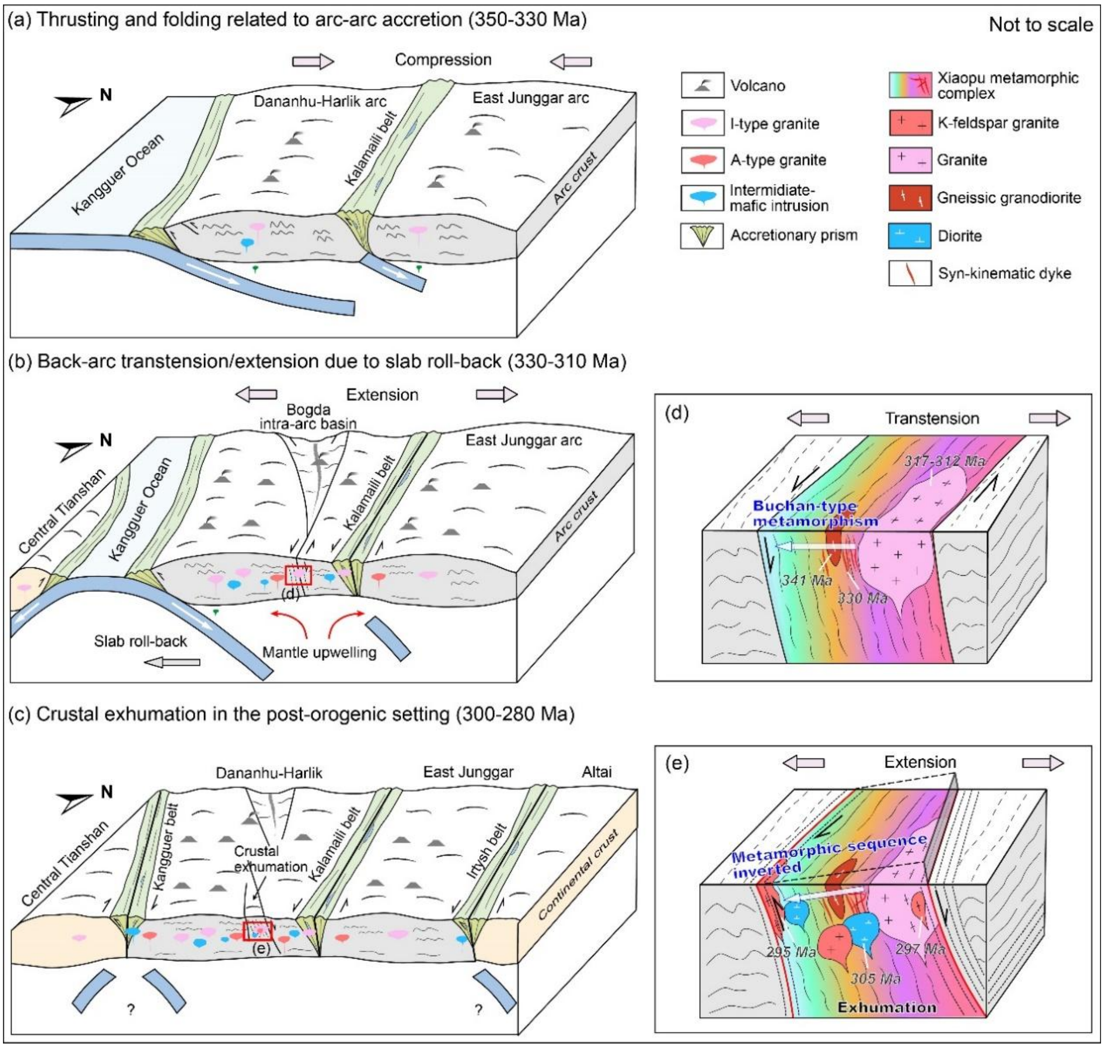

Figure 5. Evolution tectonique du Tianshan Nord du Carbonifère au Permien. (a) L'accrétion des arcs de Dananhu-Harlik et de Junggar Est pendant le Carbonifère inférieur a donné lieu à des chevauchements et des plissements ; (b) Le retrait des plaques plongeantes pendant le Carbonifère inférieur et moyen a déclenché la transtension/extension crustale dans l'arrière-arc ; (c) Une exhumation crustale localisée s'est produite en contexte post-orogénique pendant le Permien inférieur ; (d) Vue détaillée de la croûte moyenne montrant la formation du métamorphisme HT-LP de type Buchan ; (e) La séquence métamorphique de type Buchan a été inversée en raison de son exhumation asymétrique.

(4) Évolution post-orogénique au cours du Permien

Pendant le Permien inférieur, des structures extensives contrôlent l'exhumation et le refroidissement de la croûte moyenne dans la région de Harlik ainsi que la mise en place d’intrusions magmatiques(Figure 5). Les roches magmatiques du Permien dans les régions de Bogda-Harlik-Dananhu et de Kanggur-Yamansu sont soit mafiques soit felsiques, avec peu de roches intermédiaires comparées à celles du Carbonifère (Figure 5). Les roches mafiques sont principalement distribuées le long ou à proximité de failles majeures, en association étroite avec une tectonique décrochante. Les granitoïdes de type A sont répandus dans les régions du Junggar Est et de Bogda-Harlik-Dananhu, avec systématiquement des températures de saturation du zircon élevées. Les failles décrochantes d’’échelle régionale, y compris les zones de cisaillement principales de Tianshan, de Kanggur-Huangshan et d'Irtysh, ont été réactivées au Permien (290-245 Ma) et ont probablement enregistré une extrusion vers l'est du bloc du Junggar. Les mouvements différentiels le long de ces failles ont permis la rotation de ce dernier et contrôlé l'extension localisée de la croûte, dominant ainsi l'évolution post-orogénique du Tianshan oriental et du Junggar oriental.

(5) Remaniement crustal intraplaque au cours du Trias

Pendant le Trias, le magmatisme dans le Tianshan oriental était plus dispersé et moindre que celui du Paléozoïque supérieur (figure 4). La plupart des intrusions magmatiques triasiques sont post-cinématiques c’est-à-dire non-déformées et recoupant les roches pré-triasiques plissées et foliées. De plus, les roches magmatiques du Trias sont principalement felsiques, avec quelques intrusions mafiques seulement, ce qui diffère du magmatisme des marges convergentes. Les données géochimiques et isotopiques suggèrent que les roches felsiques du Trias se sont formées à partir de la fusion d'une croûte ancienne ou juvénile à des profondeurs et des températures variables. Les roches mafiques, issues de la fusion partielle du manteau lithosphérique ou asthénosphérique par décompression, ont probablement fourni une chaleur supplémentaire pour la fusion de la croûte. L'absence d'ophiolites identifiées plus jeunes que le Permien inférieur et la prédominance des environnements terrestres au Trias confirment que le Tianshan oriental a évolué vers un contexte intracontinental ou intraplaque pendant cette période. La corrélation temporelle entre les roches mafiques et les granitoïdes de type A avec les failles de décrochement, telles que la faille de Xingxingxia, suggère que certaines tectoniques transcurrentes, influencées par des effets distants du système de subduction de la Paléo-Téthys, ont joué un rôle dans l'évolution triasique de l'est du Tianshan.

Mots clés : Sud-Ouest de la Ceinture Orogénique de l'Asie Centrale (CAOB), Paléozoïque supérieur, Mésozoïque inférieur, Structures et métamorphisme, Magmatisme, Processus tectoniques

Chapter 1. General introduction

1.1 Accretionary orogens and general tectonic processes in a plate tectonic convergence

The continental crust of the Earth is unique in the solar system and preserves the rich geological history of the Earth (Hawkesworth & Kemp. 2006; Spencer et al., 2017; R. X. Zhu et al., 2021). It provides suitable habitats for human settlement and abundant natural resources for human utilization. Therefore, understanding the formation and growth of the continental crust is very important in Earth sciences (R. X. Zhu et al., 2021). The continental crust is characterized by an average intermediate bulk composition and the massive presence of felsic magmatic rocks (e.g., granitoids) in its upper part (e.g., Rudnick & Gao, 2014). Since mantle melting typically produces mafic magma, the formation of new continental crust necessitates additional processes. This involves either the fractional crystallization of mantle-derived mafic magmas or the remelting of pre-existing crustal rocks, with cumulates or residues potentially returning to the mantle (e.g., Rudnick, 1995; Hawkesworth et al., 2010; Moyen et al., 2021). The former contributes to crustal growth and the latter represents crustal reworking.

Accretionary orogens developing along convergent margins are characterized by long-lived evolution, progressing from oceanic subduction to arc-arc or arc-continent accretion, and are considered as the primary sites of continental growth on Earth (Cawood et al., 2009; Xiao & Santosh, 2014; T. Wang et al., 2023). In general, continental growth in accretionary orogens can be achieved through two efficient mechanisms: (1) lateral continental growth by the accretion of juvenile oceanic arcs, oceanic plateaus, and subduction-accretion complexes, and (2) vertical growth through magmatic underplating of mantle-derived materials (Jahn et al., 2004; Kemp et al., 2009; G. J. Tang et al., 2017; R. X. Zhu et al., 2021). These two mechanisms are complementary and often work together to facilitate continental growth during the plate convergence.

The convergence of plates and orogens is generally associated with complex tectonic processes. As demonstrated in modern Pacific-type orogenic systems, tectonic switching between advancing and retreating subduction often occurs during plate convergence (Royden, 1993; Collins, 2002; Cawood et al., 2009; Lister and Froster, 2009). The advancing subduction tends to induce crustal shortening and thickening, crustal anatexis, and formation of retro-arc foreland basins. In contrast, the retreating subduction can cause back-arc extension, crustal thinning, and development of arc-backarc systems, along with extension-related magmatism and high temperature metamorphism in the overriding plate (e.g., Collins et al., 2002). In addition, arc-arc or arc-continent accretion (or collision) following oceanic basin closure can result in crustal shortening and thickening (e.g., Teng et al., 1990; Taira, 2001). After the final amalgamation, post-collisional extension due to lithosphere delamination, accompanied by a large volume of magmatism, is a common feature of many orogenic belts (Charlton, 1991; Göğüş et al., 2016; Gómez-Frutos et al., 2023). In contrast to modern orogens, elucidating the orogenic processes of ancient orogenic belts poses a challenge due to extensive denudation (J. S. Liu et al., 2022; F. Song et al., 2024). Therefore, comprehensive research on deformation, metamorphism, and magmatism is essential for a better understanding of these ancient orogenic processes.

1.2 The southwestern Central Asian Orogenic Belt

The Central Asian Orogenic Belt (CAOB), also known as the Altaids, is a giant accretionary orogenic system in the Eurasian continent (Figure 1.1). It extends ~5500-km-long from the Okhotsk Sea in the east to the Ural Mountains in the west, surrounded by the Siberian, Tarim-North China, and Baltica (East European) cratons. The CAOB was mainly formed by the subduction of the Paleo-Asian Ocean (PAO), resulting in the multiple accretion of microcontinents, arc terranes, seamounts, and accretionary wedges between the cratons during the Neoproterozoic to late Paleozoic (Şengör et al., 1993; Jahn et al., 2000; Windley et al., 2007; W. J. Xiao et al., 2015; T. Wang et al., 2023). Recent studies indicate that the CAOB preserves the largest volume of juvenile crust compared to other typical accretionary and collisional orogens on Earth (e.g., Jahn et al., 2004; T. Wang et al., 2023). Consequently, the CAOB offers a natural laboratory to examine continental growth and the geodynamic processes of orogeny.

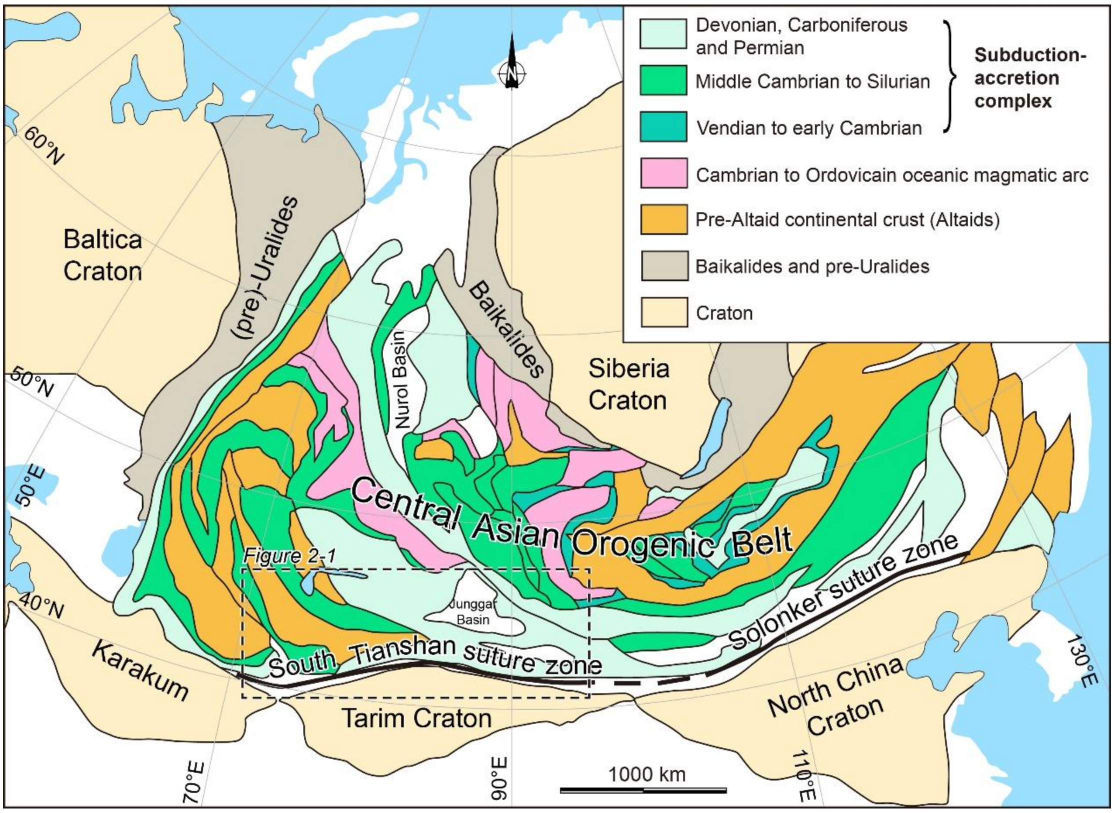

Figure 1.1. Tectonic overview and division of the Central Asian Orogenic Belt and adjacent cratons (modified from Şengör et al., 1993; Windley et al., 2007; W. J. Xiao et al., 2015).

The southwestern CAOB comprises the Tianshan Orogen and Junggar Belt in northwestern China, Kyrgyzstan, and southern Kazakhstan (Figure 2.1). It records the subduction and final closure of the two main oceanic branches of the PAO, i.e., the Junggar-North Tianshan Ocean in the north and the Paleo-Tianshan or Turkestan Ocean in the south (J. Gao et al., 1998; Biske & Seltman, 2010; B. Wang et al., 2008, 2011, 2018; Charvet et al., 2011; W. J. Xiao et al., 2013; Alexeiev et al., 2015; Käßner et al., 2017; Han & Zhao, 2018; H. Huang et al., 2020). The Tianshan Orogen and Junggar Belt include microcontinents (e.g., the Central Tianshan and Yili blocks) and Phanerozoic subduction-accretion complex (e.g., the North Tianshan, West Junggar, and East Junggar) mainly consisting of arc terranes and accretionary wedges (Figure 1.1). Most ophiolite belts exposed in these regions are of Neoproterozoic to Paleozoic age (~600-300 Ma), indicating the formation of oceanic lithosphere during this period (X. C. Xiao et al., 1992; B. Wang et al., 2006, 2011, 2018; J. Gao et al., 2022; G. C. Wang et al., 2022). Despite ongoing debates about the detailed evolution, it is widely acknowledged that the transition from syn-orogenic to post-orogenic evolution in the Tianshan and Junggar regions occurred during the late Paleozoic to early Mesozoic (B. Wang et al., 2007, 2014; Han & Zhao, 2018; H. Huang et al., 2020; Q. G. Mao et al., 2022; G. C. Wang et al., 2022; L. Du et al., 2024). During the middle Mesozic to Cenozoic, far-field effects of the Mongol-Okhotsk Ocean closure, subduction and accretion of the Tethys system, and India-Asia collision might induce the rejuvenation of the Tianshan and Junggar belts (Jolivet, 2015; Y. T. Yang et al., 2017; Z. Y. He et al., 2022; W. Li et al., 2022; F. J. Wang et al., 2022).

1.3 Scientific questions and objectives

In the eastern North Tianshan and East Junggar, Paleozoic to Mesozoic rocks, including magmatic and sedimentary rocks, as well as some high-grade metamorphic rocks, are exposed. These rocks record vital information about the tectonic evolution of the southwestern CAOB, and conducting comprehensive research on them can enhance our understanding of orogenic processes. Nonetheless, several scientific questions remain to be answered, including issues related to the crustal basement, detailed tectonic processes, the timing of the final amalgamation, and magmatic evolution.

1.3.1 What is the nature of the basement in the eastern North Tianshan and East Junggar?

The nature of the basement in the North Tianshan and Junggar regions remains controversial. Some authors proposed that these regions are underlain by ancient continental basement as old as Archean to Paleoproterozoic (X. W. Xu et al., 2015; J. Wang et al., 2020). However, many others suggested that the basement could be juvenile continental crust primarily comprising Paleozoic orogenic systems with oceanic arcs and accretionary complexes (Chen & Jahn, 2004; D. Li et al., 2016; Han & Zhao, 2018; P. Song et al., 2019; T. Wang et al., 2023), and even oceanic crust (Carroll et al., 1990; J. P. Zheng et al., 2007; S. C. Wu et al., 2018, 2023). The main reason for this debate is that, unlike in the Central Tianshan and Yili blocks, no in-situ Precambrian basement rocks have been identified in the North Tianshan and Junggar regions. Additionally, the formation of the Junggar and Turfan-Hami basins, which are covered by Cenozoic sediments, has led to speculation about the presence of an underlying ancient continental basement. For such cases, whole-rock Nd and zircon Hf isotopic compositions of magmatic rocks, typically sourced from deep levels, can offer insights into the distribution of components within the deep, unexposed crust (e.g., H. Huang et al., 2020; T. Wang et al., 2023). Accordingly, this thesis presents the spatial and temporal distributions of whole-rock Nd and zircon Hf isotopic compositions of late Paleozoic and early Mesozoic magmatic rocks in the North Tianshan and Junggar regions. By comparing these data with those from nearby microcontinents, we aim to propose a more plausible nature of the basement in these regions.

1.3.2 What are the tectonic processes involved in the convergence of the eastern Tianshan?

The detailed tectonic processes involved in the convergence of the eastern Tianshan, particularly during the late Paleozoic when the tectonic transition may have occurred, remain unclear. Previous studies have proposed that the late Paleozoic evolution of the eastern Tianshan likely involved episodic trench retreat and advance, arc-arc collision with the East Junggar, as well as post-collisional extension (C. Yuan et al., 2010; X. J. Chen et al., 2011; Y. Y. Zhang et al., 2018; D. Li et al., 2020; Gong et al., 2023). However, these suggestions are primarily based on studies of magmatism from scattered sites. In addition, the lack of evidence concerning deformation patterns and thermal states, especially the extensional structures, render the tectonic model ambiguous. To address this issue, this thesis presents a P-T-D-t (pressure-temperature-deformation-time) investigation of the Xiaopu Metamorphic Complex (XMC) in the eastern North Tianshan, showing an inverted Buchan-type (high temperature – low pressure) metamorphic sequence characterized by extension-dominated structures. Additionally, this thesis synthesizes information on Carboniferous to Triassic magmatic rocks in the eastern Tianshan and East Junggar regions, including their spatial and temporal distribution, whole-rock elemental and Nd-isotopic characteristics, and zircon Hf isotopic compositions. Together with other evidence, we attempt to establish the tectonic processes in space and time.

1.3.3 What is the timing of the final amalgamation of the eastern Tianshan?

The timing of the final amalgamation of the eastern Tianshan has been a subject of prolonged debate. Two main hypotheses have been proposed: (1) late Carboniferous to early Permian (B. Wang et al., 2014; H. Q. Liu et al., 2016; X. R. Zhang, Zhao, Sun, et al., 2016; Han & Zhao et al., 2018; Y. Y. Zhang et al., 2018, 2020; Muhtar et al., 2020; Y. J. Wang et al., 2022), and (2) late Permian to Triassic (W. J. Xiao et al., 2009; Z. Y. Chen et al., 2019; Q. G. Mao et al., 2022; Muhtar, Xiao et al., 2023). The main reasons for this controversy include the various explanations of crustal deformation and magmatism, and age constraints of the accretionary complex. In this thesis, we aim to constrain the timing of the final amalgamation through spatial and temporal changes in magmatic characteristics, alongside crustal deformation.

1.3.4 What is the magmatic evolution during the late Paleozoic to early Mesozoic and its tectonic significance?

Late Paleozoic to early Triassic magmatic rocks are distributed in the eastern Tianshan. However, the origin and tectonic significance of these rocks, particularly the

Triassic ones, remain a matter of debate. Several models have been proposed for the geodynamic setting of the Triassic magmatism: (1) intracontinental extension (F. F. Zhang et al., 2015; Y. H. Wang et al., 2016; H. S. Sun et al., 2017; N. Li et al., 2019; S. Y. Liu et al., 2020; Lei et al., 2021; Kang et al., 2022; Yuan et al., 2023); (2) tectonic transition from syn-collisional compression to post-collisional extension (X. H. Deng et al., 2017; Y. S. Wu et al., 2017); (3) tectonic transition from supra-subduction accretion to collision (Ao et al., 2021; Q. G. Mao et al., 2021, 2022); (4) continental subduction induced by the far-filed effects of Tethys subduction (Z. Z. Zhang et al., 2005, 2007; C. Z. Wu et al., 2010). In this thesis, detailed investigations of the Triassic magmatism are presented to specify the early Mesozoic geodynamic context of the eastern Tianshan. By comparing with the late Paleozoic rocks, we try to establish the magmatic evolution during the late Paleozoic to early Mesozoic.

Chapter 2. Geological background

2.1 Tectonic units of the southwestern Central Asian Orogenic Belt

The southwestern CAOB comprises the Tianshan orogen and Junggar belt in northwestern China, Kyrgyzstan, and southern Kazakhstan (Figure 2.1). According to the distributions of ophiolite belts and major faults, the Tianshan orogen is traditionally divided into four tectonic domains: South Tianshan, Central Tianshan (or Middle Tienshan), Kyrgyz North Tienshan-Yili Block, and North Tianshan (e.g., J. Gao et al., 2009). The Junggar belt, located at the north of the Tianshan orogen, includes the West Junggar and East Junggar, and the intervening Junggar Basin (Figure 2.1).

The Chinese South Tianshan and Kyrgyz South Tienshan share similar tectonics and are parts of one tectonic belt that is termed as South Tianshan (STS) here. The STS is separated from the North Tarim Craton (NTC) by the North Tarim-Xinger Fault (Figure 2.1). It mainly comprises Precambrian basement rocks representing fragments of the NTC, Early Paleozoic arc sequences, and Late Paleozoic volcano-sedimentary sequences (B. F. Han et al., 2011; X. S. Wang et al., 2018; Biske et al., 2019; L. L. Zhong et al., 2019; F. Song et al., 2024). A remarkable feature of the South Tianshan is the occurrence of two ophiolitic mélange zones. The northern ophiolitic mélange zone is defined by a series of mélanges and HP/UHP metamorphic complexes developed along the Atbashi-Nalati-Baluntai-Sangshuyuanzi Fault (Gao & Klemd, 2003; L. F. Zhang et al., 2007; W. Lin et al., 2009; Hegner et al., 2010; B. Wang et al., 2011, 2018; T. Jiang et al., 2014; Klemd et al., 2015; X. S. Wang et al., 2018; Tan et al., 2019). The ophiolitic mafic rocks mostly belong to MORB (mid-ocean-ridge basalt) and OIB (ocean-island basalt) with minor SSZ-type (supra-subduction zone) rocks, showing ages of ~600 Ma to 332 Ma (Y. P. Dong et al., 2005; L. L. Long et al., 2006; B. Wang et al., 2011, 2018; J. Gao et al., 2022). The southern ophiolitic mélange zone consists of several ophiolitic mélanges dominated by Ordovician to Devonian SSZ-type mafic rocks. Geochemical and structural studies indicate that these ophiolitic mélanges were

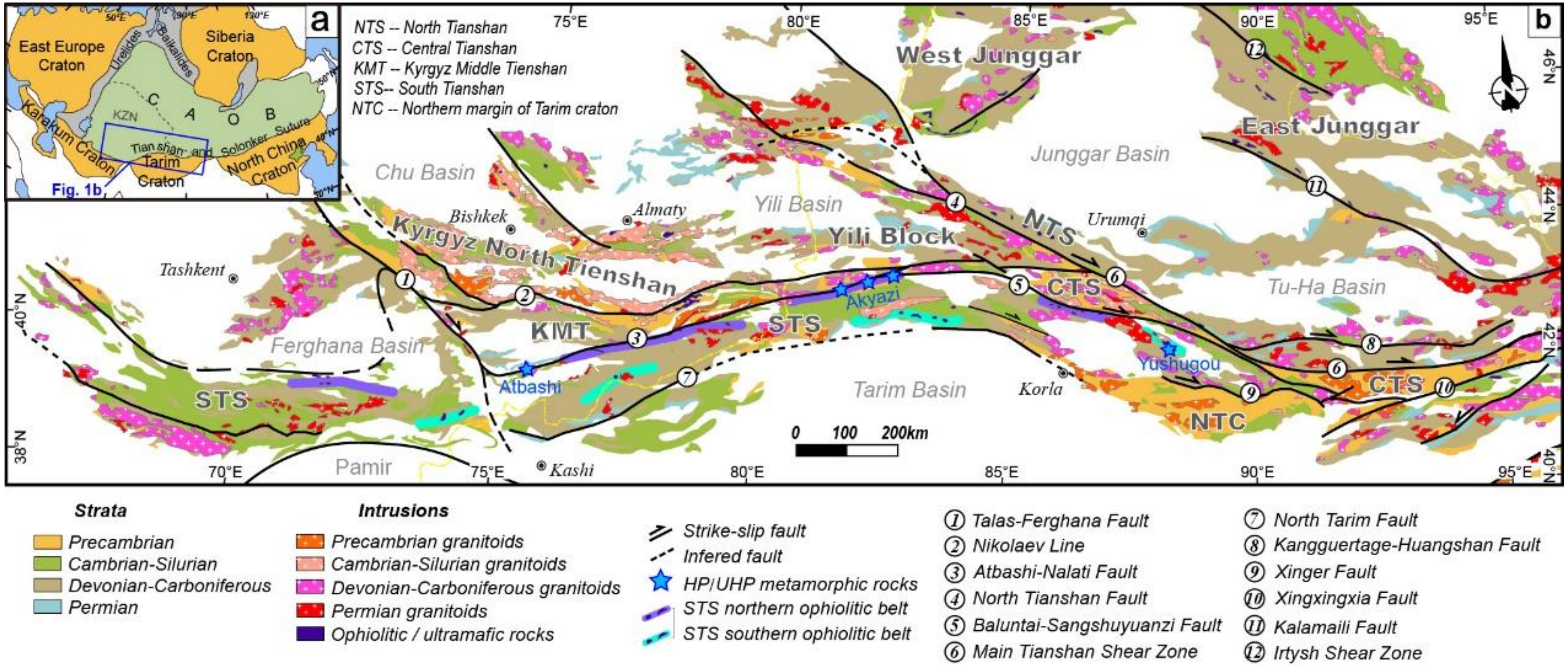

Figure 2.1. (a) Tectonic position of the Central Asian Orogenic Belt (CAOB) (modified after Sengör et al., 1993). Abbreviation: KZN, Kazakhstan microcontinent. (b) Geological map of the Tianshan Orogen and adjacent regions (modified after XBGMR, 1993; Alexeiev et al., 2015).

formed in a back-arc setting (J. Gao et al., 1998; Y. P. Dong et al., 2005; L. L. Long et al., 2006; Charvet et al., 2007; B. Wang et al., 2011).

The Central Tianshan (CTS), separated from the South Tianshan by the Atbashi-Nalati-Baluntai-Sangshuyuanzi Fault, is a strip-like continental block that extends from Xingxingxia and Baluntai areas in China and to the Middle Tienshan in Kyrgyzstan (Figure 2.1). This block contains Precambrian basements and overlying Paleozoic volcanic-sedimentary strata. The basements consist of Meso- to Neo-proterozoic schists, paragneiss and granitic gneisses (J. Gao et al., 1998; A. Q. Hu et al., 2000; S. W. Liu et al., 2004; Kröner et al., 2013; Z. Y. He et al., 2015; X. S. Wang et al., 2017; Z. Y. Huang et al., 2019). Paleozoic strata are dominated by Cambrian-Carboniferous greenschists, slates, limestones, and volcanic-siliciclastic rocks. Paleozoic magmatic intrusions with crystallization ages of ~500 to ~260 Ma are widely distributed in the region (e.g., Lei et al., 2011; Y. P. Dong et al., 2011; Seltmann et al., 2011; X. X. Ma et al., 2014; X. R. Zhang, Zhao, Eizenhöfer, et al., 2016; B. Wang et al., 2022).

The Kyrgyz North Tienshan-Yili Block (KYB) is located between the Nikolaev Line-North Nalati Fault and the North Tianshan Fault (Figure 2.1). It has basement rocks of Meso- to Neoproterozoic high-grade orthogneisses, paragneisses, amphibolites, micaschists, and marbles (H. S. Liu et al., 2014; B. Wang et al., 2014, 2022; Huang et al., 2016; X. Y. Zhu et al., 2019, 2020; Z. C. Sun et al., 2021). Unconformably overlying these basement rocks are late Neoproterozoic limestones and siltstones, early-middle Paleozoic carbonate, clastic rocks, and mid-late Paleozoic volcanosedimentary sequences. Widespread Paleozoic arc-type magmatic intrusions (~470 to ~260 Ma) are dominated by calc-alkaline felsic-intermediate magmatic suites with sparse mafic components (B. Wang et al., 2008, 2009, 2022; Biske and Seltmann, 2010; J. S. Liu et al., 2022; X. Zhao et al., 2024).

The North Tianshan (NTS) is separated from the CTS and Yili blocks to the south by the North Tianshan Fault and Main Tianshan Shear Zone (Figure 2.1; L. S. Shu et al., 1999; Laurent-Charvet et al., 2003). Late Devonian to early Carboniferous ophiolitic rocks occur along or close to the North Tianshan Fault and Main Tianshan Shear Zone, which represent accretionary wedge complexes termed the North Tianshan ophiolite belt (X. C. Xiao et al., 1992; X. Y. Xu et al., 2006). The NTS mainly consists of Paleozoic sedimentary-volcanic sequences and magmatic intrusions, without proven Precambrian rocks. The Paleozoic strata include sporadic Ordovician-Silurian tuffaceous siliciclastic rocks and limestones, widespread Devonian-Carboniferous volcanic rocks and marine limestonesiliciclastic rocks, and some Permian volcanic and terrestrial clastic rocks (X. J. Chen et al., 2014; M. Zhang et al., 2021). Paleozoic intrusive and eruptive magmatism occurred pervasively in an era between ~470 and ~260 Ma (e.g., X. J. Chen et al., 2011; W. Xie et al., 2016; Y. J. Wang, Zhu, et al., 2022; L. Gong et al., 2023; L. Du et al., 2024).

The West Junggar is characterized by the predominance of Paleozoic volcanic-sedimentary sequences and magmatic intrusions, a large number of ophiolitic fragments, and the absence of Precambrian rocks (Feng et al., 1989; Y. X. Wang et al., 2003; Choulet et al., 2012; J. E. Zhang et al., 2021). The Paleozoic volcanic-sedimentary sequences mainly contain Ordovician to Silurian low-grade schists, phyllites, and tuffaceous siliciclastic rocks, Devonian to early Carboniferous siliciclastic rocks and felsic-mafic volcanic rocks, and Permian terrestrial volcanic and clastic successions (Wei et al., 2011; J. E. Zhang et al., 2018). Paleozoic magmatic rocks have crystallization ages ranging from ~520 to 260 Ma (T. F. Zhou et al., 2008; Geng et al., 2009; J. F. Chen et al., 2010; Z. Xu et al., 2012; J. E. Zhang et al., 2021). Ophiolitic rocks in the West Junggar mostly belong to SSZ-type and MORB and have ages from ~570 Ma to 340 Ma (Y. X. Wang et al., 2003; Han & Zhao., 2018; J. E. Zhang et al., 2021; J. Gao et al., 2022).

The East Junggar is bounded by the Kalamaili Fault to the south and the Irtysh Shear Zone to the north (Figure 2.1). It is dominated by Ordovician to Permian volcanic and siliciclastic rocks, limestones, and cherts, with the early Paleozoic Zhaheba-Aermantai ophiolite belt extending through its central part (e.g., W. J. Xiao et al., 2006).

Ordovician-Permian magmatism was intensive in the East Junggar and have crystallization ages of ~460 to 260 Ma (W. Liu et al., 2013, 2021; Y. Y. Zhang et al., 2015; J. J. Zhang et al., 2017; D. Li et al., 2020, 2024; J. Wang et al., 2022).

The Junggar Basin is a large intraplate basin (an area of ~137,000 km^2) located between the West Jungar, East Junggar, and North Tianshan (Figure 2.1; Y. J. Wang et al., 2018). It is filled with thick Mesozoic to Cenozoic sediments, which precludes the investigation of its basement (e.g., Bian et al., 2010). Based on seismic profiles and drilling data, recent studies show that the basement is composed of Caboniferous volcano-sedimentary sequences and underlying strata (D. F. He et al., 2013; D. Li et al., 2015, 2016; Y. J. Wang et al., 2018; Han et al., 2019; Y. Liu et al., 2019; Wang et al., 2021).

2.2 Geology of the Chinese Eastern Tianshan and East Junggar

2.2.1 Chinese Eastern Tianshan

The Chinese Tianshan can also be divided into eastern and western parts, either by longitude ~88°E or by the Urumqi-Korla line (e.g., B. Wang et al., 2022). This study is focusing on the eastern part of Chinese Tianshan and Junggar belt, that is, the Chinese Eastern Tianshan and East Junggar. The Chinese Eastern Tianshan, from morth to south, contains the Harlik Arc, Bogda Belt, Dananhu Arc, Kanggur Belt, Yamansu Arc, and the eastern part of the CTS (Figure 2.2; W. J. Xiao et al., 2004; Han & Zhao, 2018), which are covered by the Mesozoic-Cenozoic sediments in the Turpan-Hami Basin.

The Harlik Arc is situated to the northeast of the Turpan-Hami Basin and is separated from the East Junggar Belt by the Kalamaili fault zone and associated ophiolitic mélanges (Figure 2.2). It mainly comprises Ordovician to Carboniferous sedimentary and volcanic strata, with sparse Permian and Jurassic sedimentary rocks (XBGMR, 1993). The Ordovician to Silurian Huangcaopo Group are exposed along the northeastern Harlik Mountain and consist of slate, metasandstone, conglomerate, and minor mafic to felsic volcanic rocks (X. P. Long et al., 2012; X. J. Chen et al., 2014; L.

Li et al., 2021; H. Zhao et al., 2022). The late Silurian-Devonian strata strata are locally distributed in the Harlik Mountain and is generally dominated by carbonatite, silicalite, and terrigenous clastic rocks (M. Zhang et al., 2021; H. Zhao et al., 2022). The Carboniferous strata unconformably overlie the Devonian strata and are composed of marine-terrigenous facies coarse clastic rocks with some bimodal volcanic rocks (B. Huang et al., 2018). The Permian and Jurassic strata unconformably overlie the Carboniferous strata and mainly consist of conglomerate, sandstone, and silstone. In addition, Ordovician-Silurian mafic to felsic plutonic rocks in the Harlik belt were emplaced in two episodes at 470-420 Ma and 350-280 Ma (e.g., Yuan et al., 2010; L. Du et al., 2018, 2024; D. Xiao et al., 2020; L. Li et al., 2022, 2023; P. Song et al., 2023).

The Bogda Belt is the mountain range west of the Harlik Arc, located between the Junggar and Turpan-Hami basins. It is predominantly composed of Carboniferous to Permian volcanic-sedimentary sequences (Gu et al., 2001; Shu et al., 2011; Xie et al., 2016). Devonian strata are only exposed in the east close to the Harlik Arc and contain tuff and tufficeous sandstone with some basalts and andesites interlayers (Cui et al., 2015). The Carboniferous strata are in fault contact with the Devonian rocks and consists mainly of marine volcanic ignimbrite, tuffaceous sandstone, and bimodal volcanic lava, with some conglamerate, sandstone, amd limestone (X. J. Chen et al., 2013; Xie et al., 2016; Y. Y. Zhang et al., 2017; Wali et al., 2018.; Alexeiev et al., 2019; Memtimin et al., 2020). The Permian strata unconformably overlie the Carboniferous rocks and are composed of terrestrial conglomerate, sandstone, siliceous mudstone, and limestone, intercalated with bimodal volcanic lava (X. J. Chen et al., 2011; Shu et al., 2011; D. D. Liu et al., 2018; J. L. Wang et al., 2018; Y. L. Li et al., 2022). The Triassic to Cretaceous strata are exposed in the north and south of the Bogda Mountain and mainly consist of red conglomerate, sandstone, and mudstone (J. L. Wang et al., 2018; Fang et al., 2019). Magmatic rocks in Bogda Belt have ages ranging from 350 Ma to 280 Ma. The typical characteristics of the magmatic activity are multi-stage bimodal volcanic rocks with A-type felsic endmembers, such as ~345 Ma Hongshankou bimodal volcanism, ~330 Ma Dashitou bimodal volcanism, and ~295 Ma bimodal volcanism in Baiyanggou, Qijiaojin, Hongshankou, and Cheguluquan areas (X. J. Chen et al., 2011, 2013; Y. Y. Zhang et al., 2017). Magmatic intrusions in Bogda are usually small and characterized by a large number of mafic rocks (Memtimin et al., 2020; D. H. Long et al., 2021).

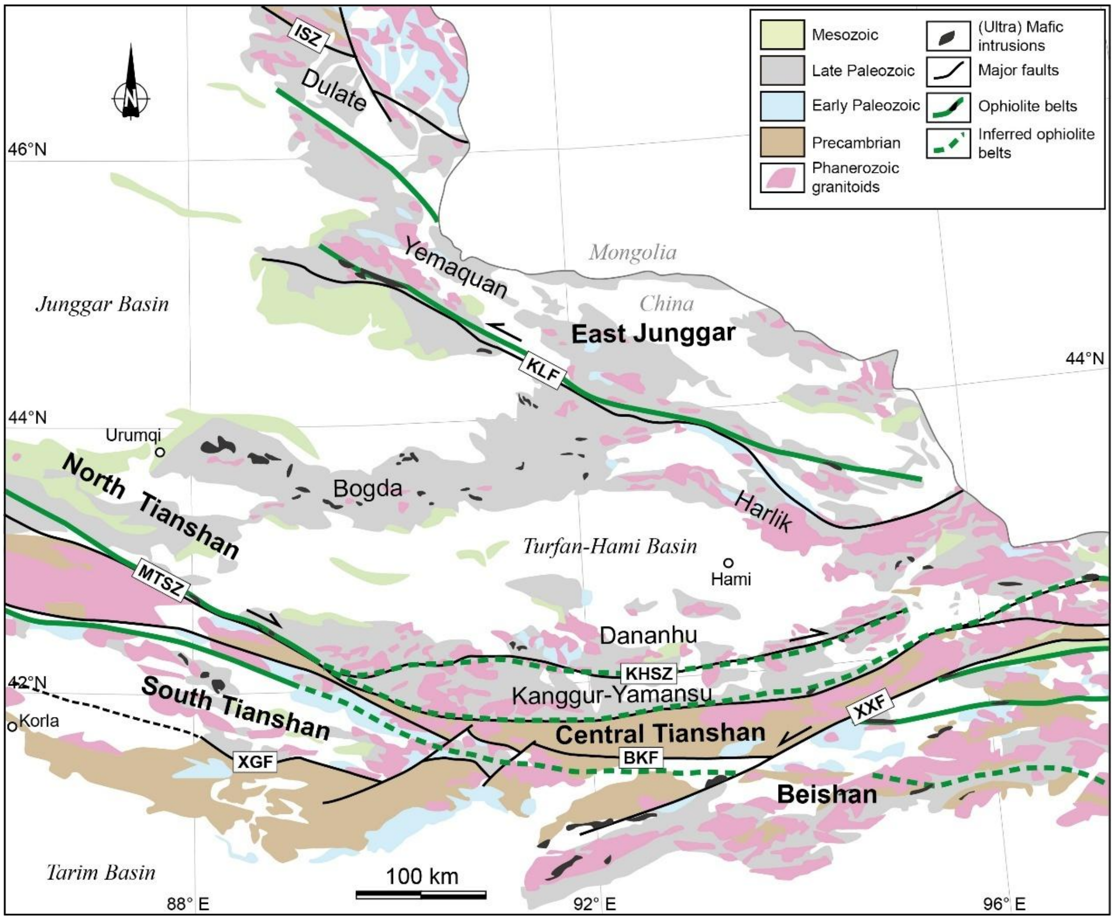

Figure 2.2. Simplified geological map of the Chinese Eastern Tianshan and East Junggar (modified after Han & Zhao, 2018). Abbreviation: ISZ, Irtysh Shear Zone; KLF, Kalamaili Fault; MTSZ, Main Tianshan Shear Zone; KHF, Kanggur-Huangshan Shear Zone; XXF, Xingxingxia Fault; BKF, Baluntai-Kawabulake Fault; XGF, Xingger Fault.

The Dananhu Arc, located to the south of the Turpan-Hami Basin, mainly consists of Ordovician to Permian volcanic and sedimentary rocks similar to that of the Harlik Arc (W. J. Xiao et al., 2004). The oldest sedimentary rocks are those of the Ordovician

Huangcaopo Group, which mainly comprises intermediate-felsic volcanic rocks interlayered with basalt and radiolarian siliceous rocks (Q. G. Mao, Wang, et al., 2021; H. Zhao et al., 2022). The Silurian strata consist of andesite and breccia lavas, dacite, tuff and tufficeous sandstone (Q. G. Mao, Wang, et al., 2021; H. Zhao et al., 2022). The Devonian strata unconformably overlie the Ordovician-Silurian strata and are composed of pyroclastic rocks and clastic sediments, interbedded with intermediate to felsic volcanic lavas (Q. G. Mao, Wang, et al., 2021). The Carboniferous rocks mainly include mafic to felsic lavas, pyroclastic rocks, greywacke, and carbonate (Z. L. Li, et al., 2011; Q. G. Mao, Wang, et al., 2021). The Permian strata consist of mafic-felsic volcanic rocks and clastic sediments (Q. G. Mao, Xiao et al., 2021; J. Y. Qin et al., 2022). The Triassic is absent in the area and the Jurassic contains black shale, sandstone,and coalbed, which lie unconformably on older strata. Paleozoic magmatic events occurred continuously in the Dananhu belt (J. Wang, Zhu, et al., 2022; Gong et al., 2023), consisting of Ordovician to Permian mafic to felsic lavas (Q. G. Mao et al., 2022a), granitic intrusions (Du et al., 2018, 2019; Y. Sun, Wang, Wang, et al., 2019; J. Wang et al., 2022), and extensive early Permian mafic-ultramafic complexes (W. J. Xiao et al., 2004; K. Z. Qin et al., 2011; Y. Sun, Wang, Lv, et al., 2019). Some Triassic magmatic intrusions that comprise mafic and granitic rocks have also been identified (S. Y. Liu et al., 2020; Y. F. Wang et al., 2022; Muhtar et al., 2024). Recently, the Dacaotan ophiolite has been identified in central part of the Dacaotan area and zircon ages of 468-417 Ma are obtained for the ophiolitic rocks (W. Wang et al., 2024). In addition, multiple types of mineral deposits have been documented in the Dananhu Arc, such as VMS (volcanogenic massive sulfide) Cu-Zn-(Au/Ag) polymetallic deposits (Deng et al., 2018; Chai et al., 2019; Q. G. Mao et al., 2020), porphyry Cu (Au/Mo) deposits associated with adakitic intrusions (C. M. Han et al., 2006; L. C. Zhang et al., 2006; Q. G. Mao et al., 2018; Gong et al., 2023); and Cu-Ni sulfide deposits associated with the Early Permian mafic-ultramafic complexes (C. M. Han et al., 2010; K. Z. Qin et al., 2011; Cheng et al., 2023).

The Kanggur Belt, also known as the Kanggur-Huangshan Shear Zone (e.g., B. Wang et al., 2014), separates the Dananhu Arc in the north and the Yamansu Arc in the south. This belt is mainly composed of Carboniferous volcanic-sedimentary rocks, including conglomerate, sandstone, siltstone, bioclastic limestone, basaltic and andesitic tuff. Most of these rocks have undergone greenschist facies metamorphism and ductile deformation (X. W. Xu et al., 2003; Y. Wang et al., 2008; B. Wang et al., 2014). The Kanggur Belt is characterized by the occurrence of pre-, syn-, and post-kinematic mafic to felsic intrusions relative to intense dextral transcurrent tectonics during the Permian (~290-245 Ma) (Y. Wang et al., 2008; Branquet et al., 2012; B. Wang et al., 2014; Muhtar et al., 2020; Muhtar, et al., 2023). The presence of many Carboniferous to early Permian mafic rocks, interpreted as ophiolitic slices, has led some authors to suggest that the Kanggur belt represents a suture zone (Z. Y. Chen et al., 2019; G. C. Wang, Zhang, et al., 2022). Additionally, this belt hosts a number of hydrothermal Au deposits (e.g., Kanggur and Shiyingtan, J. W. Mao et al., 2005; Muhtar et al., 2022) and magmatic Cu-Ni sulfide deposits (e.g., Huangshan and Huangshandong, M. F. Zhou et al., 2004; Branquet et al., 2012; C. Z. Wu et al., 2018).

The Yamansu Arc is mainly composed of Carboniferous to Permian volcanic-sedimentary rocks and Carboniferous to Triassic igneous intrusions (XBGMR, 1993; X. R. Zhang, et al., 2016a; Q. G. Mao, et al., 2022b). The Carboniferous strata comprise mafic to felsic volcanic rocks, pyroclastic rocks, clastic rocks, and interlayers of carbonate. The Permian strata contains marine and terrestrial clastic rocks with intercalated bimodal volcanic rocks and carbonates (T. Luo et al., 2016; H. J. Jiang et al., 2017; Z. Y. Sun et al., 2020; S. L. Zhang et al., 2021; B. Wu et al., 2023). The Carboniferous intrusions are widely developed and consist mainly of granite, granodiorite, and monzodiorite (T. F. Zhou et al., 2010; W. F. Zhang et al., 2016; Du et al., 2018b; L. D. Zhao et al., 2019a; X. P. Long et al., 2020). The Permian intrusions are dominated by K-feldspar granite and granodiorite (T. F. Zhou et al., 2010; Du et al., 2018b; S. L. Zhang et al., 2021). The Triassic intrusions mainly comprise granite and gabbro (L. D. Zhao et al., 2019b; Q. G. Mao, et al., 2022b). Moreover, the Yamansu belt hosts many Fe (-Cu) and Pb-Zn deposits, such as the Hongyuntan, Bailingshan, Aqishan, Duotoushan, Heijianshan, Weiquan, Chilongfeng, Yamansu, Heifengshan, Shuangfengshan and Shaquanzi deposits (J. S. Han et al., 2019; F. Liu et al., 2019; Z. Y. Sun et al., 2019, 2020; Dai et al., 2020).

The eastern part of the CTS is bounded by the Main Tianshan Shear Zone (or Aqikekudu-Weiya Fault) in the north and Xingxingxia and Baluntai-Kawablake Fault in the south. It is characterized by a Precambrian crustal basement, mainly including Mesoproterozoic and Neoproterozoic igneous rocks and Mesoproterozoic supracrustal rocks with ages of ~1.4-0.7 Ga (Hu et al., 2000; S. W. Liu et al., 2004; Z. Y. He et al., 2014, 2015; Z. Y. Huang et al., 2017). The basement is mainly composed of marbles, schists, gneisses, and migmatites, which has experienced greenschist to granulite facies metamorphism and are unconformably overlain by or in fault contact with Paleozoic strata (Z. Y. He et al., 2014). The Ordovician-Silurian sedimentary and volcanic rocks include greywacke, limestone, basalt, andesite, and pyroclastic rocks (X. J. Chen et al., 2014; Du et al., 2024). The Carboniferous strata unconformably overlie the older strata and consist of andesite, tuff, sandstone and limestone (X. J. Chen et al., 2014). Paleozoic magmatic intrusions are widely distributed in the CTS, with crystallization ages ranging continuously from ~500 to ~270 Ma (X. R. Zhang et al., 2015, 2016b; D. D. Li et al., 2019; Z. Y. He et al., 2024; K. Wang et al., 2024). Some Triassic magmatic intrusions that have crystallization ages of ~250-230 Ma are also exposed (Deng et al., 2017; N. Li et al., 2020; Lei et al., 2021; Q. G. Mao et al., 2022b). In addition, several Pb-Zn and Fe-Ti deposits have been documented in this belt, such as the Caixiashan, Yuxi, Weiya, and Tianhu deposits (R. Z. Gao et al., 2020; Shi et al., 2021).

2.2.2 East Junggar

The East Junggar is bounded by the Kalamaili Fault to the south and separated from the Chinese Altai to the north by the Irtysh Shear Zone. Similar to the North

Tianshan, the East Junggar is dominated by Paleozoic sedimentary-volcanic sequences and magmatic intrusions, without proven Precambrian rocks (e.g., W. J. Xiao et al., 2009; J. J. Zhang et al., 2017; P. Song et al., 2019). The East Junggar is traditionally divided into Dulate and Yemaquan arcs by the highly deformed and dismembered Zhaheba-Armantai ophiolite belt (e.g., W. J. Xiao et al., 2004). Zircon U-Pb dating of the ophilitic rocks indicates ages of 503 to 481 Ma for this ophiolite belt (Jian et al., 2003; W. J. Xiao et al., 2006; Zeng et al., 2015; J. Luo et al., 2017).

The Dulate arc extends along the northern side of the Zhaheba-Armantai ophiolite and are dominated by Devonian to Carboniferous volcanic-sedimentary sequence and Mesozoic coal-bearing sedimentary rocks (Z. C. Zhang et al., 2009). The Devonian strata mainly consist of basalt, andesite, dacite, tuff, tuffaceous sandstone, and siltstone. The Carboniferous strata unconformably overlie the Devonian strata and are composed of basalt, basaltic andesite, sandstone, black shale, and chert (Z. C. Zhang et al., 2009; D. Li et al., 2014). There is also an unconformity between the lower and upper Carboiferous units. Magmatic intrusions consist of dioritic and granitic rocks with crystallization ages of 390-360 Ma and 340-280 Ma (Liang et al., 2016; P. Song et al., 2019; Tang et al., 2019; Liu et al., 2021).

The Yemaquan Arc is situated south of the Zhaheba-Aermantai ophiolite and consists of Ordovician-Carboniferous clastic rocks and carbonates, along with subordinate volcaniclastic rocks. The Ordovician volcanic rocks are mainly basalt, basaltic trachyandesite, and trachyandesite with minor dacite, rhyolite, breccia, and tuff (X. W. Xu et al., 2013; Q. Q. Xu et al., 2020). The Silurian strata unconformably overlie the Ordovician units and contain conglomerate, sandstone, tuffaceous sandstone, limestone, and tuff (X. P. Long et al., 2012; Q. Q. Xu et al., 2020). The Devonian strata comprise clastic sedimentary and pyroclastic rocks, such as tuffaceous conglomerates, tuffaceous sandstone, sandstone, and tuff interbedded with limestone. The lower Carboniferous units are composed of clastic sedimentary and pyroclastic rocks, mainly siltstones, tuffaceous sandstones, conglomerates, silty mudstones, and thin-bedded tuffs.

The Upper Carboniferous unconformably overlies the Lower Carboniferous and consists of basaltic and andesitic porphyries, tuffaceous breccias, breccias, and tuffs (Q. Q. Xu et al., 2020). The Permian strata are composed of basaltic andesites, andesites, and breccia interbedded with tuff and siltstones (Bo et al., 2021). Magmatic intrusions are dominated by intermediate-felsic rocks with crystallization ages of 470-390 Ma and 330-280 Ma (Yang et al., 2011; X. W. Xu et al., 2013; J. J. Zhang et al., 2017; D. Li et al., 2024). During the late Carboniferous and Permian time, this region is characterized by the emplacement of many alkaline and A-type granitic intrusions (B. F. Han et al., 2006; Shen et al., 2011; Yang et al., 2011).

Chapter 3. Methods of study

3.1 Field observation and structural analysis

For this thesis, petrographic and structural analyses were conducted throughout the eastern Tianshan, with a primary focus on the Harlik and Bogda mountains, where outcrop conditions are excellent. Planar and linear fabrics, along with kinematic criteria related to deformation, were systematically measured. We propose new geological maps of the studied areas, accompanied by structural maps and cross-sections. Additionally, more than 100 samples were collected for petrographic and microstructural analyses. Thin sections were prepared perpendicular to the schistosity and parallel to the mineral-stretching lineation (XZ planes).

3.2 Whole-rock geochemistry

All the samples for whole-rock geochemical analysis were crushed into powders of ~200 mesh in an agate shatter box. Major and trace elements were both obtained at the ALS Minerals in Guangzhou, China. Major elements were analyzed by an ARL-9800 X-ray fluorescence spectrometry (XRF) using fused lithium tetraborate glass pellets. The accuracy of the analyses is better than 1% for most major elements. Trace elements were determined by using a Finnigan Element II ICP-MS with the GSR-3 as the reference material. Powdered samples (~50 mg) were placed in a steel-bomb with mixed HF and HNO_3 acid for 48 hours in order to assure complete dissolution of the refractory minerals. Analytical precision was 0.7-5%.

3.3 Mineral chemistry and compositional mapping

The chemical composition of main mineral phases was determined by using JEOL JXA-iHP200F field-emission electron microprobe and Cameca SX Five electron microprobe housed at ISTO in Orleans, France. Point measurements were performed at classical analytical conditions with 15 kV acceleration voltage, a 10 nA beam current, and a 1 μm spot size. Analyzed elements are Si, Ti, Al, Fe, Mn, Mg, Ca, Na, and K. All data were updated using standard ZAF correction procedures.

Two areas of migmatite 19Q22A and one area of schist 19Q21A were investigated via three maps acquired at 15 keV accelerating voltage, a specimen current of 100 nA, and a step size of 2 or 4 μm. Data reduction was performed using XMapTools (Lanari et al., 2014). All the pixels were classified and calibrated using either the internal standardization procedure including a pseudo-background correction or by manual calibration (Lanari et al., 2019). Area 1 of migmatite 19Q22A (19Q22A-1) was selected to calculate local bulk composition (LBC) based on density-corrected maps (Lanari & Engi, 2017). It is a rectangular area of 1.28 × 1.28 mm investigated with a step size of 4 μm. The X-ray maps have a resolution of 320 × 320 corresponding to a total of 102,400 pixels. The average density of each mineral phase was from the XMapTools. The mineral phases of garnet, biotite, muscovite, and plagioclase were standardized using the internal standardization procedure, whereas quartz, sillimanite, and ilmenite were standardized using manual calibrations based on theoretical compositions.

3.4 Phase modeling

Phase equilibrium modeling was conducted in the MnO-Na_2O-CaO-K_2O-FeO-MgO-Al_2O_3-SiO_2-H_2O-TiO_2 (MnNCKFMASHT) system using the Perple_X software version 7.1.1. (Connolly, 2005, 2009) with the internally consistent thermodynamic data set (hp02ver.dat) and the equation of state for H_2O of Holland & Powell (1998). The following solid solution models were used: staurolite, garnet, cordierite, chlorite, chloritoid, biotite, orthopyroxene and spinel after Holland & Powell (1998), feldspar after Fuhrman & Lindsley (1988), white mica after Coggon & Holland (2002), ilmenite from White et al. (2000), and silicate melt after Holland & Powell (2001). The pseudosection was calculated under a fluid-saturated condition for sample 22TS68B that formed under subsolidus condition. For the migmatite 19Q22A, the H_2O contents were determined by calculating T-X (H_2O) diagrams. As apatite was observed in the samples, the CaO of the WBC was corrected by assuming all of the P_2O_5 is from apatite.

The CaO of the LBC is not corrected due to the absence of apatite in the mapping area.

3.5 LA-ICP-MS zircon, monazite, and apatite U-Th-Pb dating

Zircon, monazite, and apatite grains were separated from representative samples via heavy liquid and magnetic separation, and then by hand-picking under a binocular microscope. Colorless and transparent grains without fractures or inclusions were selected for mounting in epoxy discs which were then polished. To decipher the morphology and internal texture of the minerals, cathodoluminescence (CL) images of zircon and back-scattered electron (BSE) images of monazite and apatite were obtained at the Nanjing Hongchuang Geological Service (NJHC).

LA-ICP-MS zircon U-Pb dating was carried out at the State Key Laboratory for Mineral Deposits Research (SKL-MDR) of Nanjing University, using an Agilent 7500s ICP-MS coupled with a New Wave 193 nm laser ablation system. The diameter of the laser beam is 32 μm and the repetition rate is 5 Hz. Each experiment unit includes ten analyses of unknown-age zircon grains. To monitor instrument stability and to control analytical uncertainty, an internal standard zircon GJ (608 ± 1.5 Ma; Jackson et al., 2004) was analyzed twice and an external standard zircon MudTank (732 ± 5 Ma; Black & Gulson, 1978) was analyzed once at the beginning and end of the experiment unit. The software package GLITTER (version 4.4; http://www.glitter-gemoc.com/) was used to guide analyses and to output the raw data. Common Pb was corrected by the Microsoft Excel embedded program ComPbCorr#3 15G (Andersen, 2002). Isoplot 4.15 (Ludwig, 2011) was used to plot the corrected results.

Monazite and apatite LA-ICPMS U-Th-Pb dating was carried out at SKL-MDR of Nanjing University, utilizing a system consisting of ASI RESOlution S-155 193nm ArF Excimer laser coupled to Thermo Scientific iCAP Qc quadrupole ICP-MS. Monazite was ablated with a spot size of 19 or 13 μm, a beam energy density of ~5 $J/cm^{2,}$ and a repetition rate of 3 Hz. Apatite was using a 43 or 29 μm diameter spot at a 5 Hz repetition rate with a laser fluence of 5 J/cm^2. Isotopic ratios were corrected by using Trebilcock (TIMS data at 272 ± 2 Ma, Tomascak et al. 1996) and MAD (483.33 ± 2.78 Ma, Thomson et al., 2012) as external standards for monazite and apatite respectively. Trace elements of monazite and apatite were calibrated externally against NIST SRM610, using Ce and Ca as internal standards. ICPMSDataCal version 9.9 (Liu et al., 2008) and Iolite 4 (Paton et al., 2011) were used to process the data of monazite and apatite. Isoplot version 4.15 (Ludwig, 2011) was used to make concordia plots and calculate weighted mean ages.

For zircon, given the relative imprecision of ^{207}Pb and ^{237}U measurements, ^{206}Pb/^{238}U age is used in general (Spencer et al., 2016). For monazite, ^{208}Pb/^{232}Th ages are emphasized for interpretation because excess ^{230}Th can bias ^{206}Pb/^{238}U ages (Schärer et al., 1984), while ^{207}Pb/^{235}U ages are less reliable. For apatite, as it contains a significant amount of common Pb (Chew et al., 2014), we use the Tera-Wasserburg diagram to plot the results.

3.6 Biotite ^{40}Ar/^{39}Ar dating

^{40}Ar/^{39}Ar analyses were carried out at the dating laboratory of the ISTO, Orléans University. Fresh biotite grains were selected from the sillimanite schists. Standard processes (crushing, hand-picking under a binocular microscope, and ultrasonic cleaning) were applied to achieve the highest possible purity of mineral concentrates. The neutron irradiation was conducted at the CLICIT Cd-lined slot of the Corvallis Nuclear Reactor (Oregon State University, United States) for 10 hours along with the FCS standard (28.02 ± 0.28 Ma, Renne et al., 1998). ^{40}Ar/^{39}Ar experiments were performed on fine-grain biotite populations using a high-resolution Helix SFT mass-spectrometer outfitted to a CO_2-laser-based extraction system featuring ultra-low argon blanks. More detailed operating conditions can be found in Beaudoin et al. (2020). Ages and isotope ratios are plotted and tabulated at ± 2σ and were calculated according to Scaillet (2000). WMA refers to the Weighted Mean Age calculated by inverse-variance weighing of the steps pooled in the weighted mean (as indicated by the arrows in the plots). TGA represents Total Gas Age that is computed by summing the gas fractions overall steps. Pooled age errors include procedural errors, decay constants, and isotope abundance errors.

3.7 Whole-rock Sr-Nd isotopes

Whole-rock Sr-Nd isotopic measurements were carried out at the NJHC. Samples were measured by Neptune plus MC-ICP-MS through 50ul PFA Cetac Aridus II membrane desolvation system. Normalizing factors used to correct the mass fractionation of Sr and Nd during the measurements were $^{86}Sr/^{88}Sr = 0.1194$ and $^{146}Nd/^{144}Nd = 0.7219$ with exponential law. Drift of instrument was corrected using international isotopic standards (NIST SRM 987 for Sr and JNdi-1 for Nd). BCR-2 was applied as the reference material and its isotopic ratios were in good agreement with previous publications within analytical uncertainty (Weis et al., 2006). The εNd(t) values and single-stage Nd model age (T_{DM1}) of the samples were calculated based on the Chondrite $^{147}Sm/^{144}Nd$ (0.1967) and $^{143}Nd/^{144}Nd$ (0.512638) ratios, and depleted mantle $^{147}Sm/^{144}Nd$ (0.2136) and $^{143}Nd/^{144}Nd$ (0.513151) ratios (Wasserburg et al., 1981). The two-stage Nd model ages (T_{DM2}) were calculated by assuming that the protolith of the igneous rocks evolved with an average continental Sm/Nd ratio ($^{147}Sm/^{144}Nd = 0.118$; Keto & Jacobsen, 1987) from its initial separation from the depleted mantle reservoir to the time of partial melting.

3.8 LA-MC-ICP-MS zircon Lu-Hf isotopes

Zircon Lu-Hf isotope analyses were conducted at the SKL-MDR using a Neptune MC-ICPMS equipped with an NWUP-193 FX LA system. A spot size of 38 μm was used and the spots of the Lu-Hf analyses partly or totally overlapped those of the U-Pb dating. The zircon standard MT and QH as reference materials yield weight mean of $^{176}Hf/^{177}Hf$ ratios 0.282505 ± 0.000013 (2σ; MSWD = 0.61; Woodheat and Hergt, 2005) and 0.283002 ± 0.000014 (2σ; MSWD = 0.47; Li et al., 2013), respectively. The εHf(t) values and single-staged depleted mantle model age (T_{DM1}) were calculated based on the Chondrite $^{176}Hf/^{177}Hf$ (0.282772) and $^{176}Lu/^{177}Hf$ (0.0332) ratios (Blichert-Toft and Albarède, 1997), and the present-day depleted mantle $^{176}Hf/^{177}Hf$ (0.28325) and $^{176}Lu/^{177}Hf$ (0.0384) ratios (Griffin et al. 2002). Two-stage Hf model age (T_{DM2}) was calculated by projecting the initial $^{176}Hf/^{177}Hf$ ratios of zircons back to the depleted mantle growth curve, and the average continental crust $^{176}Lu/^{177}Hf$ ratio of 0.015 was utilized (Griffin et al., 2002).

3.9 Magmatic data compiling and processing

The compilation of geochronological, geochemical, and isotopic results for Paleozoic to Mesozoic magmatic rocks has been carried out in some previous studies (e.g., Q. G. Mao et al., 2022b; Y. J. Wang et al., 2022). Following these works, we synthesized locations, petrological features, ages, whole-rock major and trace elemental and Sr-Nd isotopic compositions, and zircon Hf isotopic results of late Paleozoic to early Mesozoic (Carboniferous to Triassic) magmatic rocks in the eastern Tianshan and East Junggar from the literature. We caution that only samples with reported or reliably estimated location information were included in the present datasets.

In some cases, the location information for a given sample was not reported or marked on the geological map by the authors. However, the longitude and latitude of one or several samples—typically those subjected to geochronological dating—within the same pluton or volcanic unit, and sharing similar petrological and geochemical characteristics, are available. In such instances, the location data of the sample(s) with reported information are used to estimate other samples from the same pluton or volcanic unit lacking specific location details.

Late Paleozoic magmatic rocks are widespread in the eastern North Tianshan and East Junggar regions. Our dataset comprises 482 geochronological dating results (including 12 new results), 2378 whole-rock major and trace element compositions (including 37 new results), 707 Sr isotopic results (including 6 new results), and 808 Nd isotopic results (including 6 new results). Additionally, we have compiled 3266 zircon in situ Hf isotopic measurements from 212 late Paleozoic magmatic samples. Isotope and element imaging was conducted using an inverse distance weighted approach in ArcGIS (Mole et al., 2014). The method uses a 0.1 smoothing factor at a "power" of 2 in Geostatistical Analyst modeling feature of ArcGIS. Weighted average of isotope and element values in each location was utilized for contour mapping.

Triassic magmatism, by contrast, was much more limited compared to late Paleozoic activity. For the Triassic magmatic rocks in eastern Tianshan, our dataset includes 75 geochronological dating results (including 4 new results), 207 whole-rock major and trace element compositions (including 19 new results), 73 Sr isotopic results (including 2 new results), and 73 Nd isotopic results (including 2 new results). Furthermore, we have compiled 642 zircon in situ Hf isotopic measurements from 45 Triassic magmatic samples (including 4 new samples). Due to the low density of Triassic magmatic data, isotope and element mapping was inoperative.

Chapter 4. Late Paleozoic tectono-metamorphic evolution of the eastern North Tianshan: Insights from the Xiaopu Metamorphic Complex in the Harlik Range

4.1 Introduction

The North Tianshan (NTS) is considered as a composite arc system located in the southwestern CAOB. Its tectonic evolution is the key to understand the accretionary processes and geodynamics of the CAOB (W. J. Xiao et al., 2004; Charvet et al., 2007, 2011; Han & Zhao, 2018; Y. Y. Zhang et al., 2018; D. Li et al., 2020; G.C. Wang et al., 2022). Previous studies indicated that the evolution of the North Tianshan involved arc-arc collision/accretion and episodic trench retreat and advance (Y. Y. Zhang et al., 2018; D. Li et al., 2020; Gong et al., 2023). Yet, these interpretations are mostly based on sedimentary and magmatic records. The lack of evidence for deformation patterns and thermal states makes the tectonic model ambiguous. Consequently, the tectonic and geodynamic evolutions of the North Tianshan and CAOB remain controversial in terms of final amalgamation and tectonic transitions (W. J. Xiao et al., 2009; B. Wang et al., 2014, 2022; H. Q. Liu et al., 2016; X. R. Zhang et al., 2016a; Han & Zhao et al., 2018; Y. Y. Zhang et al., 2018, 2020; Z. Y. Chen et al., 2019; Muhtar et al., 2020; Y. J. Wang et al., 2022; Q. G. Mao, et al., 2022a; Q. G. Mao et al., 2022b; Muhtar, Xiao et al., 2024).

Inverted metamorphic sequences are composed of a suite of metamorphic rocks whose metamorphic conditions decrease with their increasing structural depth, and are commonly developed in the core of orogenic systems, such as in the Himalayas (e.g., Le Fort, 1975; Jamieson et al., 2004; Kohn, 2014; Mottram et al., 2014), the North American Cordillera (e.g., Graham & England, 1976; Gibson et al., 1999; Kidder & Ducea, 2007), and the French Variscan belt (e.g., Burg et al., 1984; Pitra et al., 2010). Understanding the mechanisms responsible for the development and exhumation of inverted metamorphic sequences is essential for deciphering the crustal evolution of orogens. Inverted metamorphic sequences are generally associated with crustal-scale thrusts (Burg et al., 1984; Beaumont et al., 2001; Jamieson et al., 2004). However, inverted metamorphic sequences associated with extensional structures are rarely identified and poorly understood.

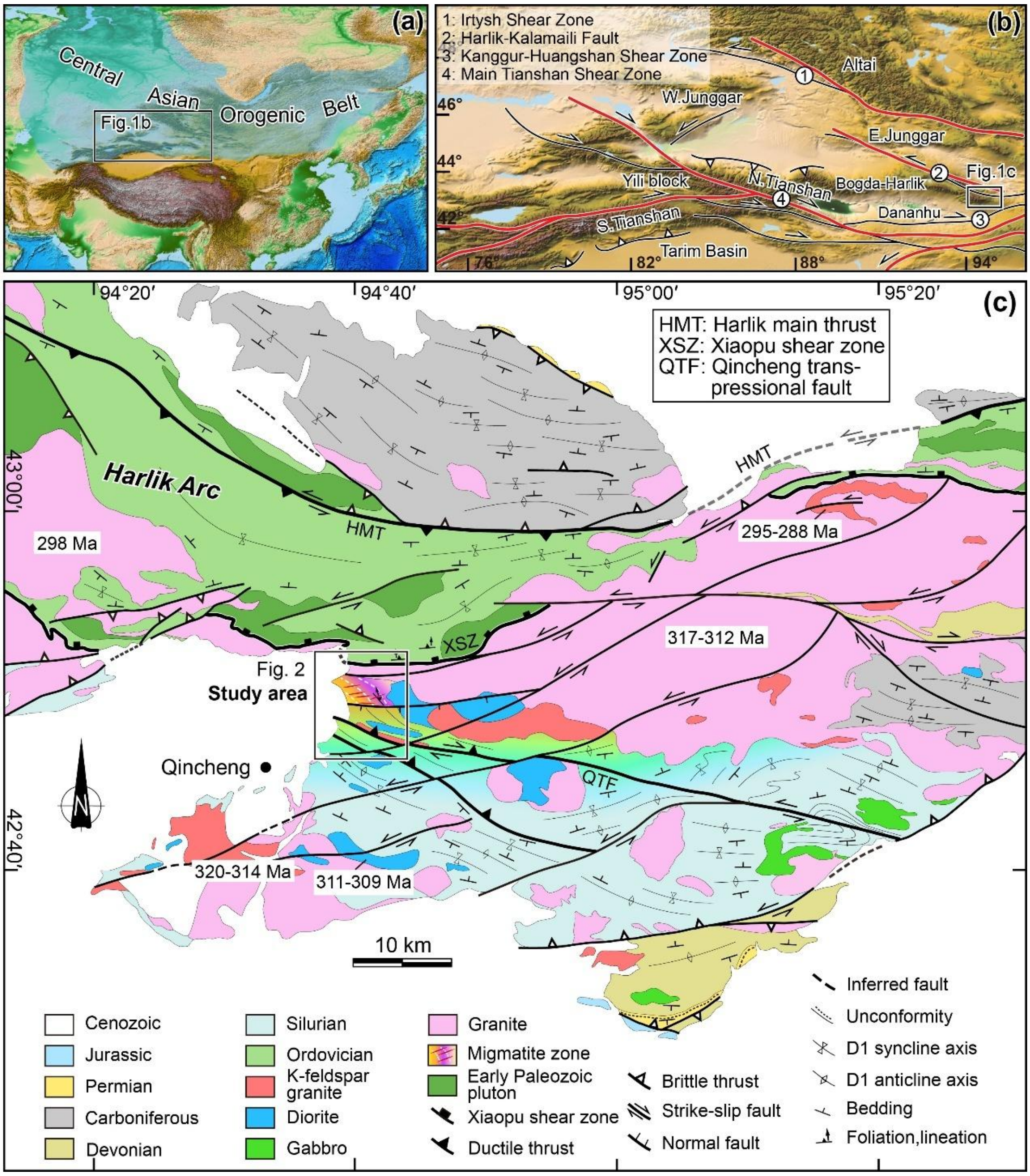

Figure 4.1. Topographic maps showing (a) the location of Central Asian Orogenic Belt (CAOB) and (b) tectonic subdivisions of the Tianshan and adjacent areas (topographic images from http://www.ngdc.noaa.gov/mgg/global). (c) Simplified geological map of the Harlik Range (modified from Sun, 2007).

In this chapter, we present a P-T-D-t (pressure-temperature-deformation-time) investigation of the Xiaopu Metamorphic Complex in the eastern North Tianshan, which shows an inverted Buchan-type (high temperature – low pressure) metamorphic sequence. Detailed structural observations, thermobarometric calculations, and geochronological data allow us to link the deformation, metamorphism, and magmatism in both space and time. Our data provide key insights into the mechanisms that generated a mid-crustal inverted metamorphic sequence in the context of crustal extension. Combined with regional data, the crustal evolution of the North Tianshan arc system from subduction-accretion to post-orogenic exhumation during the late Paleozoic is discussed.

4.2 Geology of the study area

This study focuses on the Xiaopu area of the Harlik Arc in the NTS (Figure 4.1). In this area, the Xiaopu Metamorphic Complex (XMC) covers a zone of ~10 km wide and is composed of greenschist to amphibolite facies metapelitic rocks and migmatites, as well as multiple magmatic intrusions (Figure 4.2). The XMC shows a well-preserved prograde sequence consisting of garnet, andalusite-staurolite and sillimanite-migmatite zones (Figures 4.2; M. Zhao et al., 1997; Sun, 2007).

Several magmatic intrusions, some significantly sheared, are exposed in the XMC (Figure 4.2). The largest one is the Xiaopu granitic pluton intruding the northern part of the XMC and is locally cut and deformed by the XSZ. The Xiaopu granite belongs to the high-K calc-alkaline series and was generated by partial melting of the mafic lower crust at 317-312 Ma (P. Song et al., 2018, 2023; L. Liu et al., 2020). Syn-kinematic granitic dykes from this zone yielded zircon U-Pb dates of 332-330 Ma, while undeformed leucogranite or pegmatite dykes crystallized at 309-308 Ma (X. H. Zhu et al., 2018). K-feldspar granites intruding the metapelites and the Xiaopu pluton were emplaced at 297-288 Ma (Chen & Shu, 2010; C. S. Wang et al., 2009b). A few undeformed diorites intruding the metapelites have not been dated. Most diorites and granites in the XMC show NW-orientation, whereas the leucogranite and pegmatite dykes strike along E-W or NE directions (Figure 4.2).

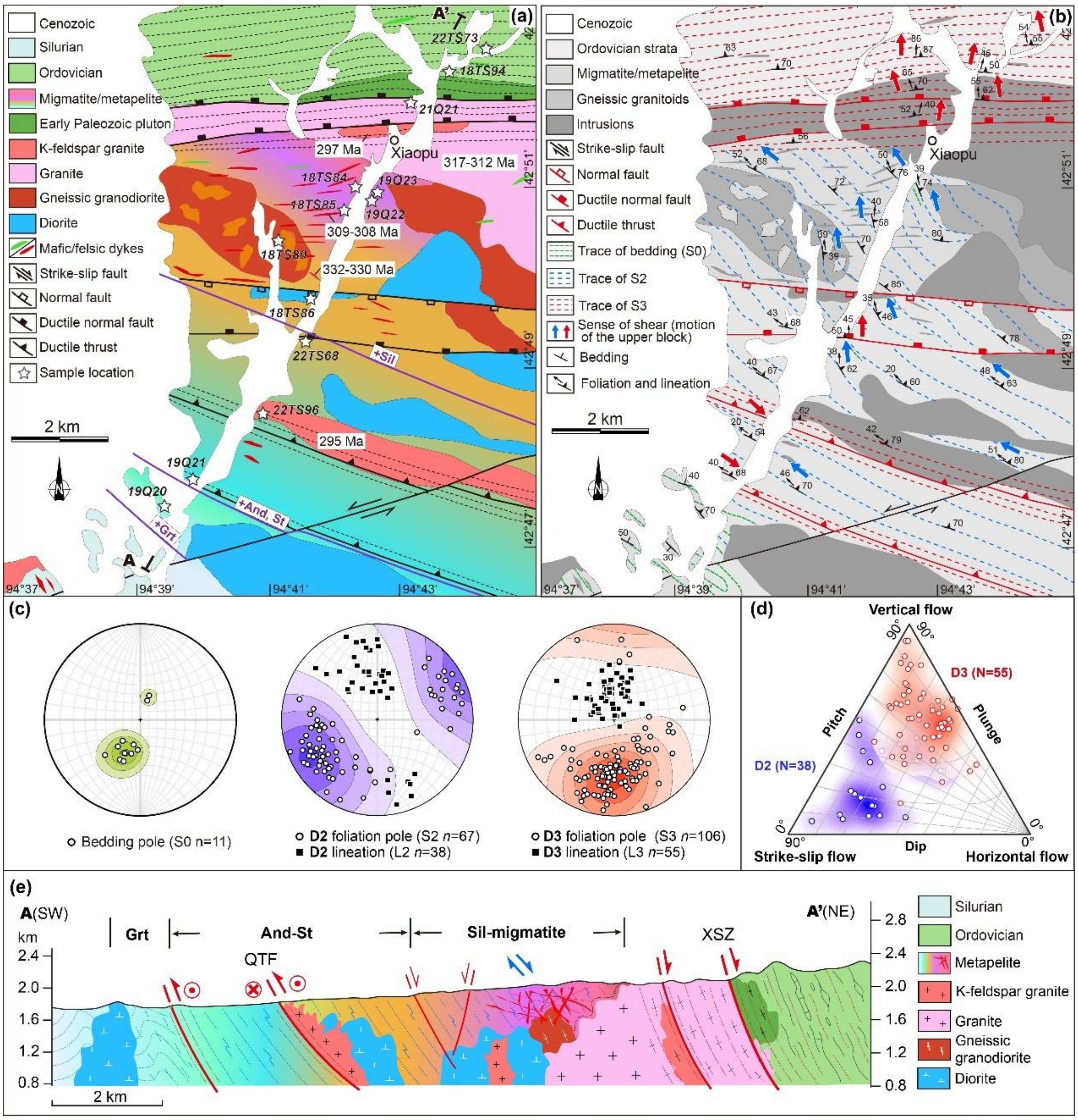

Figure 4.2. (a) Geologic map and (b) Structural sketch of the Xiaopu Metamorphic Complex (modified from Sun, 2007). Foliation trajectories were mapped after Sun (2007) and our measurements. Reference zircon U-Pb ages are from: Chen & Shu, 2010; X. H. Zhu et al., 2018; L. Liu et al., 2020; P. Song et al., 2023. (c) Stereogram of the foliation planes and lineations (lower hemisphere, equal angle). (d) Dip-Pitch-Plunge ternary diagram (after Balé & Brun, 1989 and Chardon et al., 2009). (e) Cross-section across of the Xiaopu metamorphic complex.

A maximum age of 425 Ma is given for the protolith of the metapelites based on younger detrital zircon U-Pb dates. In addition, the metapelitic rocks from the sillimanite-migmatite and andalusite-staurolite zones yielded muscovite and biotite $^{40}Ar/^{39}Ar$ cooling ages ranging from 301 to 277 Ma (Sun, 2007).

4.3 Sampling and analyzing strategies

More than 100 samples were collected from the XMC for petrographic and microstructural analyses and the locations of representative samples are presented in Figure 4.2. Four fresh samples, including two Grt-Sil migmatites (19Q22A and 19Q23A) from the sillimanite-migmatite zone and two schists (Grt-Kf schist 22TS68B and Grt-And-St schist 19Q21A) from the andalusite-staurolite zone (Figure 4.2), were selected for mineral chemical analysis and thermobarometric calculations (Table 4.1). Samples 19Q22A and 22TS68B were additionally analyzed for whole-rock geochemical compositions (WBC) to perform phase modeling using Perple_X (Connolly, 2005, 2009). In order to better constrain the protolith ages of the meta-sedimentary rocks and the timing of deformation and metamorphism, representative samples from the garnet zone, sillimanite-migmatite zone, and mylonites from the Xiaopu Shear Zone were chosen to perform LA-ICP-MS U-(Th)-Pb analyses of zircon, monazite and apatite, and $^{40}Ar/^{39}Ar$ dating of biotite (Table 4.2). Detailed analytical and computational methods are presented in Chapter 3.

4.4 Structural patterns and kinematics

In the Harlik Arc, ductile to ductile-brittle structures, such as the Harlik Main Thrust (HMT), the Xiaopu Shear Zone (XSZ), and the Qingcheng Transpressional Fault (QTF), generally strike along NW-SE or E-W directions, and are cut by brittle faults (mostly in NE-SW orientation). The XMC that consists of three metamorphic zones is separated from the Ordovician sedimentary and volcanic rocks by the XSZ (Figure 4.2). In order to characterize the deformation history of the region, detailed structural mapping was carried out based on the work of Sun (2007). The results are illustrated in a structural map, a stereogram, and a Dip-Pitch-Plunge ternary diagram (Figure 4.2). The structural analyses allow us documenting three main deformation phases (termed D1, D2, and D3) which led to the development of a series of folding, penetrative schistosity and mylonitic fabrics.

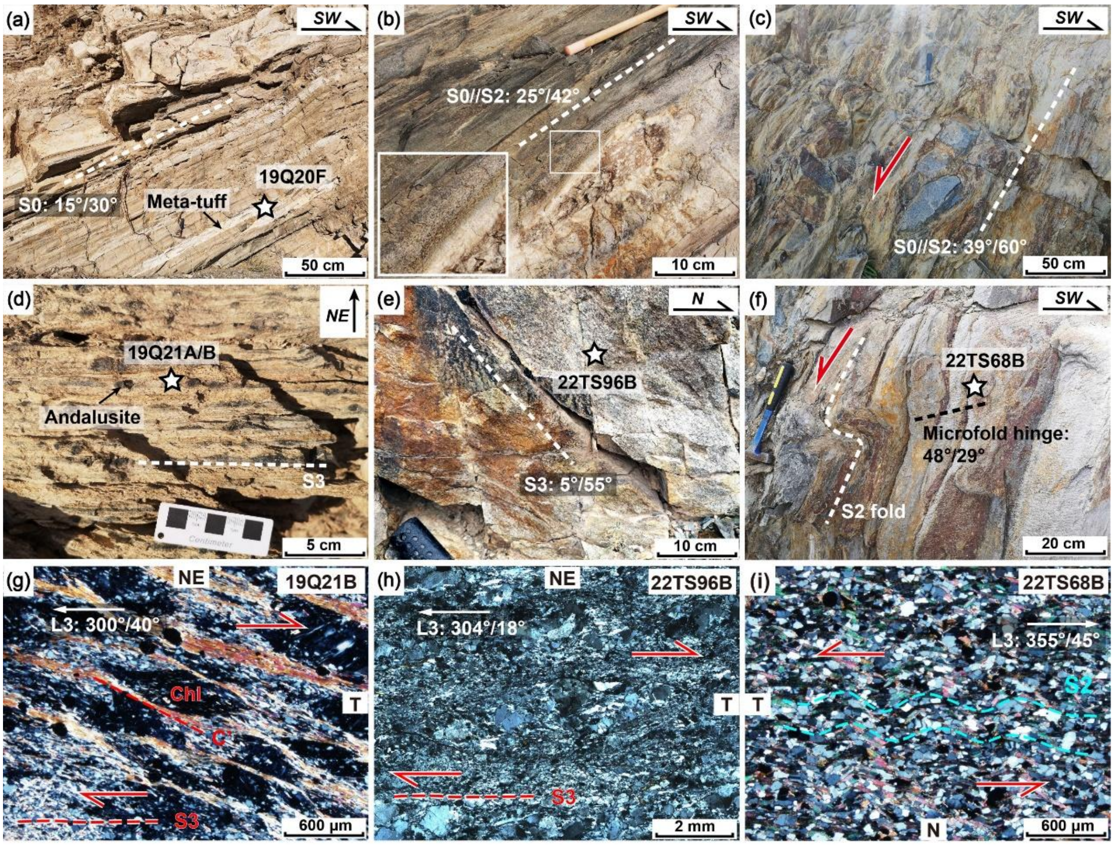

Figure 4.3. Representative photographs showing the main structures of the Grt zone (a-b) and And-St zone (c-i). (a) A field photograph in the Grt zone showing meta-tuff interbeds. (b) Parallel bedding (S0) and S2 foliation. (c) S2 parallel to S0 and lens of quartzite indicating top-to-N shearing of D2. (d) A field photograph showing andalusite-bearing rocks and the S3 foliation. (e) Mylonitic granite in the And-St zone with S3. (f) Asymmetric folds and microfolds in the Grt-Kf schist. (g) S-C' shear bands and (h) sigmoidal quartz-feldspar aggregates indicating top-to-SE shearing of D3. (i) Microfolds indicate top-to-N shearing. N, north; NE, northeast; T, top.

4.4.1 Structures of the garnet and andalusite-staurolite zones

The garnet zone is mainly composed of sandstones with interbeds of tuff and tuffaceous mudstone. The rocks are not strongly deformed so that the bedding (S0) remains recognizable in the field (Figure 4.3a). The S0 is deformed into a series of asymmetrical folds with NE-dipping axial planes (Sun, 2007), indicating a SW-NE directed shortening (D1). Tiny biotite and garnet grains are aligned to form a foliation (S2) close to the bedding (S0) in the tuffs and tuffaceous mudstones (Figure 4.3b).

The andalusite-staurolite zone comprises andalusite-staurolite schist, mica schist, garnet-K-feldspar schist and quartzite. The rocks display similar NE-dipping foliations (Figure 4.2b). The S2 foliation is locally parallel to the compositional layering (Figure 4.3c) and can be interpreted as a transposed sedimentary bedding (S0-2). Quartzite lenses in the mica schist indicate a top-to-N shearing of D2, consistent with an extension event (Figure 4.3c). Andalusite, staurolite, and biotite locally contain tiny quartz and ilmenite inclusion trails oblique or perpendicular to the S2 foliation (Figures 4.7d, 4.7f, and 4.7h), probably recording the earlier D1 phase. The D3 phase corresponds to ductile faults that heterogeneously affected both schists and K-feldspar granite (Figures 4.3d and 4.3e). The S3 foliation is parallel to S2, bearing northwest plunging lineation. Large primary biotite grains of the schists are deformed and partly replaced by chlorite along grain edges. Shear bands are mostly filled with tiny quartz, muscovite, and chlorite (Figures 4.3g and 4.8i). Both S-C' structures in the andalusite-staurolite schist and sigmoidal quartz-feldspar aggregates in the mylonitic k-feldspar granite point to a top-to-SE shearing (i.e. dextral-reverse), accounting for the QTF (Figures 4.3g and 4.3h). The mylonitic k-feldspar granite is characterized by Sub-Grain Rotation (SGR) recrystallization of quartz and kink bands of feldspar that suggest a deformation at 400-500°C (Stipp et al., 2002; Passchier & Trouw, 2005). In the northern part of the andalusite-staurolite zone, asymmetric folding of the S2 foliation associated with down-dip stretching lineation suggests the presence of a normal fault (Figures 4.3f and 4.3i). This normal fault probably occurred during the D3 stage.

4.4.2 Structures of sillimanite-migmatite zone

The sillimanite-migmatite zone is characterized by high-grade metapelites and migmatites intruded by several magmatic bodies. The foliation of sillimanite-bearing mica schists and migmatites steeply dips to the NE (S2; Figures 4.2 and 4.4). The stretching lineations (L2) have a regular NW-SE trend and low to intermediate plunge and pitch (i.e. between 20° and 60°), falling into the area close to the “strike-slip flow” of the Pitch-Plunge-Dip ternary diagram (Figure 4.2d). Leucosomes in the migmatites are parallel to the S2 foliation (Figures 4.4b and 4.4c). Locally, the S2 foliation is parallel to the compositional bands, suggesting the transposition of S0 (Figure 4.4c), and the sub-vertical compositional layering (S2) is crosscut by moderately dipping extensional melt-filled shear bands (Figure 4.4d). Shear fabrics in the schists and asymmetric strain shadows around garnet grains in the migmatites indicate that D2 is associated with a top-to-NW shearing (Figures 4.4g and 4.4h). These observations are consistent with a sinistral transtension for D2. Some garnet grains in the migmatites contain tiny quartz, biotite, and ilmenite inclusion trails oriented at a high angle to the main schistosity (Figure 4.6d), probably representing the records of the D1 phase. The gneissic granodiorites display the same foliation as the surrounding schists and both of them are crosscut by undeformed pegmatite dykes (Figure 4.4e). Undeformed diorites intruding the schists and migmatites are crosscut by a south-dipping normal fault. Such features point to the pre-D2 emplacement of the granodiorite and the post-D2 emplacement of the diorite and pegmatite, respectively.

The metamorphic grade increases from southwest to northeast and the highest grade is documented near the Xiaopu pluton where garnet and sillimanite-bearing migmatites occur. Considering the overall NE-dipping regional foliations, the spatial the structural distribution of the metamorphic subunits show an inverted Buchan-type metamorphic sequence (Read, 1952).

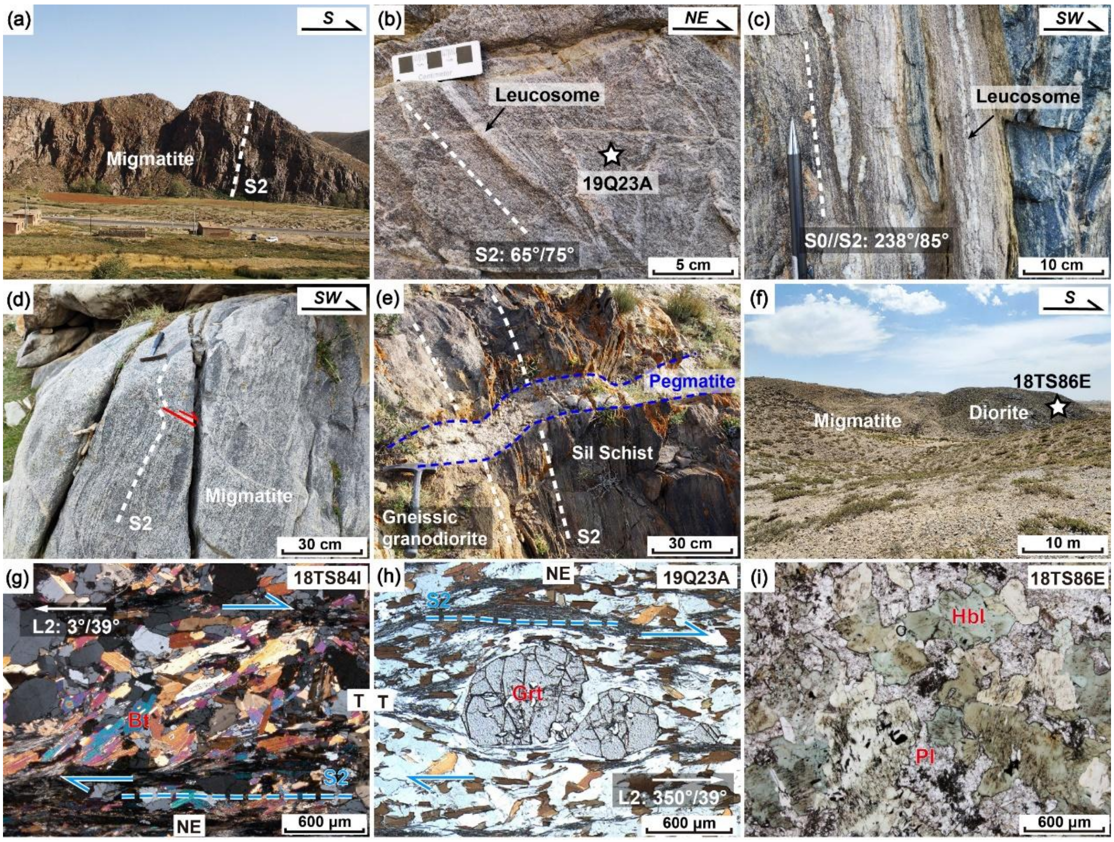

Figure 4.4. Representative photographs showing main structures of the Sil-migmatite zone. (a) A field photograph showing the S2 foliation. (b) Leucosome in the migmatite. (c) Subvertical S0 and S2 in the migmatite. (d) Subvertical migmatitic fabric (S2) with extensional shear bands. (e) Gneissic granodiorite and sillimanite-bearing schist with S2 crosscut by undeformed pegmatite. (f) Undeformed diorite crosscut the metapelitic rocks. (g) Shear bands and (h) strain shadow around garnet indicating top-to-NW shearing of D2. (i) Undeformed diorite made of hornblende and plagioclase.

4.4.3 Structures of the Xiaopu Shear Zone

The E-W-trending Xiaopu Shear Zone (XSZ) represents a major tectonic discontinuity between the Xiaopu Metamorphic Complex (footwall) and low-grade rocks in the north (hanging wall). The shear zone is more than 3 km wide, involving the Xiaopu pluton and the early Paleozoic granitoids, marbles, tuffs, and volcanic rocks (Figures 4.5a and 4.5e). Some mafic dykes intruding the Xiaopu granite are also highly deformed and both of them are crosscut by undeformed felsic dykes (Figure 4.5b).

Table 4.1. Mineral occurrence and P-T estimates of metamorphic samples from the Xiaopu Metamorphic Complex

Sample	Sample location	Dist. (km)	Mineral occurrence								Peak (M2)		Retrograde (M3)		Method (T & P)	Latitude (N)	Longitude (E)
			Grt	Bt	Ms	Pl	And	Sil	Qz	Other	T (°C)	P (kbar)	T (°C)	P (kbar)			
19Q23A	Sil-migmatite zone	0.9	x	xxx	x	xx	-	x	xxx	Ilm	654 (±25)	4.4 (±1.2)	603 (±25)	2.3 (±1.2)	GB & GBPQ	42°50'53"	94°42'49"
											653 (±25)	4.3 (±1.8)	599 (±25)	3.5 (±1.8)	GB & GBAQ		
											610-690	-	590-700	-	Ti-in-Bt		
19Q22A	Sil-migmatite zone	1.1	x	xxx	x	xx	-	x	xxx	Ilm	669 (±25)	3.4 (±1.2)	626 (±25)	2.8 (±1.2)	GB & GBPQ	42°50'50"	94°42'27"
											671 (±25)	4.3 (±1.8)	614 (±25)	3.9 (±1.8)	GB & GBAQ		
											600-720	-	560-700	-	Ti-in-Bt		
22TS68B	And-St zone	4.1	x	xxx	x	xx	-	-	xxx	Kf/Ilm	629 (±25)	4.5 (±1.2)	-	-	GB & GBPQ	42°48'21"	94°40'21"
											610-670	-	-	-	Ti-in-Bt		
19Q21A	And-St zone	7.7	x	xx	xx	x	xx	-	xx	St/Chl/Ilm	591 (±25)	4.9 (±1.2)	-	-	GB & GBPQ	42°47'43"	94°39'50"

											581 (±25)	3.4 (±1.8)	-	-	GB & GBAQ		
											540-580	-	-	-	Ti-in-Bt		

Note. Dist. refers to the minimum distance from the Xiaopu pluton. x, <10%; xx, 10-30%; xxx, 30-50%. GB: garnet-biotite geothermometer (Holdaway, 2000). GBPQ: garnet-biotite-plagioclase-quartz geobarometer (Wu et al., 2004). GBAQ: garnet-biotite-Al2SiO5-quartz geobarometer (Wu, 2017). Ti-in-Bt: Ti-in-biotite geothermometer (Henry et al., 2005)

Table 4.2. Dating results of samples from the Xiaopu Metamorphic Complex

Sample	Rock type	Sample location	Method	Age (Ma)	± 2σ	Age (Ma)	± 2σ	Latitude (N)	Longitude (E)
22TS90F	Mylonitic tuff	XSZ	Zircon U-Pb	490	3			42°54'09"	94°42'23"
19Q20F	Meta-tuff	Grt zone	Zircon U-Pb	435	7			42°47'29"	94°39'21"
18TS80B	Gneissic granodiorite	Sil-migmatite zone	Zircon U-Pb	341	3			42°50'24"	94°41'04"
18TS86E	Undeformed diorite	Sil-migmatite zone	Zircon U-Pb	305	3			42°49'52"	94°41'45"
18TS84E	Sil schist	Sil-migmatite zone	Monazite U-Th-Pb	313	1			42°51'00"	94°42'16"
19Q23A	Grt-Sil migmatite	Sil-migmatite zone	Monazite U-Th-Pb	311	1			42°50'53"	94°42'49"
21Q21A	Mylonitic granite	XSZ	Apatite U-Pb	285	10			42°51'59"	94°43'13"
22TS92B	Mylonitic tuff	XSZ	Apatite U-Pb	~280[a]		492[b]	13	42°53'45"	94°42'31"
18TS84E	Sil schist	Sil-migmatite zone	^{40}Ar-^{39}Ar (biotite)	298[c]	1	295[d]	6	42°51'00"	94°42'16"
18TS84I	Sil schist	Sil-migmatite zone	^{40}Ar-^{39}Ar (biotite)	293[c]	1	296[d]	6	42°51'00"	94°42'16"
18TS84J	Sil schist	Sil-migmatite zone	^{40}Ar-^{39}Ar (biotite)	287[c]	1	288[d]	6	42°51'00"	94°42'16"
18TS85A	Sil schist	Sil-migmatite zone	^{40}Ar-^{39}Ar (biotite)			275[d]	5	42°50'41"	94°42'06"

Note. [a]Recrystallization age. [b]Protolith or crystallization age. [c]Weighted mean age. [d]Total gas age

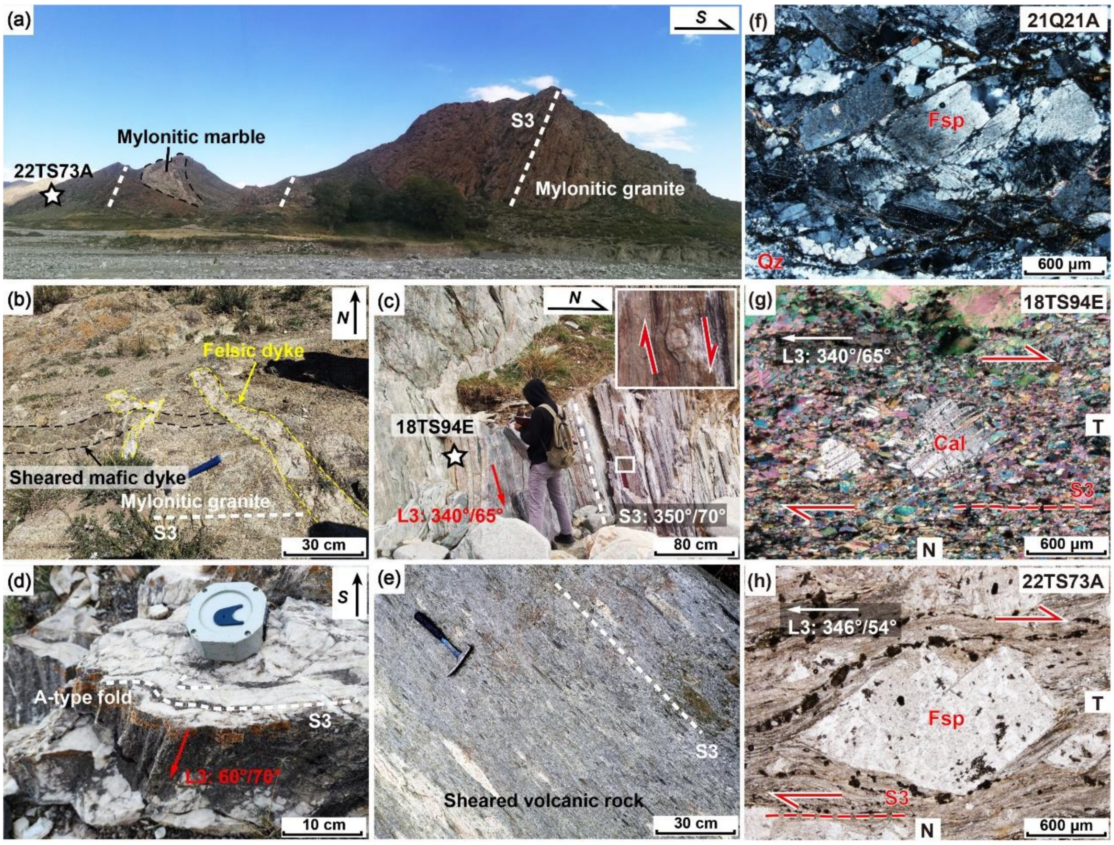

Figure 4.5. Representative photographs showing main structures of the Xiaopu Shear Zone (XSZ). (a) A field photograph showing the S3 foliation. (b) Highly deformed granite and mafic dyke crosscut by felsic dykes. (c) S3 with stretching lineation in the mylonitic marble. Sigmoidal porphyroclasts indicate a top-to-N shearing. (d) A-type fold in the mylonitic marble. (d) Highly deformed volcanic rocks. (f) Undulose extinction and folding of feldspar. (g-h) Calcite and feldspar porphyroclasts indicate a top-to-N shearing.

The foliation of the shear zone (S3) mostly dips ~50°-70° to the north (Figure 4.2c). The stretching lineation (L3) is down-dipping on foliation planes, and cluster in the higher-central part of the Pitch-Plunge-Dip ternary diagram (Figure 4.2d). Such features indicate that the D3 is characterized by a dominant "vertical flow" mode. Sigmoidal porphyroclasts and A-type folds in the mylonitic marbles indicate a top-to-N shearing (Figures 4.5c, 4.5d, and 4.5g). This sense of shear can be confirmed by the σ-shape of feldspar clasts in the mylonitic volcanic rocks (Figure 4.5h). Feldspar grains in the mylonitic granites are characterized by undulose extinction, kink bands, and microfolding, while quartz grains are dominantly recrystallized by SGR (Figure 4.5f). These observations suggest that the D3 deformation occurred at 400-500°C (Stipp et al., 2002; Passchier & Trouw, 2005).

4.5 Pressure-temperature evolution

4.5.1 Metamorphic assemblages

The mineral assemblages of four representative samples were counted by rule-of thumb and can be found in Table 4.1. Mineral abbreviations throughout the text, figures, and tables are after Whitney & Evans (2010).

Grt-Sil migmatites 19Q23A and 19Q22A were sampled from the sillimanite-migmatite zone at ~0.9 km and 1.1 km to the southwest of the Xiaopu pluton, respectively (Figure 4.2a). They mainly consist of garnet (5-10 vol.%), sillimanite (5-10 vol.%), biotite (~30 vol.%), muscovite (<10 vol.%), plagioclase (10-20 vol.%), quartz(~30 vol.%) and ilmenite (~1 vol.%). The schistosity (S2) is defined by aligned sillimanite and biotite-rich layers intercalated with plagioclase and quartz-rich layers. In the sample 19Q23A, garnet crystals cluster in the plagioclase and quartz-rich layers (leucosomes), with most being inclusion-free. A few garnet crystals, especially in the biotite-rich layers, are texturally zoned with inclusion-rich cores and inclusion-poor rims (Figures 4.6a and 4.6b). Minute quartz (Qz_1) and ilmenite (Ilm_1) inclusions are found in the garnet core. In the garnet rim, biotite (Bt_2) inclusions and elongated quartz (Qz_2) parallel to the crystal edges are observed. Garnet is usually rimmed by biotite (Bt_3), sillimanite (Sil_3), muscovite (Ms_3), plagioclase (Pl_3) and quartz (Qz_3). In the sample 19Q22A, most garnet crystals in biotite-rich domains also display core-rim textures with inclusion-rich cores and inclusion-poor rims. Minute quartz (Qz_1), biotite (Bt_1), and ilmenite (Ilm_1) occur in the garnet core as inclusion trails oriented at a high angle to the main schistosity (Figure 4.6d). The garnet core also contains abundant negative crystal cavities filled with polymineralic inclusions (Figures 4.6e and 4.6f),

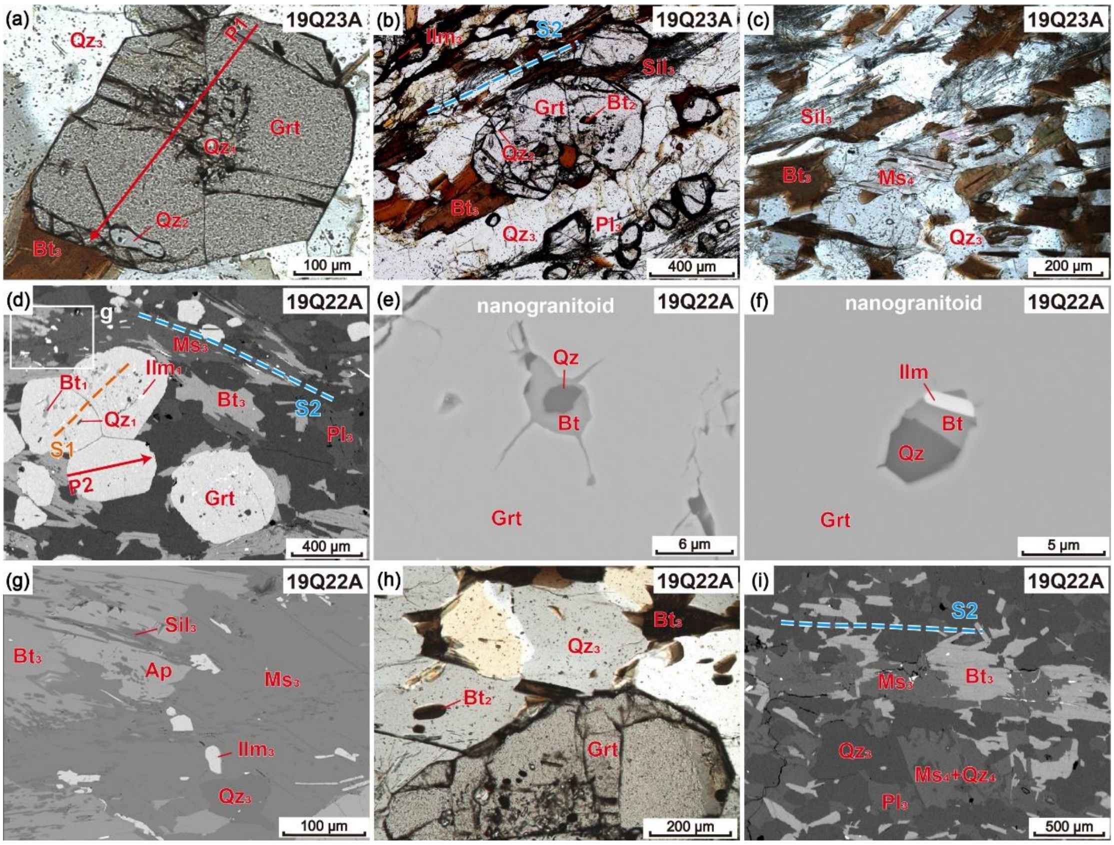

Figure 4.6. Representative photomicrographs showing mineral assemblages of the Grt-Sil migmatites (19Q23A and 19Q22A). Red arrows refer to garnet profiles. (a, b) Subhedral heterogeneous garnet with a core containing tiny quartz (Qz_1) and ilmenite (Ilm_1), and inclusion-poor rim including biotite (Bt_2) and elongated quartz (Qz_2) parallel to the crystal edges. Garnet rimmed by Sil_3 + Bt_3 + Qz_3. (c) Oriented biotite (Bt_3) replaced by muscovite (Ms_4). (d) Subhedral heterogeneous garnet with a core containing Bt_1 + Qz_1 + Ilm_1 oriented at high angle with the external foliation (S2). (e-f) Nanogranitoid inclusions with crystals of quartz and biotite in the garnet core. (g) Sil_3 + Bt_3 + Ms_3 + Ilm_3 aligned in the S2 foliation plane. (h) Rounded biotite (Bt_2) inclusion in the quartz. (i) Symplectitic muscovite (Ms_4) and quartz (Qz_4).

which is evidence of partial melting ("nanogranitoid"; Cesare et al., 2009). Sillimanite either occurs as inclusions in garnet or partly replaces biotite in the matrix (Figure 4.6g). Some rounded biotite (Bt_2) inclusions are also preserved within the quartz matrix (Figure 6h). In both samples, two generations of muscovite are present (Figures 4.6c and 4.6i). The first generation (Ms_3) replaces biotite and is parallel to the schistosity, while the second one (Ms_4) crosscuts the schistosity and grows with tiny quartz grains (Qz_4).

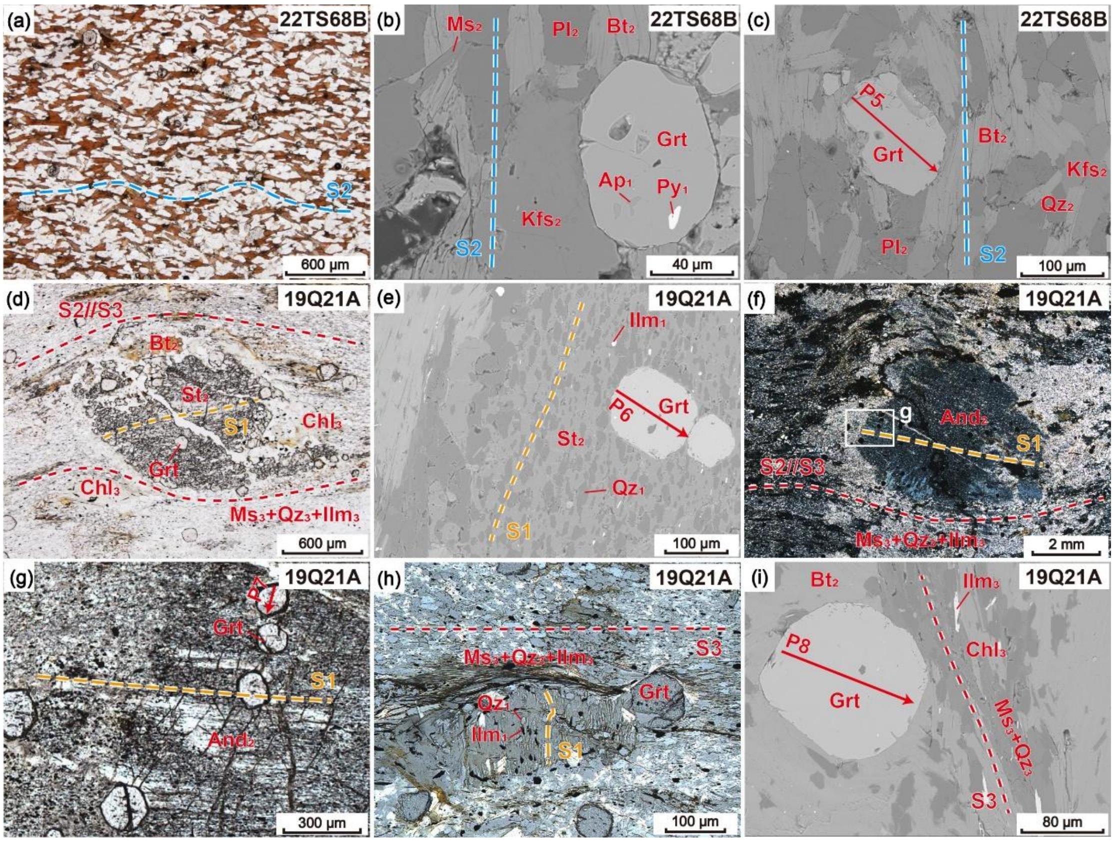

Figure 4.7. Representative photomicrographs showing mineral assemblages of the Grt-Kf schist (22TS68B) and Grt-And-St schist (19Q21A). Red arrows refer to garnet profiles. (a) The schistosity (S2) affected by D3. (b-c) Grt + Bt_2 + Pl_2 + Kf_2 + Ms_2 + Qz_2 aligned to form the S2 foliation with Qz_1 + Py_1 in the garnet. (d-g) Staurolite and andalusite porphyroblasts (St_2 + And_2) including small garnet and inclusion trails of Qz_1 + Ilm_1 at middle angle with the external foliation (S3). Chl_3 partially replaced Bt_2. Ms_3 + Qz_3 + Ilm_3 aligned to form the S3 foliation. (h) Chloritized biotite containing inclusion trails of Qz_1 + Ilm_1 at high angle with the external foliation (S3). (i) Chl_3 + Ms_3 + Qz_3 + Ilm_3 aligned in the S3 foliation plane.

Grt-Kf schist 22TS68B was sampled from the andalusite-staurolite zone at 4.1 km to the southwest of the Xiaopu pluton (Figure 4.2a). This sample contains garnet (~2 vol.%), biotite (~40 vol.%), muscovite (~3 vol.%), plagioclase (~10 vol.%), K-feldspar (~10 vol.%), quartz (~30 vol.%) and ilmenite (~1 vol.%) with a distinct schistosity (S2) defined by oriented biotite (Bt_2) and by elongated plagioclase (Pl_2), K-feldspar (Kf_2) and quartz (Qz_2; Figures 4.7a and 4.7c). The S2 foliation was affected by the D3 event to form asymmetric microfolds (Figure 4.7a). Most garnets are inclusion-free but a few grains contain apatite (Ap_1) and pyrite (Py_1) inclusions (Figure 4.7b).

Grt-And-St schist 19Q21A was collected from the andalusite-staurolite zone at 7.7 km to the southwest of the Xiaopu pluton (Figure 4.2a). It is mainly made of garnet (~5 vol.%), biotite (~20 vol.%), andalusite (~20 vol.%), staurolite (5-10 vol.%), muscovite (10-20 vol.%), plagioclase (5-10 vol.%), quartz (~20 vol.%), chlorite (~10 vol.%), and ilmenite (~1 vol.%). The main fabric is defined by aligned andalusite, staurolite, biotite, muscovite, and quartz grains. Andalusite (And_2) and staurolite (St_2) porphyroblasts and large biotite (Bt_2) grains containing tiny quartz (Qz_1) and ilmenite (Ilm_1) inclusions are fractured and the σ-shape of porphyroblasts suggests pre-kinematic growth (Figures 4.7d, 4.7g, and 4.7h). Garnet crystals occur as either euhedral to subhedral inclusions in the andalusite, staurolite, and biotite or rounded grains in the matrix. Andalusite and staurolite porphyroblasts and garnet inclusions usually contain the same trails of minerals (quartz and ilmenite) (Figures 4.7e and 4.7g). Small muscovite (Ms_3), quartz (Qz_3) and ilmenite (Ilm_3) often wrap around the andalusite (And_2), staurolite (St_2), and biotite (Bt_2). Biotite grains are partly or fully replaced by chlorite (Chl_3) along the shear planes (Figures 4.7d, 4.7h, and 4.8i), indicating retrograde fluid alteration during shearing. Sericitization of andalusite and plagioclase is also frequent (Figure 4.7f).

4.5.2 Mineral compositions

Garnet

Garnet from the Grt-Sil migmatite (19Q23A) displays a weak zonation from core to rim with a thin overgrowth (Figure 4.9a). The core has a homogeneous almandine (72-71%), pyrope (10%), and spessartine (16-17%). Compared to the core, the rim exhibits a slight decrease in almandine (72-68%) and pyrope (10-9%) and an increase in spessartine (17-20%). The overgrowth shows a small increase in almandine (70%) and a decrease in pyrope (8%) and spessartine (19%). Grossular (2-3%) content is invariant. There is a small increase of Fe# (Fe/(Fe+Mg)) from the core to overgrowth (87-89%).

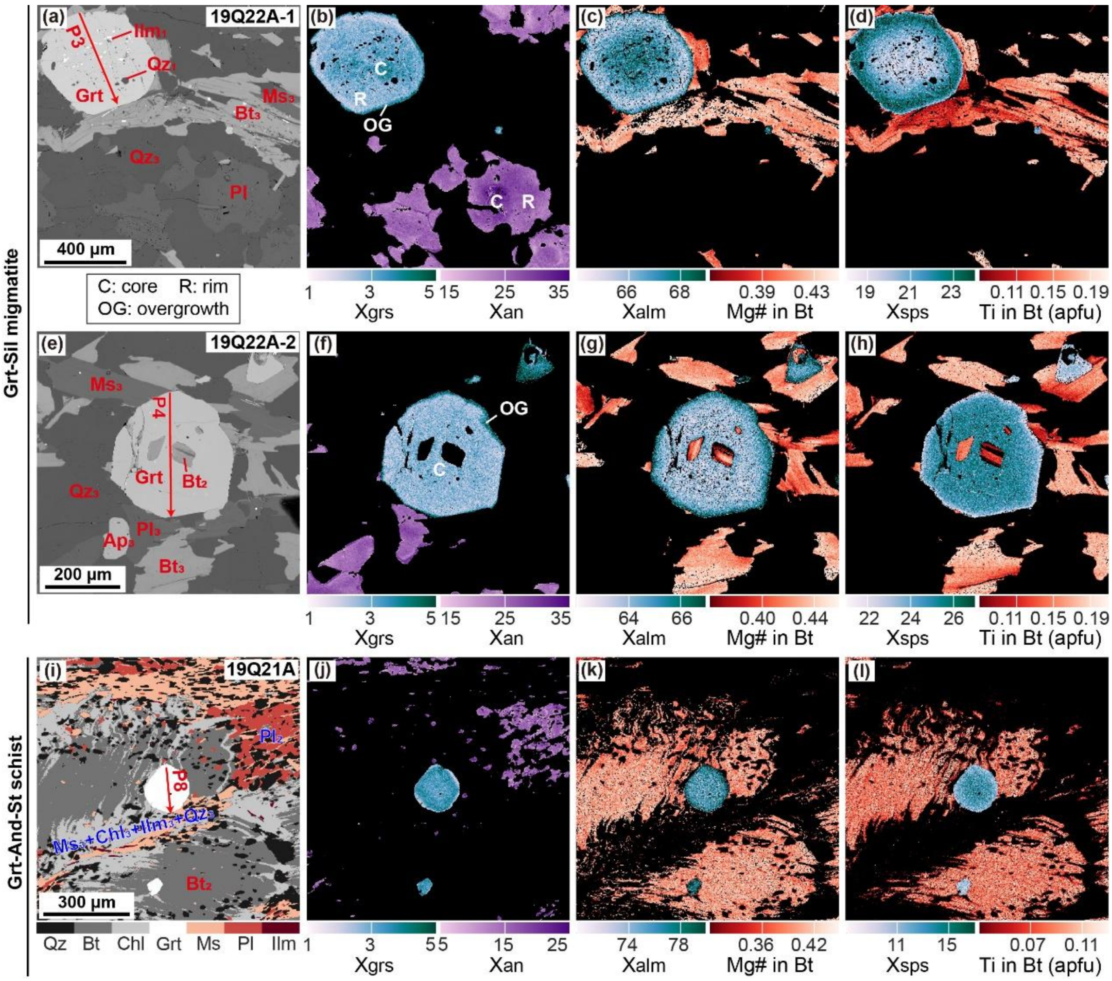

Figure 4.8. Compositional mapping of (a-h) the Grt-Sil migmatite (19Q22A) and (i-l) the Grt-And-St schist (19Q21A). Mapping data were processed using XMapTools 4.1 (Lanari et al. 2014, 2019).

Two large subhedral garnet grains from the Grt-Sil migmatite (19Q22A) display uniform zonation and include a chemically distinct overgrowth (Figures 4.8 and 4.9). They are characterized by a gradual decrease in almandine (68-65%), pyrope (10-9%), and grossular (4-2%) from core to rim, reversely correlated with an increase in spessartine from 18 to 23%. The overgrowth records an increase in almandine (66-68%) and grossular (2-4%), and a decrease in pyrope (9-7%) and spessartine (22-20%). The Fe# continuously increases from core to overgrowth (88-90%). A smaller anhedral garnet grain in 19Q22A (Figures 4.8 and 4.9d) has a weak compositional zonation with a pattern similar to the rim and overgrowth of the large grain. It shows an increase in almandine (63-67%) and grossular (2-4%) and a decrease in pyrope (9-7%) and spessartine (25-21%).

Garnet from the Grt-Kf schist (22TS68B) has a weak zonation (Figure 4.9e) characterized by a slight increase in almandine (45-52%) and pyrope (5-7%), and a decrease in spessartine (46-39%) and grossular (4-2%) from core to rim. The core has a higher Fe# (~91%) than the rim (~89%).

The small garnet crystals included in biotite and staurolite from the Grt-And-St schist (19Q21A) share a similar core-to-rim zonation pattern (Figures 4.8 and 4.9f). The core has a homogeneous grossular (4-3%) and pyrope (~8%) with a slightly increasing almandine (75-78%) and decreasing spessartine (14-11%) towards the rim. The rim records a decrease in grossular (2%). The garnet grains included in andalusite have compositions similar to the garnet rims in biotite and staurolite (Figure 9f).

Biotite and Muscovite

In the Grt-Sil migmatite (19Q23A), biotite included in the garnet rim (Bt_2) has the highest Mg# (0.44-0.45) and a medium Ti content (0.16-0.17 a.p.f.u.). Biotite included in the quartz matrix (Bt_2) and biotite in the matrix show a wider range of Mg# (0.37-0.42) and Ti content (0.12-0.21 a.p.f.u.). Muscovite parallel to S2 (Ms_3) has a Ti content varying between 0.03 and 0.06 a.p.f.u. (Figure 4.10). Muscovite (Ms_4) cutting across the S2 foliation has a wider range of Ti content (0.00-0.05 a.p.f.u.).

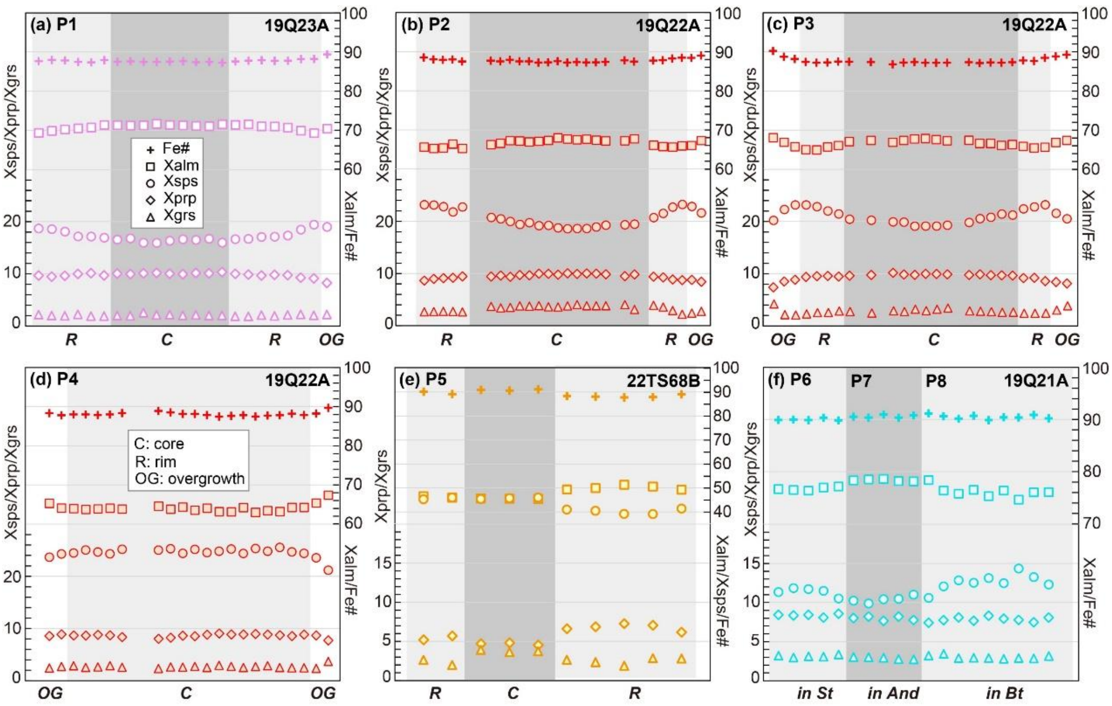

Figure 4.9. Compositional profiles of garnet in (a) the Grt-Sil migmatite (19Q23A), (b-d) the Grt-Sil migmatite (19Q22A), (e) the Grt-Kf schist (22TS68B), and (f) the Grt-And-St schist (19Q21A).

In the Grt-Sil migmatite (19Q22A), biotite included in the garnet core (Bt_1) shows a large spread of Mg# (0.35–0.49) and a moderate Ti content (0.11-0.17 a.p.f.u.). Biotite in the garnet rim (Bt_2) has Mg# ranging from 0.40 to 0.48 and Ti between 0.12 and 0.17 a.p.f.u. (Figure 4.10). Biotite included in matrix quartz (Bt_2) shows lower Mg# of 0.36-0.43 and higher Ti of 0.17-0.24 a.p.f.u. Biotite in the matrix (Bt_3) also shows lower Mg# (0.37-0.48) and a Ti content varying between 0.09 and 0.22 a.p.f.u. The Mg# and Ti contents of biotite appear to be negatively correlated (Figures 4.8g, 4.8h, and 4.10). Muscovite parallel to S2 (Ms_3) shows a relatively high Ti content (0.04-0.08 a.p.f.u.), while that (Ms_4) without orientation and/or growing along with quartz are poorer in Ti (0.01-0.05 a.p.f.u.) (Figure 4.10).

In the Grt-Kf schist (22TS68B), biotite (Bt_2) has high Mg# (0.46-0.52) and moderate Ti (0.11-0.17 a.p.f.u.). Muscovite (Ms_2) has Ti around 0.03 a.p.f.u. (Figure 4.10).

In the Grt-And-St schist (19Q21A), biotite grains (Bt_2) have Mg# ranging from 0.39 to 0.41 and Ti from 0.09 to 0.11 a.p.f.u. (Figures 4.8l and 4.10). Muscovite (Ms_3) in the shear bands has a low Ti of ~0.01 a.p.f.u. (Figure 4.10).

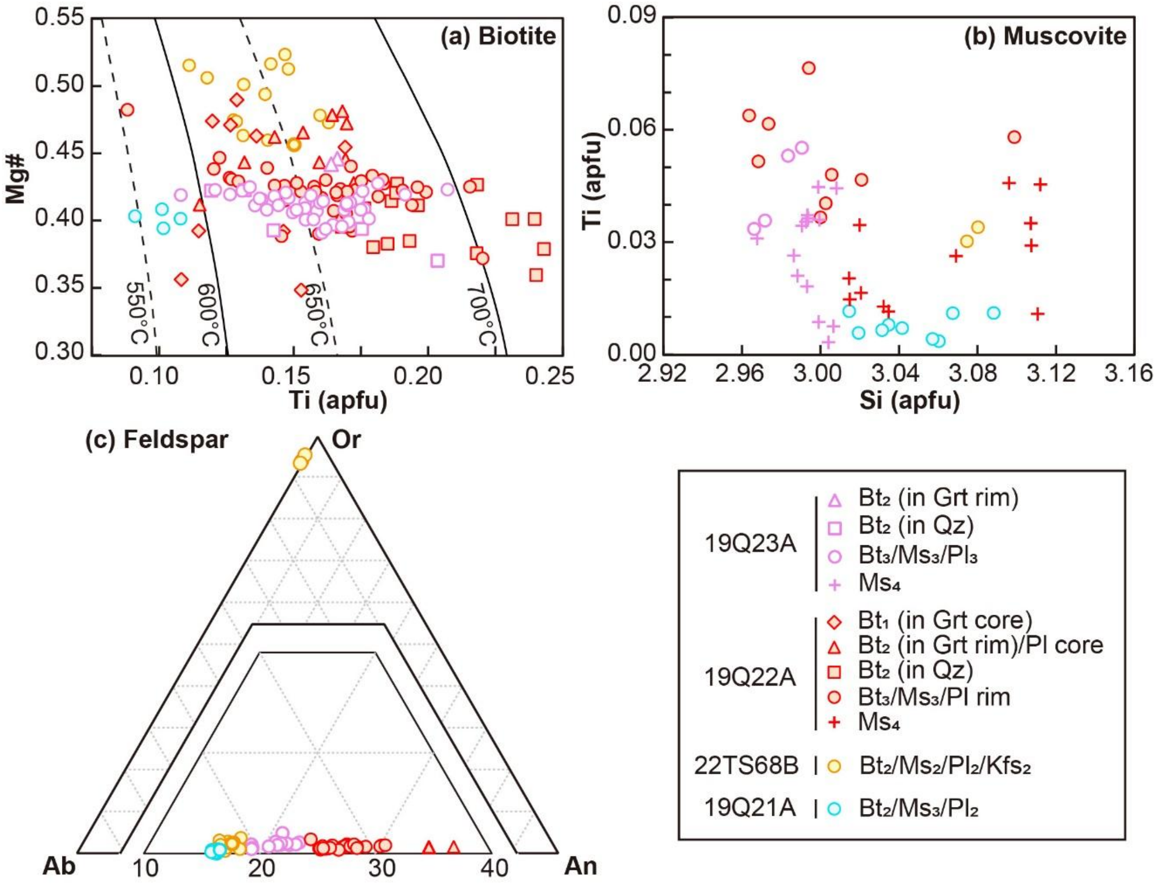

Figure 4.10. Composition of (a) biotite, (b) muscovite, and (c) feldspar in the metapelitic samples. Isotherms drawn in (a) were calculated using the Ti-in-biotite thermometer of Henry et al. (2005).

Feldspar and Staurolite

Feldspar in the Grt-Sil migmatite (19Q23A) is plagioclase. The grains are preserved in the matrix and have anorthite contents ranging from 19 to 23% (Figure 4.10). In 19Q22A, plagioclase grains were observed in the matrix. Most have anorthite of 24-31%, with some grains having a higher anorthite contents in the core (37-34%)

than in the rim (27-24%). Feldspar in the Grt-Kf schist (22TS68B) includes both plagioclase and orthoclase, with the plagioclase having anorthite of 16-18% (Figure 4.10). Feldspar in the Grt-And-St schist (19Q21A) is plagioclase. The grains are small and show homogenous anorthite of 16-17% (Figures 4.8 and 4.10). Staurolite was observed in 19Q21A and has a composition of low Mg# (0.10-0.14) and high Si of 7.7-8.0 a.p.f.u.

Assemblage	Prograde	Peak	Retrograde	Retrograde
Grt-Sil migmatites (19Q22A, 19Q23A)	M1: Qz_1+Ilm_1±Bt_1	M2: Grt(core)+Bt_2+Sil_2+Qz_2+Ilm_2+melt±Pl(core)	M3: Grt(rim)+Bt_3+Sil_3+Ms_3+Qz_3+Ilm_3±Pl(rim)	M4: Ms_4+Qz_4
Grt-Kf schist (22TS68B)	M1: Grt (core)	M2: Grt(rim)+Pl_2+Kf_2+Bt_2+Ms_2+Qz_2+Ilm_2		
Grt-And-St schist (19Q21A)	M2: Qz_1+Ilm_1	M2: Grt+And_2+St_2+Bt_2+Pl_2+Qz_2+Ilm_2		M3: Chl_3+Ms_3+Qz_3+Ilm_3
Deformation stage	D1?	D2		D3

Figure 4.11. Mineral parageneses of the Grt-Sil migmatites, Grt-Kf schist, and Grt-And-St schist.

Mineral Parageneses

Based on petrographic features and mineral compositions, the prograde, peak and retrograde metamorphic assemblages can be distinguished in the different samples (Figure 4.11). In migmatites (19Q23A and 19Q22A), the prograde assemblage (M1) is represented by Qz_1 + Ilm_1 ± Bt_1. The peak assemblage (M2) is composed of Grt (core) + Bt_2 + Sil_2 + Qz_2 + Ilm_2 + melt ± Pl (core). Two retrograde assemblages (M3 and M4) consist of Grt (rim) + Bt_3 + Sil_3 + Ms_3 + Qz_3 + Ilm_3 ± Pl (rim) and Ms_4 + Qz_4, respectively. The M2 and M3 assemblages formed during the occurrence of D2, while M4 is much later. In the Grt-Kf schist (22TS68B), except for the garnet core, the other minerals of the prograde assemblage were not well preserved. The peak assemblage (M2) contains Grt (rim) + Pl_2 + Kf_2 + Bt_2 + Ms_2 + Qz_2 + Ilm_2, which grew synchronously with D2. In the Grt-And-St schist (19Q21A), the prograde assemblage (M1) is represented by Qz_1 + Ilm_1. The peak assemblage (M2) consists of Grt + And_2 + St_2 + Bt_2 + Pl_2 + Qz_2 + Ilm_2 and a retrograde assemblage (M3) is composed of Chl_3 + Ms_3 +

Qz_3 + Ilm_3. The M2 and M3 assemblages are probably associated with D2 and D3, respectively.

4.5.3 Conventional thermobarometry

Multiple empirical geothermobarometers were used to estimate the pressure-temperature conditions of the migmatites and schists. Geothermobarometric methods and results are presented in Table 4.1 and Figure 4.12.

Garnet-biotite (GB) thermometer of Holdaway (2000) was applied to our samples combined with the garnet-biotite-plagioclase-quartz (GBPQ) geobarometer (Wu et al., 2004) and garnet-biotite-Al_2SiO_5-quartz (GBAQ) geobarometer (Wu, 2017). The mineral pairs used for estimating peak conditions consist of garnet with low spessartine and high pyrope contents and adjacent Bt_2 (showing textural equilibrium) with low Mg# and high Ti content. The garnet crystals with the highest spessartine and adjacent Bt_3 were used to estimate the retrograde conditions. For the migmatite (19Q23A), peak (M2) P-T conditions are estimated at 654 ± 25°C – 4.4 ± 1.2 kbar and 653 ± 25°C – 4.3 ± 1.8 kbar by the GB-GBPQ and GB-GBAQ geothermobarometers, respectively. Retrograde (M3) conditions are constrained at 603 ± 25°C – 2.3 ± 1.2 kbar and 599 ± 25°C – 3.5 ± 1.8 kbar. For the migmatite (19Q22A), peak (M2) conditions are estimated at 669 ± 25°C – 3.4 ± 1.2 kbar and 671 ± 25°C – 4.3 ± 1.8 kbar by the GB-GBPQ and GB-GBAQ geothermobarometers, respectively. Retrograde (M3) conditions are constrained at 625 ± 25°C – 2.8 ± 1.2 kbar and 614 ± 25°C – 3.9 ± 1.8 kbar. For the Grt-Kf schist (22TS68B), peak (M2) conditions are estimated at 629 ± 25°C – 4.5 ± 1.2 kbar. For the schist (19Q21A), peak (M2) condition was estimated at 591 ± 25°C – 4.9 ± 1.2 kbar by the GB-GBPQ geothermobarometer and 581 ± 25°C – 3.4 ± 1.8 kbar by the GB-GBAQ geothermobarometer.

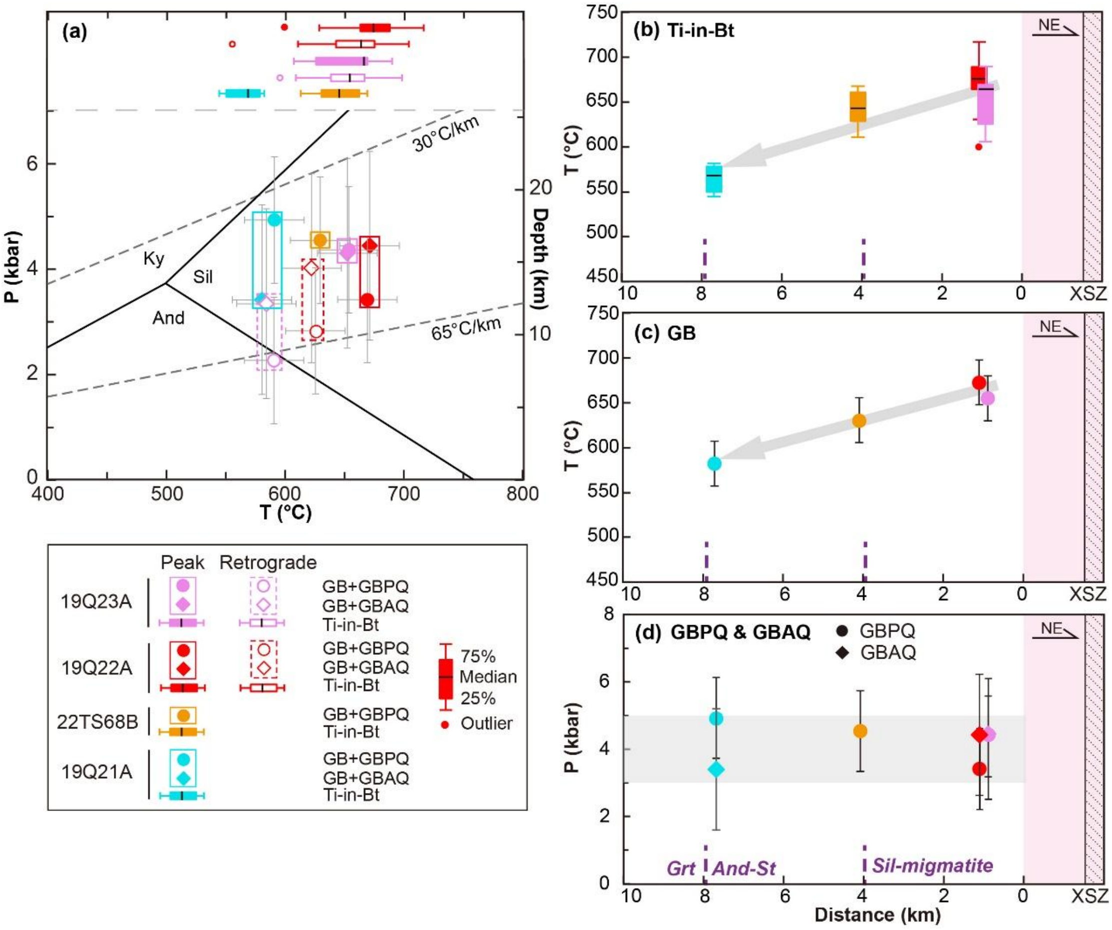

Figure 4.12. (a) Results of conventional geothermobarometry for the metapelitic rocks. Colored spots refer to P-T conditions calculated by GB-GBPQ and GB-GBAP geothermobarometers (Holdaway, 2000; Wu et al., 2004; Wu, 2017). Horizontal boxplots represent temperature estimated from the Ti-in-biotite thermometer (Henry et al., 2005). (b-d) Peak temperature estimated by Ti-in-biotite thermometer and GB thermometer, and peak pressure estimated by GBPQ and GBAP barometers vs distance from the Xiaopu pluton (pink area). The diagonal lines refer to the location of Xiaopu Shear Zone (XSZ).

The Ti-in-biotite geothermometer of Henry et al. (2005) was additionally used to estimate crystallization temperatures of biotite in different samples. Calculated temperature isotherms are outlined in Figure 4.10. The precision of the method is ± 25°C. For the migmatite (19Q23A), estimates for biotite (Bt_2) of the peak assemblage range from 610 to 690°C with a median of 665°C, and the retrograde biotite (Bt_3) yields similar results of 590-700°C (median at 654°C). For the migmatite (19Q22A), biotite of the peak and retrograde assemblages yields temperatures of 600-720°C (median at 675°C) and 560-700 °C (median at 663°C), respectively. For the schists (22TS68B, 19Q21A), the estimated peak temperatures are 610-670 °C (median at 645°C) and 540-580°C (median at 568°C).

Peak temperatures estimated by GB and Ti-in-biotite geothermometers for different samples decrease with the distance from the Xiaopu pluton (Figures 4.12). In contrast, estimated peak pressures remain invariant within errors (4 ±1 kbar), regardless of the distance from the pluton (Figure 4.12d).

4.5.4 Phase modeling

T-X (H_2O) pseudosections at 4 kbar were used to determine the appropriate H_2O content for the whole-rock composition (WBC) and local bulk composition (LBC) of 19Q22A (Figure 4.13). The selected pressure of 4 kbar derives from the thermobarometry presented above. The changes in X(H_2O) correspond to water content ranging from an anhydrous composition to 3 wt.% or 4 wt.% (i.e., excess water). A H_2O content of 1.2 wt.% was finally selected for both the WBC and LBC based on the observed peak assemblage (Sil + Grt + Bt + Pl + Qz + Ilm + Liq).

The P-T pseudosection calculated by the WBC of 19Q22A is shown in Figure 4.14a. The peak assemblage (Sil + Grt + Bt + Pl + Qz + Ilm + Liq) is predicted to be stable from 655 to 710°C, and from 3.4 to 5.6 kbar. A P-T condition of 665 ± 10°C and 3.8 ± 0.6 kbar was refined using garnet rim ($Xalm_{63-62}Xsps_{23-25}Xgrs_{2-3}$) and plagioclase rim ($An_{25-27}$) compositions. The garnet core-rim zonation indicates a retrograde history marked by a first cooling and decompression stage at supra-solidus conditions, though the core composition cannot be perfectly constrained (Figure 4.14a). Then, the increase in almandine and grossular and the decrease in pyrope and spessartine of the garnet overgrowth testify to a second cooling stage, nearly isobaric in the stability field of sillimanite across the solidus. Muscovite occurs near and below the solidus along the P-T path, in agreement with muscovite replacing biotite and forming rims around garnet (Figure 4.6d).

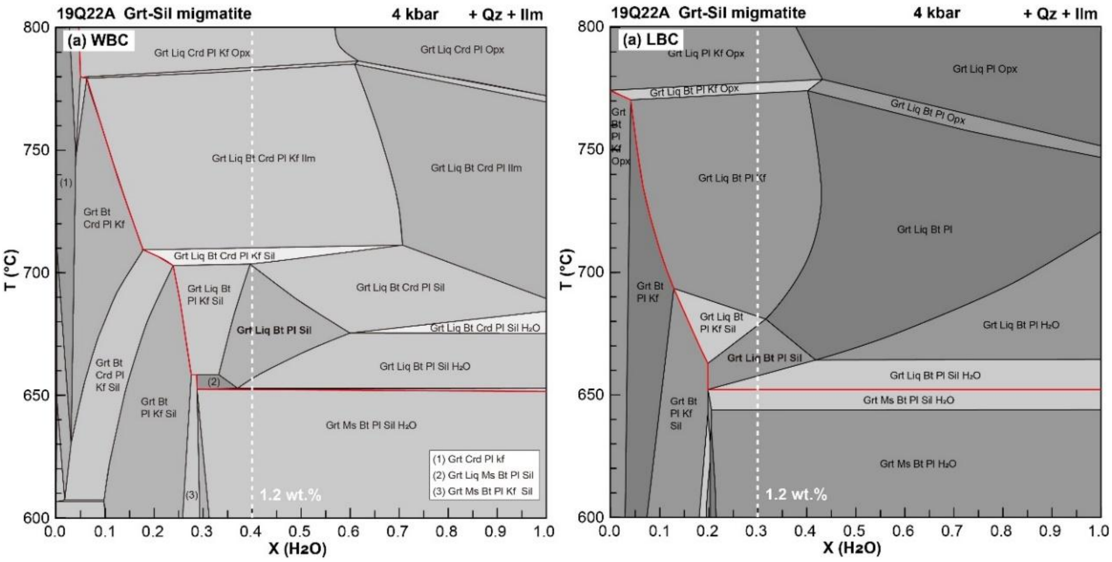

Figure 4.13. T-X (H_2O) pseudosections for the Grt-Sil migmatite 19Q22A at 4 kbar by (a) whole-rock bulk composition (WBC) and (b) local bulk composition (LBC). The dashed white line and bold number denote H_2O value selected to construct P–T pseudosections.

The P-T pseudosection calculated by the LBC shows a similar P-T range of ~655-685°C and ~3.4-5.0 kbar for the peak mineral assemblage (Figure 4.14b). The rim compositions of garnet and plagioclase allow us to refine the P-T condition at 655 ± 10°C and 3.8 ± 0.4 kbar. A cooling and decompression history across the solidus is constrained using the garnet core to rim zonation.

The P-T pseudosection for 22TS68B has been modelled by the WBC under fluid-saturated conditions (Figure 4.14c). The peak assemblage (Grt + Pl + Kf + Bt + Ms + Qz + Ilm) is stable throughout a wide P-T range at sub-solidus conditions. Garnet rim composition ($Xalm_{50-52}Xsps_{39-41}Xgrs_{2-3}$) matches the modeled isopleths within this field at 605 ± 5°C and 3.4 ± 0.7 kbar. The composition of the garnet core ($Xalm_{45-46}Xsps_{45-}$

$_{46}X_{grs3.5-4}$) is consistent with the calculated isopleths at 580 ± 5°C and 3.7 ± 0.3 kbar. Therefore, a P-T path involving pre-peak heating with slight decompression can be recovered.

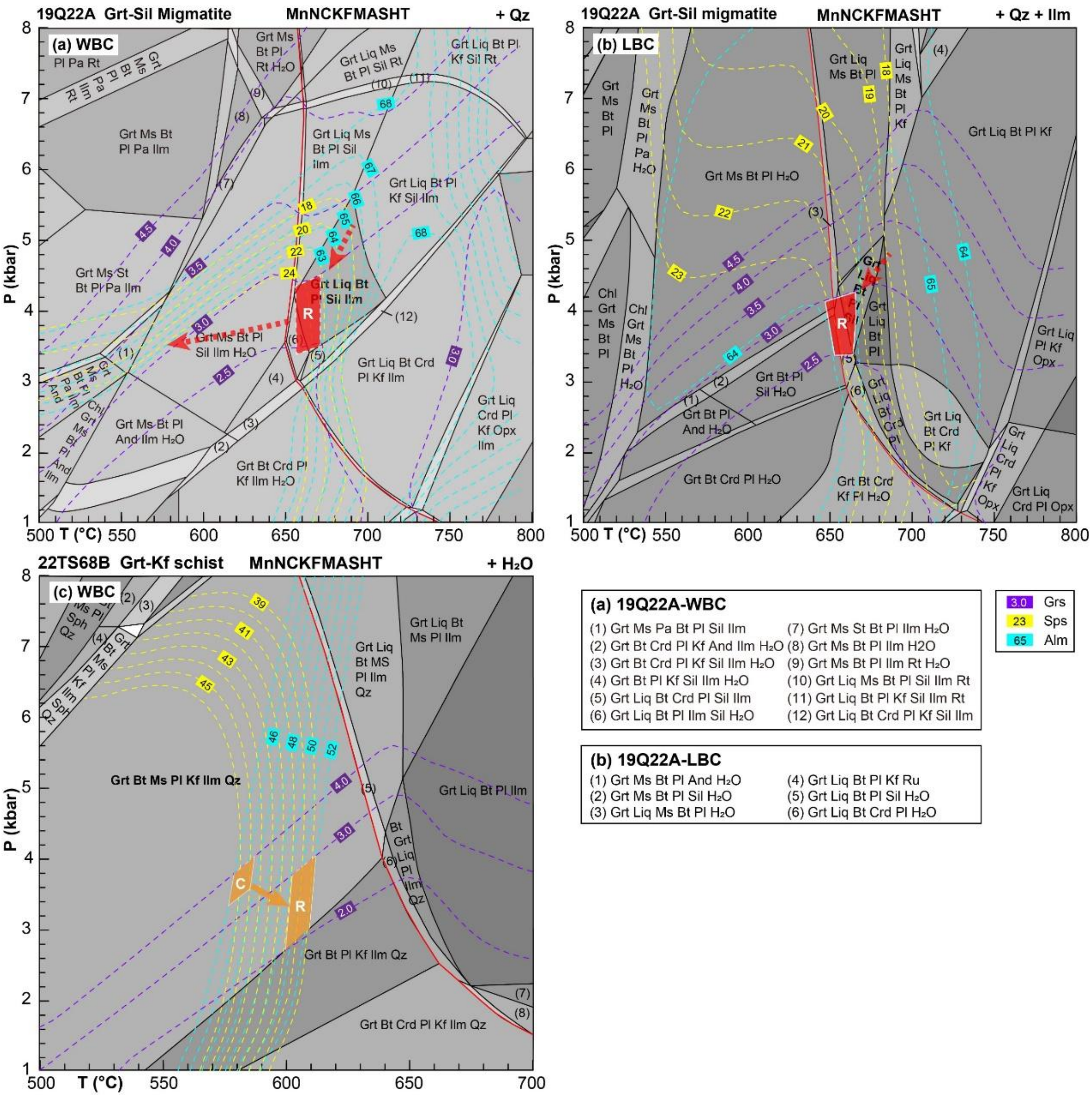

Figure 4.14. Calculated phase diagrams for the metapelitic rocks. (a) P-T pseudosection for the Grt-Sil migmatite (19Q22A) by whole-rock bulk composition (WBC) and (b) local bulk composition (LBC). (c) P-T pseudosection for the Grt-Kf schist (22TS68B) by whole-rock bulk composition (WBC). The thin red line represents the solidus of the system. The arrows are the inferred P-T paths. C and R for garnet core and rim, respectively.

4.6 Depositional age and provenances of the meta-sedimentary rocks

4.6.1 Geochronological results

A total of 55 and 192 zircon grains from the meta-sandstone sample 12TS119F and three mica-schist samples were chosen for U-Pb dating, respectively. The CL images of the representative grains are presented in Figure 4.15. According to the CL images, four types of zircons can be recognized. (1) Type 1 zircons have core-rim textures in which the cores are bright with oscillatory zoning and the rims are relatively dark and un-zoned, corresponding to originally magmatic zircons surrounded by metamorphic overgrowths (Hoskin and Schaltegger, 2003). (2) Type 2 zircons also show core-rim textures with bright un-zoned cores, which could be originally metamorphic then subjected to secondary metamorphic or hydrothermal overgrowth. Alternatively, they could also be originally magmatic but were intensively “reworked” (via solid-state recrystallization or local dissolution-reprecipitation) by the subsequent metamorphism or alteration so that the original magmatic oscillatory zoning was totally erased. In the latter case, the overgrowth rims may have formed synchronously with the reworking of the cores or even reflect a later metamorphic and/or hydrothermal event (Hoskin and Schaltegger, 2003). (3) Type 3 zircons have homogeneous dark to black CL images without visible oscillatory zoning, likely formed by metamorphism or hydrothermal alteration (Connelly, 2001; Corfu et al., 2003; Hoskin and Schaltegger, 2003). (4) Type 4 zircons are characterized by prismatic shapes and moderately bright CL images with clearly concentric magmatic oscillatory zoning, and no visible overgrowths.

In order to obtain sufficiently representative zircon populations, all four types of zircons from each sample were analyzed. Most analyses plot on or close to the Concordia, but a few zircons show remarkable discordance, especially for the sample 12TS119E (Figure 4.16). One reason for discordant ages can be Pb loss due to metamorphic or hydrothermal alteration. In addition, analytical mixing between two parts of zircons with different origins (e.g., older cores and younger rims) is also highly possible as some of the discordant zircons with core-rim texture are quite small. The geological meaning of the discordant ages is ambiguous; therefore, they are excluded from further discussion and only concordant ages (concordance > 90%) are considered.

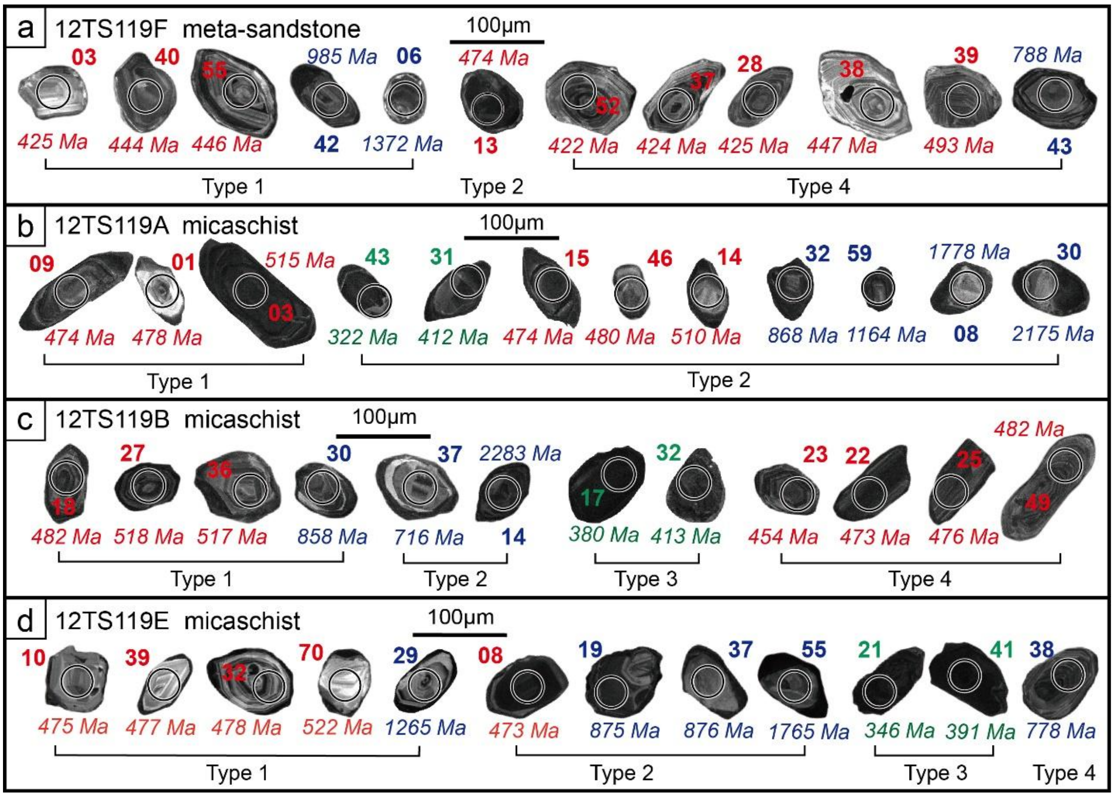

Figure 4.15. Cathodoluminescence images for representative detrital zircons from meta-sandstone (12TS119F) and mica schists (12TS119A, B and E) showing their apparent $^{206}Pb/^{238}U$ ages (<1000 Ma) or $^{207}Pb/^{206}Pb$ ages (>1000 Ma). Four types of zircons can be recognized. See text for more explanations.

Most zircons in sample 12TS119F have euhedral to sub-euhedral shapes and belong to type 4, indicating original magmatic sources (Connelly, 2001; Corfu et al., 2003; Hoskin and Schaltegger, 2003). A small group of zircons show stubby or sub-rounded shapes and have complex core-rim textures, comprising irregular cores with blurry or patchy zoning and structureless rims (type 1). The rest few zircons are rounded and unzoned or sector zoned, indicative of type 2. Forty-five out of fifty-five grains yielded concordant ages, a large majority of which have ages < 540 Ma, with two major age peaks at 425 Ma (n = 14; 31.1%) and 445 Ma (n = 10; 22.2%), as well as a minor age peak at ca. 490 Ma. The Precambrian zircons show sub-peaks at ~580 Ma, ~780 Ma, and in a range of 850-1000 Ma; only two Mesoproterozoic grains (1280 Ma and 1372 Ma) were found (Figure 4.16a). The remaining ten analyses yielded discordant ages probably due to Pb loss or disequilibrium of their isotopic systems (Connelly, 2001). Twenty-three zircons with ages around 445-425 Ma were analyzed for rare earth element (REE) compositions. Most grains are characterized by steeply-rising REE patterns with remarkable positive Ce and negative Eu anomalies (Figure 4.17a), together with their high Th/U ratios (mostly > 0.4) (Figure 4.16b), generally consistent with typical magmatic zircons (Hoskin and Schaltegger, 2003; Rubatto, 2017). Only two zircons (No. 38 and 51) display relatively higher LREE values and weaker Ce anomalies in comparison to the other zircons, and their REE patterns (Figure 4.17a) are similar to those of hydrothermal-related zircons (Hoskin, 2005).

For the mica-schist sample 12TS119A, fifty-eight out of sixty dated zircons yielded concordant ages (Figure 4.16c) ranging from 313 to 2175 Ma showing a dominant age peak at 477 Ma (n = 19; 32.8%), two younger age peaks at 322 Ma (n = 4; 6.9%) and 414 Ma (n = 4; 6.9%), and other populations of 500-550, 600-750, 850-1000,1100-1500, 1600-1800 and 2175 Ma (Figure 4.16d). The youngest nine ages (peaked at 322 and 414 Ma) are obtained exclusively from type 2 zircons with Th/U ratios mostly lower than or near 0.4, showing bright or dark cores characterized by surface-controlled alteration (Corfu et al., 2003) and encircled by thin and dark rims (Figure 4.15b). Zircons defining the major age peak of 477 Ma mainly belong to the type 1 and type 2, and show Th/U ratios higher than 0.4. The other older zircons cover types 1 and 2, and have variable Th/U ratios mostly higher than 0.4 (Figure 4.16d).

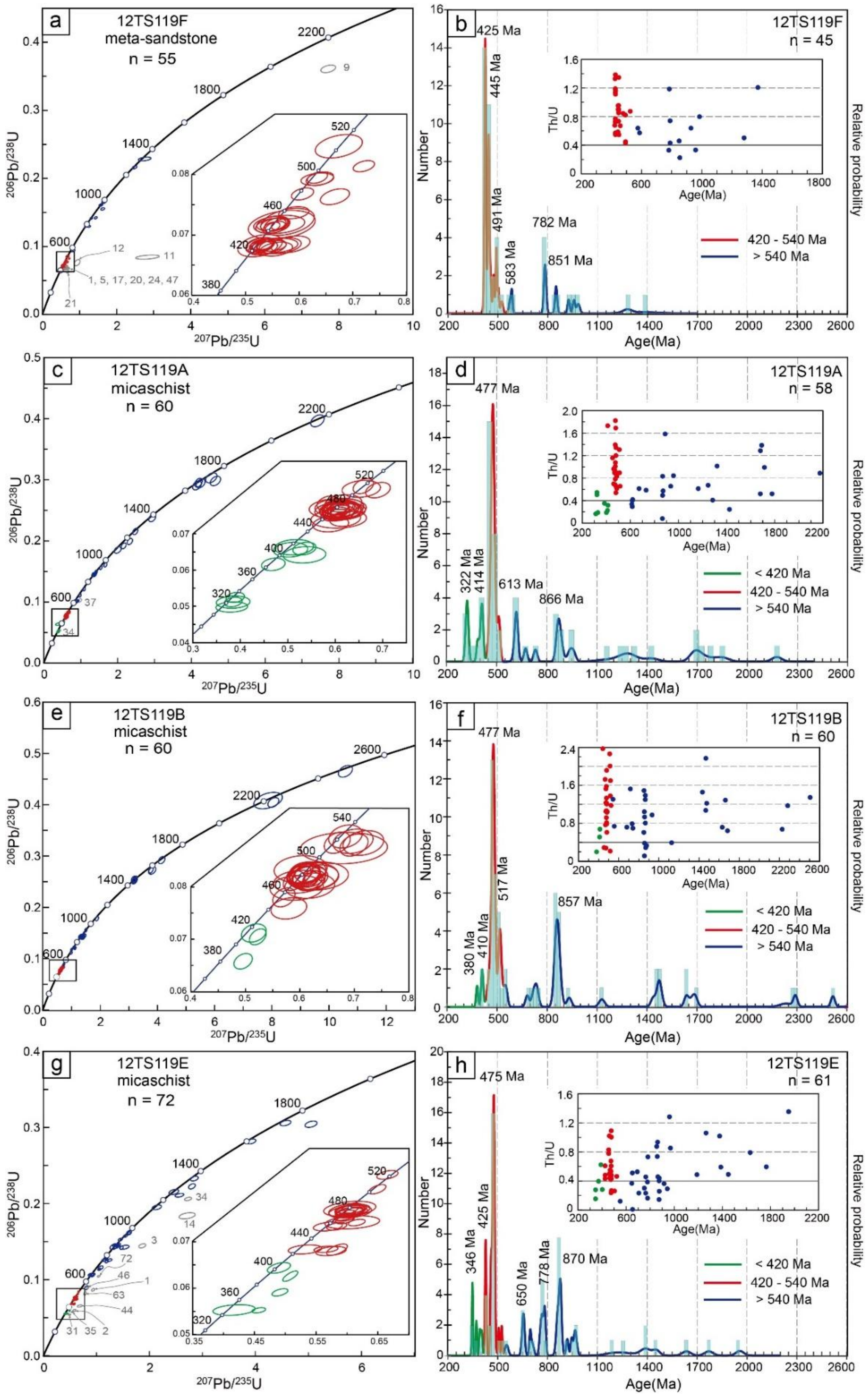

Figure 4.16. Concordia diagrams (a, c, e and g) and U-Pb age probability diagrams (b, d, f and h), and insets are plots of Th/U ratios vs. U-Pb age for detrital zircons from the meta-sedimentary rocks, southern Harlik Range.

Sixty zircons were dated from the mica-schist sample 12TS119B and all of them yielded concordant ages (Figure 4.16e). Their age populations are very similar to those of the sample 12TS119A. Therein, three youngest zircons (380-413 Ma) belong to the type 3 displaying homogeneous dark to black CL images and Th/U ratios around 0.4. Twenty zircons (33.3%) of type 1 and minor type 2 and type 4 (Figure 4.15c) define an age peak at 477 Ma and show Th/U ratios mostly higher than 0.4. Other ages around 500-550, 600-750, 850-1000, 1100-1500, 1600-1800 and 2200-2500 Ma were obtained from zircons of all four types, most of which show Th/U ratios higher than 0.4 (Figure 4.16f).

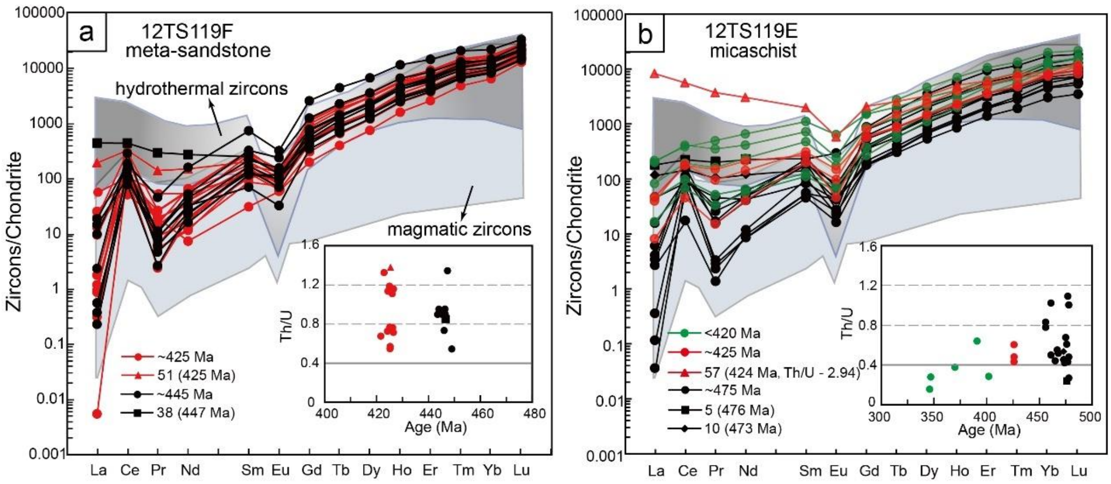

Figure 4.17. Chondrite-normalized REE patterns for detrital zircons from meta-sandstone 12TS119F (a) and mica schist 12TS119E (b). Only the Paleozoic detrital zircons with $^{206}Pb/^{238}U$ ages between 425 Ma and 475 Ma were analyzed for REE abundances. The grey shaded area is the REE composition of hydrothermal zircons (after Hoskin, 2005; W. B. Yang et al., 2014) and magmatic zircons of various igneous rocks (Belousova et al., 2002; Hoskin, 2005; W. B. Yang et al., 2014). Insets are plots of Th/U ratios against U-Pb age. Chondrite normalization values are from Sun and McDonough (1989).

As for the sample 12TS119E, sixty-one out of seventy-two zircons provided concordant ages ranging from 346 to 1765 Ma (Figure 4.16g). A major age peak at 475 Ma (n = 11; 18.0%) and a minor age peak at 425 Ma (n = 5; 8.2%) are mainly defined by types 1 and 2 zircons (Figure 4.15d), which mostly show Th/U ratios higher than 0.4. These zircons show steeply-rising REE patterns, remarkable positive Ce anomalies and negative Eu anomalies (Figure 4.17b). Thus, these ages are indicative of magmatic events (Hoskin and Schaltegger, 2003; Hoskin, 2005). One exceptional zircon (No. 57; ~424 Ma) shows a quite high Th/U ratio. For some unclear reasons, a V-shaped REE pattern due to its high LREE content is similar to that of some "hydrothermal" zircons (Figure 4.17b). Five zircons of types 2 and 3 with dark, homogenous CL images yielded ages of 346 to 402 Ma, they display gently-rising REE patterns with weak Ce anomalies and Th/U ratios mostly lower than 0.4, similar to zircons of hydrothermal origin (Figure 4.17b). With only a few exceptions, the other age populations (500-550, 600-800, 850-1000, 1100-1400 and 1600-1800 Ma) correspond to all four zircon types with Th/U ratios mostly higher than 0.4 (Figure 4.16h).

4.6.2. Provenance of the meta-sedimentary rocks

The studied meta-sedimentary rocks contain both Paleozoic and Proterozoic detrital zircons (Figure 4.16). Among overall 224 concordant detrital zircons, 126 grains (56%) yielded Paleozoic ages and 98 zircons (44%) yielded Proterozoic ages. For the Paleozoic ages, the U-Pb system of detrital zircons younger than 420 Ma was likely affected by post-depositional metamorphism. Thus, these zircons and their ages should be rejected for provenance investigation. The Ordovician to Silurian detrital zircons (~480-420 Ma with peaks at ~475, ~445 and ~425 Ma) are dominant constituents in the meta-sedimentary rocks. This is consistent with the study of G. H. Sun et al. (2007) who found a predominant Ordovician to Silurian zircon population (482-418 Ma) in low-grade sandstones from the study area.

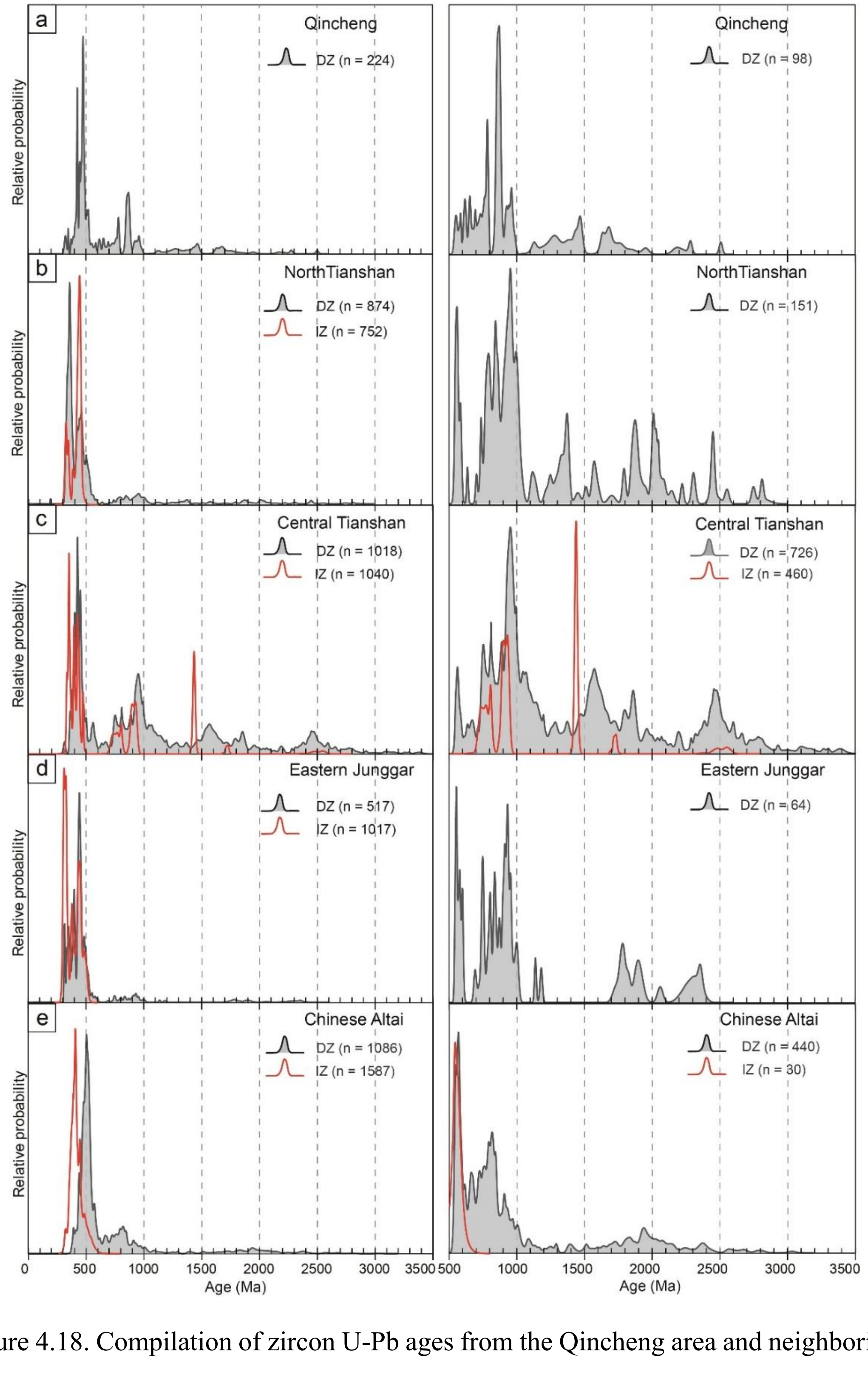

Figure 4.18. Compilation of zircon U-Pb ages from the Qincheng area and neighboring tectonic units. The right columns show the age distributions of Precambrian zircons only. DZ: Detrital zircons from sedimentary rocks; IZ: Zircons from igneous rocks (Inherited zircons were excluded).

As discussed above, the early Paleozoic zircons are mainly derived from magmatic rocks. Numerous early Paleozoic magmatic rocks of 440-450 Ma were previously reported both in the Harlik and Dananhu arcs, while magmatic rocks of 420-430 Ma mostly crop out in the Dananhu area (X. H. Ma et al., 2015; L. Du et al., 2018, 2024; H. Zhao et al., 2022; Gong et al., 2023; L. Li et al., 2023). In addition, In addition, very few ~475 Ma magmatic rocks have been reported so far in the North Tianshan, and only rhyolites at 469 ± 9 Ma were documented from the Harlik area (J. T. Li et al., 2017). The angular to sub-angular early Paleozoic detrital zircons indicate short distances of transportation (G. H. Sun et al., 2007), while samples come from the Qincheng area which is situated between the Harlik Arc and Dananhu Arc. As a consequence, it can be suggested that these early Paleozoic detrital zircons (~480-420 Ma) likely came from magmatic rocks of the Harlik and Dananhu arcs.

Ordovician to Silurian arc-type magmatic rocks are also exposed in the Central Tianshan and East Junggar-Altai belts, which are potential sources for the meta-sedimentary rocks. However, the North Tianshan was separated from East Junggar-Altai belts before the early Carboniferous (>340 Ma) by the Kalamaili oceanic basin (J. Y. Li et al., 2009; G. Huang et al., 2012; Y. Y. Zhang et al., 2013; X. W. Xu et al., 2015; Han & Zhao, 2018; G. C. Wang et al., 2019), while the depositional age of protoliths of the meta-sedimentary rocks is roughly constrained between ~425 to ~322 Ma.. Therefore, the available data cannot sufficiently prove or disprove that the East Junggar-Altai magmatic arcs might be the possible sources for the Ordovician-Silurian detrital zircons of the meta-sedimentary rocks in the Qincheng area.

In addition, it is suggested that the North Tianshan (Harlik-Dananhu Arc) was amalgamated with the Yamansu Arc and Central Tianshan Block at~320-300 Ma along the Kanggur shear zone after the closure of the Kanggur Ocean (e.g., Y. Y. Zhang et al., 2020; G. C. Wang et al., 2022). However, the rock sequences on both sides of this shear zone are comparable and might have been located within the North Tianshan belt (B. Wang et al., 2014; Branquet et al., 2012). According to the studies on ophiolites of the

North Tianshan Suture zone and Kanggur belt, the North Tianshan (or Kanggur) Ocean opened before the mid-late Carboniferous (X. Y. Xu et al., 2006; Z. Y. Chen et al., 2019; G. C. Wang et al., 2022). Considering that the Precambrian zircons most likely came from the Central Tianshan Block (see discussion below), it is possible that the Central Tianshan Block also provided certain early Paleozoic detritus for the sediments in the Qincheng area.

The main population of Proterozoic zircons in the meta-sedimentary rocks is the Neoproterozoic group (550-1000 Ma) showing a peak at ~870 Ma and a subordinate peak at ~780 Ma. Minor zircon populations of 1.1-1.5 Ga, 1.6-2.0 Ga, 2.1-2.3 Ga and ~2.5 Ga with peaks at ~1.45 Ga and ~1.7 Ga are also recognized (Figure 4.18). However, there is no Precambrian basement exposed in the NTB (W. J. Xiao et al., 2004; L. Du et al., 2024). Thus, these Proterozoic zircons were most likely transported from nearby Precambrian-based continental blocks. Some authors suggested that the Harlik Range is a part of the Tuva-Mongol-Altai Arc (e.g., X. J. Chen et al., 2014). Nevertheless, the available data indicate that the Tuva-Mongol-Altai Arc and the East Junggar Belt both lack magmatic events and detrital records in the ~1.35-1.45 Ga interval (Jiang et al., 2011), which are common in the North Tianshan (Figure 4.18; X. J. Chen et al., 2014). In contrast, a large quantity of Mesoproterozoic granitic rocks of ~1.40-1.45 Ga have been documented in the Central Tianshan Block (Z. Y. He et al., 2014, 2015; Z. Y. Huang et al., 2017). Moreover, the Central Tianshan Block has a detrital zircon age spectrum similar to that of the Harlik Range and the entire North Tianshan, all display zircon populations of 750-800 Ma, 850-1000 Ma, ~1.45 Ga, 1.6-1.8 Ga and ~2.5 Ga. More importantly, the igneous rocks in Central Tianshan formed during ~800, ~900 Ma and ~1.45 Ga episodes, identical with the detrital zircon age peaks of the meta-sedimentary rocks from the Harlik Range, which are absent in the other neighboring units (Figure 4.18). Therefore, the Central Tianshan Block is the most probable provenance area for the Precambrian detrital zircons in the studied meta-sedimentary rocks.

The Precambrian zircons in the meta-sedimentary rocks are anhedral in shape and show complex core-rim textures (Figure 4.15), indicating that they were multiple-cycled. Thus, these Precambrian zircons were probably transported from the Central Tianshan Block to the North Tianshan Belt (Dananhu Arc) before the opening of the North Tianshan (or Kanggur) Ocean, and thereafter re-transported into the Harlik area. This is in agreement with the fact that zircon populations of Devonian flyschs in the Dananhu Arc are comparable with that of the Central Tianshan Block (G. C. Wang et al., 2022). However, due to uncertainty on their deposition age, these zircons could have been transported directly from the Central Tianshan Block as well.

Clastic sediments derived from orogens are generally a mixture of multifarious detritus from metamorphic, sedimentary and igneous rocks (e.g., S. Han et al., 2017). Mixing and preferential elimination of certain zircons during transport can significantly modify zircon populations in sediments, especially in old multiple-cycled populations (Hay & Dempster, 2009; S. Han et al., 2017). Therefore, comparison of detrital zircon populations must be undertaken with much care. In the present case, provenance from the Central Tianshan block is most likely, but considering the limited size of the database, other provenances cannot be completely excluded.

4.7 Structural and metamorphic evolution of the Xiaopu Metamorphic Complex

4.7.1 Geochronological results

Zircon U-Pb dating

Zircon U-Pb dating was performed on four samples, including one mylonitic tuff from the Xiaopu Shear Zone (22TS90F), one meta-tuff from the garnet zone (19Q20F), one pre-D2 gneissic granodiorite (18TS80B) and one post-D2 diorite (18TS86E) from the sillimanite-migmatite zone (Table 4.2).

Zircon grains from the meta-tuff (22TS90F) are mostly prismatic. Almost all grains exhibit igneous oscillatory zoning without metamorphic rims (Figure 4.19a).

Twenty-four grains were analyzed, all of which have high Th/U ratios (> 0.1). Twenty-two analyses define one single date population with a weighted mean of 490 ± 3 Ma (MSWD = 1.2). One single concordant date of ca. 510 Ma is interpreted to correspond to an inherited or detrital zircon.

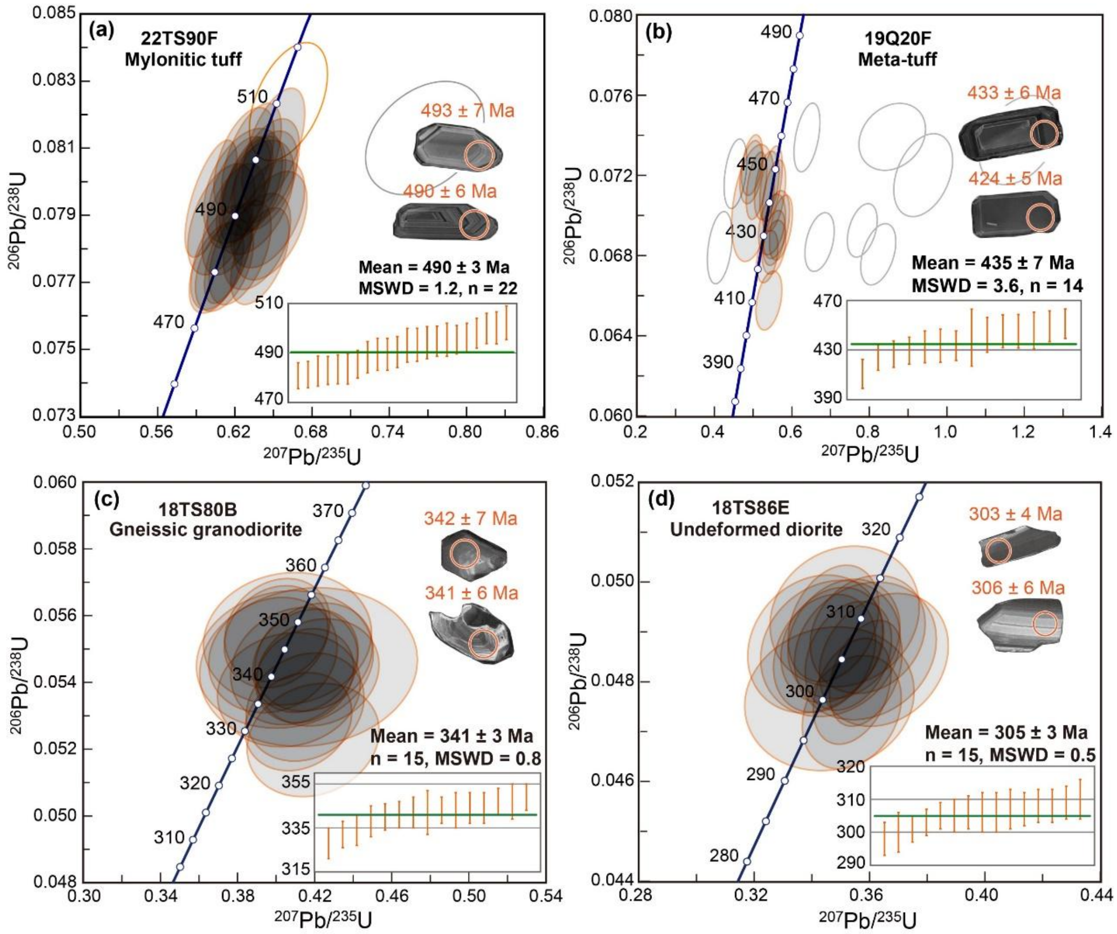

Figure 4.19. Zircon U-Pb concordia diagrams for the dated samples. Unconcordant dates (gray ellipses) are precluded. Insets show CL images of representative zircon grains and weight mean ages.

Zircons from the meta-tuff (19Q20F) are euhedral to sub-euhedral with a few cracked grains. Most display igneous oscillatory zoning without metamorphic rims (Figure 4.19b). Twenty-three analyses were conducted and all of them have high Th/U ratios (> 0.1). Fourteen grains yielded concordant dates to form a cluster with a weighted mean of 435 ± 7 Ma (MSWD = 3.6).

Zircon grains from the gneissic granodiorite 18TS80B have sub-euhedral to sub-rounded shapes. Almost all show core-rim texture in Cathodoluminescence (CL) images (Figure 4.19c). The dark metamorphic rims are too thin to be analyzed. Therefore, fifteen analyses were performed on the zircon cores that display oscillatory zoning. Most of the analyzed grains have high Th/U ratios (> 0.1), consistent with igneous origin. All the dates are concordant and define a single population with a weighted mean of 341 ± 3 Ma (MSWD = 0.8).

Zircons from the diorite 18TS86E are euhedral to sub-euhedral. All of the grains display magmatic oscillatory zoning without metamorphic rims (Figure 4.19d). Fifteen zircons were analyzed and all the dates were concordant to form a single population. The weighted average is 305 ± 3 Ma (MSWD = 0.5).

Monazite U-Th-Pb dating and trace element composition

One sillimanite schist (18TS84E) and one garnet-sillimanite migmatite (19Q22A) were chosen for monazite U-Th-Pb dating. Both are from the sillimanite-migmatite zone (Table 4.2).

Monazite grains from the sillimanite schist (18TS84E) are sub-equant and irregular in shape and 40-100 μm across. Backscattered electron (BSE) images show that most grains are homogenous. Only a few grains show patchy zoning with a dark core and bright rim. There is no apparent correlation between the date and the location within the grain (Figure 4.20). Thirty-two analyses yielded $^{208}Pb/^{232}Th$ dates between 324 and 306 Ma, with a weighted mean of 313 ± 1 Ma (MSWD = 2.0). Most monazite spots have similar REE patterns (Figure 4.20) and uniform $(Gd/Yb)_N$ ratios (< 25; Figure 4.22). Eu/Eu* values are low (0.05-0.11) and show a positive correlation with dates (Figure 4.22), indicating stronger Eu negative anomalies in younger monazite domains.

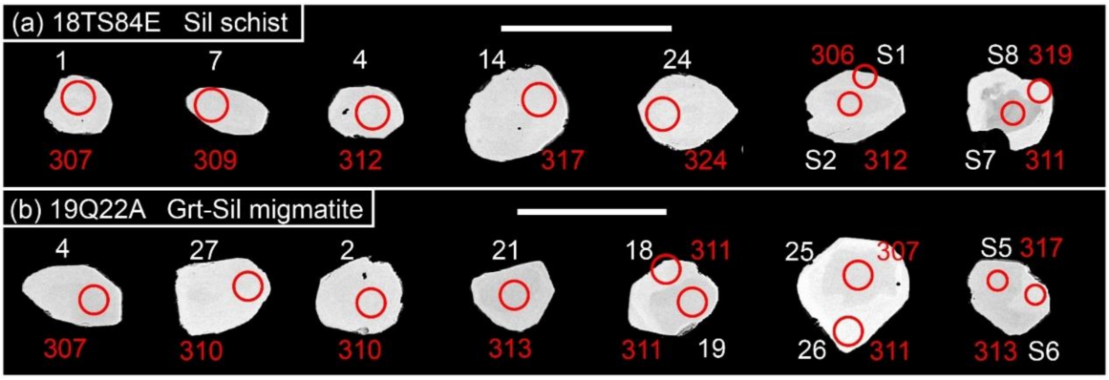

Figure 4.20. Representative back-scattered electron (BSE) images of monazite from the metapelitic rocks showing the analyzed spot locations and numbers (white number) and relevant ages (in Ma, red number). The scale bars are 100 μm.

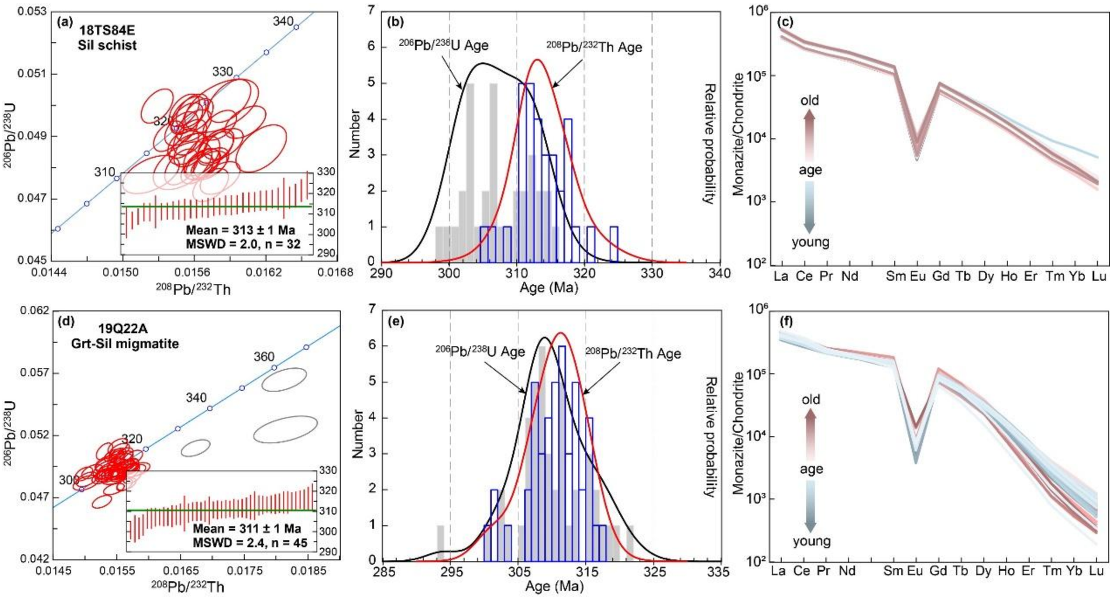

Figure 4.21. (a and d) $^{206}Pb/^{238}U$ vs $^{208}Pb/^{232}Th$ concordia plots and (b and e) probability diagrams of dates for monazite in the Sil schist (18TS84E) and Grt-Sil migmatite (19Q22A). Unconcordant dates (gray ellipses) are precluded. (c and f) REE patterns of monazite; chondrite normalization values from Sun and McDonough (1989).

Monazites from the garnet-sillimanite migmatite (19Q22A) show similar textures and dates. They are small (40-100 μm in length), sub-equant and irregularly shaped. Some grains have patchy zonation but there is no apparent correlation between the date and the textural position (Figure 4.20). Except for three disconcordant spots, forty-five analyses yielded $^{208}Pb/^{232}Th$ dates from 317 to 301 Ma and the weighted average is 311 ± 1 Ma (MSWD = 2.4). The REE patterns show a steep slope of the HREE (Figure 4.21). The $(Gd/Yb)_N$ ratios are high (34-169) and generally decrease with younger dates. Eu/Eu* also shows lower values in younger monazite domains (Figure 4.22).

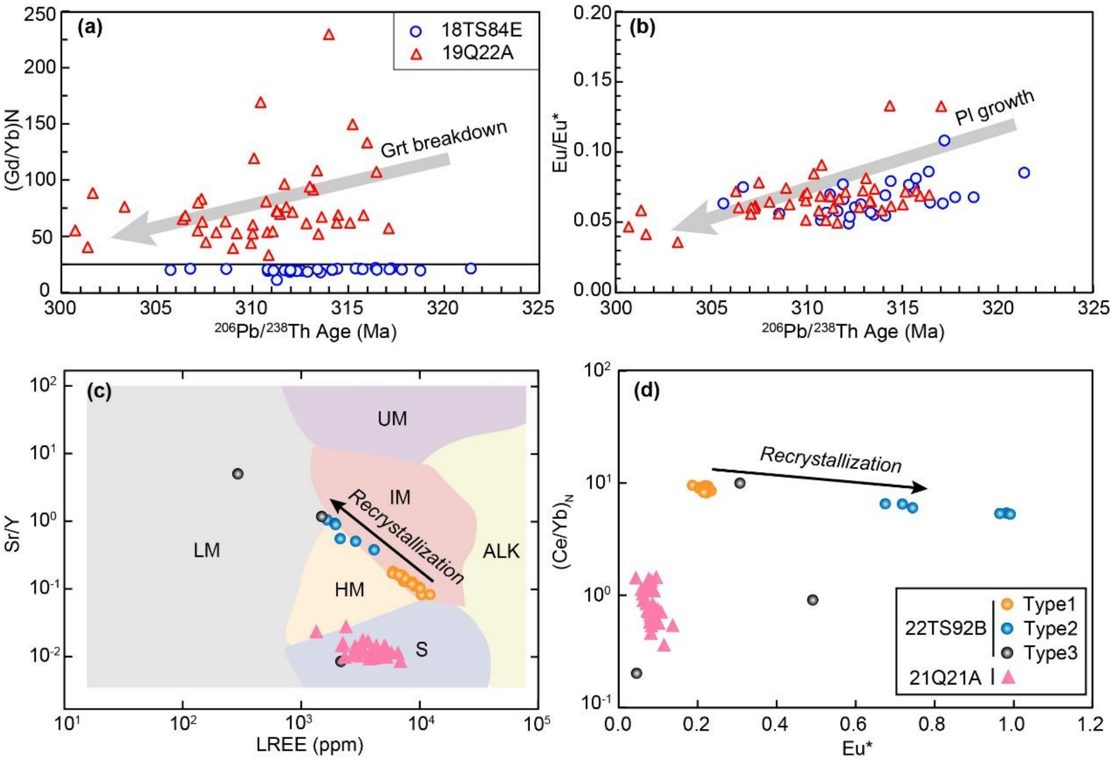

Figure 4.22. (a) (Gd/Yb)N and (b) Eu/Eu* vs $^{208}Pb/^{232}Th$ age plots for monazites from the Sil schists and Grt-Sil migmatites. (c) Biplot of Sr/Y vs LREE (La-Nd) of apatite grains (O'Sullivan et al., 2020). ALK: alkali-rich igneous rocks; IM: mafic I-type granitoids and mafic igneous rocks; UM: ultramafic rocks; LM: low- and medium-grade metamorphic and metasomatic; HM: partial-melts/leucosomes/high-grade metamorphic; S: S-type granitoids and magmatic rocks with high aluminum saturation index. (d) Biplot of Ce/Yb vs Eu* for apatite.

Apatite U-Pb dating and trace element composition

Apatite U-Pb dating was performed on one mylonitic granite (21Q21A) and one mylonitic tuff (22TS92B) from the Xiaopu Shear Zone. The U-Pb zircon date of the mylonitic granite is 316-312 Ma (P. Song et al., 2018; L. Liu et al., 2020) and that of the mylonitic tuff is ~490 Ma (from our sample 22TS90F).

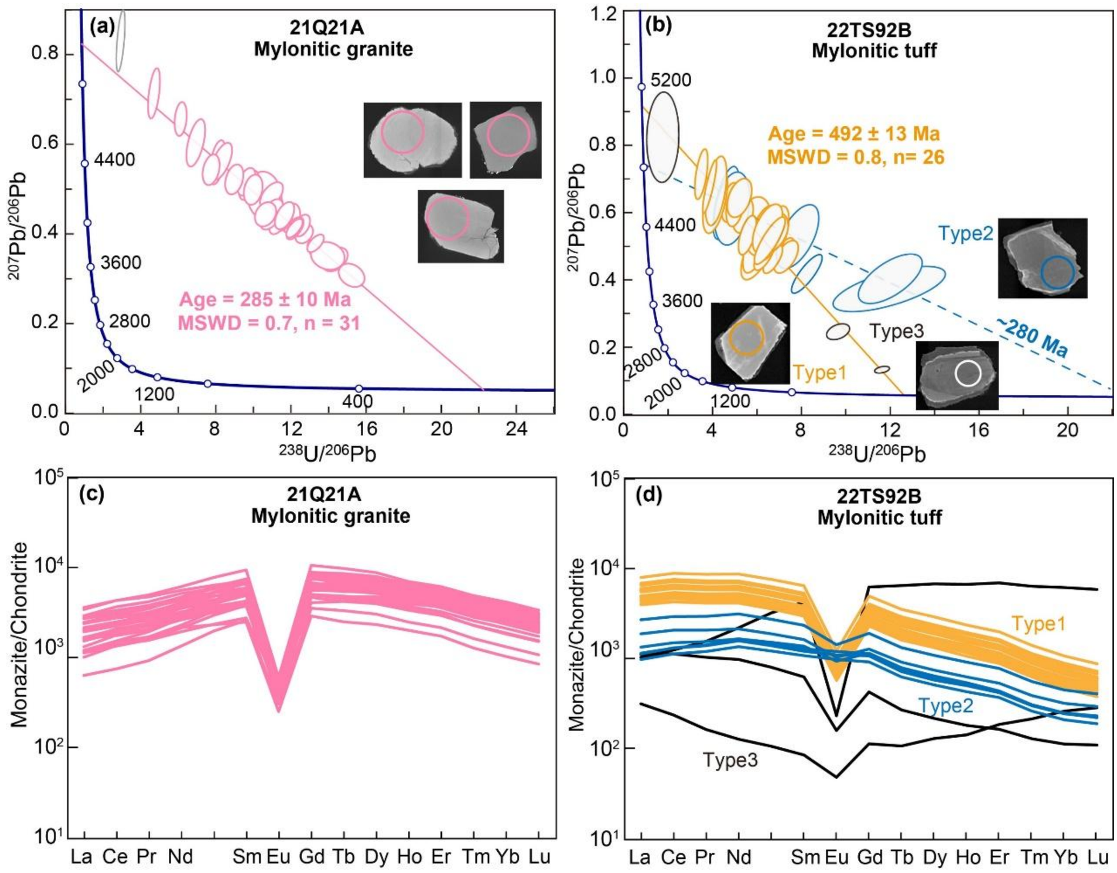

Figure 4.23. (a and b) Tera-Wasserburg diagrams of apatite U-Pb data with BSE images of representative apatite grains. (c and d) REE patterns of apatite grains; chondrite normalization values from Sun and McDonough (1989).

Apatite from the mylonitic granite (21Q21A) is sub-euhedral to subrounded with some fractured grains. Backscattered electron (BSE) images show that most apatite grains are homogeneous (Figure 4.23). A total of 32 analyses were acquired and all of them contain a significant amount of common Pb. One analysis deviates from the main trend of the data and is excluded from further discussion. The remaining data define a well-distributed linear array and yield an isochron with a lower intercept of 285 ± 10 Ma (MSWD = 0.7). All the apatite grains have slightly concave REE patterns with strong negative Eu anomalies. They have Sr/Y ratios and LREE contents similar to S-type granites with a minor trend towards the low and medium grade metamorphic and metasomatic apatite fields (Figure 4.22; O'Sullivan et al., 2020). Their Eu* and $(Ce/Yb)_N$ ratios are about 0.1 and 1.0, respectively.

Apatite from the mylonitic tuff (22TS92B) is mostly sub-euhedral to sub-rounded. BSE images show that almost all grains have core-rim textures (Figure 4.23). Apatite can be divided into three groups, based on texture and REE content. The type 1 has BSE-light cores, the highest REE contents, strong negative Eu anomalies (Eu* = 0.19-0.21), and $(Ce/Yb)_N$ about 10. The type 2 has relatively BSE-dark cores, low REE contents, slight negative Eu anomalies (Eu* = 0.72-0.99), and low $(Ce/Yb)_N$ ratios (5.3-6.5). The type 3 has BES-dark cores but shows various REE patterns, Eu anomalies (Eu* = 0.05-0.49), and $(Ce/Yb)_N$ ratios between 0.2 and 10. Twenty-six analyses of type 1 and type 3 define a well-distributed linear array and yield an isochron with a lower intercept of 492 ± 13 Ma (MSWD = 0.8). Six analyses of type 2 yielded an isochron with a lower intercept of ~280 Ma, consistent with the dating result of 21Q21A.

Biotite $^{40}Ar/^{39}Ar$ dating

Four sillimanite-bearing schists from the sillimanite-migmatite zone were selected for biotite $^{40}Ar/^{39}Ar$ dating. Three samples (18TS84E, 18TS84I, and 18TS84J) are from the same outcrop. They yielded complex age spectra, but all of them have nearly flat segments accounting for >60% of the total ^{39}Ar released. The weighted mean ages (WMA) are 298 ± 1 Ma (MSWD = 1.4), 293 ± 1 Ma (MSWD = 2.4) and 287 ± 1 Ma (MSWD = 1.9) and the total gas ages (TGA) are 295 ± 6 Ma, 296 ± 6 Ma and 288 ± 6 Ma, respectively. Another sample, 18TS85A, was analyzed three times, but all runs yielded discordant age spectra. These three analyses yielded the same TGA of 275 ± 5 Ma (Figure 4.24).

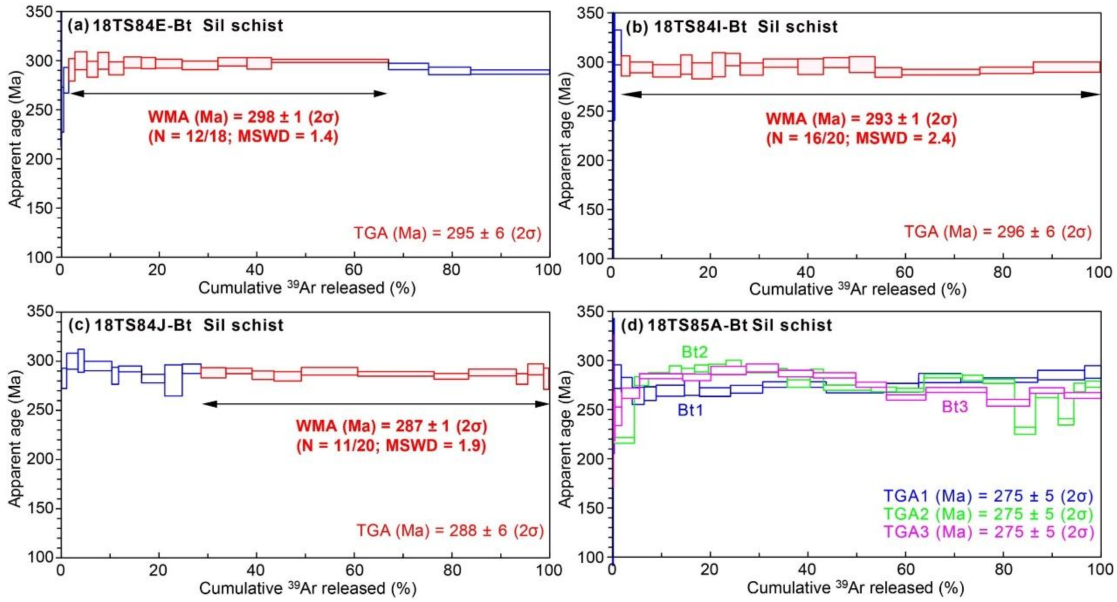

Figure 4.24. $^{40}Ar/^{39}Ar$ age spectra for analyzed samples, reporting Weight Mean Age (WMA) and Total Gas Age (TGA) with the respective estimated error. Arrows span consecutive steps included in the weight mean ages. Boxes represent the heating-steps, with the width representing the percentage of ^{39}Ar released and thickness corresponding to the analytical error.

4.7.2 Interpretation of the geochronological results

The low-grade mylonitic tuff from the Xiaopu shear zone yields a zircon U-Pb date of 490 ± 3 Ma (Figure 4.19). This date can be considered as the depositional age of the tuff since all dated zircons are of igneous origin. The type1 and type3 apatite from another mylonitic tuff sample yielded a U-Pb date of 492 ± 13 Ma, in accord with the zircon U-Pb date. Furthermore, volcanic rocks from the same strata have a zircon U-Pb date of 469 ± 9 Ma (J. T. Li et al., 2017). Therefore, the age of the volcanic-sedimentary rocks involved in the Xiaopu Shear Zone is likely late Cambrian to early Ordovician.

The meta-tuff from the garnet zone has a zircon U-Pb date of 435 ± 7 Ma (Figure 4.19). This date represents the depositional age of the tuff because all dated zircons are of igneous origin. This result is consistent with previous U-Pb dating of detrital zircons from meta-sandstones and mica schists, which show youngest peaks at 425 and 445 Ma (Sun et al., 2007 and this thesis). Therefore, the protoliths of the metapelitic rocks are of the middle to late Silurian age, rather than Carboniferous (contrary to previous suggestions; XBGMR, 1966).

The D1 event, i.e. folding of the Silurian strata, must have occurred after ~430 Ma. As the Silurian to Devonian strata in the Harlik area are part of a continuous transgressive sequence in a back-arc basin environment (M. Zhang et al., 2021), it is unlikely that the D1 compressional event occurred during this period. Furthermore, there are unconformities between pre-Carboniferous and early Carboniferous rocks, both of which are overlain by unconformable late Carboniferous strata (Y. Y. Zhang et al., 2013; G. C. Wang et al., 2019; D. Li et al., 2020). Considering that the early Carboniferous and older rocks were deformed under NE-SW-directed shortening, it is most likely that D1 occurred during the early Carboniferous.

Magmatic zircons from the pre-D2 gneissic granodiorite and post-D2 diorite yield U-Pb zircon dates of 341 ± 3 Ma and 305 ± 3 Ma, respectively (Figure 4-19). Therefore, D2 must have occurred between these two dates. In addition, some syn-D2 granitic dykes have crystallization ages of 332-330 Ma. Undeformed leucogranite or pegmatite dykes yield zircon U-Pb dates of 309-308 Ma (X. H. Zhu et al., 2018). All these dates indicate that D2 at least started at ~330 Ma and was completed before ~310 Ma.

Monazites in sillimanite-bearing samples 18TS84E and 19Q22A are mostly distributed in the matrix and have dates ranging from 324 to 306 Ma and 317 to 301 Ma, respectively. Interestingly, monazite grains in the garnet-free schist 18TS84E show less HREE depletion and have uniform $(Gd/Yb)_N$ ratios lower than 25. Whereas, monazites from the garnet-baring migmatite 19Q22A are more HREE-depleted and have higher $(Gd/Yb)_N$ ratios of 34-169 (Figure 4.22). These features indicate that garnet crystallization controls HREE depletion of monazite (e.g., Foster et al., 2002; Rubatto et al., 2006). Monazites in 19Q22A display an increase in HREE and a decrease in $(Gd/Yb)_N$ ratios with decreasing age, which may reflect the breakdown of garnet (e.g., Soret et al., 2019, 2022; Ding et al., 2021). In addition, monazite in both samples shows a trend to a stronger negative Eu anomaly at younger ages (Figure 4.22), which could result from K-feldspar or plagioclase growth (Buick et al., 2010; Rubatto et al., 2013). The monazite therefore likely records the garnet resorption and melt crystallization along the retrograde path; this is consistent with monazite dissolution during partial melting and growth during cooling and melt crystallization (Kelsey et al., 2008; Yakymchuk & Brown, 2014). Accordingly, the monazite mean dates (313-311 Ma) are interpreted as the ages of retrograde metamorphism (M3). The peak metamorphism (M2) probably occurred around or before the oldest monazite dates (317-324 Ma). Combined with the metamorphic zircon U-Pb date of ~322 Ma, we suggest that the peak metamorphism occurred at around 320 Ma. The M2 and M3 were synchronous with D2, consistently with petrographic observations.

The mylonitic granite involved in D3 yielded an apatite U-Pb date of 285 ± 10 Ma (Figure 4.23), which is younger than its zircon U-Pb date (317-312 Ma). Given the closure temperature of ~400-550°C for the apatite U-Pb system (Chamberlain & Bowring, 2001; Chew & Spikings, 2015), this date is interpreted to represent the age of shearing (deformation temperature ~400-500°C). Apatite from the mylonitic tuff gave two dates at 492 ± 13 Ma and ~280 Ma (Figure 4.23). The former is compatible with the zircon U-Pb date and thus records the age of initial crystallization of apatite. The latter is similar to the apatite U-Pb date of the nearby mylonitic granite, which likely represents the recrystallization/deformation age. The changes in LREE, Sr/Y, and Eu* for different apatite groups probably indicate the effects of apatite recrystallization and/or fluid interaction (Figure 4.22; Odlum & Stockli, 2020; Ribeiro et al., 2020). Overall, D3 is dated at around 285 Ma.

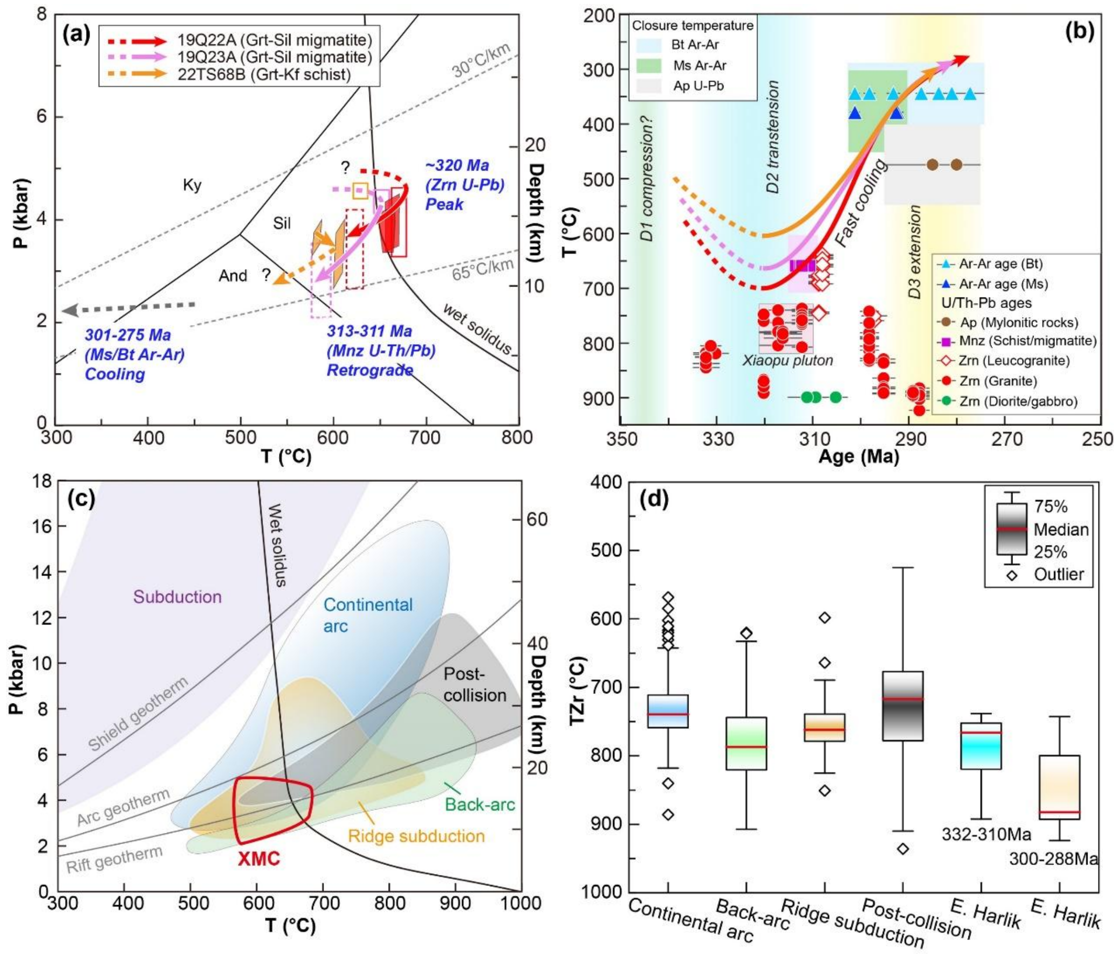

Figure 4.25. (a) Synthetized P-T-t paths for the Grt-Sil migmatites (19Q22A and 19Q23A) and Grt-Kf schist (22TS68B). Hollow and solid boxes refer to conditions estimated from geothermobarometers and thermodynamic modelling, respectively (see Figures 4.13 and 4.14). (b) Thermal and structural evolution of the Xiaopu Metamorphic Complex. Temperature for the monazite crystallization is estimated at 650 ± 50°C according to the metamorphic conditions. Temperature for the granitic magmatism is calculated by the zircon saturation thermometry (Waston & Harrison, 1983), while that for the diorite/gabbro is assumed at 900°C. Closure temperatures of different isotopic systems are from Chew & Spikings (2015) and Wan et al. (2021). Horizontal black bars represent age errors. (c) Comparison of P-T conditions between the Xiaopu Metamorphic Complex (XMC) and various geological settings (modified from Hopkins et al., 2008 and Penniston-Dorland et al., 2015). (d) Comparison of

zircon saturation temperature (TZr) for granitoids in the eastern Harlik and various geological settings.

Biotite from sillimanite-bearing schists yield $^{40}Ar/^{39}Ar$ dates ranging from 298 to 275 Ma (Figure 4.24), broadly consistent with the muscovite $^{40}Ar/^{39}Ar$ dates of 301-293 Ma and biotite $^{40}Ar/^{39}Ar$ dates of 301-277 Ma obtained by Sun (2007). Considering (1) the high-temperature condition (600-700°C) and older age (~320-310 Ma) of the metamorphism, and (2) the low closure temperature of the Ar/Ar system of muscovite (300-450°C) and biotite (280-400°C; Harrison et al., 1985, 2009; Wan et al., 2021), the $^{40}Ar/^{39}Ar$ dates correspond to cooling ages.

4.7.3 Structural evolution and P-T-t history

A combination of structural, petrological, and geochronological data allows for deciphering the P-T-t history of the XMC. The synthesized P-T-t paths and thermal and structural evolution of the XMC based on available data are shown in Figure 4.25.

The Silurian sedimentary sequences were probably folded under a NE-SW compression (D1) regime during the early Carboniferous. Assuming a crustal density of 2,700 kg/m^3, the rocks were buried to mid-crustal depth (15-20 km) as recorded by the highest pressure of ~4-5 kbar (Figure 4.25a). The internal foliation defined by inclusion trails in the garnet core and in andalusite and staurolite porphyroblasts are attributed to this deformation event. The granodiorite bodies (~341 Ma) showing NW-SE trending long axes were also emplaced during this stage.

During the 330-310 Ma period, a NW-SE transtension along NW-SE trending lineaments (D2) affected the pelitic rocks, resulting in the development of the S2 foliation. This event is also recorded by the crystallization of the peak assemblage (M2) of the Grt-Kf schists as well as peak and retrograde assemblages (M2 and M3) of the Grt-Sil migmatites. Phase equilibria modeling of the Grt-Kf schist 22TS68B reveals a pre-peak heating and slight decompression from ~580°C – 3.7 kbar to ~605°C – 3.4

kbar, corresponding to an increase of the thermal gradient from 42°C/km to 47°C/km (Figure 4.25). Moreover, phase equilibria modeling of the migmatites together with conventional thermobarometry indicates cooling and decompression across the solidus in the sillimanite stability field (Figure 4.25a). The peak conditions of samples 19Q22A and 19Q23A are ~680°C – 4.3 kbar and ~650°C – 4.3 kbar, respectively, indicating high thermal gradients of ~40°C/km. They underwent partial retrogression at ~600°C – 3 kbar with a slightly higher thermal gradient of 50°C/km. Such P-T paths and high temperature and low pressure (HT-LP) conditions are consistent with tectonic context of extension or transtension (Sandiford & Powell, 1986).

The age of the peak metamorphism is ~320 Ma inferred from the metamorphic zircon U-Pb dates, while the retrogression occurred at 313-311 Ma according to the monazite U-Th-Pb crystallization ages. Coeval I-type and A-type granites derived from the partial melting of juvenile mafic lower crust and uppermost mantle were emplaced during this period (P. Song et al., 2018, 2023). These granites show zircon saturation temperatures of 720-900°C. Moreover, the peak temperatures of our studied samples increase toward the Xiaopu pluton (Figure 4.12). The constant peak pressure indicates that peak metamorphism occurred at a same depth. It is therefore most likely that the emplacement of the Xiaopu pluton at 317-312 Ma represents the heating source for the metamorphism (Figure 4.25). Some 309-308 Ma S-type leucogranite dykes have zircon saturation temperatures of 640-700°C similar to peak metamorphic conditions of the migmatites (Figure 4.25). They are therefore interpreted as melts extracted from the migmatites.

The D3 phase is characterized by strain partitioning and localized ductile faulting. The XSZ and QTF both affected the early Permian K-feldspar granites and show similar deformation temperatures of 400-500°C. Therefore, they are interpreted to be coeval and controlled the exhumation of the XMC (Figure 4.26). Exhumation occurred at ~285 Ma as constrained by apatite U-Pb dates, contemporaneous with the fast cooling of the XMC (Figures 4.25a and 4.25b). Coeval A-type granites and mafic intrusions of early

Permian ages were also emplaced in the Harlik region, suggesting crust thinning and partial melting of lower crust and upper mantle (Gu et al., 1999; C. S. Wang et al., 2009b; Yuan et al., 2010; X. J. Chen et al., 2016; Yao et al., 2020). Therefore, D3 is interpreted to be responsible for the exhumation and cooling of the XMC in an extensional setting during the early Permian. A few early Permian granitoids occurred within the XMC and some are close to the shear zones (Figures 4.1c and 4.2). The emplacement of such Permian magmas is interpreted to have increased the buoyancy of the mid-crust and promoted the exhumation.

In summary, we infer that the XMC experienced the D1 compression and folding during the early Carboniferous. At 330-310 Ma, the D2 sinistral transtension sheared the rocks and facilitated the emplacement of large plutons which served as additional heating source for the high-T metamorphism and partial melting of the metapelites. Subsequently, the D3 extension occurred during the early Permian, resulting in the exhumation and cooling of the XMC.

4.8 Implications for inverted metamorphism

Mechanisms that are suggested to control the development of inverted metamorphic sequences include: (1) a local inversion of geothermal gradients attributed to the ironing effect of a hot crustal channel or thrust nappe (Le Fort, 1975; Jamieson et al., 2004; Pitra et al., 2010), or to shear heating along thrust zones (Graham & England, 1976); (2) a post-metamorphic tectonic process, such as a ductile extrusion that overturns isograds (Grujic et al., 1996), folding of isograds (Mohan et al., 1989), and tectonic juxtaposition (Jamieson et al., 1996, Soret et al., 2017).

It is, therefore, crucial to decipher the relationships between metamorphism and deformation. Our data on the XMC show that the metamorphism was intimately related, both texturally and temporally, to the sinistral transtension (D2) in the Harlik arc, and ~30 Ma before the exhumation (D3). In addition, low-grade rocks of the hanging wall of the XSZ are in direct contact with the high-grade rocks of the XMC. Therefore, it is excluded that advective heat from a hot nappe or shear heating along the shear zone produced inverted thermal gradients. Instead, the metamorphism was contemporaneous with the emplacement of the Xiaopu pluton which likely represents the heating source of metamorphism. Therefore, we propose that sinistral trantension quickly followed by magma intrusion could make the pluton-ward increasing isograds with sub-vertical fabrics (Figure 4.26d). The isograds were probably rotated by the subsequent asymmetric exhumation that may have a high exhumation rate along the XSZ (Figure 4.26e). This interpretation is supported by the fact that the XSZ is much wider than the QTF (Figures 4.1 and 4.2), though more evidence is needed.

4.9 Implications for the tectonic evolution of the eastern North Tianshan

The XMC data presented here elucidate a complex history of: 1) compression, 2) transtension and heating, and 3) exhumation and cooling of the North Tianshan crust. An early Carboniferous stage of NE-SW compression is tentatively attributed to the closure of the Kalamaili Ocean and the accretion between the Dananhu-Harlik and East Junggar arcs at ~350-330 Ma (Figure 4.26). This hypothesis is based on the following evidence: (1) the SSZ-type ophiolites in the Kalamaili belt were formed between ~420 and 330 Ma with late Devonian to early Carboniferous radiolarian fossils in the cherts (Shu & Wang, 2003; Han & Zhao, 2018; Gao et al., 2022); (2) NW-SE trending folds and thrusts affect the early Carboniferous and older strata in the Kalamaili belt (G. C. Wang et al., 2019; D. Li et al., 2020); (3) early Carboniferous (~340 Ma) tuffs and molasse deposits uncomformably overlie the ophiolite mélanges in places (G. Huang et al., 2012; Y. Y. Zhang et al., 2013; X. W. Xu et al., 2015); (4) the crust thickness of Harlik-Dananhu arc increased at 350-330 Ma according to magmatic Sr/Y ratios (Gong et al., 2023). In addition, Ordovician-Silurian rocks in the northern Harlik are affected by ductile thrusts, notably the Harlik Main Thrust and Koumenzi Fault (W. S. Lei et al., 2018; Zha et al., 2020). These thrusts predate 300 Ma, as evidenced by being cut by ~300 Ma undeformed intrusions, and may result from this arc-arc accretion.

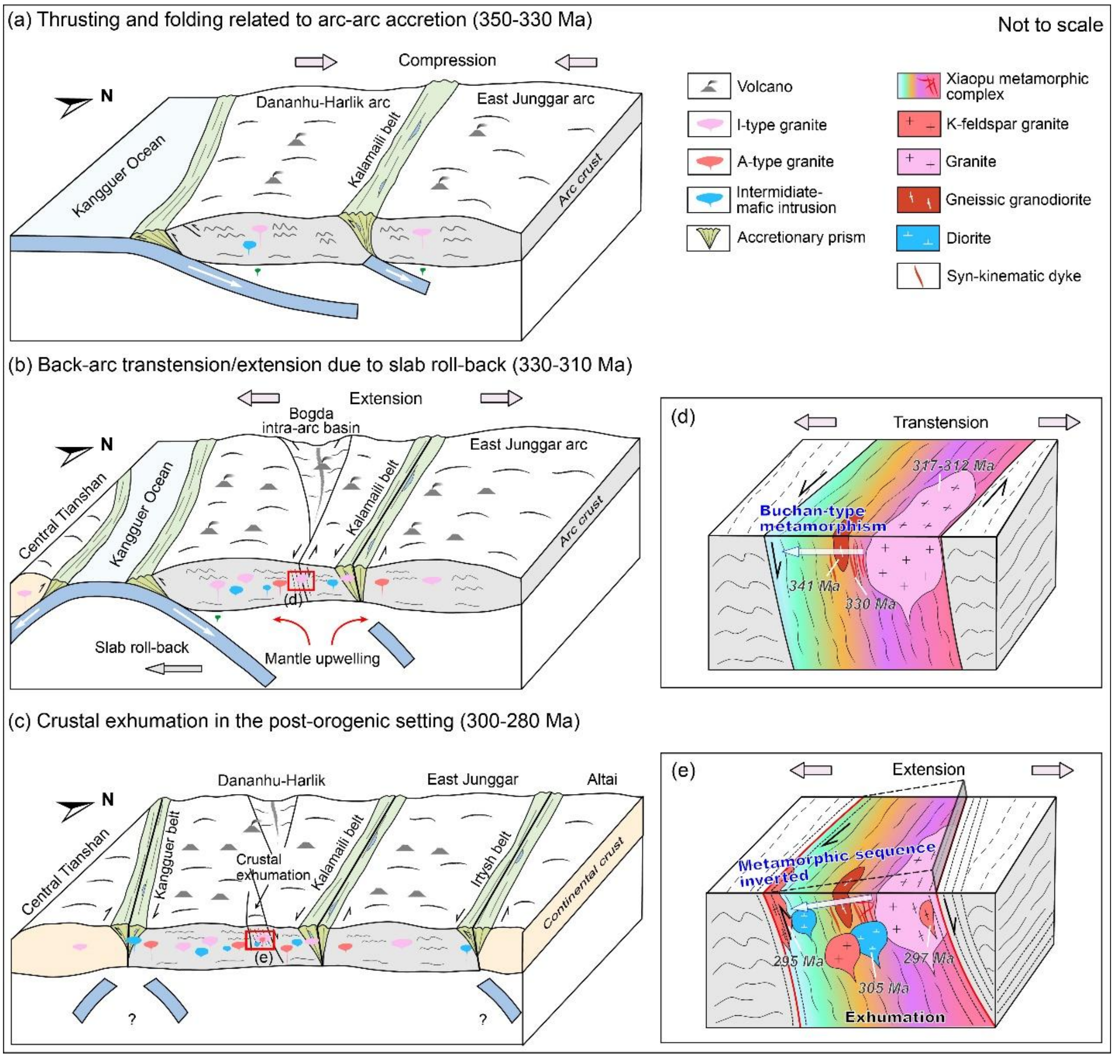

Figure 4.26. Tectonic sketches correlate the Carboniferous to Permian crustal evolution of the North Tianshan. (a) Accretion of the Dananhu-Harlik and East Junggar arcs during the early Carboniferous gave rise to thrusting and folding. (b) Subduction retreat during the middle to late Carboniferous triggered the crustal transtension/extension at the back-arc place. (c) Localized crustal exhumation occurred in a post-orogenic setting during the early Permian. (d) Close-up view of the mid-crust showing the formation of the Buchan-type metamorphism. (e) The Buchan-type metamorphic sequence was inverted due to the asymmetric exhumation.

The sinistral transtension occurred since ~330 Ma and was quickly followed by the emplacement of large plutons and HT-LP metamorphism. The high geothermal gradient (41-50°C/km) similar to that of modern rifts is consistent with an extensional setting (Figure 4.25). Extension in orogenic systems, such as back-arc extension, ridge subduction, and post-collisional collapse, is commonly associated with such gradients (Figure 4.25c). High-grade metamorphism can be intimately related to coeval magmatism. In continental arc, back-arc, ridge subduction, and post-collisional settings, granitoids have zircon saturation temperature at 640-820°C, 630-910°C, 680-820°C, and 530-910°C, respectively (Figure 4.25d). The zircon saturation temperature range of granitoids (720-900°C) synchronous with the metamorphism in the eastern Harlik area mostly resembles the back-arc setting, though it is also partially overlapped with other settings (Figure 4.25d). Early to late Carboniferous subduction-related magmatism is widespread in the Harlik-Dananhu arc and exhibits a southward-younging trend in the Dananhu area (Xie et al., 2016; Y. Y. Zhang et al., 2018; D. Li et al., 2020; Q. G. Mao et al., 2022b). To the south of Dananhu, the Kanggur Belt comprises Carboniferous MORB-like lavas, pyroclastic rocks, and cherts, which represent the remnants of the Kanggur Ocean (Z. Y. Chen et al., 2019; G. C. Wang et al., 2022). Therefore, the northward subduction of the Kanggur Ocean during the Carboniferous likely generated the Harlik-Dananhu arc. At ~330-300 Ma, A_2-type granites intruded in the Harlik and East Junggar areas along the Kalamaili belt (L. Y. Wang et al., 2016; D. Li et al., 2020; J. Wang et al., 2022; P. Song et al., 2023) and extensional structures in Carboniferous strata in the eastern Junggar Basin were revealed by seismic reflection data (D. Li et al., 2020). Meanwhile, a bimodal magmatism occurred in the Bogda area (Y. Y. Zhang et al., 2017) and the volcano-sedimentary succession indicates a progressively deepening environment during the late Carboniferous, which may suggest an intra- or back-arc basin (Memtimin et al., 2019). These data allow us to suggest that the oblique subduction and southward rollback of the Kanggur oceanic slab at 330-310 Ma have caused sinistral trantension in Harlik together with a back-arc extension in Bogda (Figure 4.26b). Such extensional tectonics led to uplift and decompression melting of the metasomatized upper mantle and the juvenile lower mafic crust (Y. Y. Zhang et al., 2017; P. Song et al., 2023). Subsequent ascent and emplacement of the resulting melt could yield high thermal gradients and promote partial melting of the mid-crust (Figure 4.26d). This interpretation is supported by the crustal thinning and increasing magma temperature in Harlik and Dananhu since ~330 Ma (Y. Y. Zhang et al., 2018; Gong et al., 2023). The ductile sinistral shearing overprints on the Harlik Main Thrust (H. D. Ma et al., 2008) and Koumenzi Fault (Zha et al., 2020) are probably related to structural reactivation during this stage.

During the early Permian, mid-crustal rocks of the Harlik Arc were exhumed by extensional structures and associated magma emplacement (Figure 4.26). In the meantime, mafic intrusions (Gu et al., 1999, 2001; Yuan et al., 2010) and A_2-type granites, diagnostic of crustal thinning, occurred in Tianshan and Junggar regions (Han & Zhao, 2018). Therefore, the exhumation and cooling of the Harlik mid-crust were achieved in a post-orogenic setting (Figure 4.26c). Other lines of evidence supporting this interpretation include: (1) there is no confirmed ophiolites younger than 300 Ma in the Tianshan and Junggar regions (Han & Zhao, 2018; Gao et al., 2022); (2) paleomagnetic data show insignificant relative latitudinal motion between the Yili, Junggar, and Turpan-Hami blocks since the late Carboniferous (B. Wang et al., 2007; X. Zhu et al., 2019; W. Xu et al., 2023); (3) magmatic rocks in the Tianshan and Junggar regions show changes of Boron and zircon Oxygen isotopes at ~300 Ma, suggesting a tectonic transition from subduction to post-collision or intraplate setting (H. Q. Liu et al., 2016; G. J. Tang et al., 2019); (4) in the North Tianshan, a switch to terrestrial environment occurred during the early Permian, marked by unconformable molasse deposition (XBGMR, 1993; Shu et al., 2005); (5) major transcurrent faults (e.g., the Main Tianshan Shear Zone, Kanggur-Huangshan Shear Zone, and Irtysh Shear Zone) took place at ~290-245 Ma, and likely recorded an eastward escape of the Junggar Terrane (Laurent-Charvet et al., 2003; Y. Wang et al., 2008; Z. Y. He et al., 2021; P. F. Li et al., 2021; W. W. Hu et al., 2023; Muhtar et al., 2023).

Chapter 5. Late Paleozoic evolution in magmatism of the eastern North Tianshan and East Junggar: Spatial and temporal constraints

5.1 Introduction

Elemental and isotopic features of magmatic rocks are governed by several factors, e.g., the nature of source regions, conditions of partial melting, and magmatic differentiation and assimilation within the crust. Theoretically, changes in these factors in space and time could be ultimately decided by tectonic regimes (Eby, 1992; Whalen and Hildebrand, 2019). The ever-increasing archive of datasets makes employing geochemical proxies extracted from a large number of magmatic samples a novel approach to reconstructing terrane-, orogen- to global-scale geodynamic histories (e.g., M. Tang et al., 2016; Chapman et al., 2017; T. Wang et al., 2023; Qiu et al., 2023; H. Huang et al., 2024). Examining both temporal changes and spatial variations in isotopic signatures (e.g., whole-rock Nd and zircon Hf isotopes) and element indices (e.g., La/Yb and Sr/Y ratios) over time and space, provides valuable insights into lithospheric architecture and the history of continental growth (e.g., Chapman et al., 2017; H. Huang et al., 2020, 2024; T. Wang et al., 2023).

Late Paleozoic magmatic rocks are widespread in the eastern Tianshan and East Junggar regions, and a substantial amount of data has been reported. In this chapter, we present a dataset of late Paleozoic magmatic rocks from these regions, which includes new samples as well as compiled data from the literature. By examining the spatial and temporal variations in rock types, isotopic signatures, and certain elemental indices, I discuss the crustal architecture and tectonic evolution of the eastern North Tianshan and East Junggar during the late Paleozoic. The findings provide significant insights into the evolution of accretionary orogens, from subduction-related to post-orogenic settings.

5.2 Magmatic dataset

Our dataset comprises 482 geochronological dating results (including 12 new results), 2378 whole-rock major and trace element compositions (including 37 new results), 707 Sr isotopic results (including 6 new results), and 808 Nd isotopic results (including 6 new results) for late Paleozoic magmatic rocks in the eastern North Tianshan and East Junggar regions. Additionally, we have compiled 3266 zircon in situ Hf isotopic measurements from 212 late Paleozoic magmatic samples.

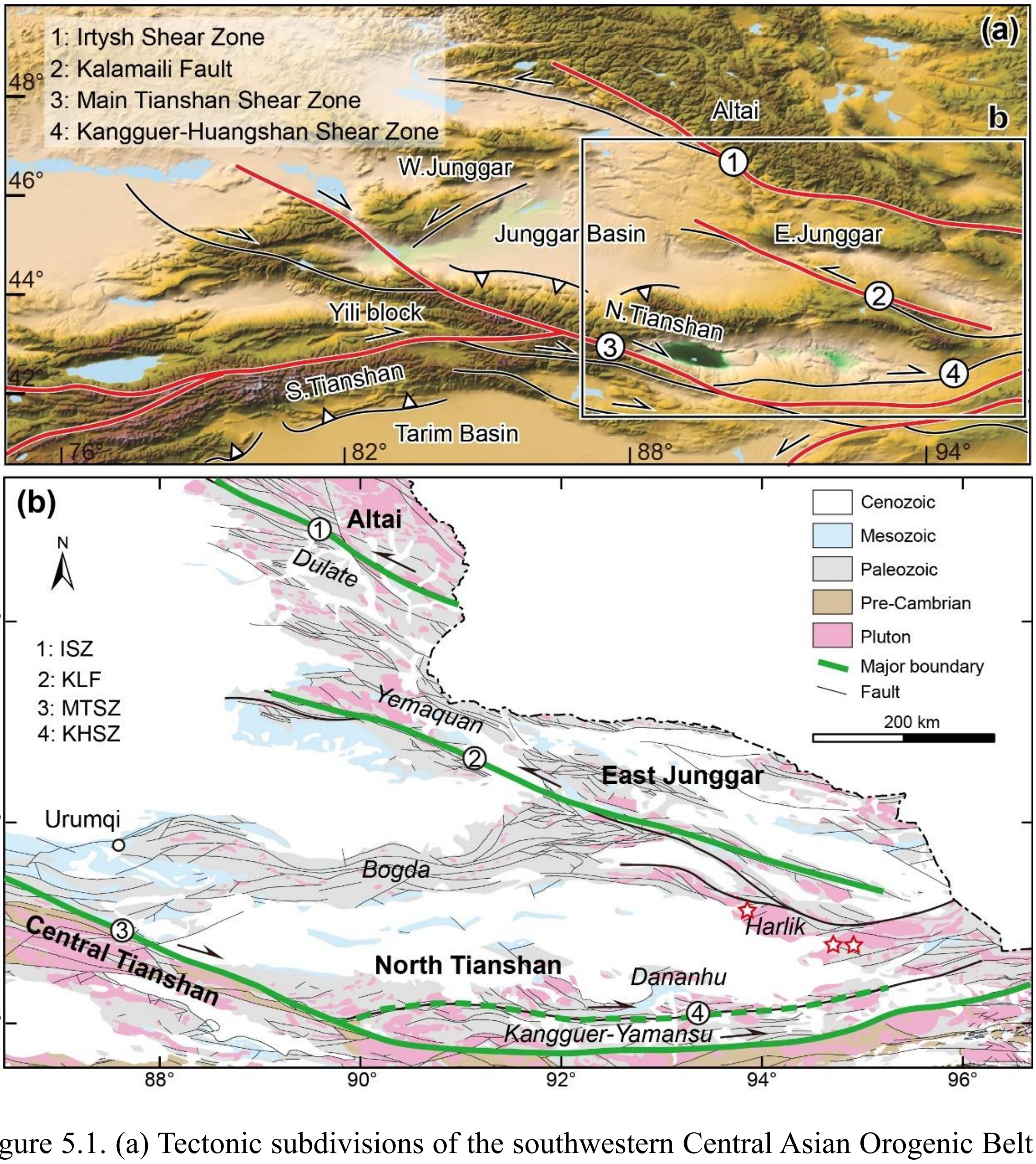

Figure 5.1. (a) Tectonic subdivisions of the southwestern Central Asian Orogenic Belt (topographic images from http://www.ngdc.noaa.gov/mgg/global). (b) Simplified geological map of the eastern North Tianshan and East Junggar. Red stars indicate the location of new samples.

Our new samples were collected from Qincheng and Nanshankou areas in the Harlik Arc (Figure 5.1). The samples consist of diorite, granodiorite, granitic dyke, K-feldspar granite, and rhyolite (Figure 5.2). There zircon LA-ICP-MS zircon U-Pb dating resuts are shown in Figure 5.3. The diorite rocks are non-deformed and have zircon U-Pb dates of 305 ± 3 Ma to 301 ± 3 Ma. The granodiorite and its dioritic enclaves are also non-deformed and yielded zircon U-Pb dates of 307 ± 2 Ma and 310 ± 3 Ma, respectively. The granitic dykes occur in the high-grade meta-pelites and show shape-preferred orientation (SPO) themselves. Their zircon U-Pb dating results are from 332 ± 3 Ma to 330 ± 3 Ma. The K-feldspar granite shows no deformation and has a zircon U-Pb date of 299 ± 3 Ma. The rhyolite samples were collected from the Upper Carboniferous strata. The strata were folded but show no foliations. Zircon U-Pb dating indicates that they have crystallization ages of 303 ± 3 Ma.

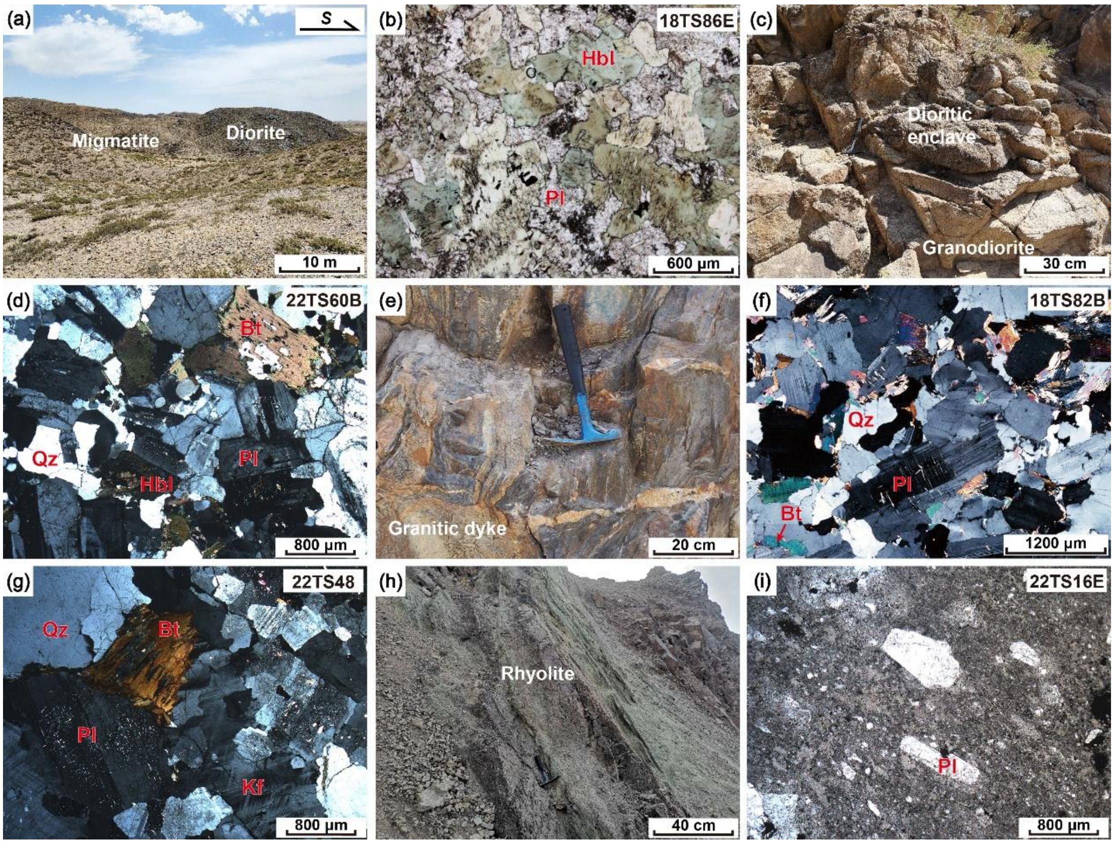

Figure 5.2. Field photos and microphotographies of the magmatic rocks in Harlik Arc.

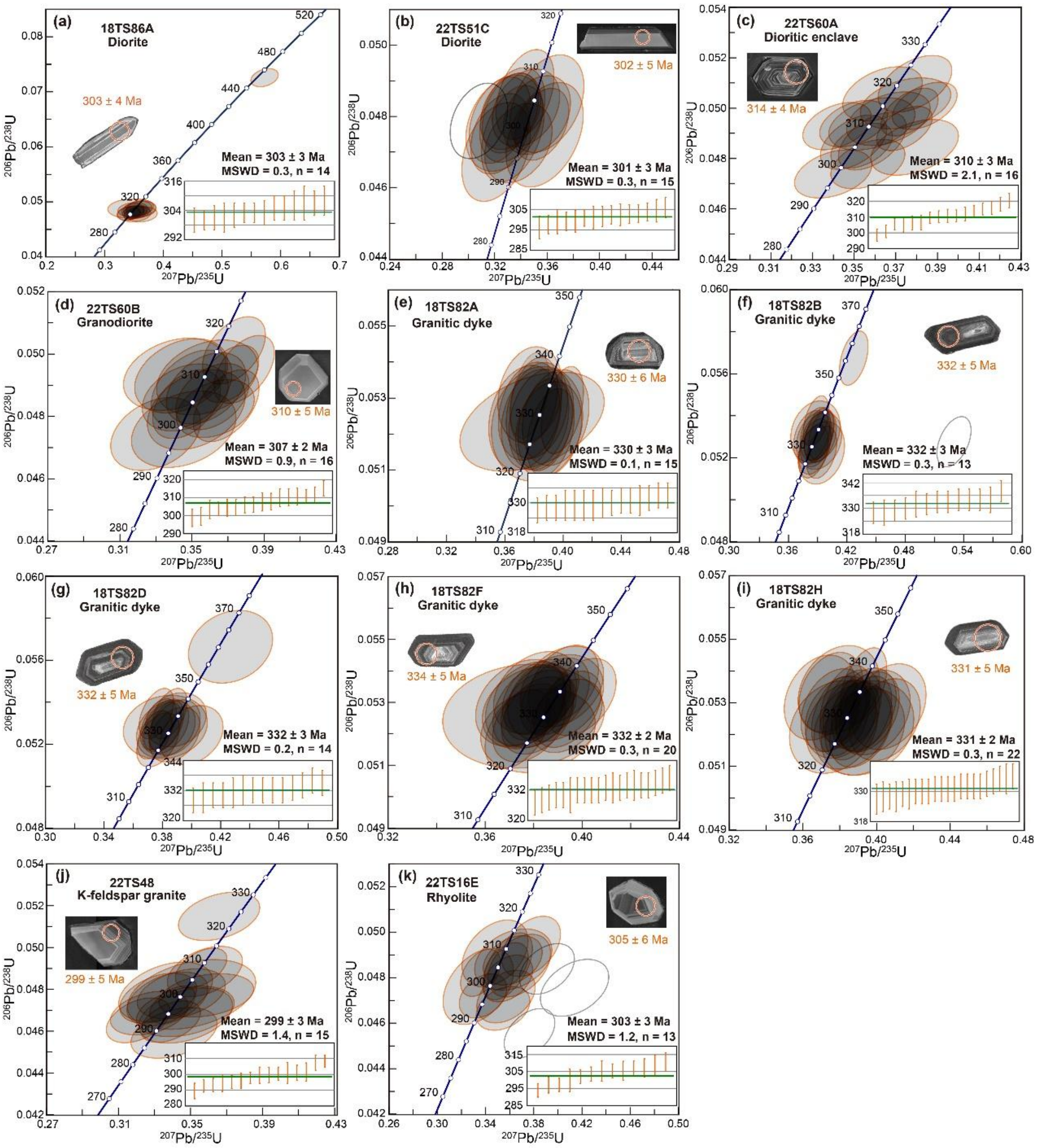

Figure 5.3. Zircon U-Pb concordia diagrams for the dated samples. Unconcordant dates (gray ellipses) are precluded. Insets show CL images of representative zircon grains and weight mean ages.

The compiled data are from both volcanic and plutonic rocks with crystallization ages from Carboniferous to Permian. These rocks include basalt to rhyolite from Carboniferous to Permian strata and peridotite to granite from magmatic intrusions. The compiled data also include some unpublished data of borehole core samples from the Junggar Basin provided by the Research Institute of Petroleum Exploration and

Development-Northwest, PetroChina.

5.3 Late Paleozoic magmatic belts in the eastern North Tianshan and East Junggar

As discussed in Chapter 4, two significant tectonic events may have occurred at approximately 330 Ma and 300 Ma: the amalgamation of the East Junggar with the eastern North Tianshan and the final assembly of the eastern Tianshan. Therefore, we divide the Carboniferous to Permian magmatism into three episodes, including early to middle Carboniferous (360-330 Ma), middle to late Carboniferous (330-300 Ma), and Permian (300-260 Ma). In addition, the magmatic rocks with <52 wt%, 52-65 wt%, and >65 wt% SiO_2 are defined as mafic, intermediate, and felsic rocks here, respectively. According to the evolving SiO_2 composition of magmatic rocks, there are magmatic nulls or change of magmatic compositions during ~300-290 Ma (Figure 5.4), consistent with a possible tectonic transition during this time time. At ~330 Ma, mafic magmatism start to increase in the East Junggar (Figure 5.4a).

5.3.1 Early to middle Carboniferous magmatism (360-330 Ma)

In East Junggar, the early to middle Carboniferous magmatism mostly occurred in the Dulate Arc and the eastern Yemaquan Arc (Figure 5.5a). The magmatic rocks consist of intermediate to felsic rocks, which are mainly I-type with a few A-type granitoids. The intermediate rocks are characterized by arc-like geochemical signitures (Table 5.1).

In the eastern North Tianshan, the early to middle Carboniferous magmatic rocks mostly distributed along the Harlik, Dananhu, and Yamansu arcs, and are scarce in the Bogda Belt (Figure 5.5a). The magmatic rocks comprise mafic to felsic rocks (Figure 5.4b). In the Bogda-Harlik-Dananhu region, the magmatic rocks include I-type and A-type granitoids, adakitic rocks, and mafic to intermidiate rocks with arc-like geochemical features (Table 5.1). In the Kanggur-Yamansu region, the magmatic rocks are mianly I-type granitoids with some S-type granitoids. There are some mafic rocks showing arc-like geochemical signitures. A few mafic rocks in the Kanggur Belt are featured by MORB-like geochemistry, which may represent ophioitic rocks (Table 5.1).

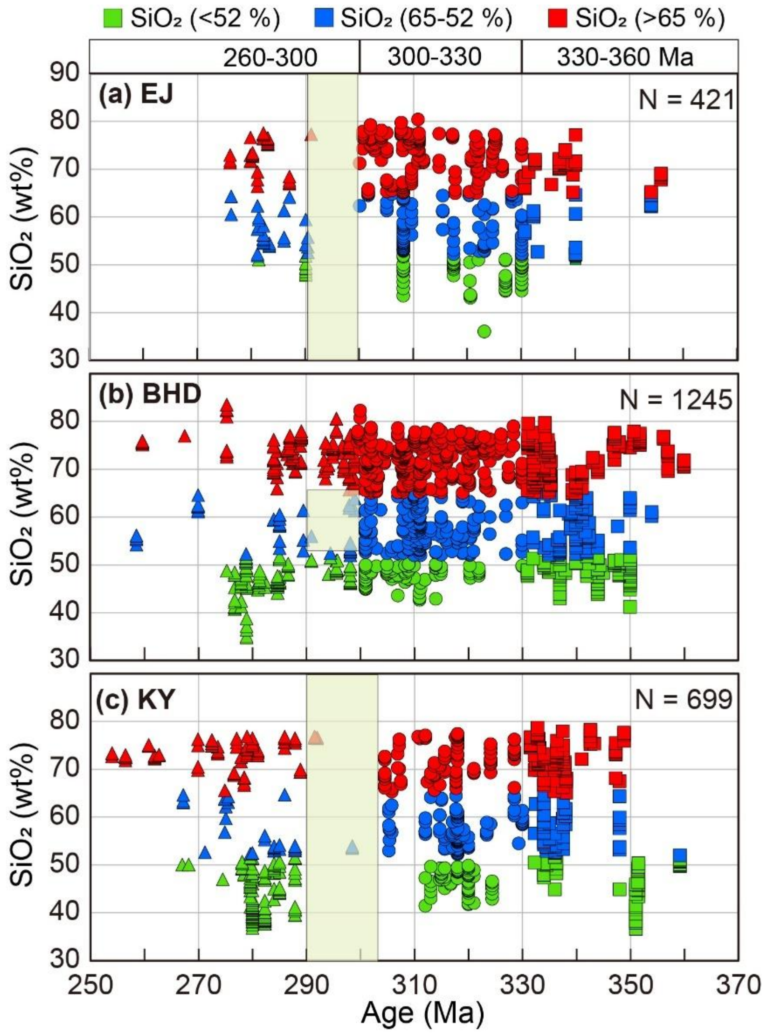

Figure 5.4. Evolving SiO_2 composition of magmatic rocks from the East Junggar (EJ), Bogda-Harlik-Dananhu (BHD), and Kanggur-Yamansu (KY). Shaded areas showing the magmatic null or the reduce of intermediate magmatism.

5.3.2 Middle to late Carboniferous magmatism (330-300 Ma)

Middle to late Carboniferous magmatic rocks are prevalent in the eastern North Tianshan and East Junggar (Figure 5.5b). In East Junggar, the magmatic rocks consist of mafic to felsic rocks (Figure 5.4a). Most of them are A-type and I-type granitoids with some granitoids in the Dulate Arc bearing adakitic affinities. The mafic and intermediate rocks generally show arc-type geochemical features (Table 5.1).

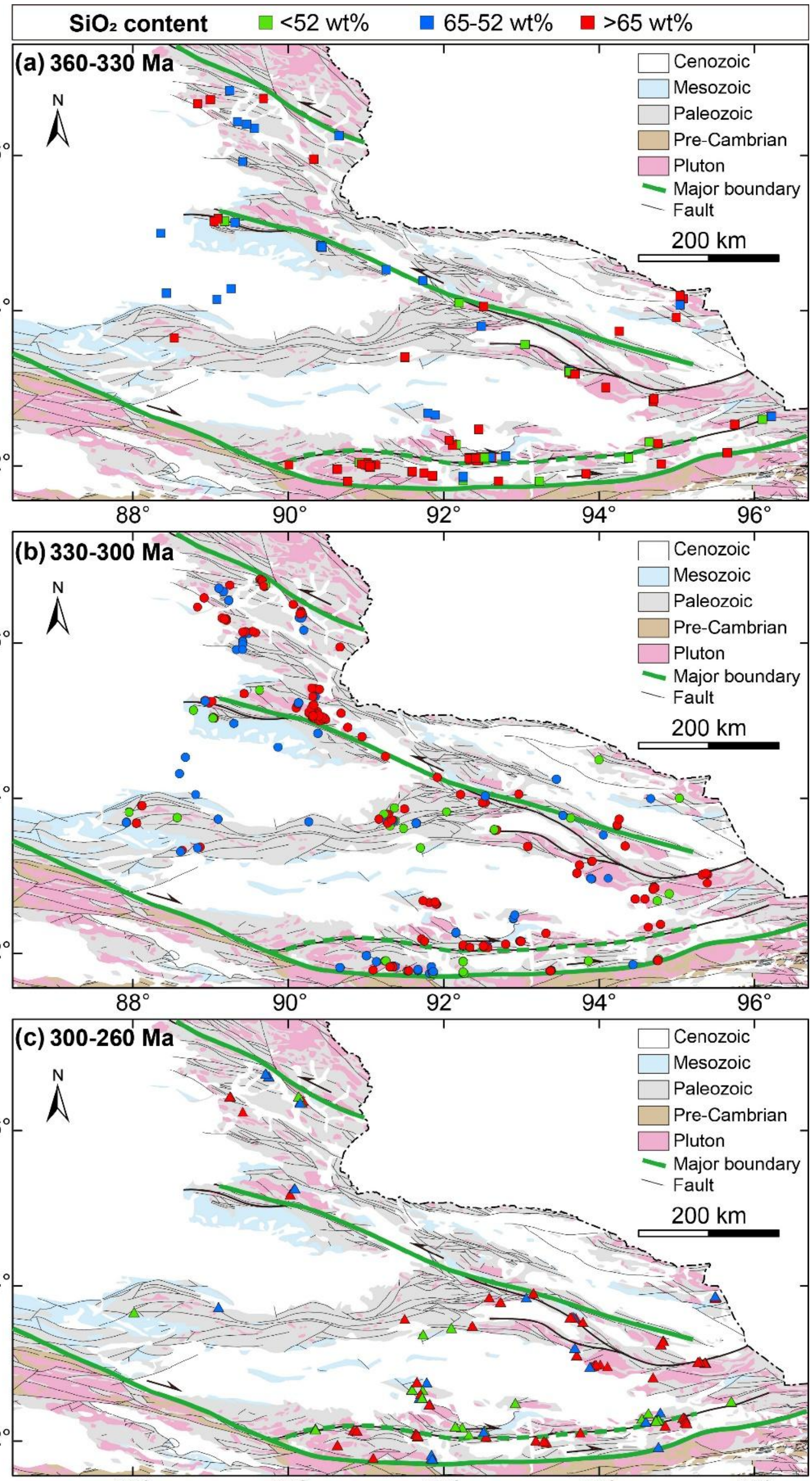

Figure 5.5. Maps showing ages and types of Carboniferous to Permian magmatic rocks. Green, blue, and red sympols stand for mafic (<52 wt.%), intermediate (52-65 wt%), and felsic (>65 wt%) magmatic rocks, respectively.

Table 5.1 Magmatic characteristics in the eastern North Tianshan and East Junggar.

Magmatic belts	Rock types		
	260-300 Ma	300-330 Ma	330-360 Ma
East Junggar	A-type and some I-type granitoids; arc-like mafic to intermidiate rocks	A-type and I-type granitoids; adakitic rocks; arc-like mafic to intermidiate rocks	I-type and a few A-type granitiods
Bogda-Harlik-Dananhu	A-type granitoids, some I-type and a few S-type granitoids; arc-like and MORB-like mafic rocks	I-type, A-type, and some S-type granitoids; adakitic rocks; arc-like mafic to intermidiate rocks	I-type and A-type granitoids; adakitic rocks; arc-like mafic to intermidiate rocks
Kanggur-Yamansu	I-type granitoids, some S-type and A-type granitoids; arc-like and MORB-like mafic rocks	I-type granitoids; arc-like mafic to intermidiate rocks	I-type and some S-type granitoids; arc-like and MORB-like mafic rocks

In the Bogda-Harlik-Dananhu region, the middle to late Carboniferous magmatic rocks comprise both mafic and felsic varieties (Figure 5.4b). The mafic rocks are predominantly found along the Harlik and Bogda belts (Figure 5.5b) and exhibit resemblance to the back-arc basalt (e.g., Xie et al., 2016). Intermediate rocks are widespread, also displaying arc-like signatures. The felsic rocks primarily consist of I-type and A-type granitoids, with some S-type granitoids present. Additionally, a few adakitic rocks can be found in the Dananhu area (Table 5.1).

In the Kanggur-Yamansu region, the magmatic rocks comprise mafic to felsic rocks (Figure 5.4c). The mafic and intermediate rocks are characterized by arc-like geochemical signatures, with some mafic rocks exhibiting MORB-like compositions. The felsic rocks primarily belong to I-type granitoids (Table 5.1).

5.3.3 Permian magmatism (300-260 Ma)

The Permian period may represent the waning stage of magmatism in the eastern North Tianshan and East Junggar. In East Junggar, Permian magmatism predominantly occurred near the tectonic zones (Figure 5.5c). The magmatic rocks mainly consist of intermediate and felsic types, with a few mafic rocks (Figure 5.4a). Most of the rocks belong to A-type and some are I-type granitoids. The mafic and intermediate rocks generally show arc-type geochemical signitures (Table 5.1).

In the Bogda-Harlik-Dananhu region, the Permian magmatic rocks are dominated by mafic and felsic rocks with a significant reduction of intermediate rocks compared to the Carboniferous magmatic rocks (Figure 5.4b). The mafic rocks mostly display arc-like geochemical features, with a few showing MORB-like compositions. The felsic rocks are characterized mainly by A-type granitoids, along with some I-type and a few S-type granitoids (Table 5.1).

In the Kanggur-Yamansu region, the magmatic rocks are also mainly composed of mafic and felsic rocks, with a few intermediate rocks (Figure 5.4c). The mafic rocks predominantly occur along the Kanggur Belt and exhibit various geochemical compositions, including both MORB-like and arc-like signatures. The felsic rocks are mainly I-type granitoids, with some S-type and A-type granitoids. In addition, some intermediate to felsic rocks display adakitic features (Table 5.1).

5.4 Spatial and temporal variations in whole-rock Nd and zircon Hf isotopes

Whole-rock Nd and zircon Hf isotopic compositions are powerful tools in tracing the nature of crustal rocks and determining the evolutionary history of crust (Griffin et al., 2002; Kemp et al., 2006; Belousova et al., 2010; Dhuime et al., 2012; T. Wang et al., 2023). In general, magmatic rocks derived directly from the depleted mantle exhibit highly positive whole-rock $\varepsilon_{Nd}(t)$ and zircon $\varepsilon_{Hf}(t)$ values. On the contrary, magmatic rocks generated entirely by the reworking of ancient continental crust display low or negative whole-rock $\varepsilon_{Nd}(t)$ and zircon $\varepsilon_{Hf}(t)$ values. Magmatic rocks formed with mixing source or by magma mixing usually display various $\varepsilon_{Nd}(t)$ and $\varepsilon_{Hf}(t)$ values.

To minimize the bias derived from inter-sample variations in the zircon $\varepsilon_{Hf}(t)$ values, we calculated the zircon average $\varepsilon_{Hf}(t)$ values for single samples by excluding the xenocrystic zircons. Then such zircon average $\varepsilon_{Hf}(t)$ values were used to show the spatial tendency (Figures 5.6 and 5.7). To capture important information from single zircon grains, εHf(t) values of all zircon grains (excluding xenocrystic zircons) were utilized to demonstrate the temporal trends (Figure 5.8).

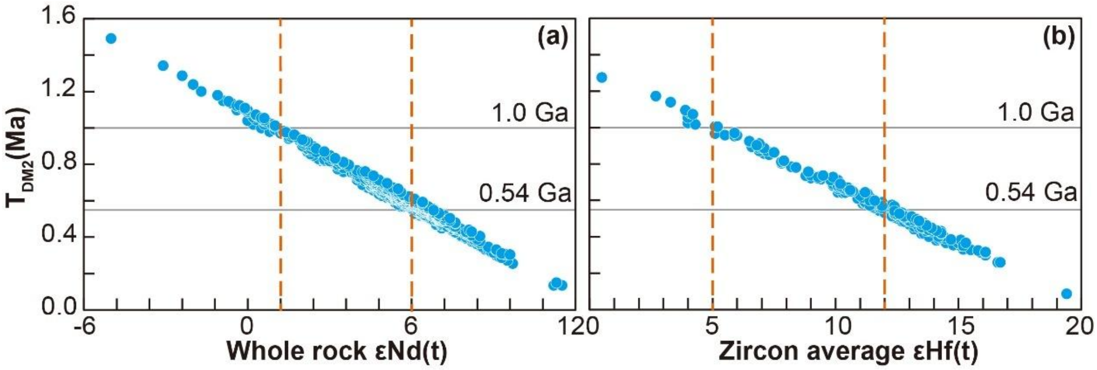

Figure 5.6. Diagrams for whole-rock ε_{Nd}(t) and zircon ε_{Hf}(t) values versus T_{DM2} ages.

Two-stage Nd or Hf depleted mantle model ages (T_{DM2}) have been used to estimate the age of the crustal sources (e.g., F. Y. Wu et al., 2007; T. Wang et al., 2023). In the eastern Tianshan and East Junggar, the Carboniferous to Permian magmatic rocks have whole-rock ε_{Nd}(t) ranging from -5 to +10 and zircon ε_{Hf}(t) values from 0 to +17, except for a few samples with very high values. The T_{DM2} range mostly from 0.2 Ga to 1.5 Ga (Figure 5.6). Whole-rock ε_{Nd}(t) values of +1 and +6 and zircon average ε_{Hf}(t) values of +5 and +11 roughly correspond to T_{DM2} of 1.0 Ga and 0.6 Ga, respectively. Therefore, these ε_{Nd}(t) and ε_{Hf}(t) values were used to separate Mesoproterozoic, Neoproterozoic, and Phanerozoic crust sources (Figures 5.6 and 5.7).

5.4.1 Early to middle Carboniferous magmatism (360-330 Ma)

Early to middle Carboniferous magmatic rocks in the East Junggar and Bogda-Harlik-Dananhu regions exhibit depleted zircon Hf and whole-rock Nd isotopic characteristics (Figures 5.7 and 5.8). For instance, in East Junggar, the magmatic rocks formed during this period mostly show intermediate to high ε_{Nd}(t) values (+3 to +7) and zircon average ε_{Hf}(t) values (+7 to +16), suggesting Neoproterozoic and Phanerozoic crust sources (0.3 to 0.9 Ga). In the Bogda-Harlik-Dananhu region, the early to middle Carboniferous magmatic rocks have $\varepsilon_{Nd}(t)$ values ranging from +2 to +9 and zircon average $\varepsilon_{Hf}(t)$ values from +5 to +16, indicating similar crust sources to that of the East Junggar. The magmatic rocks in the Bogda Belt typically exhibit more depleted $\varepsilon_{Nd}(t)$ values than that in Harlik and Dananhu belts, probably suggesting more juvenile crust sources there (0.4 to 0.6 Ga).

In contrast, early to middle Carboniferous magmatic rocks in the Kanggur-Yamansu region show variations in zircon Hf and whole-rock Nd isotopic compositions (Figures 5.7 and 5.8). The $\varepsilon_{Nd}(t)$ values range from -5 to +7 and the zircon average $\varepsilon_{Hf}(t)$ values from +3 to +13, corresponding to dominant Mesoproterozoic to Neoproterozoic crust sources. Magmatic rocks with enriched εNd(t) and zircon average εHf(t) values are predominantly found in the western part of the Kanggur-Yamansu region, suggesting the presence of ancient crustal materials in that area (Figures 5.7a and 5.7b).

Interestingly, in the East Junggar and Bogda-Harlik-Dananhu regions, some rocks dating to approximately 340-330 Ma exhibit low εNd(t) and zircon εHf(t) values, although the median values remain high (Figure 5.8). In the Kanggur-Yamansu region, εNd(t) and εHf(t) values show considerable variation, with consistently low median values during the 360-330 Ma period (Figure 5.8).

5.4.2 Middle to late Carboniferous magmatism (330-300 Ma)

Middle to late Carboniferous magmatic rocks in the East Junggar, Bogda-Harlik-Dananhu, and Kanggur-Yamansu regions exhibit zircon Hf and whole-rock Nd isotopic compositions similar to those of the early to middle Carboniferous magmatic rocks (Figures 5.7c and 5.7d). In East Junggar, the magmatic rocks formed during this period mostly show intermediate to high $\varepsilon_{Nd}(t)$ values (mostly +3 to +10) and zircon average $\varepsilon_{Hf}(t)$ values (+10 to +19), indicative of dominant Phanerozoic crust sources with some Neoproterozoic materials (0.4 to 0.7 Ga). In the Bogda-Harlik-Dananhu region, the magmatic rocks show $\varepsilon_{Nd}(t)$ values ranging from +3 to +10 and zircon average $\varepsilon_{Hf}(t)$

values from +8 to +15, consistent with Neoproterozoic to Phanerozoic crust sources (0.3 to 0.8 Ga). In the Kanggur-Yamansu region, the early to middle Carboniferous magmatic rocks possess various $\varepsilon_{Nd}(t)$ values (-3 to +8) and zircon average $\varepsilon_{Hf}(t)$ values (+5 to +17), in favor of the variations in crust sources.

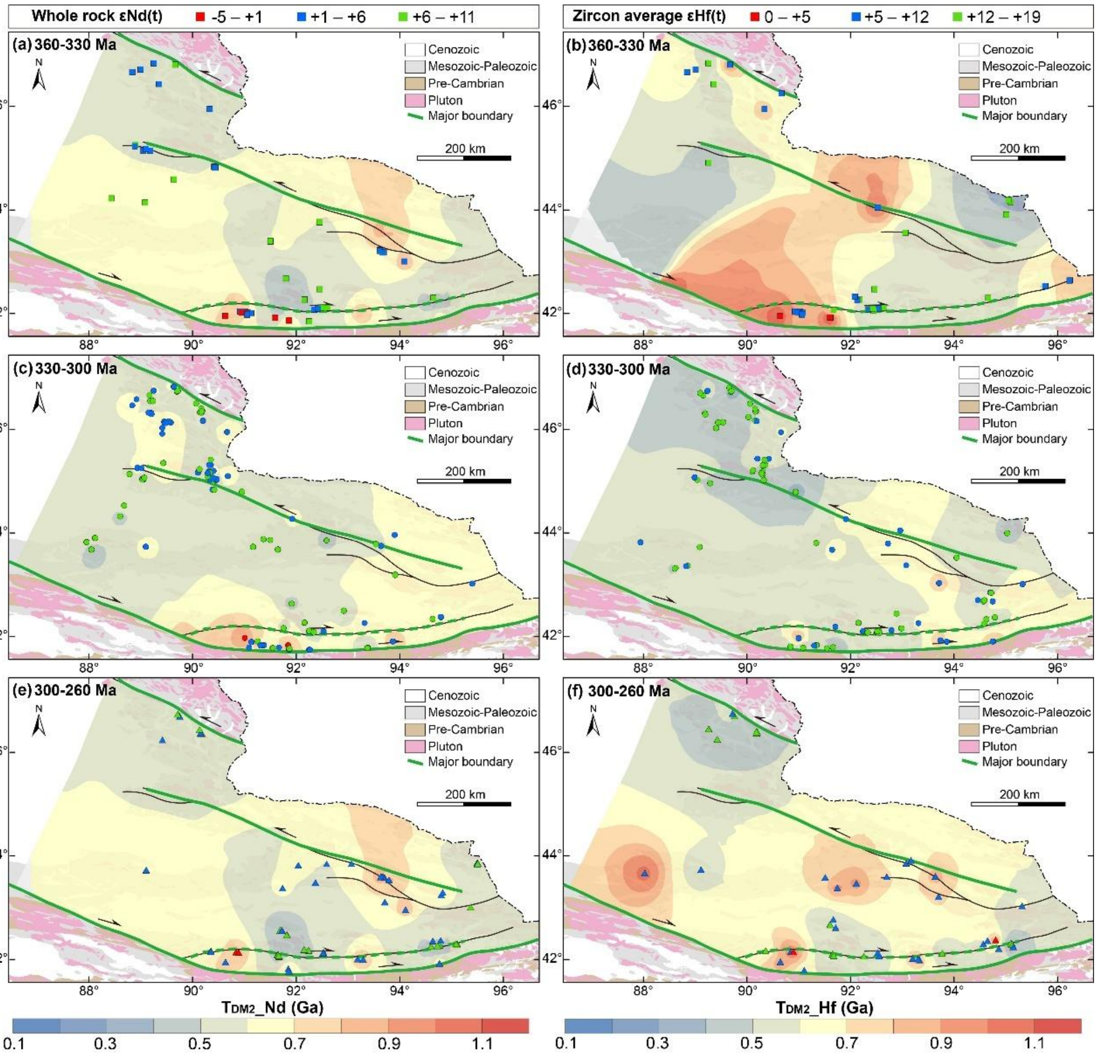

Figure 5.7. Maps showing whole-rock $\varepsilon_{Nd}(t)$ and zircon average $\varepsilon_{Hf}(t)$ values of the late Paleozoic magmatic rocks. Green, blue, and red symbols stand for high, intermediate, and low $\varepsilon_{Nd}(t)$ or $\varepsilon_{Hf}(t)$ values, respectively. Contour images illustrate two-stage Nd or zircon Hf depleted mantle model ages (T_{DM2}).

During this period, the magmatic rocks in East Junggar show an increase in $\varepsilon_{Nd}(t)$

and $\varepsilon_{Hf}(t)$ values around ~330 Ma. During ~310-300 Ma, some magmatic rocks display both enriched and highly depleted $\varepsilon_{Nd}(t)$ values, along with a slight decrease in $\varepsilon_{Hf}(t)$ values (Figures 5.8a and 5.8b). The magmatic rocks in the Bogda-Harlik-Dananhu region show a slight increase of $\varepsilon_{Nd}(t)$ values during 330 to 310 Ma but a slight decrease of $\varepsilon_{Hf}(t)$ values. During ~310-300 Ma, there is a notable decrease in both $\varepsilon_{Nd}(t)$ and $\varepsilon_{Hf}(t)$ values (Figures 5.8f and 5.8g). The magmatic rocks in the Kanggur-Yamansu region display a significant increase in $\varepsilon_{Nd}(t)$ and $\varepsilon_{Hf}(t)$ values during 330-320 Ma and a slight decrease $\varepsilon_{Nd}(t)$ and $\varepsilon_{Hf}(t)$ values at ~310 to 300 Ma (Figures 5.8k and 5.8l).

5.4.3 Permian magmatism (300-260 Ma)

Permian magmatic rocks in East Junggar exhibit high $\varepsilon_{Nd}(t)$ values from +5 to +7, along with zircon average $\varepsilon_{Hf}(t)$ values of +11 to +14 (Figures 5.7a and 5.7b), suggesting dominant Phanerozoic crust sources (0.4 to 0.6 Ga). In the Bogda-Harlik-Dananhu region, especially in Harlik, the Permian magmatic rocks are characterized by moderate $\varepsilon_{Nd}(t)$ and zircon average $\varepsilon_{Hf}(t)$ values (Figures 5.7c and 5.7d), indicative of dominant Neoproterozoic crust sources (0.6 to 1.0 Ga). In the Bogda and Dananhu belts, the Permian magmatic rocks show various $\varepsilon_{Nd}(t)$ and zircon average $\varepsilon_{Hf}(t)$ values, similar to that of the Kanggur-Yanmansu region (Figures 5.7e and 5.7f). In the Kanggur-Yamansu region, the Permian magmatic rocks have $\varepsilon_{Nd}(t)$ values of -2 to +10 and zircon average $\varepsilon_{Hf}(t)$ values of +4 to +15, consistent with various crust sources (0.4 to 1.1 Ga).

During the Permian, the $\varepsilon_{Nd}(t)$ and zircon $\varepsilon_{Hf}(t)$ values of the magmatic rocks in East Junggar remain high and stable (Figures 5.8a and 5.8b). The magmatic rocks in the Bogda-Harlik-Dananhu region, however, show decreasing trends in $\varepsilon_{Nd}(t)$ and zircon $\varepsilon_{Hf}(t)$ values with a transient increase at ~280 Ma (Figures 5.8f and 5.8g). Moreover, it is important to note that some rocks of 300-290 Ma show relatively enriched $_{Nd}(t)$ and zircon $\varepsilon_{Hf}(t)$ values. The magmatic rocks in the Kanggur-Yamansu region also show roughly decreasing trends in $\varepsilon_{Nd}(t)$ and zircon $\varepsilon_{Hf}(t)$ values with increases at ~280 Ma and ~260 Ma (Figures 5.8k and 5.8l).

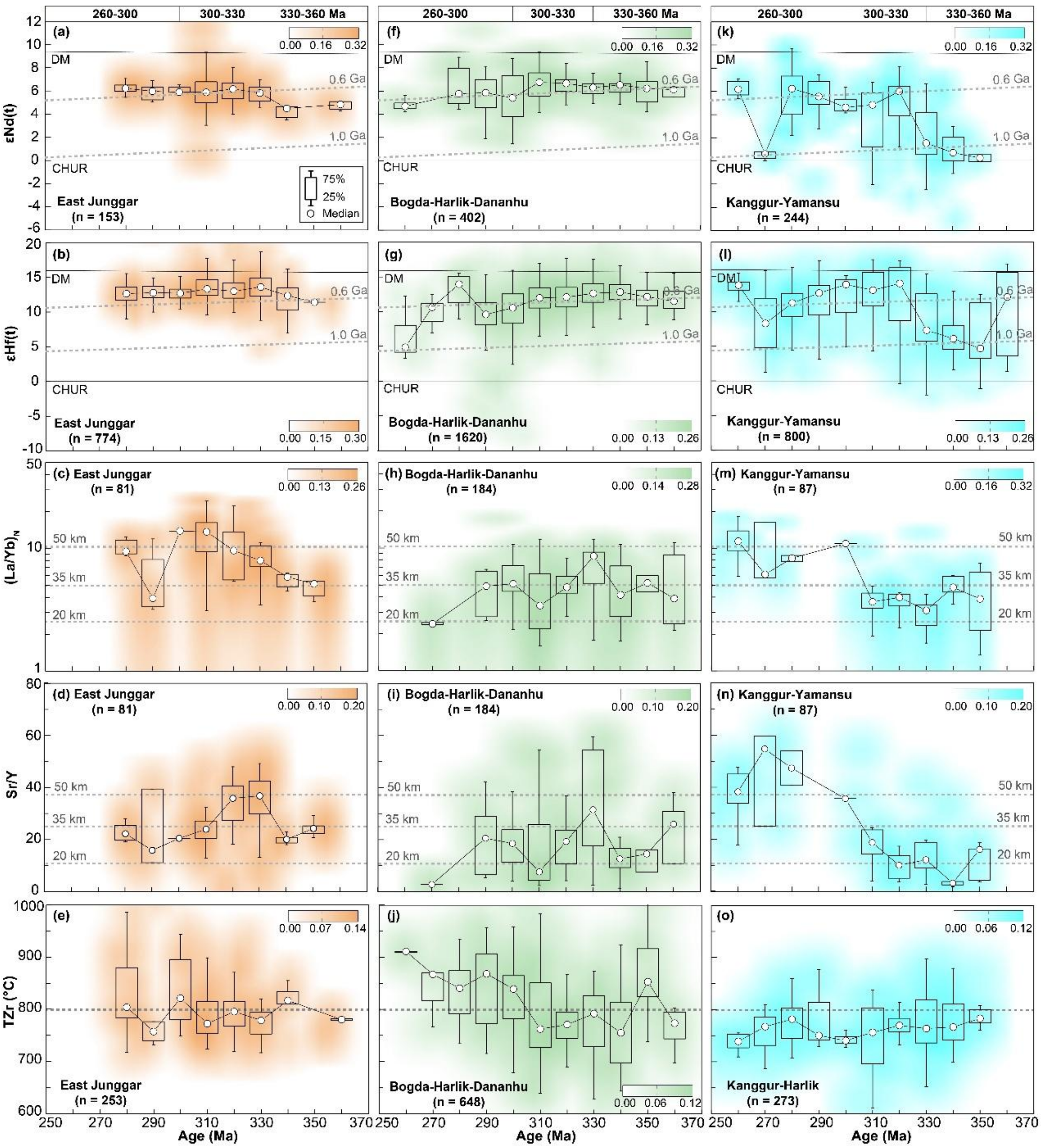

Figure 5.8. Plots of changes in whole-rock εNd(t), zircon εHf(t), $(La/Yb)_N$, Sr/Y, and zircon saturation temperature (TZr) of late Paleozoic magmatic rocks from the East Junggar, Bogda-Harlik-Dananhu, and Kanggur-Yamansu regions over time. Box plots show statistics of samples in 10 Myr bins. Colored background indicates sample density distribution as measured by bivariate kernel density.

5.5 Spatial and temporal variations of crustal thickness and magma temperature

The $(La/Yb)_N$ and Sr/Y ratios of selected samples can serve as indicators of the depth of their magma sources (i.e., the depth of partial melting or fractional crystallization of the initial melt) and can thus be used as statistical tools to reveal temporal and spatial variations in crustal thickness in ancient orogenic regions (Chapman et al., 2015; Profeta et al., 2015; Sundell et al., 2021). Accorddingly, we estimated the crustal thickness of the eastern North Tianshan and East Junggar during the late Paleozoic by the methods from Profeta et al. (2015) (Equation 1 and 2). To avoid mantle-derived and higly fractionated rocks, and rocks formed from melting of metasedimentary rocks, we selected samples with composotions of SiO_2 (55-75 wt%), MgO (1-6 wt%), Rb/Sr (0.05-0.25). Samples with high Sr/Y (>60) were discarded as they might be derived from slab melting (Profeta et al., 2015). The filtered data show that the $(La/Yb)_N$ and Sr/Y ratios have no correlations with SiO_2 content, which indicates insignificant effects of fractional crystallization (Figure 5.9).

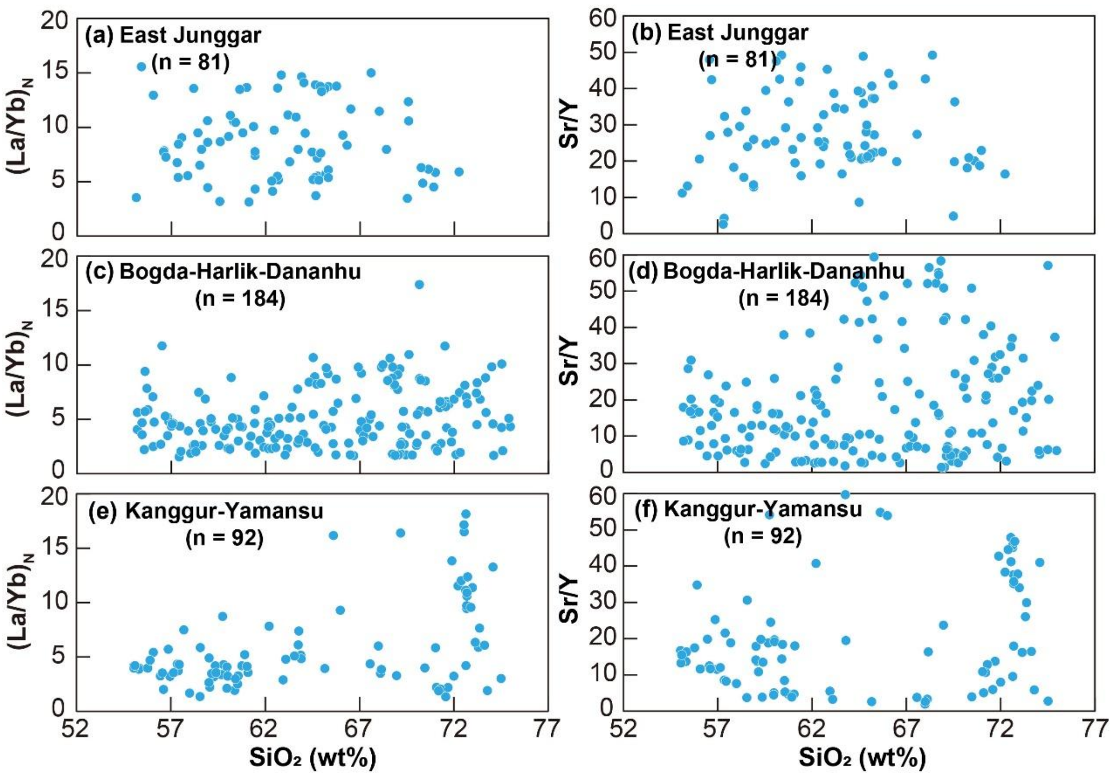

Figure 5.9. Diagrams for $(La/Yb)_N$ and Sr/Y ratios versus SiO_2 content of late Paleozoic magmatic rocks in East Junggar (EJ), Bogda-Harlik-Dananhu (BHD), and Kanggur-Yamansu (KY).

$$Crustal\ thickness\_\ Sr/Y = 1.11*Sr/Y + 8.05 \quad (1)$$

$$Crustal\ thickness\_(La/Yb)_N = 21.277\ \ln\ (1.0204*La/Yb_N) \quad (2)$$

Experimental studies have demonstrated that the saturation behair of zircon in crustal melts is a function of both temperature and composition (Watson & Harrison, 1983; Hanchar & Waston, 2003; Equation 3). Based on their results, we calculated zircon saturation temperature (TZr) for the magmatic samples in the East Junggar and eastern North Tianshan. As shown in Figure 5.10, there is a clear TZr inflection at low silica values <60 wt%. The low silica samples are likely to be the product of fractional crystallization from hotter magmas, and TZr cannot be strictly applied (e.g., Collins et al., 2016). Therefore, we selected samples with >60 wt% SiO_2 and 1.0-2.0 M values [M = (Na + K + 2 × Ca)/(Al × Si) cation fractions] and summarize the spatio-temporal variations of TZr. Samples with TZr of ≥800 °C were classified as hot granitoids, while those with TZr of <800 °C were categorized as cold granitoids (Miller et al., 2003).

$$\ln D_{Zr}^{zircon/melt} = (-3.80 - [0.85(M - 1)]) + 12900/T \quad (3)$$

It is important to note that these estimations are statistically valid only when supported by extensive data sets. When using these geochemical indices to infer long-term, regional-scale crustal evolution, greater emphasis should be placed on their spatial and temporal trends rather than their absolute values. This principle is especially relevant when estimating crustal thickness, as some magmas may originate from sources much shallower than the MOHO depth. Consequently, low estimated values may not always reflect the true crustal thickness. Despite this limitation, the overall spatial and temporal trends can still provide valuable insights into dynamic crustal changes.

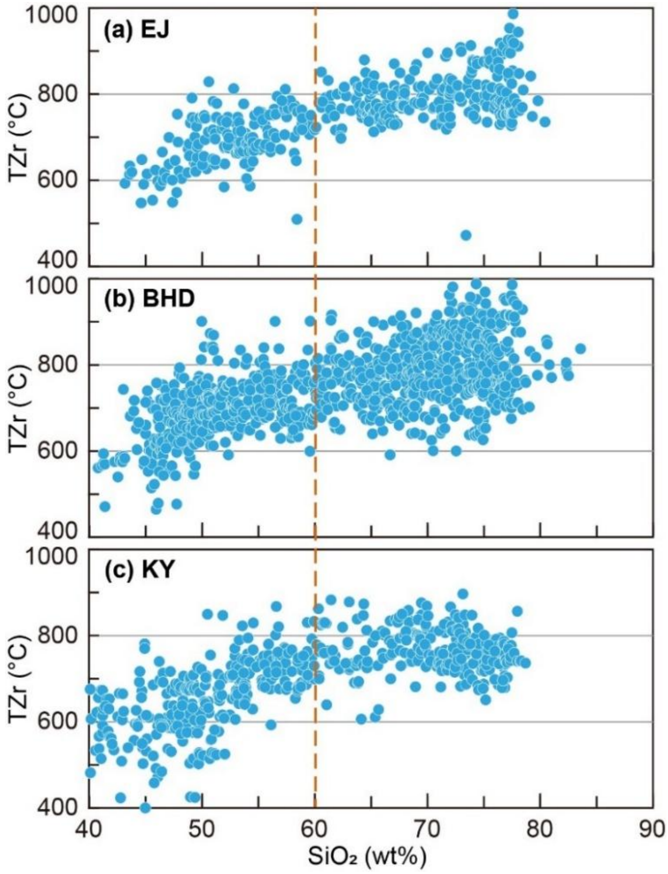

Figure 5.10. Diagrams for zircon saturation temperature (TZr) versus SiO_2 content of late Paleozoic magmatic rocks in East Junggar (EJ), Bogda-Harlik-Dananhu (BHD), and Kanggur-Yamansu (KY).

5.5.1 Early to middle Carboniferous magmatism (360-330 Ma)

The samples used to estimate the depth of partial melting display a roughly decreasing trend from northeast to southwest during the early to middle Carboniferous (Figures 5.8 and 5.11). In East Junggar, the estimated crustal thickness during this period was relatively high in the north (40 to 60 km), decreasing to 20-30 km in the south. In the Bogda-Harlik-Dananhu region, the estimated crustal thickness in Dananhu generally ranges from 40 to 50 km, higher than that in Harlik (20 to 40 km) and Bogda (15 to 25 km). Notably, significant crustal thickening occurred during 340 to 330 Ma in both East Junggar and Bogda-Harlik-Dananhu (Figure 5.8). In the Kanggur-Yamansu region, the estimated crustal thickness during this period was consistently between 20 and 35 km, showing no signs of notable thickening.

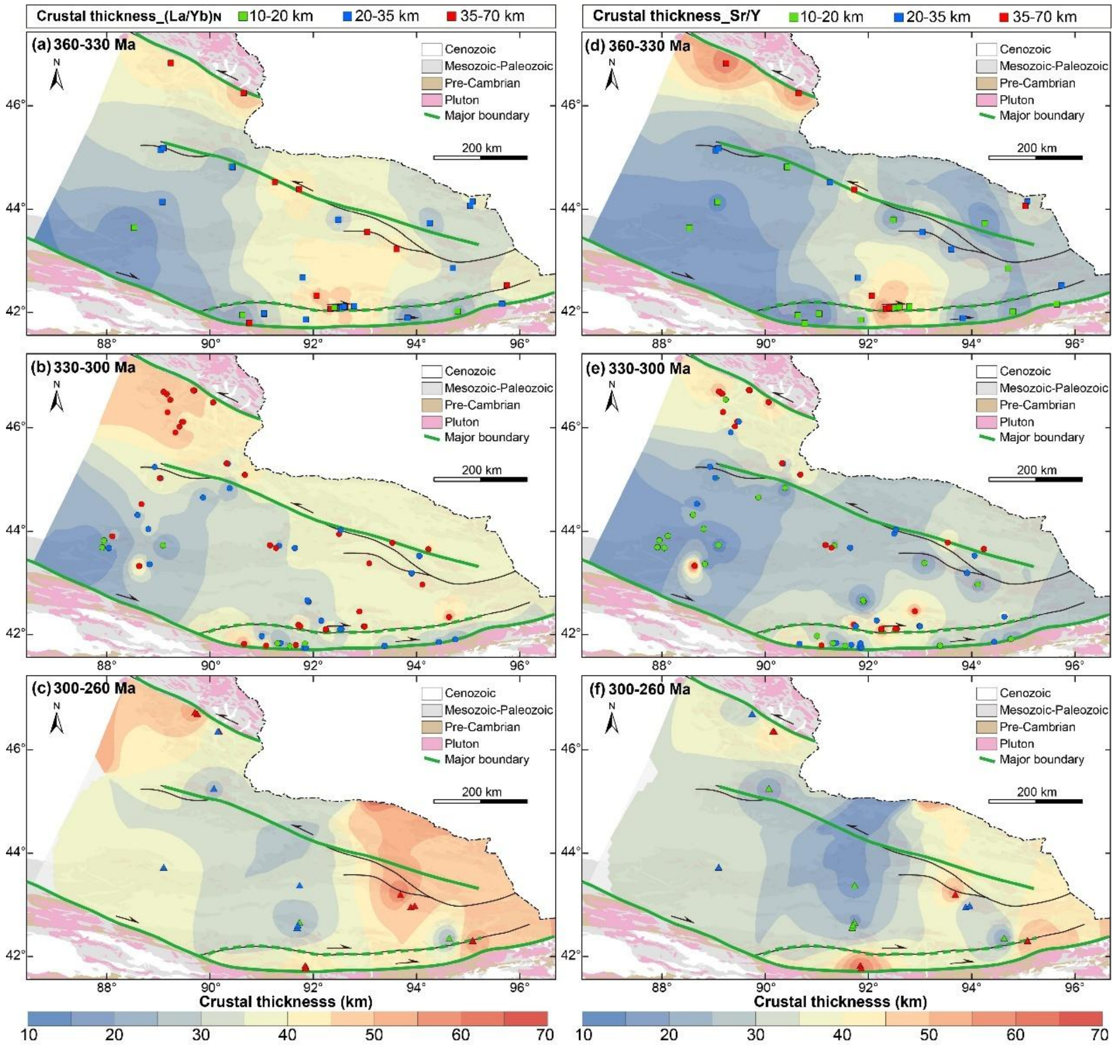

Figure 5.11. Maps showing estimated crustal thickness of the eastern North Tianshan and East Junggar in (a and d) 360-330 Ma, (b and e) 330-300 Ma, and (c and f) 300-260 Ma. Left and right columns are crustal thickness estimated by $(La/Yb)_N$ and Sr/Y ratios, respectively. Green, blue, and red symbols stand for thin (10-20 km), intermediate (20-35 km), and thick (35-70 km) crust. Contour images illustrate two-stage Nd or zircon Hf depleted mantle model ages (T_{DM2}).

In East Junggar, the granitoids exhibit a low zircon saturation temperature (TZr) in the north (700 to 800 °C), increasing to 800 to 850 °C in the south (Figure 5.12). In the Bogda-Harlik-Dananhu region, granitoids in Bogda and Harlik have high TZr (800 to 900 °C), while those in Dananhu show lower temperatures of 700 to 800 °C. In the Kanggur-Yamansu region, the zircon saturation temperature for the granitiods exhibits a increasing trend from 700 to 800 °C in the west to 800 to 850 °C in the east (Figure 5.12).

5.5.2 Middle to late Carboniferous magmatism (330-300 Ma)

During the middle to late Carboniferous, the East Junggar continued to exhibit a thick crust of 40 to 60 km in the north (Figures 5.8 and 5.11). In the south, the crust thickened to 30 to 40 km, despite some differences in the $(La/Yb)_N$ and Sr/Y ratios. In the Bogda-Harlik-Dananhu region, the crust in Harlik and Dananhu was generally 30 to 45 km thick, while the crust in Bogda was relatively thin (10-25 km). During 330 to 310 Ma, the Bogda-Harlik-Dananhu region experienced significant crustal thinning from ~50 km to 20-30 km (Figure 5.8). Subsequently, a slight crustal thickening occurred during 310 to 300 Ma, resulting in crustal thickness of 30-35 km. In the Kanggur-Yamansu region, the crustal thickness remained thin (<35 km) during 330 to 310 Ma. During 310-300 Ma, the crust thickened significantly, reaching over 50 km (Figure 5.8).

During the middle to late Carboniferous, more granitiods in the northern East Junggar show TZr higher than 800 °C (Figures 5.8 and 5.12). Granitoids in the south exhibit various TZr of 750 to 800 °C. In the Bogda-Harlik-Dananhu region, granitiods in Bogda and Harlik continue to exhibit higher TZr (800 to 850 °C) than those in Dananhu (700 to 800 °C). In the Kanggur-Yamansu region, granitiods are mostly cold with TZr of 700 to 800 °C.

5.5.3 Permian magmatism (300-260 Ma)

Permian samples that are capable of estimating crustal thickness are scarce in the East Junggar and the eastern North Tianshan (Figure 5.11). In East Junggar, the Permian samples indicated a relatively thin crust (30-50 km) compared to the Carboniferous (Figures 5.8 and 5.11). In the Bogda-Harlik-Dananhu region, the crust in Bogda and Dananhu was 10 to 35 km thick, while that in Harlik was thicker (45-60 km). During 300 to 270 Ma, there was a crustal thinning from ~35 km to ~20 km (Figure 5.8). In contrast, the Kanggur-Yamansu region during this period had a crust thickness exceeding 40 to 50 km (Figures 5.8 and 5.11).

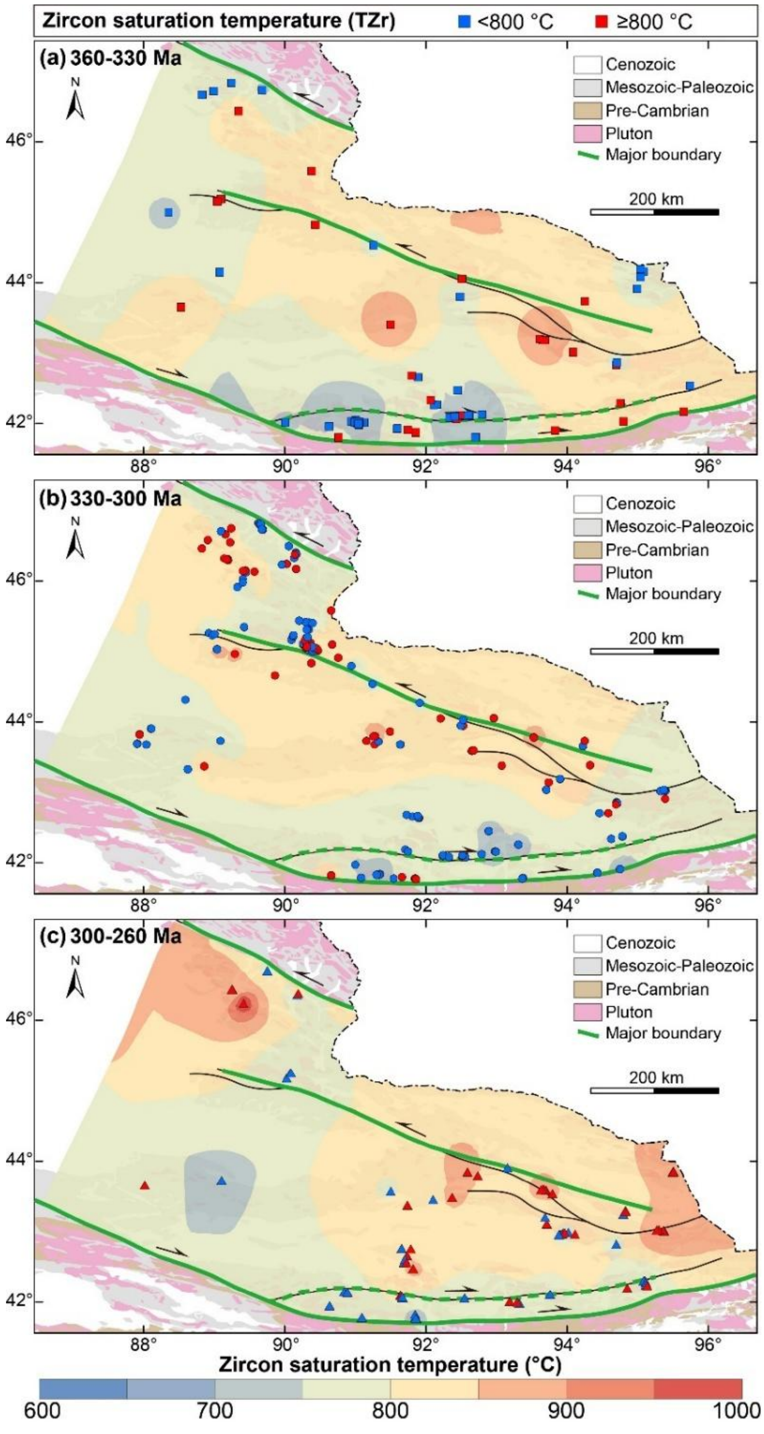

Figure 5.12. Maps showing changes of zircon saturation temperature (TZr) of the eastern North Tianshan and East Junggar. Blue and red symbols stand for cold (TZr <800 °C) and hot (TZr ≥800 °C) granitoids, respectively.

During the Permian, granitoids in the East Junggar and Bogda-Harlik-Dananhu regions typically show high TZr of 800 to 900 °C (Figure 5.12). In the Kanggur-Yamansu region, in contrast, granitoids have relatively low temperatures (700 to to 800 °C).

5.6 Spatial and temporal constraints on the crustal architecture of the eastern North Tianshan and East Junggar

Carboniferous to Permian magmatic rocks in the East Junggar and Bogda-Harlik-Dananhu regions, including some drill samples from the eastern Junggar Basin, have positive whole-rock $\varepsilon_{Nd}(t)$ and zircon average $\varepsilon_{Hf}(t)$ values (Figure 5.7). Their T_{DM2} ages mostly range from 0.3 Ga to 0.8 Ga, indicating Neoproterozoic and Phanerozoic crust sources. According to recent studies, early Paleozoic magmatic rocks in the East Junggar and Bogda-Harlik-Dananhu regions also exhibit high and positive whole-rock $\varepsilon_{Nd}(t)$ and zircon $\varepsilon_{Hf}(t)$ values with T_{DM2} ages ranging from 0.4 to 1.0 Ga (X. W. Xu et al., 2013; X. H. Ma et al., 2015; L. Du et al., 2018; R. An et al., 2021; X. H. He et al., 2021; H. Zhao et al., 2022; D. Li et al., 2024). These isotopic features are distinct from those of the Central Tianshan and Yili blocks and the Tarim Craton, where many magmatic rocks show low to negative $\varepsilon_{Nd}(t)$ and zircon $\varepsilon_{Hf}(t)$ values with T_{DM2} ages older than 1.0 Ga (Y. G. Han et al., 2019; P. Song et al., 2019; H. Huang et al., 2020; Y. J. Wang et al., 2022; Z. Y. He et al., 2024). Therefore, we argue that, unlike the Central Tianshan and Yili blocks, the East Junggar and Bogda-Harlik-Dananhu belts lack ancient continental basements older than the Neoproterozoic. Instead, they are characterized by a significant portion of Phanerozoic juvenile crust, with some Neoproterozoic components primarily located in the northern East Junggar and Harlik regions.

In contrast, many Carboniferous to Permian mgamtic rocks in the western Kanggur-Yamansu region show low to negative whole-rock $\varepsilon_{Nd}(t)$ and zircon $\varepsilon_{Hf}(t)$ values with T_{DM2} ages older than 1.0 Ga, similar to contemporaneous magmatic rocks in the Central Tianshan Block (e.g., Y. J. Wang et al., 2022). Consequently, a continental basement (or fragment) similar to the Central Tianshan Block likely exists in the western Kanggur-Yamansu region. The eastern Kanggur-Yamansu region exhibits depleted Nd and Hf isotopic features, similar to those of the East Junggar and Bogda-Harlik-Dananhu belts, suggesting the absence of ancient continental basements in this area.

During the Carboniferous, the East Junggar region was characterized by a thick crust ranging from 35 to 60 km, with an decreasing trend in crust thickness from northeast to southwest (Figure 5.11). Combined with its depleted isotopic signatures, this suggests the presence of a large volume of juvenile crust in the area. In addition, it shows a crustal thickening from the early to middle Carboniferous (Figures 5.8 and 5.11), likely resulting from the arc-arc accretion of the East Junggar with the eastern North Tianshan. The Dananhu and Harlik regions exhibit a relative thick crust of 30-50 km during the Carboniferous, while the Bogda region had a thin crust ranging 15 to 30 km (Figure 5.11). From the early to late Carboniferous, the Harlik and Bogda regions underwent a crustal thinning, which could be attributed to back-arc extension related to roll-back of the subducting Kanggur oceanic slab. The crust of the Kanggur-Yamansu region, however, was about 20-35 km thick during the Carboniferous and thickened to 40-50 km during the latest Caboniferous to Permian (Figures 5.8 and 5.11). This crustal thickening might be associated with the closure of the Kanggur Ocean.

5.7 Spatial and temporal constraints on the tectonic evolution of the eastern North Tianshan and East Junggar

5.7.1 Arc-arc accretion between the eastern North Tianshan and East Junggar around 340-330 Ma

The Kalamaili Ocean was closed around 340-330 Ma, accompanied by the arc-arc accretion between the East Junggar and the eastern North Tianshan. This is supported by several pieces of evidence. Firstly, both the crust in East Junggar (especially the southern part) and in eastern North Tianshan underwent notable thickening around 340-330 Ma (Figure 5.8). Secondly, some rocks with relatively enriched Nd and Hf isotopes were formed during this time period, although there is no significant decrease in the median values (Figure 5.8). Thirdly, there is an increasing number of cold granitoids in the East Junggar and eastern North Tianshan regions, resulting in a decrease in median TZr around 340-330 Ma (Figure 5.8). Other lines of evidence, such as the age of ophiolitic rocks, compressional structures, and regional unconformities, are already provided in Section 4.9.

5.7.2 Roll-back of the Kanggur oceanic slab and back-arc extension in the Bogda-Harlik region during 330 to 310 Ma

During 330 to 310 Ma, the Bogda-Harlik-Dananhu region underwent a crustal thinning (Figure 5.8). Specifically, the East Junggar and Dananhu regions showed thick crust, while the Bogda-Harlik region in between had relatively thin crust (Figure 5.10), consistent with the architecture of an arc-backarc system. In addition, a large number of mafic rocks with arc-like features and A-type granitoids, showing bimodal compositional affinities, widely occurred in the Bogda-Harlik and southern East Junggar regions during this period (Figure 5.5; Y. Y. Zhang et al., 2017). Likewise, "hot" granitoids occurred in the Bogda-Harlik and southern East Junggar regions while "cold" granitoids distributed in the Dananhu and northern East Junggar regions (Figure 5.12). Moreover, magmatic rocks formed during this period exhibit more depleted Nd isotope in the Bogda region. These features, consistent with the transtensional tectonics and high-temperature metamorphism in the Harlik region (see Chapter 4), suggest that the tectonics in the Bogda-Harlik region during 330 to 310 Ma may have been influenced by back-arc or intra-arc extension. The late Carboniferous volcano-sedimentary succession in the Bogda region also supports the presence of an intra- or back-arc basin in this area (Memtimin et al., 2019). Such back-arc or intra-arc extension was most likely induced by the roll-back of the Kanggur oceanic slab (e.g., Gong et al., 2023).

5.7.3 Final amalgamation of the eastern North Tianshan at around 300 Ma

The timing of the final amalgamation of the eastern Tianshan has been a topic of long-standing debate, with suggestions that it occurred either during the latest Carboniferous to early Permian (B. Wang et al., 2014; H. Q. Liu et al., 2016; X.R. Zhang et al., 2016a; Han & Zhao et al., 2018; Y.Y. Zhang et al., 2018, 2020; Muhtar et al., 2020; Y. J. Wang et al., 2022) or during the early to middle Triassic (W. J. Xiao et al., 2009; Z.Y. Chen et al., 2019; Q. G. Mao et al., 2022a, 2022b; Muhtar et al., 2024). Considering the following points: (1) the magmatic lull observed in the East Junggar and Kanggur-Yamansu regions, coupled with a sudden reduction of intermediate magmatic rocks in the Bogda-Harlik-Dananhu region (Figure 5.5); (2) the decrease in whole-rock $\varepsilon_{Nd}(t)$ and zircon $\varepsilon_{Hf}(t)$ values, alongside more enriched Nd and Hf isotopic signatures in some samples from the Bogda-Harlik-Dananhu region around 300 Ma (Figure 5.8); and (3) a notable increase in crustal thickness in both the Bogda-Harlik-Dananhu and Kanggur-Yamansu regions around 300 Ma (Figure 5.8), it can be inferred that the closure of the Kanggur Ocean and the final amalgamation of the eastern Tianshan occurred around this time. This is also supported by a series of evidence in ophiolites, sedimentation, paleomagnetic data, and Boron and zircon Oxygen isotopes, as shown in Section 4.9.

5.7.4 Post-orogenic evolution during the Permian

After the closure of the Kanggur Ocean, the eastern North Tianshan evolved into a post-orogenic setting. It is characterized by changes in magmatic rock types, spatial distribution of magmatic rocks, crust thickness, and isotopic compositions. For instance, Permian magmatic rocks in the Bogda-Harlik-Dananhu and Kanggur-Yamansu regions predominantly consist of mafic and felsic rocks, with fewer intermediate rocks compared to the Carboniferous (Figure 5.4). The mafic rocks are primarily distributed along or near major faults and exhibit diverse compositions with both arc-like and MORB-like signatures (Figure 5.5; B. Wang et al., 2014; Muhtar et al., 2024), indicating a close association with transcurrent tectonics in a post-orogenic setting (Branquet et al., 2012). Additionally, A-type granitoids are widespread in the East Junggar and Bogda-Harlik-Dananhu regions (e.g., Han & Zhao, 2018), showing high zircon saturation temperatures throughout (Figure 5.12). Moreover, Permian magmatic rocks in the Bogda-Harlik region display more enriched Nd and Hf isotopes compared to those in the East Junggar and Dananhu regions, in contrast to the isotopic characteristics observed during the Carboniferous (Figure 5.7). These data, combined with the extensional tectonics and crustal exhumation in the Harlik region (see Chapter 4), are in favor of a post-orogenic setting during the Permian. In the Kanggur-Yamansu region, the crust was relatively thick during this period and the granitoids are "cold" (Figures 5.11 and 5.12), probably indicating a transpression instead of extension in this area.

Chapter 6. Early Mesozoic intraplate magmatism in the eastern Tianshan: New constraints from the Bogda belt

6.1 Introduction

The Chinese Tianshan, located in the southwestern Central Asian Orogenic Belt (CAOB), consists of amalgamated arc terranes and microcontinents composed mainly of juvenile and ancient crust, respectively (J. Gao et al., 1998; W. J. Xiao et al., 2013; H. Huang et al., 2020). It is characterized by voluminous magmatic rocks that significantly contributed to crustal growth during the Paleozoic subduction/accretion (Jahn et al., 2000; Y. J. Wang et al., 2022; T. Wang et al., 2023; L. Du et al., 2024). The switch between accretionary orogeny and intraplate evolution is still poorly time-constrained and the tectonic setting of the Mesozoic magmatism may provide a clue to the debate. Several Triassic magmatic intrusions and volcanic rocks have recently been reported in the eastern part of the Chinese Tianshan (e.g., Z. Z. Zhang et al., 2005; Y. H. Wang et al., 2016; X. R. Zhang et al., 2017; N. Li et al., 2019; L. D. Zhao et al., 2019a; Feng & Zheng, 2021; Lei et al., 2021; Q. G. Mao et al., 2022b; J. G. Yuan et al., 2023; Muhtar et al., 2024), suggesting the importance of Triassic magmatism for the crustal evolution in this region. However, the tectonic setting and formation mechanism of these Triassic magmatic rocks still remain debated due to the lack of comprehensive and integrative studies.

Whole-rock Nd and zircon Hf isotopic compositions have been used to define crustal growth (Belousova et al., 2010; Dhuime et al., 2012; T. Wang et al., 2023). The use of Nd and zircon Hf isotopes allows the discrimination of juvenile crust from ancient crust as they have different $\varepsilon_{Nd}(t)$ and $\varepsilon_{Hf}(t)$ values. However, the reworking of juvenile crust results in positive $\varepsilon_{Nd}(t)$ and $\varepsilon_{Hf}(t)$ values that are similar to those of mantle-derived materials, leading to overestimation of crustal growth (e.g., Y. W. Tang et al., 2020). Therefore, it is necessary to reconcile isotopic data with bulk major and trace compositions to identify crustal or mantle sources (Zheng & Gao, 2021; Remink et al., 2023).

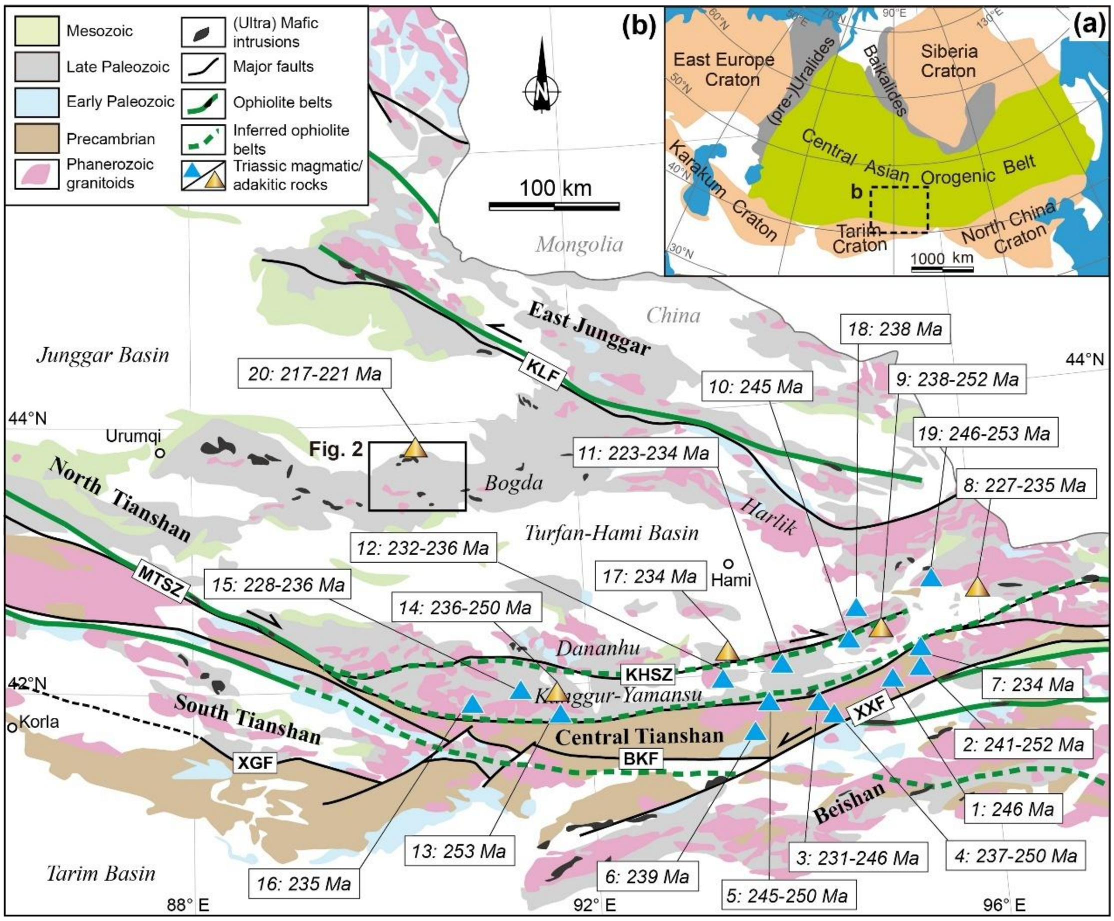

Figure 6.1. (a) Tectonic framework of the Central Asian Orogenic Belt (CAOB) and surrounding regions. (b) Simplified map showing the Triassic magmatism in the eastern Tianshan (Modified from Han & Zhao, 2018). Details of each item of ages and data sources are given in Table 4.2. BKF: Baluntai-Kawabulak Fault; KLF: Kalamaili Fault; KHSZ: Kanggur-Huangshan Shear Zone; MTSZ: Main Tianshan Shear Zone; XGF: Xinger Fault; XXF: Xingxingxia Fault.

In this chapter, we present petrographic, geochronologic, geochemical, and isotopic data from two newly identified Triassic granitoids in the Bogda Belt of the eastern Tianshan with the aim of clarifying their origin and combined with published data, specifying the early Mesozoic geodynamic context of this part of the CAOB. Based on our new results and compiled dataset, we show the spatial and temporal distribution of the Triassic magmatism in the eastern Tianshan. We suggest that reworking of ancient to juvenile crust at variable depths and temperatures with the addition of some mantle-derived materials in an intraplate setting is responsible for the Triassic magmatism in the eastern Tianshan.

6.2 Geological context and sampling

Paleozoic intrusive, volcanic, and sedimentary rocks are extensive in the eastern Tianshan, with some Triassic magmatic rocks also exposed, especially in the Central Tianshan and Yamansu Arc (Figure 6.1; Han & Zhao., 2018; Q. G. Mao et al., 2022b; L. Du et al., 2024). The newly identified granitic porphyries are exposed in the northern Bogda Belt near the town of Mulei (Figure 6.2a). In this area, early to late Carboniferous strata are folded, thrusted and intruded by dominantly mafic and intermediate magmatic rocks (Figure 6.2 and 6.3a). The intrusions are considered to be of late Carboniferous age (D. H. Long, 2021), and a few small plutons have been dated as late Jurassic to early Cretaceous (S. B. Liu et al., 2019; F. J. Wang et al., 2024).

The granite porphyry and adakitic porphyry occur as undeformed sills within the Upper Carboniferous Saleisaierk Formation, which consists mainly of tuffaceous sandstone, sandstone, siltstone, and limestone (Figure 6.2). The granite porphyry exposure is about 20m x 10m (Figures 6.3b and 6.3c). The adakitic porphyry is exposed close to the granite porphyry, with an area of ~500 m^2 (Figures 6.3b and 6.3c). The intrusive relationship between the porphyries and the wall rocks is clear (Figures 6.3d and 6.3e). In the granite porphyry, small mafic enclaves can be observed (Figures 6.3f).

The granite porphyry shows typical porphyritic texture, with anhedral quartz and euhedral feldspar phenocrysts with embayed crystal margins (Figures 6.3g and 6.3h). The feldspar phenocrysts are dominated by plagioclase with some K-feldspar. The matrix is mainly composed of tiny crystals of plagioclase, K-feldspar, quartz and Fe-Ti oxides. The adakitic porphyry also shows typical porphyritic texture with euhedral plagioclase and some biotite (Figure 6.3i). The matrix is mainly composed of tiny crystals of plagioclase and quartz with some Fe-Ti oxides.

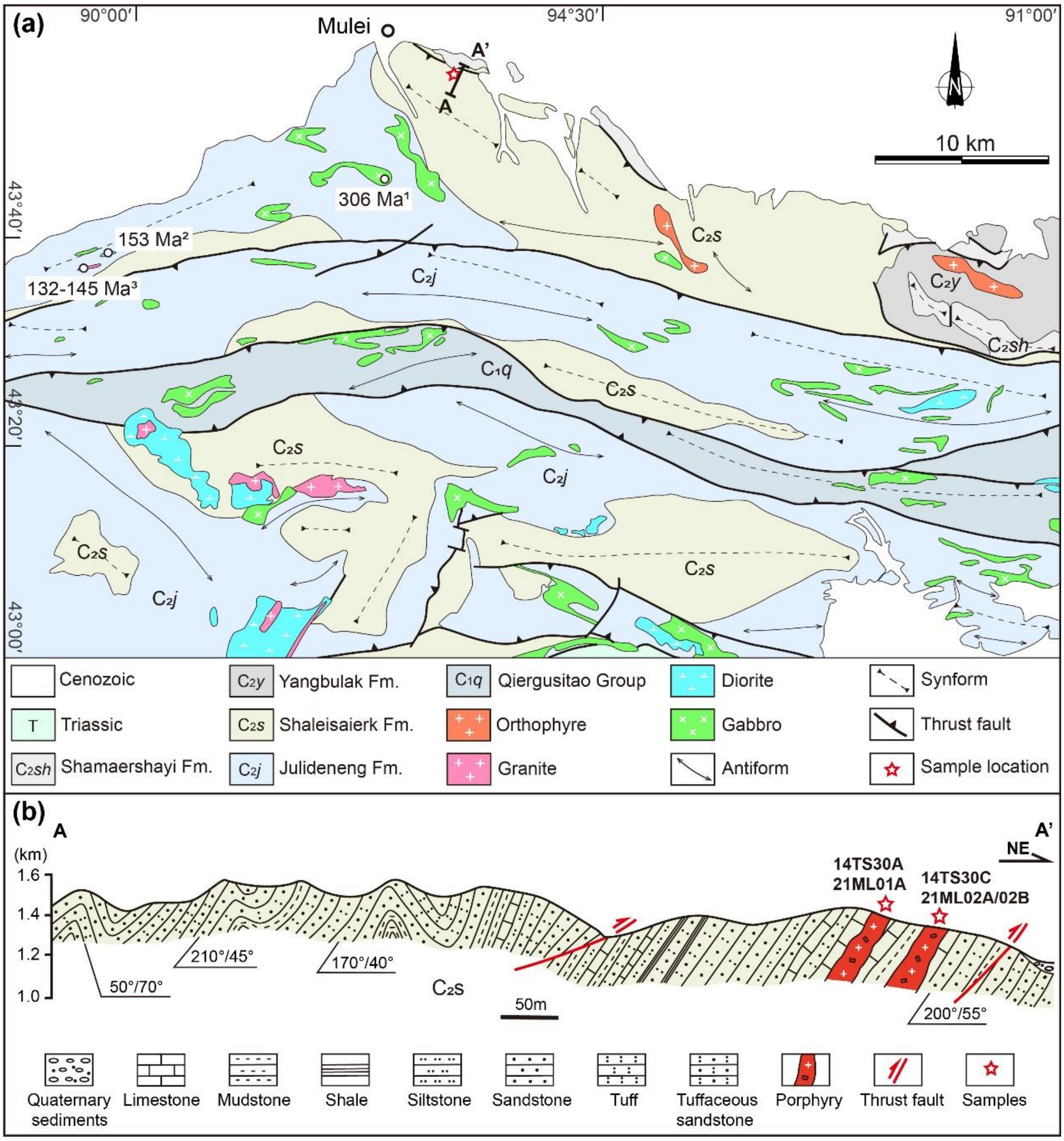

Figure 6.2. (a) Geological map of the Mulei area in Bogda Range (Modified from XBGMR, 1966). (b) Cross-section showing the contact between the granitic porphyries and wall rocks. Zircon U-Pb ages are from: 1, D. H. Long, 2021; 2, S. B. Liu et al., 2019; 3, F. J. Wang et al., 2024.

Eight and eleven fresh samples were collected from the granite porphyry and adakitic porphyry, respectively. Four samples were chosen for LA-ICP-MS zircon U-

Pb dating and in-situ Lu-Hf isotopic analyses, all nineteen samples for whole-rock major and trace element analyses, and two for whole-rock Sr-Nd isotopic analyses. The brief descriptions and coordinates of samples dated are summarized in Table 6.1.

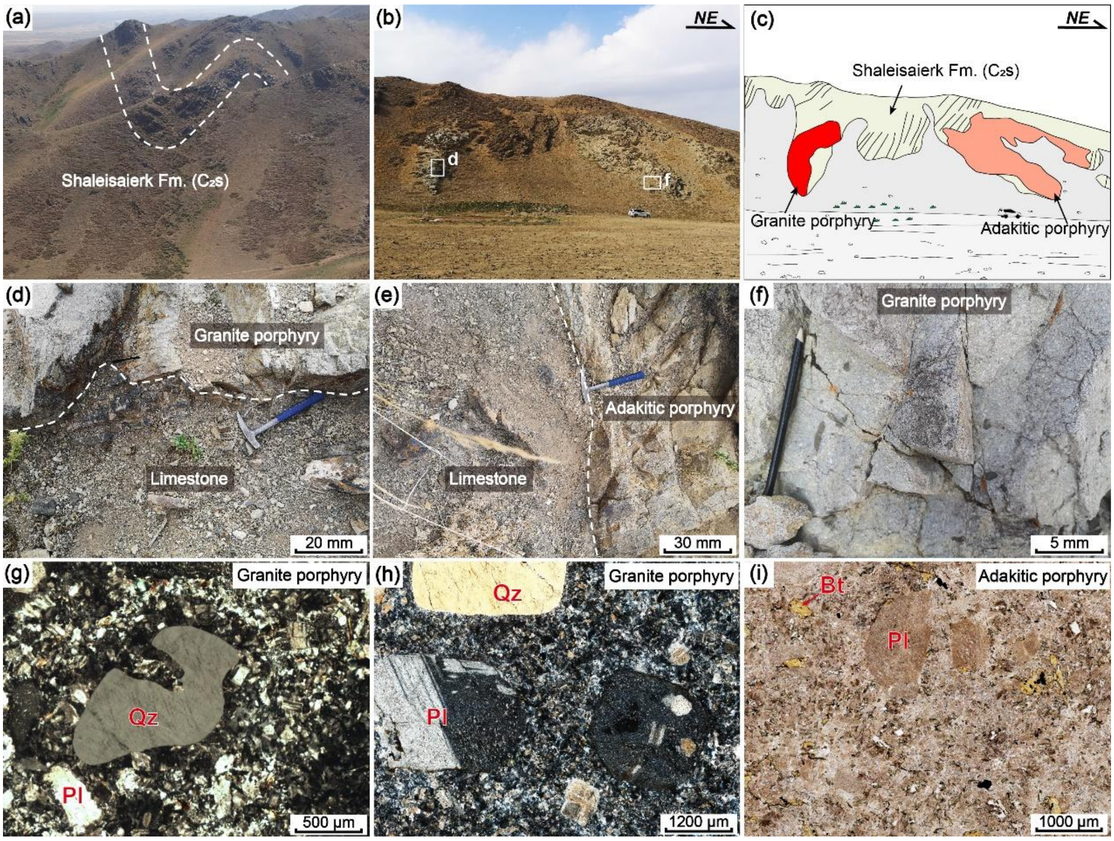

Figure 6.3. Representative photographs and photomicrographs showing the structures and textures of the granitic porphyries and wall rocks. (a) Folding of the late Carboniferous strata. (b) and (c) Spatial relationship between the granite porphyry and adakitic porphyry. (d) and (e) Intrusive relationship between the porphyries and limestone. (f) Granite porphyry with small enclaves. (g) and (h) Quartz and plagioclase phenocrysts in the granite porphyry. (i) Biotite and plagioclase phenocrysts in the adakitic porphyry. Qz: quartz; Pl: plagioclase; Bt: biotite.

Table 6.1. Brief Sample Descriptions and A Summary of Analyzing Results

Sample No.	Rock type	Latitude (N)	Longitude (E)	Age (Ma)	$(^{87}Sr/^{86}Sr)_i$	$\varepsilon_{Nd}(t)$	Zircon $\varepsilon_{Hf}(t)$
14TS30A	Granite porphyry	43°47'37"	90°20'51"	219 ± 3			13.4~17.6
21ML01A	Granite porphyry	43°47'37"	90°20'51"	217 ± 2	0.70377	7.9	12.5~17.2
21ML02A1	Adakitic porphyry	43°47'39"	90°20'55"	220 ± 3	0.70393	7.2	13.1~16.7
21ML02B4	Adakitic porphyry	43°47'39"	90°20'55"	221 ± 2			14.0~16.5

Table 6.2. Summary of Triassic magmatic rocks in the eastern Tianshan.

No.	Location	Rock type		E	N	Mineral	Analytical method	Age (Ma)	2σ (Ma)	Data sources
Central Tianshan										
1	Xingxingxia	Granite	I-type	95.03	41.82	Zircon	LA-ICP-MS	246	1	X. R. Zhang et al., 2017
2	Xiaobaishitou	Biotite granite	Un.	95.30	41.89	Zircon	LA-ICP-MS	242	2	X. F. Deng et al., 2017
	Xiaobaishitou	Mo-mineralized granite	Un.	95.30	41.90	Zircon	LA-ICP-MS	241	2	X. F. Deng et al., 2017
	Xiaobaishitou	Biotite granite	I-type	95.29	41.89	Zircon	LA-ICP-MS	246	2	N. Li et al., 2019
	Xiaobaishitou	Biotite granite	Un.	95.29	41.89	Zircon	LA-ICP-MS	248	2	N. Li et al., 2020
	Xiaobaishitou	Biotite granite	Un.	95.29	41.89	Zircon	LA-ICP-MS	252	3	N. Li et al., 2020
3	Weiya	Gabbro	Arc-type	94.33	41.75	Zircon	SHRIMP	236	6	Z. Z. Zhang et al., 2005
	Weiya	Quartz syenite	Un.	94.23	41.73	Zircon	SHRIMP	246	6	Z. Z. Zhang et al., 2005
	Weiya	Diorite porphyry	Un.	94.30	41.71	Zircon	SHRIMP	233	8	Z. Z. Zhang et al., 2005
	Weiya	Fine-grained granite	Un.	94.30	41.73	Zircon	SHRIMP	237	9	Z. Z. Zhang et al., 2005
	Weiya	Gabbro	Un.	94.33	41.77	Zircon	LA-ICP-MS	236	6	Y. W. Wang et al., 2008
	Weiya	Hornblende gabbro	Arc-type	94.34	41.77	Zircon	SIMS	242	1	Feng & Zheng, 2021

	Weiya	Syenogranite	A-type	94.22	41.73	Zircon	LA-ICP-MS	238	2	Feng & Zheng, 2021
	Weiya	Granodiorite	I-type	94.34	41.75	Zircon	SIMS	231	1	Feng & Zheng, 2021
	Weiya	Anorthosite	Arc-type	94.37	41.78	Zircon	SIMS	238	1	Shi et al., 2021
	Weiya	Quartz syenite	A-type	94.22	41.73	Zircon	LA-ICP-MS	231	3	Q. G. Mao et al., 2022
	Weiya	Monzonitic granite	A-type	94.33	41.75	Zircon	LA-ICP-MS	236	3	Q. G. Mao et al., 2022
4	Tianhu	Granite	I-type	94.46	41.67	Zircon	LA-ICP-MS	244	3	H. G. Zhao et al., 2017
	Tianhu	Granite	I-type	94.52	41.65	Zircon	LA-ICP-MS	242	2	H. G. Zhao et al., 2017
	Tianhu	Monzogranite	I-type	94.47	41.66	Zircon	LA-ICP-MS	248	2	Lei et al., 2021
	Tianhu	Granodiorite	I-type	94.47	41.64	Zircon	LA-ICP-MS	250	2	Lei et al., 2021
	Tianhu	Microgranular enclave	I-type	94.47	41.66	zircon	LA-ICP-MS	251	2	Lei et al., 2021
	Tianhu	Monzonitic granite	A-type	94.47	41.67	Zircon	LA-ICP-MS	237	2	Mao et al., 2022
5	Yamansu	Granite	I-type	93.83	41.69	Zircon	LA-ICP-MS	245	1	X. R. Zhang et al., 2017
	Yamansu	Granite	I-type	93.83	41.69	Zircon	LA-ICP-MS	250	1	X. R. Zhang et al., 2017
6	Shadong	Granite	I-type	93.45	41.54	Zircon	LA-ICP-MS	239	2	C. Chen et al., 2018
7	Baishiquan	Monzonitic granite	A-type	95.28	42.06	Zircon	LA-ICP-MS	234	2	Q. G. Mao et al., 2022
North Tianshan										
8	Baishan	Monzogranite	Adakitic	95.92	42.52	Zircon	SIMS	228	2	Y. H. Wang et al., 2016
	Baishan	Granite porphyry	Adakitic	95.92	42.52	Zircon	SIMS	227	2	Y. H. Wang et al., 2016
	Baishan	Granite porphyry	Adakitic	95.92	42.52	Zircon	LA-ICP-MS	228	4	D. Y. Zhang et al., 2015
	Jianquan	Monzogranite	Adakitic	96.03	42.47	Zircon	LA-ICP-MS	235	2	Q. G. Mao et al., 2021
	Baishandong	Granodiorite	Adakitic	96.27	42.54	Zircon	LA-ICP-MS	237	2	Yuan et al., 2023
	Baishandong	Granodiorite	Adakitic	96.08	42.44	Zircon	LA-ICP-MS	237	1	Yuan et al., 2023
	Baishandong	Biotite monzogranite	Adakitic	96.26	42.57	Zircon	LA-ICP-MS	235	2	Yuan et al., 2023
	Baishandong	Biotite monzogranite	Adakitic	96.01	42.49	Zircon	LA-ICP-MS	234	2	Yuan et al., 2023

	Baishandong	Muscovite monzogranite	I-type	96.14	42.53	Zircon	LA-ICP-MS	229	1	Yuan et al., 2023
9	Hancaohu	Granite	Adakitic	95.05	42.20	Zircon	LA-ICP-MS	238	2	Q. G. Mao et al., 2021
	Hancaohu	Granodiorite	Adakitic	95.06	42.20	Zircon	LA-ICP-MS	243	2	Q. G. Mao et al., 2021
	Shuangchagou	Granodiorite	Un.	94.88	42.13	Zircon	LA-ICP-MS	252	3	Zhou et al., 2010
	Shuangchagoubei	Granite dyke	Un.	95.09	42.31	zircon	LA-ICP-MS	243	3	Muhtar et al., 2023
	Shuangchagou	Granodiorite	I-type	95.07	42.21	Zircon	LA-ICP-MS	244	2	Muhtar et al., 2024
	Shuangchagou	Two-mica granite	I-type	95.07	42.22	Zircon	LA-ICP-MS	242	1	Muhtar et al., 2024
	Shuangchagou	Two-mica granite	I-type	93.29	42.01	Zircon	LA-ICP-MS	242	2	Muhtar et al., 2024
	Shuangchagou	Monzogranite	I-type	95.00	42.21	Zircon	LA-ICP-MS	250	2	Muhtar et al., 2024
	Shuangchagou	K-feldspar granite	I-type	94.95	42.21	Zircon	LA-ICP-MS	248	1	Muhtar et al., 2024
	Shuangchagou	K-feldspar granite	I-type	94.94	42.20	Zircon	LA-ICP-MS	241	2	Muhtar et al., 2024
10	Huangshannan	Monzonitic granite	I-type	94.65	42.17	Zircon	LA-ICP-MS	245	1	Q. G. Mao et al., 2022
11	Yamansubei	Granite	I-type	93.96	41.99	Zircon	LA-ICP-MS	228	1	Lei et al., 2013
	Yamansubei	Monzonitic granite	I-type	93.96	41.99	Zircon	LA-ICP-MS	234	2	Q. G. Mao et al., 2022
	Yamansubei	Granite	I-type	93.96	41.99	Zircon	LA-ICP-MS	223	1	X. R. Zhang et al., 2017
12	Donggebi	Porphyritic granite	A-type	93.36	41.92	Zircon	LA-ICP-MS	235	3	H. S. Sun et al., 2017
	Donggebi	Fine-grained granite	A-type	93.36	41.92	Zircon	LA-ICP-MS	232	2	H. S. Sun et al., 2017
	Donggebi	Porphyritic granite	A-type	93.35	41.92	Zircon	LA-ICP-MS	236	2	Y. S. Wu et al., 2017
	Donggebi	Porphyritic granite	A-type	93.35	41.91	Zircon	SIMS	234	3	F. F. Zhang et al., 2015
	Donggebi	Porphyritic granite	A-type	93.35	41.91	Zircon	SIMS	232	3	F. F. Zhang et al., 2015
13	Heijianshan-Chilongfeng	Syenite	Un.	91.68	41.76	Zircon	LA-ICP-MS	253	1	L. D. Zhao et al., 2018
14	Hongshanliang	Granodiorite	Adakitic	91.60	41.93	Zircon	LA-ICP-MS	250	4	L. D. Zhao et al., 2019
	Hongshanliang	Monzogranite	Adakitic	91.60	41.92	Zircon	LA-ICP-MS	236	2	L. D. Zhao et al., 2019
15	Bailingshan	Granite	I-type	91.29	41.90	Zircon	LA-ICP-MS	228	2	Z. W. Gao et al. 2021

	Bailingshan	Gabbro	Arc-type	91.29	41.90	Zircon	LA-ICP-MS	236	3	Z. W. Gao et al. 2021
16	Aqishan	High-Mg andesite	Arc-type	90.81	41.82	Zircon	LA-ICP-MS	235	1	Kang et al. 2022
17	Baijiantan	Monzogranite	Adakitic	93.47	42.13	Zircon	LA-ICP-MS	234	1	Q. G. Mao et al., 2021
	Hongtannan	K-feldspar granite	Un.	93.39	42.11	zircon	LA-ICP-MS	237	1	Muhtar et al., 2023
18	Sanchakou	Hornblende gabbro	E-MORB	94.80	42.37	Zircon	LA-ICP-MS	238	5	Y. F. Wang et al., 2022
19	Jingerquan	Gabbro	E-MORB	95.59	42.55	Zircon	LA-ICP-MS	249	1	S. Y. Liu et al., 2020
	Jingerquan	Gabbro	E-MORB	95.59	42.55	Zircon	LA-ICP-MS	251	3	S. Y. Liu et al., 2020
	Jingerquan	Gabbro	E-MORB	95.59	42.55	Zircon	LA-ICP-MS	247	2	S. Y. Liu et al., 2020
	Jingerquan	Gabbro	E-MORB	95.59	42.55	Zircon	LA-ICP-MS	248	1	S. Y. Liu et al., 2020
	Jingerquan	Muscovite granite	S-type	95.59	42.55	Monazite	SIMS	253	2	S. Y. Liu et al., 2020
	Jingerquan	Muscovite granite	S-type	95.59	42.55	Monazite	SIMS	246	2	S. Y. Liu et al., 2020
	Jingerquanbei	Granite	I-type	95.62	42.49	Zircon	LA-ICP-MS	250	4	Muhtar et al., 2020
20	Mulei	Granite porphyry	I-type	90.35	43.79	Zircon	LA-ICP-MS	219	3	This study
	Mulei	Granite porphyry	I-type	90.35	43.79	Zircon	LA-ICP-MS	217	2	This study
	Mulei	Adakitic porphyry	Adakitic	90.35	43.79	Zircon	LA-ICP-MS	220	3	This study
	Mulei	Adakitic porphyry	Adakitic	90.35	43.79	Zircon	LA-ICP-MS	221	2	This study
Note. Un.: Unclarified										

6.3 Analytical results

6.3.1 Zircon U-Pb dates and trace elements

Zircon grains from the granite porphyry 14TS30A are mostly euhedral and transparent. Almost all grains exhibit igneous oscillatory zoning and a few grains show inherited cores (Figure 6.4a). Fifteen grains were analyzed and all of them have high Th/U ratios (0.32-1.10). Fourteen analyses define one single date population with a weighted mean of 219 ± 3 Ma (MSWD = 1.3), which is interpreted as the crystallization age. One single concordant date of ca. 244 Ma likely corresponds to an inherited or detrital zircon.

Zircons from the granite porphyry 21ML01A are euhedral to sub-euhedral, exhibiting igneous oscillatory zoning (Figures 6.4b). Sixteen analyses were conducted and their Th/U ratios range from 0.42 to 0.84. Twelve grains yielded concordant dates to form a cluster with a weighted mean of 217 ± 2 Ma (MSWD = 1.6). This age is interpreted to be the crystallization age. The zircons have low Ti contents (4.5-16.9 ppm) and are characterized by normalized REE patterns with a steeply rising slope from light rare earth elements (LREE) to heavy rare earth elements (HREE) (Figure 6.5). They have LREE/HREE ratios ranging from 0.04 to 0.07 and negative Eu anomalies (0.61-0.74).

Zircon grains from the adakitic porphyry 21ML02A1 are mostly transparent prismatic crystals with igneous oscillatory zoning (Figures 6.4c). Sixteen analyses were performed and all of them have high Th/U ratios (0.41-1.31), consistent with igneous origin. All the dates are concordant and define a single population with a weighted mean of 220 ± 3 Ma (MSWD = 2.7). Most of the zircons have low Ti contents (4.5-12.2 ppm) with only one relatively high (20.1 ppm). The normalized REE patterns exhibit a steeply rising slope from light rare earth elements (LREE) to heavy rare earth elements (HREE) with negative Eu anomalies (0.55-0.74). Their LREE/HREE ratios are from 0.03 to 0.08 (Figure 6.5).

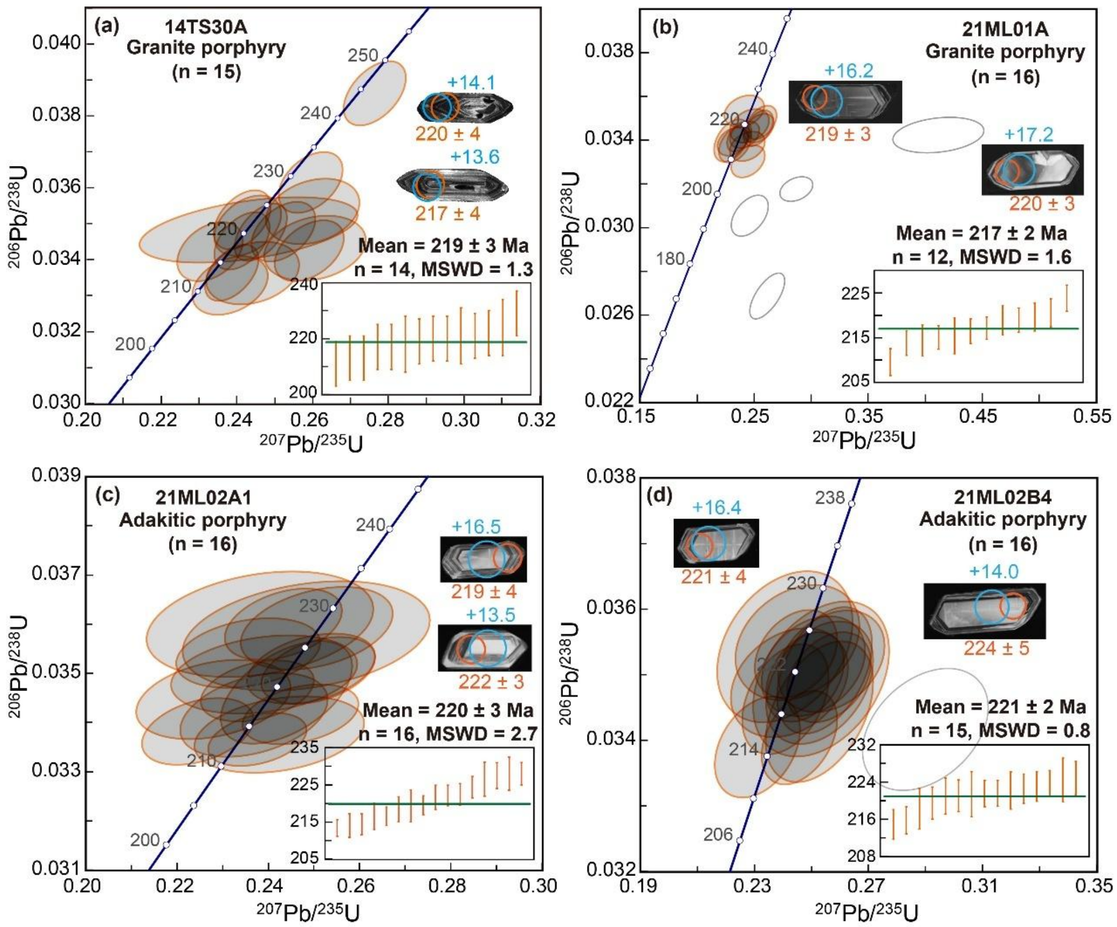

Figure 6.4. Zircon U-Pb concordia diagrams for (a) and (b) granite porphyry, and (c) and (d) adakitic porphyry with representative CL images. Orange and blue numbers stand for zircon U-Pb ages and εHf(t), respectively.

Zircons from adakitic porphyry 21ML02B4 are euhedral to sub-euhedral. All of the grains display magmatic oscillatory zoning (Figures 6.4d). Fifteen zircons were analyzed and their Th/U ratios range from 0.42 to 1.29. Fourteen dates are concordant to form a single population. The weighted average is 221 ± 2 Ma (MSWD = 0.8), which can be interpreted as the crystallization age. Most of the zircons have low Ti contents (<10 ppm) except two grains (18.5 and 21.7 ppm). The normalized REE patterns exhibit a steeply rising slope from light rare earth elements (LREE) to heavy rare earth elements (HREE) with negative Eu anomalies (0.44-0.71) (Figure 6.5). Their LREE/HREE ratios range from 0.03 to 0.05 (Figure 6.5).

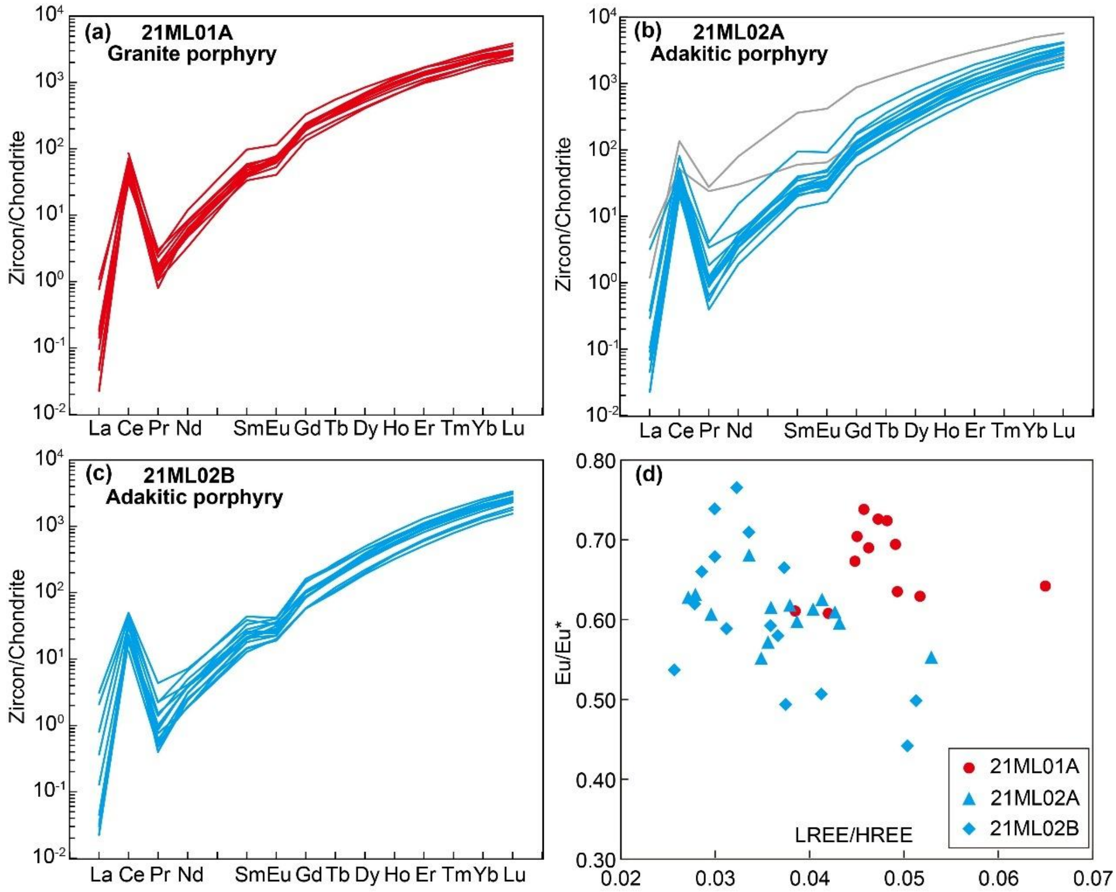

Figure 6.5. REE patterns for zircons from (a) the granite porpgyry and (b) and (c) the adakitic porphyry. (d) Eu/Eu* versus LREE/HREE diagram for zircons.

6.3.2 Whole-rock major and trace elements

The granite porphyry samples have high SiO_2 (72.39-74.15 wt%) and total alkali ($Na_2O + K_2O$ = 8.67-9.43 wt%) contents with high K_2O/Na_2O ratios (0.9-1.1), and low TiO_2 (0.15-0.18 wt%), TFe_2O_3 (0.94-1.32 wt%), MgO (0.30-0.64 wt%), Al_2O_3 (13.79-14.23 wt%), CaO (0.42-0.84 wt%), Cr (2.9-10.0 ppm), and Ni (2.0-4.9 ppm) contents (Figures 6.6 and 6.7). They have low $Mg^{\#}$ values (36-40) except a higher one of 53. With high K_2O (4.14-4.61 wt%) contents and high A/CNK values (1.0-1.1), they belong to high-K calc-alkaline series and peraluminous group (Figures 6.6c and 6.6d). They are characterized by low rare earth element contents (ΣREE = 25-46 ppm) with slightly negative Eu anomalies (Eu/Eu* = 0.7-0.9) and low $(La/Yb)_N$ values of 5.2 to 6.3 (Figure 6.8a). In the primitive mantle-normalized multielement diagrams, the granite porphyry samples are enriched in Rb, Ba, Th, and U, and depleted in Nb and Ti (Figure 6.8b). They show negative Sr anomalies with low Sr/Y (9.0-10.8) ratios.

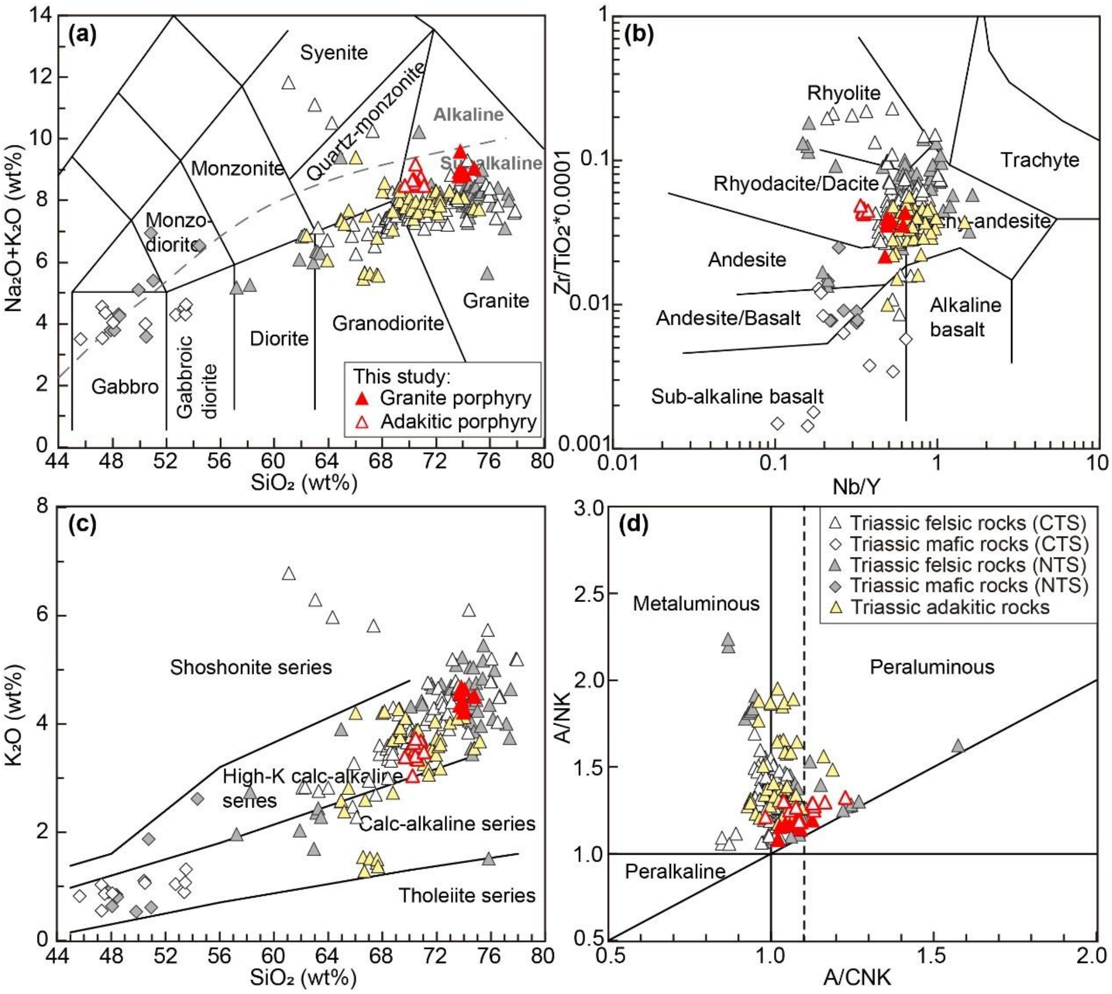

Figure 6.6. (a) Total alkalis versus SiO_2 diagram (Le Bas et al., 1986; Middlemost, 1994). (b) Zr/TiO_2 versus Nb/Y diagram (after Winchester and Floyd, 1977). (c) K_2O versus SiO_2 diagram (after Peccerillo & Taylor, 1976). (d) A/NK versus A/CNK diagram (after Maniar & Piccoli, 1989).

Compared with the granite porphyry, the adakitic porphyry samples show lower SiO_2 (68.54-70.17 wt%), K_2O (2.99-3.65 wt%) contents, but higher TiO_2 (0.35-0.38 wt%), TFe_2O_3 (2.24-2.49 wt%), MgO (1.01-1.32 wt%), Al_2O_3 (14.90-15.65 wt%), Cr

(18.4-21.5 ppm), and Ni (9.7-11.8 ppm) contents (Figures 6.6 and 6.7). They have moderate Mg# values (45-51) and K_2O/Na_2O ratios (0.5-0.7). They belong to calc-alkaline to high-K calc-alkaline series, and are peraluminous with A/CNK values of

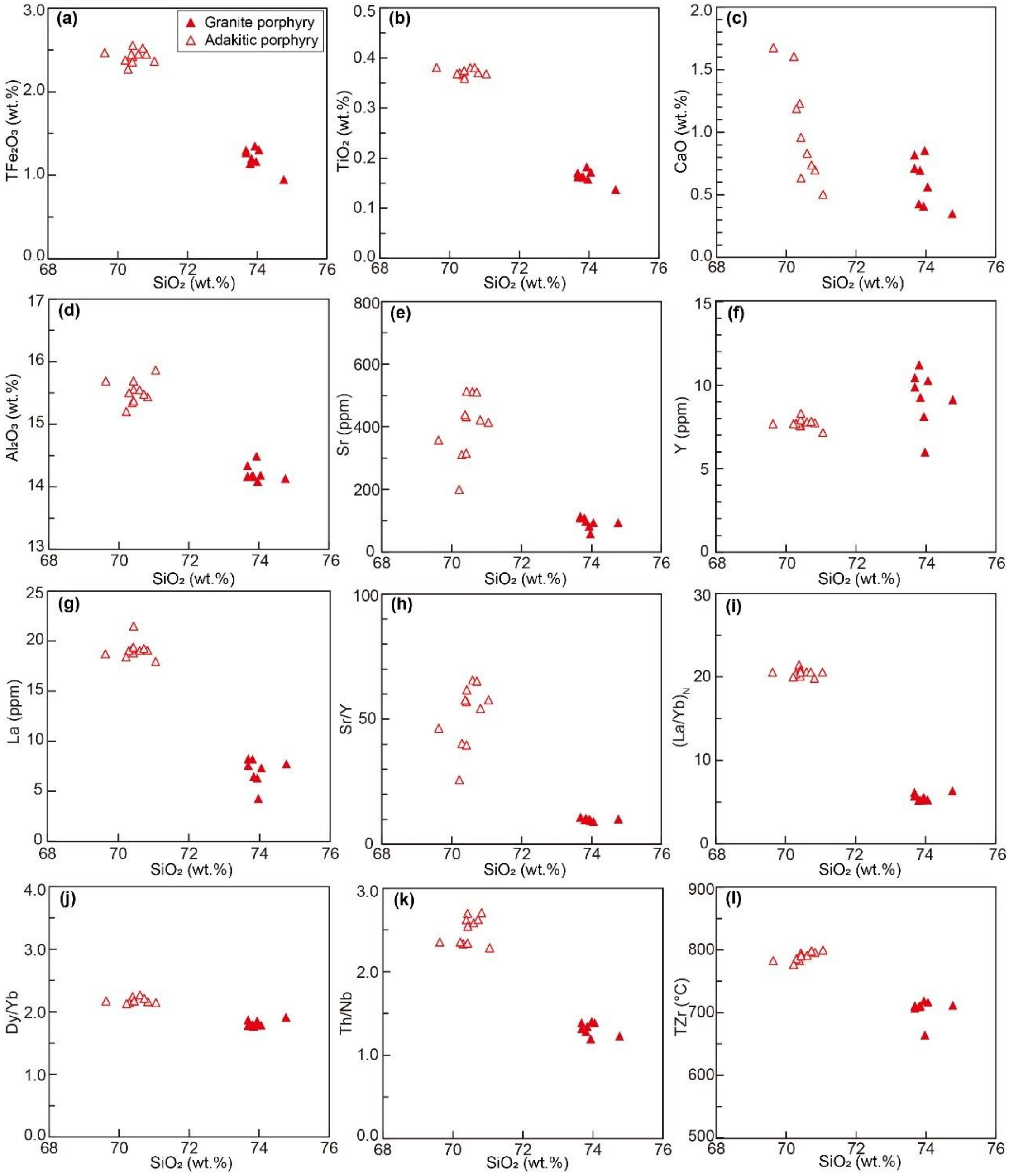

Figure 6.7. Bivariate diagrams of selected major elements (TFe_2O_3, TiO_2, CaO, Al_2O_3), trace elements (Sr, Y, La), trace element ratios (Sr/Y, (La/Yb)N, Dy/Yb, Th/Nb), and TZr versus SiO_2.

1.0-1.2 (Figures 6.6c and 6.6d). In addition, they show LREE enrichment and HREE depletion ($(La/Yb)_N$ = 19.8-20.6) with weak Eu anomalies (Eu/Eu* = 0.9-1.1), similar to the published Triassic adakitic rocks from the NTS (Figure 6.8c). In the primitive mantle-normalized multi-element diagrams, the adakitic porphyry samples are enriched in Rb, Ba, Th, and U, and depleted in Nb, Ta, and Ti (Figure 6.8d). They show variable Sr (199-512 ppm), and low Y (7.2-8.3 ppm) and Yb (0.6-0.8 ppm) contents, leading to high Sr/Y ratios of 26 to 66.

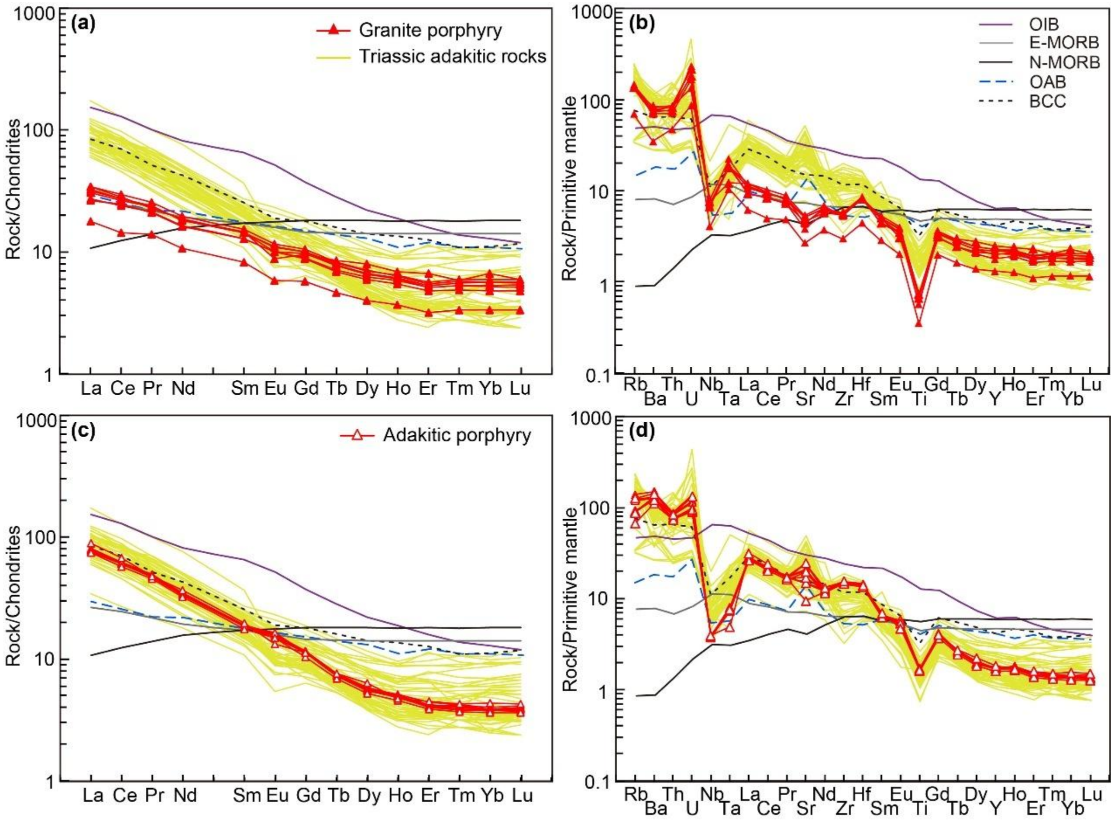

Figure 6-8. (a) and (c) Chondrite-normalized rare earth element patterns. (b) and (d) Primitive mantle-normalized multielement diagrams. Triassic adakitic rocks from the eastern Tianshan are shown for comparison. Chondrite and primitive mantle normalizing values are from Sun and McDonough (1989). The data of OIB, E-MORB, N-MORB, OAB (oceanic arc basalt), and BCC (bulk continental crust) are from Sun and McDonough (1989), Kelemen et al., 2014, and Rudnick and Gao (2014).

6.3.3 Whole-rock Sr-Nd isotopic compositions

The whole-rock Sr and Nd isotopic compositions of the samples from the Bogda Belt are summarized in Table 6.1. The zircon U-Pb ages of the samples were used to calculate their initial $^{87}Sr/^{86}Sr$ ratios and $\varepsilon_{Nd}(t)$ values . Both the granite porphyry and the adakitic porphyry have low initial $^{87}Sr/^{86}Sr$ isotopic ratios (0.70377-0.70393) and high $\varepsilon_{Nd}(t)$ values of +7.2 to +7.9, similar to the late Paleozoic mafic rocks of the North Tianshan (Figure 6.9; Table 6.1). The two-stage model ages (T_{DM2}) are from 354 to 414 Ma.

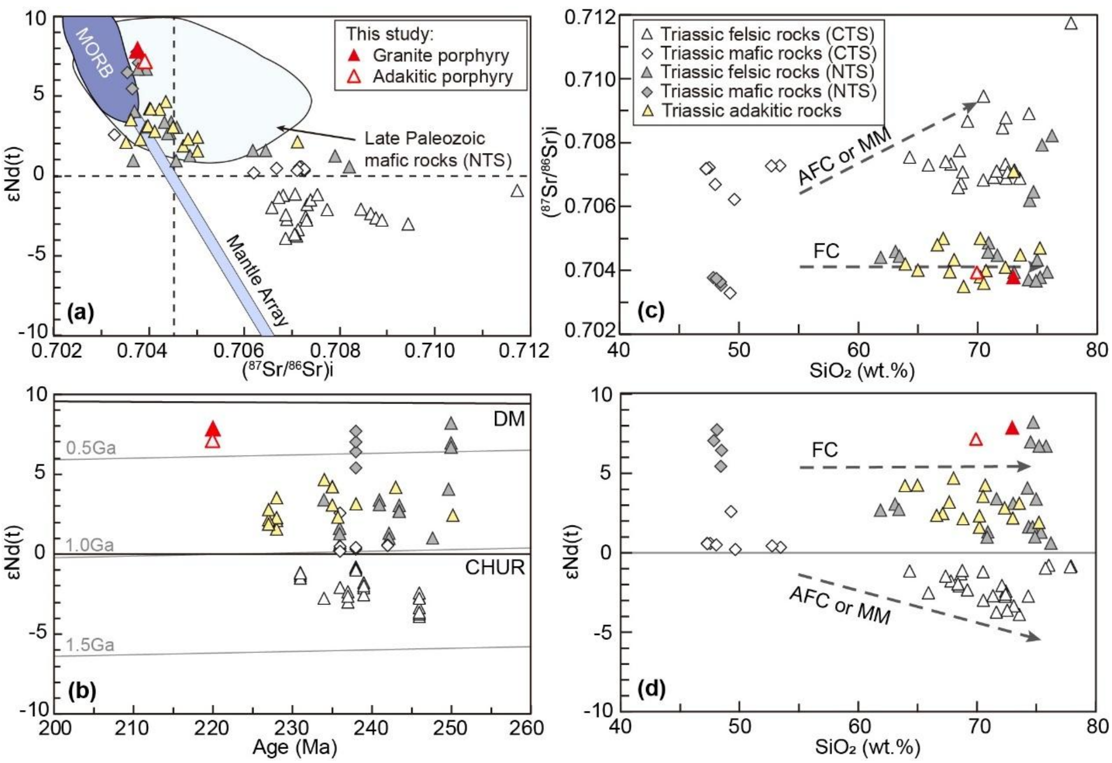

Figure 6.9. (a) $\varepsilon_{Nd}(t)$ versus $(^{87}Sr/^{86}Sr)_i$ diagram. Data for late Paleozoic mafic rocks in the NTS are from D. Y. Zhang et al. (2013), Xie et al. (2016, 2022), Y. F. Deng et al. (2020), J. L. Wang et al. (2020), D. Li et al. (2021), and reference therein. (b) $\varepsilon_{Nd}(t)$ versus crystallization age diagram. (c) $(^{87}Sr/^{86}Sr)_i$ versus SiO_2 diagram. (d) $\varepsilon_{Nd}(t)$ versus SiO_2 diagram. CHUR: chondritic uniform reservoir; DM: depleted mantle; FC: fractional crystallization; AFC: assimilation and fractional crystallization; MM: magma mixing.

6.3.4 Zircon Lu-Hf isotopic compositions

The analytical results of the zircon Lu-Hf isotopic compositions are summarized in Table 6.1. The $\varepsilon_{Hf}(t)$ values of the zircons were calculated by using their determined U-Pb dates. Thirteen Hf isotopic spot analyses on zircons from granite porphyry 14TS30A gave $\varepsilon_{Hf}(t)$ values of +13.4 to +17.6 and T_{DM2} model ages of 137-394 Ma. Ten zircons from granite porphyry 21ML01A show similar Lu-Hf isotopic compositions with $\varepsilon_{Hf}(t)$ values of +12.5 to +17.2 and T_{DM2} model ages of 152-454 Ma. Ten analyses on zircons from adakitic porphyry 21ML02A1 yielded $\varepsilon_{Hf}(t)$ values of +13.1 to +16.7 and T_{DM2} model ages of 189-415 Ma. Ten zircons from adakitic porphyry 21ML02B4 gave $\varepsilon_{Hf}(t)$ values of +14.0 to +16.5 and T_{DM2} model ages of 152-454 Ma (Figure 6.10).

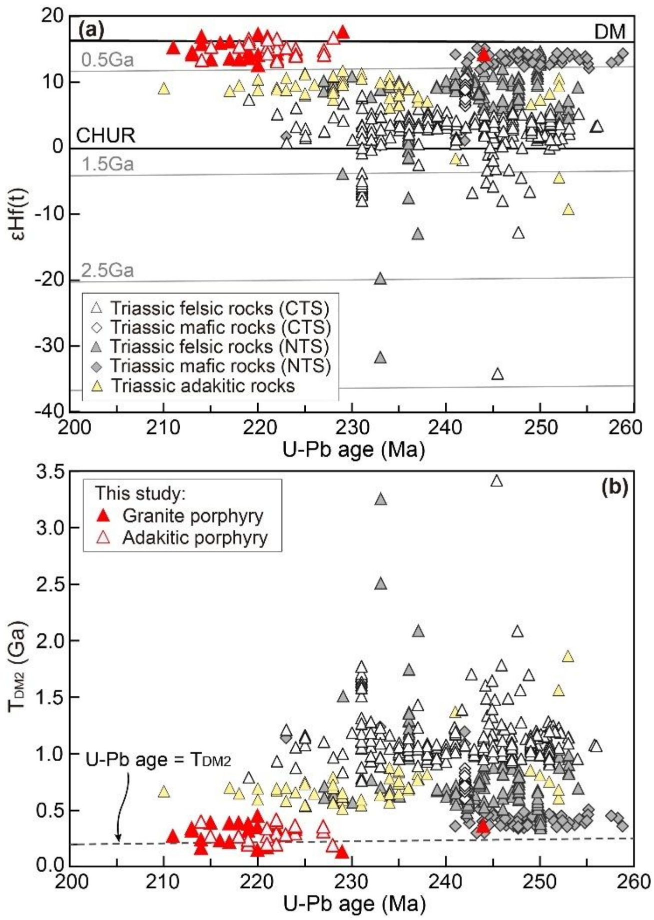

Figure 6.10. (a) Zircon $\varepsilon_{Hf}(t)$ versus zircon U-Pb age diagram. (b) Zircon T_{DM2} versus

U-Pb age diagram.

6.4 Petrogenesis of the granitoids

The adakitic porphyry and low Sr/Y granite porphyry samples from the Bogda Belt have low HFSE contents (Zr + Nb + Ce + Y <350 ppm), low Zr contents (<250 ppm), and relatively low Ga/Al ratios (Figures 6.11a and 6.11b). These characteristics differ from those of A-type granites but are consistent with fractionated I-type or S-type granites (Whalen et al., 1987). They are weakly peraluminous with A/CNK values of 1.0-1.2 (Figure 6.6d). However, they exhibit a negative correlation between P_2O_5 and SiO_2, and a positive correlation between Th and Rb (Figures 6.11c and 6.11d), which are typical features of I-type rather than S-type granites (Chappell, 1999; Chappell and White, 2001). Combined with the lack of Al-rich minerals (e.g., muscovite and cordierite), we suggest that both the adakitic porphyry and the low Sr/Y granite porphyry are I-type granitoids.

6.4.1 Adakitic porphyry

The adakitic porphyry samples show high SiO_2 (>68 wt%) and Sr (199-512 ppm), and low Y (7.2-8.3 ppm) and Yb (0.6-0.8 ppm) contents, with high Sr/Y (26-66) and $(La/Yb)_N$ (19.8-20.6) ratios, corresponding to a high-SiO_2 adakitic character (Figures 6.11e and 6.11f; Martin et al., 2005). Several petrogenetic models have been proposed to interpret the origin of high-SiO_2 adakitic rocks: (1) partial melting of subducted oceanic slab, followed by interaction with the overlying mantle wedge (e.g., Defant & Drummond, 1990; Rapp et al., 1999; Martin, 2005); (2) partial melting of thick lower crust (e.g., Chung et al., 2003; Hou et al., 2004; X. P. Long et al., 2015; C. Wu et al., 2023); (3) fractionation of parental mafic magma with likely crustal assimilation (e.g., Castillo et al., 1999; Macpherson et al., 2006; Richard & Kerrich, 2007); (4) partial melting of delaminated lower crust (e.g., J. F. Xu et al., 2002; Q. Wang et al., 2006; P. L. He et al., 2020).

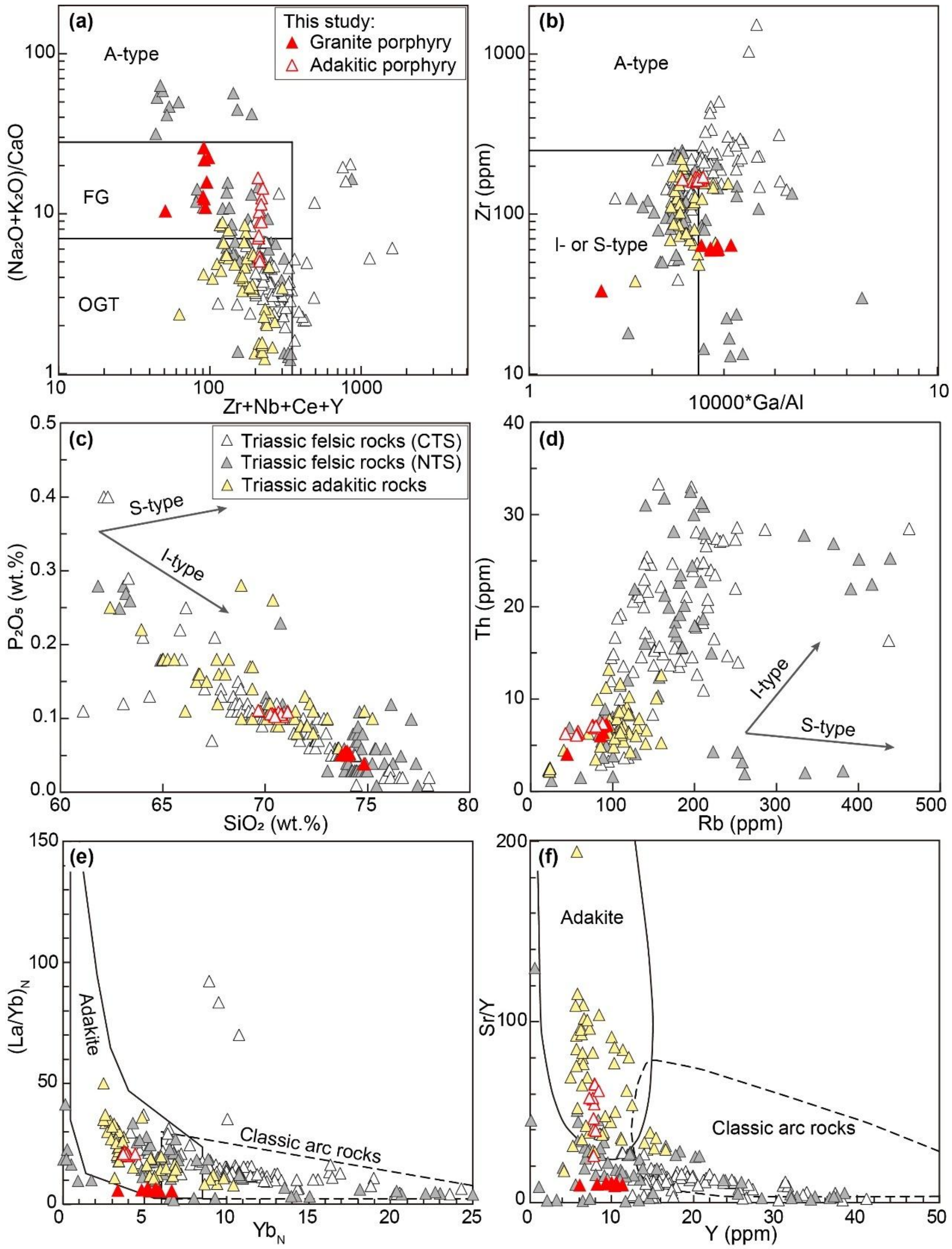

Figure 6.11. (a) $(K_2O+Na_2O)/CaO$ versus Zr + Nb + Ce + Y and (b) Zr versus Ga/Al diagrams (after Whalen et al., 1987). (c) P_2O_5 versus SiO_2 diagram. (d) Th versus Rb diagram. (e) $(La/Yb)_N$ versus Yb_N and (f) Sr/Y versus Y diagrams (after Defant & Drummond, 1990). FG: fractionated M-, I-, and S- type granites; OGT: unfractionated M-, I-, and S- type granites.

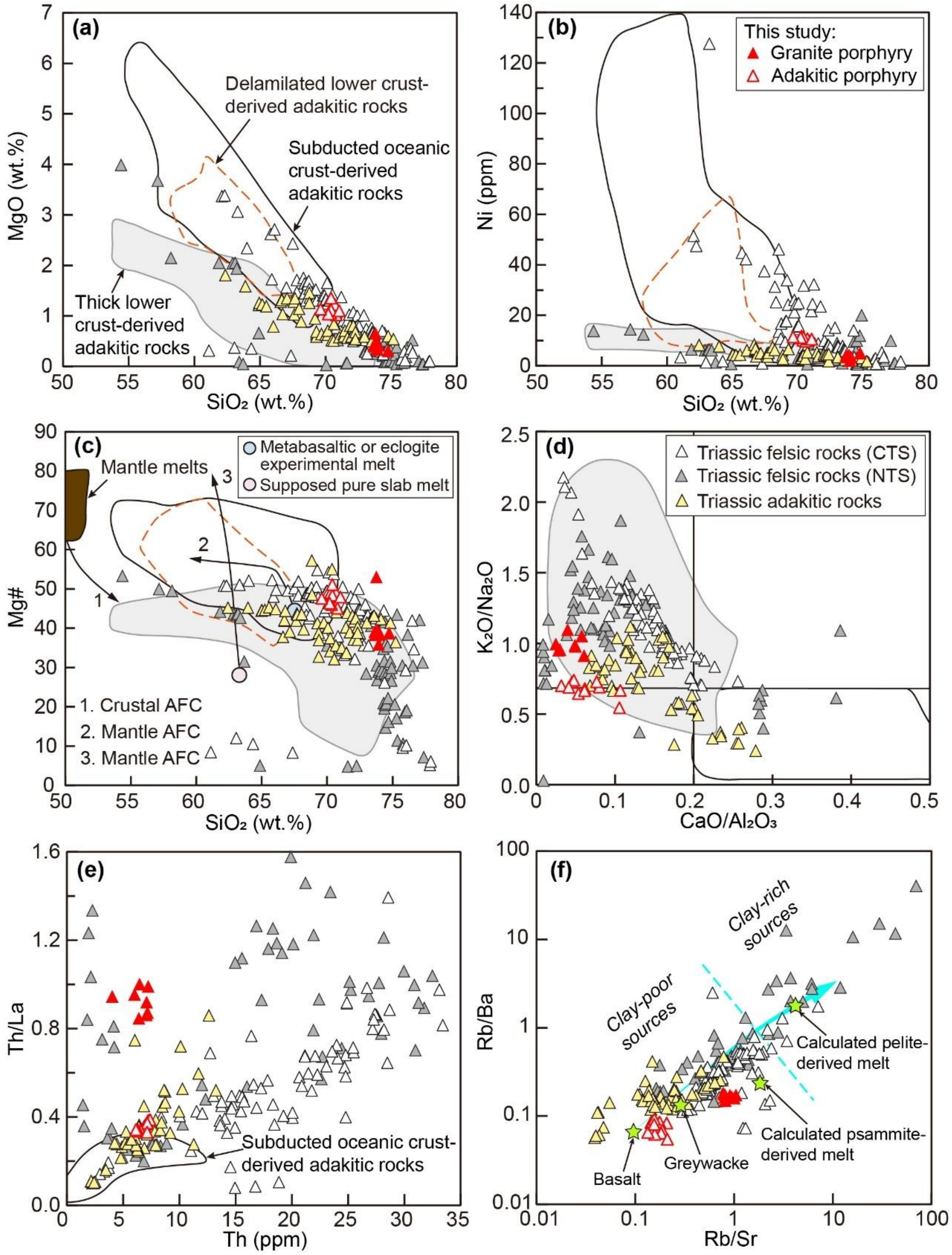

Figure 6.12. (a) MgO versus SiO_2, (b) Ni versus SiO_2, and (c) $Mg^{\#}$ ($Mg^{2+}/(Mg^{2+} + Fe^{2+})$) versus SiO_2 diagrams (after Q. Wang et al., 2006). (d) K_2O/Na_2O versus CaO/Al_2O_3 diagram (after Karsli et al., 2019). (e) Th/La versus Th diagram (after Q. Wang et al., 2008). (f) Rb/Ba versus Rb/Sr diagram (after Sylvester, 1998).

Adakitic rocks generated by fractionation of parental mafic magma usually contain mafic minerals (e.g., amphibole and clinopyroxene) and exhibit systematic variations in geochemical composition (Castillo et al., 1999; Macpherson et al., 2006). In contrast, the adakitic porphyry samples show uniform geochemical compositions without fractionation trend in bivariate diagrams (Figure 6.7). For example, the La and Y contents, as well as $(La/Yb)_N$ and Dy/Yb ratios of the samples, remain stable across varying SiO_2 contents, indicating that there is no significant fractionation of garnet or amphibole (J. F. Xu et al., 2022). Combined with the absence of amphibole and clinopyroxene in the samples (Figure 6.2), the lack of contemporary basaltic to intermediate rocks, and their depleted Sr-Nd isotopes (Figure 6.9), we suggest that the adakitic rocks of the Bogda Belt are unlikely to have been generated by assimilation and fractional crystallization (AFC) of mafic magma.

The adakitic porphyry samples have low MgO (1.01-1.32 wt%) and high K_2O (2.99-3.65 wt%) contents, with high K_2O/Na_2O (0.5-0.7), Th/Nb (>2) and Th/La (>0.3) ratios, which are different from adakitic rocks derived from the melting of an oceanic slab (Figure 6.12; Martin, 2005; X. S. Wang et al., 2022b). These geochemical features, together with their relatively low $Mg^{\#}$ (45-51), Cr (18.4-21.5 ppm), and Ni (9.7-11.8 ppm) contents, are not consistent with the extensive melt-mantle interaction that usually occurs during the delamination of the lower crust (J. F. Xu et al., 2002; Q. Wang et al., 2006). Consequently, the possibility that these rocks formed by partial melting of subducted oceanic slab or delaminated lower crust can be excluded. Conversely, the adakitic porphyry samples resemble adakitic rocks derived from thick lower crust, which generally have low MgO, Cr, and Ni contents, high SiO_2 and K_2O contents, and high K_2O/Na_2O ratios (Figure 6.12; Hou et al., 2004; X. P. Long et al., 2015; Karsli et al., 2019). Therefore, we suggest that the adakitic porphyry is most likely derived from the partial melting of thick lower crust. The adakitic porphyry shows high $\varepsilon_{Nd}(t)$ (+7.2) and zircon $\varepsilon_{Hf}(t)$ (+13.1 to +16.7) values, and low initial $^{87}Sr/^{86}Sr$ ratio (0.70393), indicative of a juvenile crust source (<0.5 Ga). Notably, their Sr-Nd isotopic compositions are comparable to those of late Paleozoic mafic rocks (Figure 6.9). Moreover, the low Rb/Ba and Rb/Sr ratios of the adakitic porphyry are similar to those of basalt-derived melt (Figure 6.12f; Sylvester, 1998). Overall, we suggest that the source of the adakitic porphyry was most likely the NTS lower crust, which is in part composed of late Paleozoic arc-type mafic rocks. The enrichment of Rb, Ba, Th, and U and depletion of Nb, Ta, and Ti are likely inherited from the source rocks (Q. Ma et al., 2015).

In the La/Sm and $(La/Yb)_N$ versus La diagrams, the adakitic rocks from the North Tianshan are positively correlated, indicating that their geochemical variations were controlled by the degree of partial melting (Figures 6.13a and 6.13b). The positive correlation between $(Dy/Yb)_N$ and $(La/Yb)_N$ ratios suggests the dominant role of garnet but not amphibole in the restites (Figures 6.13c). Given that plagioclase is enriched in Sr and Eu while garnet is depleted in LREE (e.g., La) and enriched in HREE (e.g., Yb) and Y, the relatively large variation in Sr/Y ratios with weak Eu anomalies, and high La/Yb and Sr/Y ratios of the adakitic rocks, reflect the presence of residual garnet and only a few plagioclase in their sources (Figures 6.13d and 6.13e). The Nb/Ta and Dy/Yb ratios for the adakitic rocks are relatively low, supporting an origin by melting of garnet amphibolite (~10-15 kbar), rather than rutile eclogite (Figure 6.13f; X. P. Long et al., 2015; X. S. Wang et al., 2022b). The zircon saturation temperatures (T_{Zr}) indicate that the minimum partial melting temperature is approximately 790 °C.

6.4.2 Low Sr/Y granite porphyry

The low Sr/Y granite porphyry is spatially close to the adakitic porphyry (Figure 6.3) and shows slightly younger crystallization ages (Figure 6.4). The low Sr/Y granite porphyry samples have high SiO_2 (72.39-74.15 wt%) and K_2O (4.14-4.61 wt%) contents, and low TFe_2O_3 (0.94-1.32 wt%), MgO (0.30-0.64 wt%), Cr (2.9-10.0 ppm), and Ni (2.0-4.9 ppm) contents, along with high K_2O/Na_2O ratios (0.9-1.1) and low $Mg^\#$ values (Figure 6.12), suggesting that they are also derived from partial melting of crust without extensive melt-mantle interaction. In the bivariate diagrams (e.g., CaO, Sr, La, Sr/Y, $(La/Yb)_N$, and Dy/Yb versus SiO_2 diagrams), the adakitic porphyry and the low Sr/Y granite porphyry samples do not show any common fractionation trend (Figure 6.7). Therefore, the low Sr/Y granite porphyry is unlikely to be derived from the earlier adakitic rocks by fractional crystallization. Its lower Th/Nb values, as well as the lower initial $^{87}Sr/^{86}Sr$ ratio and higher $\varepsilon_{Nd}(t)$ value compared to the adakitic porphyry, further preclude an origin via assimilation and fractional crystallization (AFC) processes acting on the adakitic magma (Figures 6.7 and 6.9).

The low Sr/Y granite porphyry shows depleted Sr-Nd and zircon Hf isotopes similar to those of the adakitic porphyry, indicating that they at least partly share similar juvenile crust sources (Figures 6.9 and 6.10). The low Sr/Y granite porphyry samples have higher Rb/Ba and Rb/Sr ratios than the adakitic porphyry, which reflects the involvement of more felsic components in its source (Figure 6.12f). The negative Sr and Eu anomalies, as well as the low Sr/Y and La/Yb ratios of the granite porphyry, suggest the presence of plagioclase with little or no garnet in the restites (Figures 6.13d and 6.11e; Q. Wang et al., 2016). Combined with the low Nb/Ta and Dy/Yb ratios, we suggest that the low Sr/Y magma was likely formed by partial melting of crustal rocks at a relatively low pressure (<8 kbar; Q. Wang et al., 2016; X. S. Wang et al., 2022b). Moreover, the zircon saturation temperatures (T_{Zr}) indicate that the low Sr/Y granite porphyry may have a minimum partial melting temperature around ~700 °C (Figure 6.14).

In summary, the adakitic porphyry and low Sr/Y granite porphyry of the Bogda Belt were both derived from partial melting of juvenile crust. The adakitic magma was formed by partial melting of mafic lower crust in the garnet stability field at moderate temperatures, while the low Sr/Y magma was generated by partial melting of relatively felsic crust at shallower depths (in the plagioclase stability field) and lower temperatures.

6.5 Spatial and temporal distribution of Triassic magmatism

In this contribution, we present late Triassic LA-ICP-MS zircon U-Pb ages (221-217 Ma) of four samples of adakitic porphyry and I-type granitic porphyry from the Bogda Belt, thus providing the first direct evidence of Triassic magmatism in this area (Figures 6.2, 6.3, 6.4, and 6.11). In recent years, some Triassic (253-223 Ma) undeformed gabbro, granodiorite, monzogranite, and granite, were reported in the eastern Tianshan as well (Table 6.2). These magmatic rocks are mostly located in the southern part of the North Tianshan (i.e. Dananhu and Kanggur-Yamansu regions) and in the Central Tianshan (Figure 6.1).

In the Dananhu and Kanggur-Yamansu regions, the Triassic magmatic rocks include mafic rocks, adakitic rocks, I-type, A-type and S-type granitoids, and a few intermediate rocks (Figures 6.6 and 6.14a). The mafic rocks, dated at 251-247 and 238-236 Ma (Table 6.2), were classified as arc-type and E-MORB-type gabbro based on their REE and trace-element features (S. Y. Liu et al., 2020; Z. W. Gao et al., 2021; Y. F. Wang et al., 2022). In combination with whole-rock Sr-Nd and zircon Hf isotopes (Figures 6.9 and 6.10), they were suggested to derive from various mantle sources (Z. W. Gao et al., 2021; Y. F. Wang et al., 2022).

The adakites have zircon U-Pb ages of 250-227 Ma (Table 6.2). They are characterized by low MgO, Ni and $Mg^{\#}$ values, and high SiO_2 and K_2O contents with high K_2O/Na_2O ratios (Figure 6.12), together with moderate $\varepsilon_{Nd}(t)$ and zircon $\varepsilon_{Hf}(t)$ values (Figures 6.9 and 6.10), indicative of thick lower crust sources (~0.5-1.0 Ga) without significant mantle input (L. D. Zhao et al., 2019b; Q. G. Mao et al., 2022b; J. G. Yuan et al., 2023). In addition, the variable Th/La and Rb/Sr ratios of the adakitic rocks suggest the presence of mafic and felsic components in their sources (Figure 6.12). Their negligible Eu anomalies, along with high Sr/Y and La/Yb ratios and low Nb/Ta ratios (Figure 6.13), indicate that they were likely derived from the melting of garnet amphibolite with little or no residual plagioclase. The zircon saturation temperatures (T_{Zr} = 666-804 °C) suggest partial melting at moderate temperatures (Figure 6.14).

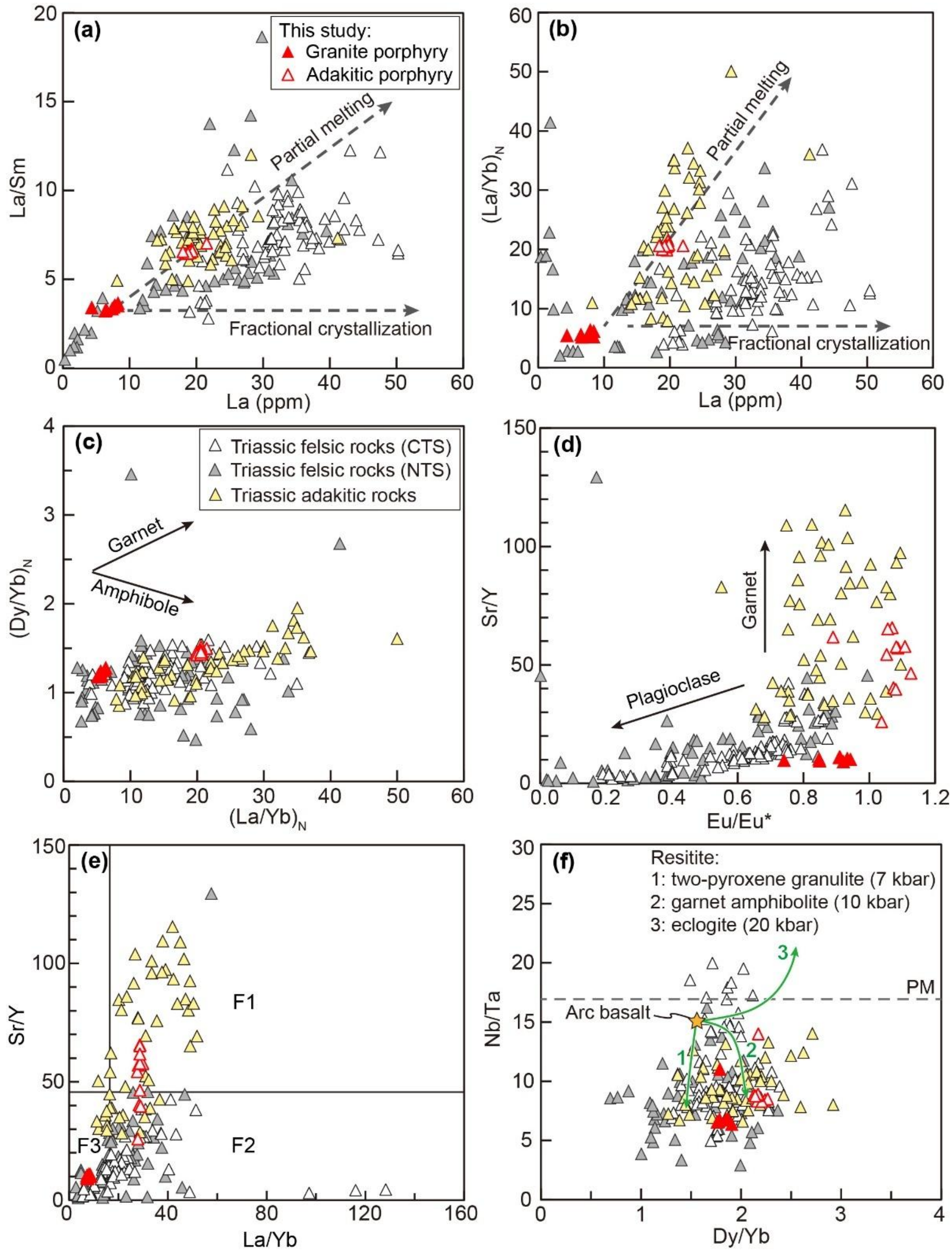

Figure 6.13. (a) La/Sm versus La and (b) $(La/Yb)_N$ versus La diagrams. (c) $(Dy/Yb)_N$ versus $(La/Yb)_N$ diagram. (d) Sr/Y versus Eu/Eu* diagram. (e) Sr/Y versus La/Yb diagram (after Q. Wang et al., 2016). F1: adakitic melts derived from eclogitic rocks in the stability field of garnet with little or no plagioclase; F2: crustal melts in the stability field of plagioclase and garnet; F3: crustal melts in the stability field of plagioclase with little or no garnet. (f) Nb/Ta versus Dy/Yb diagram. The curves are from X. S. Wang et al. (2022b). PM: primitive mantle.

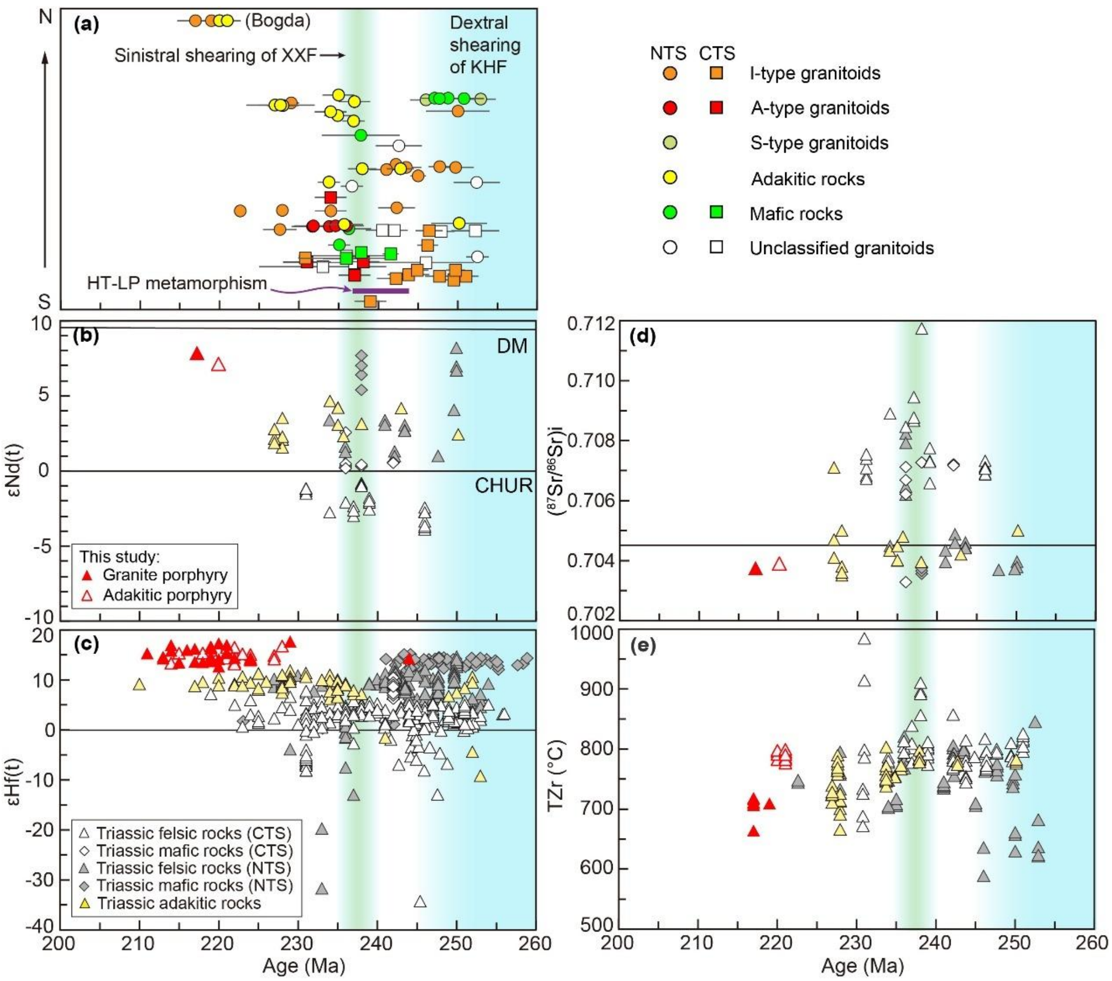

Figure 6.14. (a) Distribution of the Triassic magmatism in the eastern Tianshan. Data sources are summarized in Table 6.2. The timescale of high-temperature and low-pressure (HT-LP) metamorphism is from L. J. Mao et al. (2015). (b) $\varepsilon_{Nd}(t)$ versus crystallization age diagram. (c) Zircon $\varepsilon_{Hf}(t)$ versus zircon U-Pb age diagram. (d) $(^{87}Sr/^{86}Sr)_i$ versus crystallization age diagram. (e) Zircon saturation temperature (T_{Zr}; Waston & Harrison, 1983) versus crystallization age diagram. Ages for the Xingxingxia Fault (XXF) and Kanggur-Huangshan Shear Zone (KHSZ) are from Y. Wang et al. (2008, 2010) and Muhtar et al. (2023).

The S-type, I-type and A-type granitoids have ages of 253-246 Ma, 250-223 Ma, and 236-232 Ma, respectively (Table 6.2). The S-type granitoids occur at the periphery of the mafic rocks and have the same ages (Figure 6.14a), suggesting that they were formed by middle to upper crustal melting associated with the emplacement of the mafic magma (S. Y. Liu et al., 2020). The I-type and A-type granitoids have low MgO, Ni and Mg# values, and high K_2O contents with high K_2O/Na_2O ratios, indicative of crustal sources without mantle-derived materials (Figure 6.12; Muhtar et al., 2024). They show a range of Th/La and Rb/Sr ratios, along with variable Sr-Nd and zircon Hf isotopes, reflecting the heterogeneity of their crustal sources that include mafic to felsic components ranging from <0.5 Ga to >1.0 Ga (Figures 6.9, 6.10 and 6.12). In addition, their negative Eu anomalies, low Sr/Y ratios, and the negative correlation between Dy/Yb and La/Yb ratios suggest a dominant role of plagioclase and amphibole as residual minerals (Figure 6.13). The zircon saturation temperatures (T_{Zr}) for the granitoids range from 588 to 844 °C, indicating low to moderate partial melting temperatures (Figure 6.14).

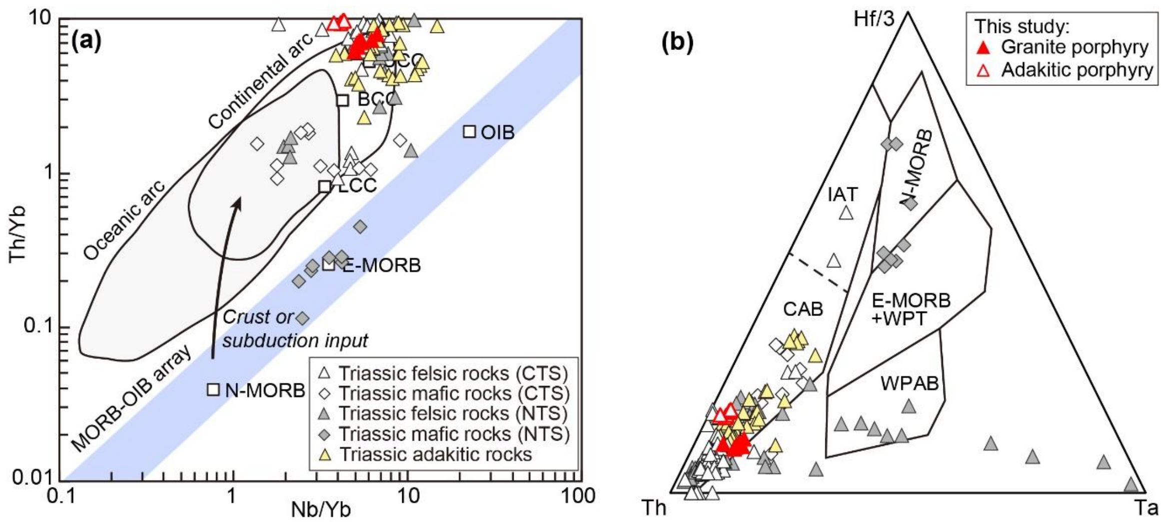

Figure 6.15. (a) Nb/Yb versus Th/Yb diagram (after Pearce & Peate, 1995). (b) Hf/3-Th-Ta diagram (after Wood, 1980).

In the Central Tianshan, the Triassic magmatism is geochemically bimodal with mafic rocks and I- and A-type granitoids (Figures 6.7a and 6.14a). The mafic rocks, mostly gabbro and anorthosite, are exposed in the Weiya area and have been dated at 242-236 Ma (Feng & Zheng, 2021; Shi et al., 2021). They exhibit arc-type geochemical features with relatively enriched Sr-Nd and zircon Hf isotopes (Figures 6.9 and 6.15), which was interpreted as resulting from source contamination associated with previous subduction events (Feng & Zheng, 2021). The I-type granitoids have ages ranging from 251 to 231 Ma, while the A-type granitoids are slightly younger, with ages from 238 to 231 Ma (Figure 6.14a). These I-type and A-type granitoids are characterized by moderate to low MgO, Ni, and $Mg^{\#}$ values, high K_2O and Th contents, and elevated K_2O/Na_2O, Th/La, and Rb/Sr ratios (Figure 6.12). Additionally, they exhibit enriched Sr-Nd and zircon Hf isotopes with T_{DM2} ranging from ~0.8 to 1.8 Ga (Figures 6.9 and 6.10). These features indicate that they were derived from partial melting of ancient crustal components with some mantle input (C. Chen et al., 2018; N. Li et al., 2019; R. X. Lei et al., 2021; Q. G. Mao et al., 2022b). The negative Eu anomalies with low Sr/Y ratios and various La/Yb ratios reflect the presence of residual plagioclase and garnet in their sources (Figure 6.13; Q. Wang et al., 2016). The zircon saturation temperatures (T_{Zr} = 671-984 °C) of the granitoids indicate partial melting of crustal rocks at moderate to high temperatures (Figure 6.14).

Notably, the mafic magmatism in the North and Central Tianshan occurred simultaneously with the dextral shearing of the KHF and the sinistral shearing of the XXF (Figure 6.14a). The A-type magmatism also occurred during the development of the XXF, corresponding to an increase in the zircon saturation temperatures (Figure 6.14e). From south to north, there is a decrease in $(^{87}Sr/^{86}Sr)_i$ and an increase in εNd(t) and zircon εHf(t) (Figures 6.16). More specifically, the magmatic rocks in the Central Tianshan have totally enriched isotopic compositions, while those in the North Tianshan exhibit gradually depleted Sr-Nd and zircon Hf isotopes towards the north. Such changes indicate the involvement of a decreasing amount of ancient materials away from the Central Tianshan. In addition, the magmatic rocks exhibit a decrease in zircon saturation temperatures from the Central Tianshan to the North Tianshan (Figure 6.16g). From west to east, the magmatic rocks in the Central Tianshan have invariant enriched isotopic compositions, while those in the North Tianshan show an increase in $(^{87}Sr/^{86}Sr)_i$ and a decrease in $\varepsilon_{Nd}(t)$ and zircon $\varepsilon_{Hf}(t)$ at 93°-95° E (Figures 6.16).

Similarly, there is an eastward increase in zircon saturation temperatures at 93°-95° E (Figure 6.16h).

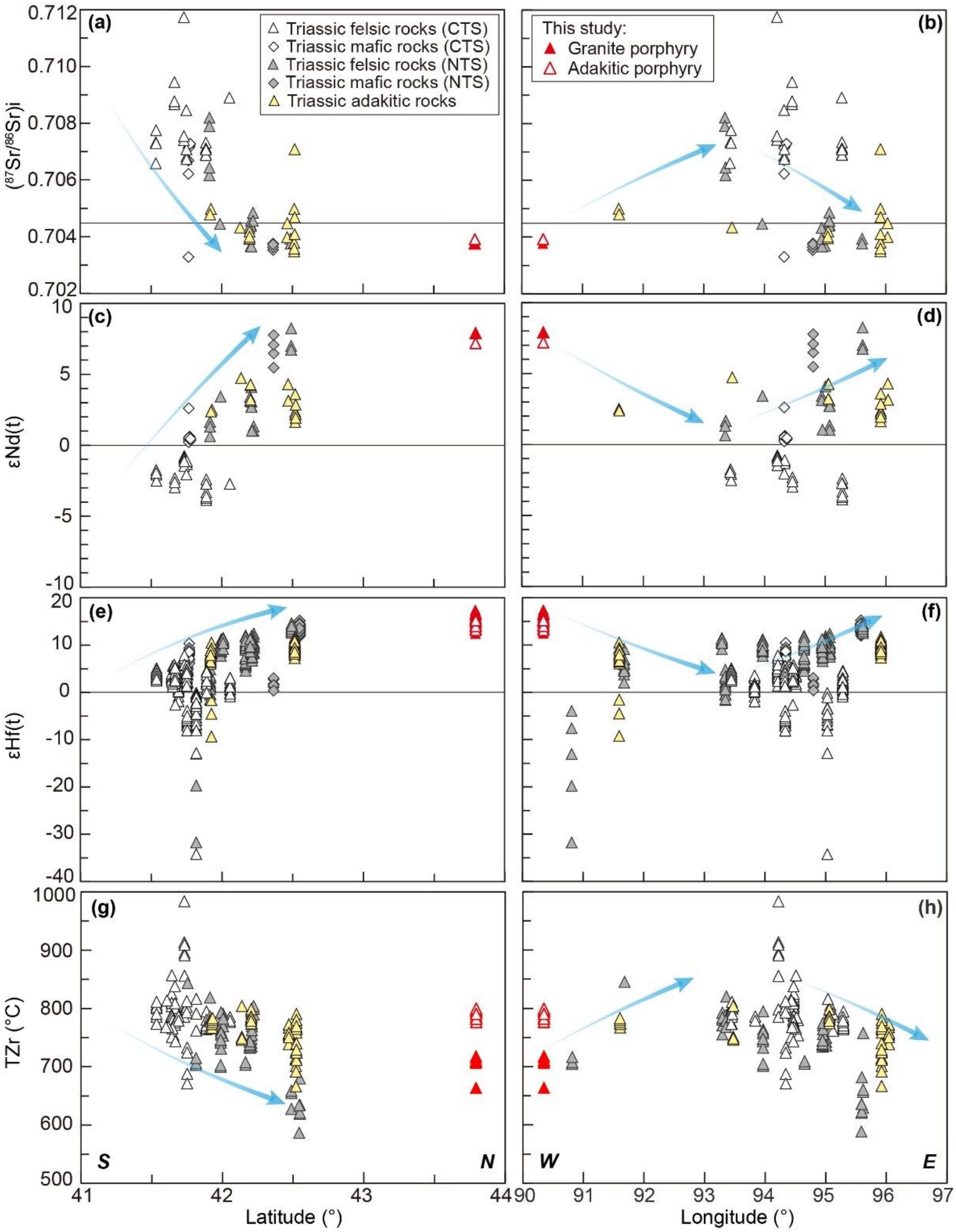

Figure 6.16. Spatial variations in whole-rock Sr-Nd and zircon Hf isotopes, and zircon saturation temperature (T_{Zr}) for the Triassic magmatism. (a) $(^{87}Sr/^{86}Sr)_i$, (c) $\varepsilon_{Nd}(t)$, (e) $\varepsilon_{Hf}(t)$, and (g) T_{Zr} versus Latitude diagrams. (b) $(^{87}Sr/^{86}Sr)_i$, (d) $\varepsilon_{Nd}(t)$, (f) $\varepsilon_{Hf}(t)$, and (h) T_{Zr} versus Longitude diagrams.

6.6 Implications for the crustal reworking in the eastern Tianshan

6.6.1 Variable pressure and temperature of crustal reworking and heterogeneous sources

As discussed above, the nearly contemporaneous adakitic porphyry and low Sr/Y granite porphyry in the Bogda Belt were derived from the partial melting of juvenile crust (<0.5 Ga) at different depths and temperatures. The former was generated by lower crustal melting at high pressures (~10-15 kbar, corresponding to depths of 33-50 km) and moderate temperatures, while the latter was formed by crustal melting at lower pressures (<8 kbar, corresponding to depths of <27 km) and temperatures. In the Dananhu and Kanggur-Yamansu regions, the adakitic rocks were sourced from somewhat older crustal materials (~0.5-1.0 Ga; Figures 6.9 and 6.10). Given the presence of residual garnet with little or no plagioclase and the zircon saturation temperature data, they were likely formed by crustal melting at high pressures (~10-15 kbar, corresponding to depths of 33-50 km) and moderate temperatures. The S-type, I-type, and A-type granitoids were derived from crustal melting with residual plagioclase and amphibole at low pressures (<8 kbar, corresponding to depths of <27 km) and low to moderate temperatures, with source ages ranging from <0.5 Ga to >1.0 Ga (Figures 6.9 and 6.10). In the Central Tianshan, the I-type and A-type granitoids were sourced from ancient crustal materials (~0.8-1.8 Ga) likely with some mantle input (Figures 6.9 and 6.10). They were mainly generated by crustal melting with residual garnet and plagioclase at moderate pressures (5-12 kbar, corresponding to depths of 15-40 km; Q. Wang et al., 2016) and moderate to high temperatures.

Therefore, crust melting occurred in the eastern Tianshan during the Triassic at variable depths and temperatures, from the thick lower crust to the middle and upper crust. Generally, the Central Tianshan features high temperature partial melting of the crust at relatively low pressures in comparison to the North Tianshan. Moreover, the gradual change of Sr-Nd and zircon Hf isotopic compositions of the magmatic rocks from the Central Tianshan to the North Tianshan probably indicate a shift in crustal compositions (Figure 6.16). The Bogda Belt and the Central Tianshan predominantly consist of juvenile and ancient crusts, respectively, while the Kanggur-Yamansu belt have crust with transitional compositions. In addition, the more enriched isotopic compositions and higher zircon saturation temperatures at 93°-95° E suggest a greater presence of ancient crustal sources and higher partial melting temperatures (Figure 6.16).

6.6.2 Tectonic setting and mechanism for crustal reworking

The tectonic setting and origin of the Triassic magmatism in the eastern Tianshan are still a matter of debate. Several models have been proposed: (1) intracontinental extension (F. F. Zhang et al., 2015; Y. H. Wang et al., 2016; H. S. Sun et al., 2017; N. Li et al., 2019; S. Y. Liu et al., 2020; R. X. Lei et al., 2021; J. G. Yuan et al., 2023); (2) tectonic transition from syn-collisional compression to post-collisional extension (X. H. Deng et al., 2017; Y. S. Wu et al., 2017); (3) tectonic transition from supra-subduction accretion to collision (Ao et al., 2021; Q. G. Mao et al., 2021, 2022b); (4) continental subduction induced by the Tethys subduction system (Z. Z. Zhang et al., 2005, 2007; C. Z. Wu et al., 2010).

During the middle Permian to Triassic, the eastern Tianshan was characterized by localized strike-slip deformation instead of regional contraction (Laurent-Charvet et al., 2003; Y. Wang et al., 2008, 2010). Most of the Triassic magmatic intrusions are undeformed and usually cut through the folded or foliated pre-Triassic rocks (R. X. Lei et al., 2021; J. G. Yuan et al., 2023). Moreover, there is no regional metamorphism related to collision or continental subduction in the eastern Tianshan since the Permian (B. Wang et al., 2014). Therefore, the eastern Tianshan unlikely underwent any collisional event or continental subduction during the Triassic. Some Triassic mafic rocks (e.g., Weiya gabbro) and granitoids exhibit arc-type trace-element signatures, accordingly, some authors suggested that the oceanic subduction lasted until the middle

Triassic (Q. G. Mao et al., 2022b; Muhtar et al., 2024). However, arc-type geochemical signatures do not always indicate oceanic subduction as post-orogenic magmatism derived from previously metasomatized mantle source also shows such features (e.g., Zheng & Chen, 2016; Feng & Zheng, 2021). In contrast with typical arcs that include a wide range of rocks from basalt to rhyolite without compositional gaps (Ducea et al., 2015; Zheng & Chen, 2016), the Triassic magmatism in the eastern Tianshan is bimodal (Figure 5). Considering that: (1) no confirmed ophiolites younger than early Permian (G. C. Wang et al., 2022); (2) totally terrestrial environments prevailed during the Triassic (Fang et al., 2019; J. L. Wang et al., 2019), it may be inferred that the eastern Tianshan evolved into an intracontinental or intraplate setting during the Triassic.

The Triassic mafic rocks in the eastern Tianshan were either derived from partial melting of the metasomatized mantle lithosphere due to asthenosphere upwelling (Feng & Zheng, 2021), or directly from decompression partial melting of the upwelling asthenospheric mantle (Y. F. Wang et al., 2022). The relatively high temperatures and low pressures of crustal melting in the Central Tianshan and at 93°-95° E might be attributed to thinning and warming of the lithosphere due to asthenosphere upwelling. This interpretation is supported by the occurrence of contemporaneous A-type granitoids and high-temperature and low-pressure metamorphism at this area (Figure 6-14; L. J. Mao et al., 2015). Ascent and underplating of the mantle-derived mafic magma would have provided additional heat to the crustal melting and generated felsic magmatism (S. Y. Liu et al., 2020; Feng & Zheng, 2021; R. X. Lei et al., 2021). In the North Tianshan, the reworking of the lower crust at relatively high pressures and low temperatures suggests that it was thicker and cooler than that of the Central Tianshan, suggesting limited effects of the asthenosphere upwelling in the north. Triassic magmatic rocks from the Beishan Belt, including I-type and A-type granitoids, adakitic rocks, and some mafic dykes were also interpreted to be formed in relation to asthenosphere upwelling in a post-orogenic or intraplate setting (S. Li et al., 2012; H. R. Sun et al., 2020; R. Q. Liu et al., 2023). This interpretation is consistent with ours.

The mafic rocks and A-type granitoids were temporally related to the strike-slip faulting, suggesting a correlation between asthenosphere upwelling and transcurrent tectonics (Figure 6.14). It has been suggested that the sinistral Xingxingxia Fault was a sub-branch of the Altyn Tagh fault system during the Triassic (Y. Wang et al., 2010), with its activity attributed to the far-field stress effects of the Paleo-Tethys system (J. H. Li et al., 2020). In addition, low-temperature thermochronological studies provide clear evidence for Triassic tectonic reactivation in the eastern Tianshan, which is thought to be related to distal effects of the subduction of Paleo-Tethys system (Z. Y. He et al., 2022). Therefore, it is likely that the far-field effects of the Paleo-Tethys system played a significant role in the Triassic tectonics of the eastern Tianshan (Y. Wang et al., 2010; X. R. Zhang et al., 2017; R. X. Lei et al., 2021).

Chapter 7. General discussion on the late Paleozoic - early Mesozoic tectonic evolution of the eastern Tianshan

7.1 Crustal basement in the eastern Tianshan and East Junggar regions and its significance on continental growth

As mentioned above, the nature of the crustal basement in the North Tianshan and Junggar regions (also referred to as the Junggar Terrane by some authors) has been the subject of long-standing debate regarding whether it consists of ancient continental crust (e.g., X. W. Xu et al., 2015; J. Wang et al., 2020; T. Wang et al., 2023; L. Du et al., 2024). To address this issue, this thesis compiles whole-rock Nd and zircon Hf isotopic data of Carboniferous to Triassic magmatic rocks from these regions, comparing them with isotopic data of contemporaneous magmatic rocks from nearby microcontinental blocks (i.e., the Central Tianshan Block), which have confirmed the presence of Mesoproterozoic to Paleoproterozoic crustal basement there (e.g., Z. Y. He et al., 2018).

The Carboniferous to Triassic magmatic rocks in the East Junggar and Bogda-Harlik-Dananhu regions show similar two-stage Nd and zircon Hf depleted mantle model ages (T_{DM2}), predominantly ranging from 0.3 to 0.8 Ga with peaks at around 0.5 Ga (Figure 7.1). This is obviously different from the Central Tianshan Block, where the magmatic rocks exhibit T_{DM2} ages of 0.7 to 1.5 Ga, with a peak at around 1.0 Ga (Figure 7.1). Consequently, the basement of the East Junggar and Bogda-Harlik-Dananhu belts unlikely contains ancient continental crust as that of the Central Tianshan Block, but rather consists of juvenile crust formed during the Neoproterozoic to Paleozoic. In the Kanggur-Yamansu region, the late Paleozoic, particularly the Carboniferous, magmatic rocks display two populations of T_{DM2} ages: one ranging from 0.2 to 0.7 Ga, peaking at 0.5 Ga, and another from 0.8 to 1.2 Ga, peaking at 1.0 Ga. The former is comparable to the juvenile components of the East Junggar and Bogda-Harlik-Dananhu belts, while the latter is similar to the continental crust of the Central Tianshan Block. As presented in Chapter 5, the western part of the Kanggur-Yamansu belt exhibits more enriched Nd and Hf isotopic compositions than its eastern part. Therefore, the basement of the Kanggur-Yamansu region comprises an old continental basement in the west and only juvenile crust in the east.

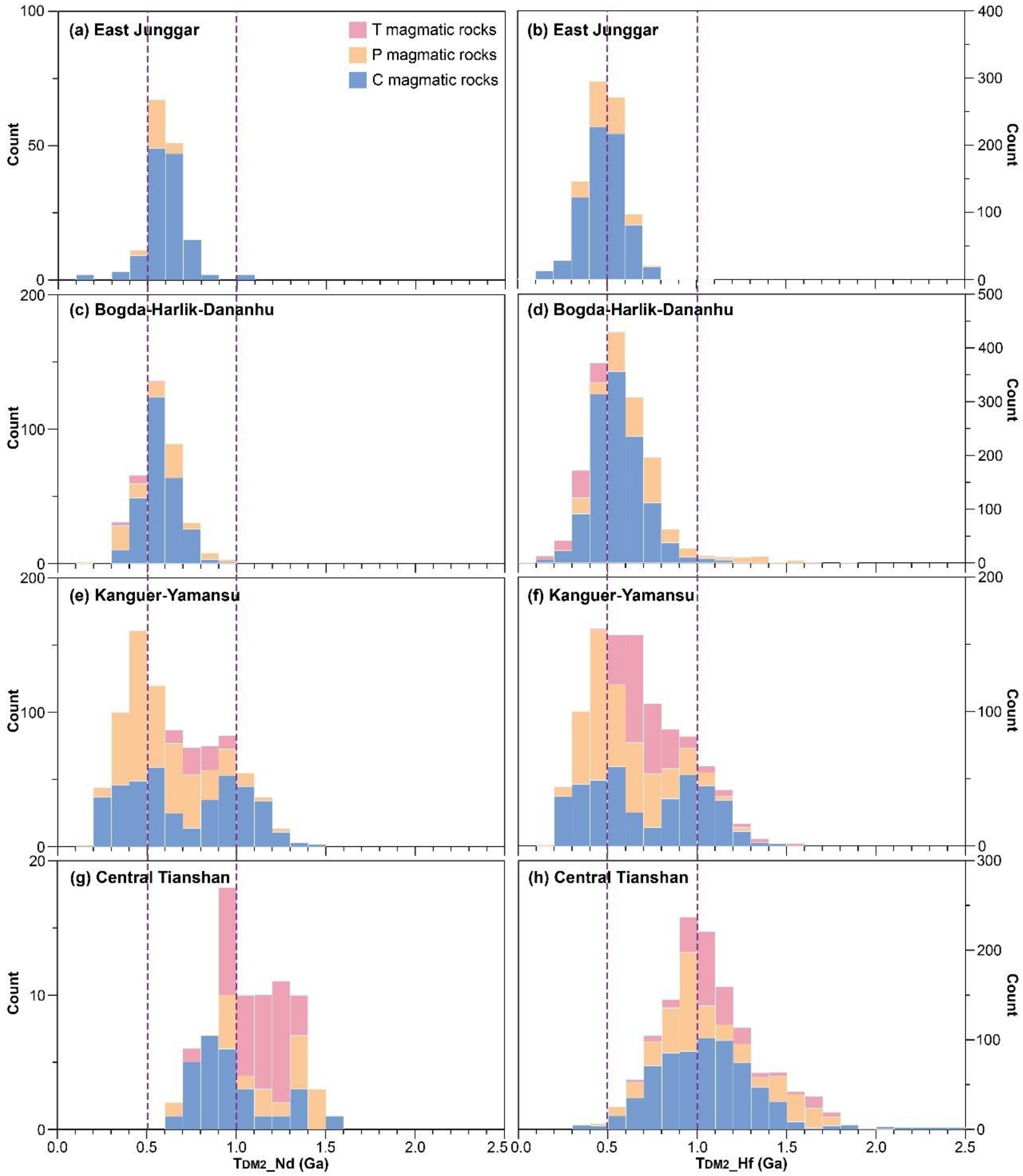

Figure 7.1. Statistics of two-stage Nd and zircon Hf depleted mantle model ages (T_{DM2}) of the East Junggar, Bogda-Harlik-Dananhu, Kanggur-Yamansu, and Central Tianshan regions.

The thicknesses of late Caborniferous crust of the East Junggar and Dananhu-Harlik regions were estimated to be 30 to 60 km (see Chapter 5). If this is reliable, the volume of juvenile crust in the southwestern CAOB would be substantial. The formation and preservation of such juvenile crust indicate significant continental growth during the Neoproterozoic to Paleozoic.

7.2 Late Paleozoic to early Mesozoic tectonic evolution: from oceanic subduction to intraplate tectonics

During the Carboniferous, the eastern Tianshan and East Junggar were characterized by widespread mafic to felsic volcanism and intrusions with arc-type geochemical signatures (see Chapter 4). Along with the presence of Carboniferous ophiolitic rocks (e.g., J. Gao et al., 2022; G. C. Wang et al., 2022; and reference therein), the subduction of several oceanic branches of the PAO during this time can be inferred (e.g., Han & Zhao, 2018).

In the Harlik region, an early Carboniferous stage of NE-SW compression is speculated (Chapter 4). The crust in the East Junggar and Bogda-Harlik-Dananhu regions thickened at around 340-330 Ma, coinciding with the formation of some rocks showing relatively enriched Nd and Hf isotopic compositions (see Chapter 5). In combination with ages of the Kalamaili ophiolite belt (~420 to 330 Ma; Shu & Wang, 2003; J. Gao et al., 2022) and regional unconformities between the Carboniferous strata and older rocks (G. Huang et al., 2012; Y. Y. Zhang et al., 2013; X. W. Xu et al., 2015), the accretion between the Bogda-Harlik-Dananhu and East Junggar arc systems, following the closure of the Kalamaili Ocean, is tentatively proposed to have occurred around 340-330 Ma. During 330 to 310 Ma, sinistral transtension occurred in the Harlik region, immediately followed by the emplacement of granitic batholiths and HT-LP metamorphism (see Chapter 4). In the meantime, the crust in the Bogda-Harlik-Dananhu region underwent notable thinning, with thicker crust observed in the Dananhu and East Junggar regions, while the Bogda-Harlik region exhibited relatively thin crust (see Chapter 5). Additionally, mafic magmatism with arc-type characteristics and “hot” granitoids were presented in the Bogda-Harlik and southern East Junggar regions, whereas “cold” granitoids were found in the Dananhu region (see Chapter 5). The late Carboniferous volcano-sedimentary succession in the Bogda region also suggests the presence of an intra- or back-arc basin (Memtimin et al., 2019). These lines of evidence indicate the presence of an arc-backarc system in the eastern North Tianshan, attributed to the rollback of the subducting Kanggur oceanic slab.

At around 300 Ma, a magmatic quiescence was recognized for the East Junggar and Kanggur-Yamansu regions, coupled with a sudden reduction of intermediate magmatic rocks in the Bogda-Harlik-Dananhu region (see Chapter 5). Concurrently, both the Bogda-Harlik-Dananhu and Kanggur-Yamansu regions experienced significant crustal thickening. The whole-rock $\varepsilon_{Nd}(t)$ and zircon $\varepsilon_{Hf}(t)$ values also decreased during this time, with more enriched Nd and Hf isotopic signatures found in some samples from the Bogda-Harlik-Dananhu region. In addition, a transition from marine to terrestrial environments took place during the early Permian, marked by unconformable molasse deposits (XBGMR, 1993; Shu et al., 2005). A significant decrease in whole-rock $\delta^{11}B$ values and increase in zircon $\delta^{18}O$ values at around 300 Ma likely indicates a tectonic shift from subduction to a post-collision or intraplate setting (H. Q. Liu et al., 2016; G. J. Tang et al., 2019). Furthermore, previous paleomagnetic studies show negligible relative latitudinal motion between the Yili Block, Turpan-Hami Basin, and Yamansu Belt since the late Carboniferous (B. Wang et al., 2007; X. Zhu et al., 2019; W. Xu et al., 2021). Therefore, it is reasonable to infer that the closure of the Kanggur Ocean and the final amalgamation of the eastern Tianshan occurred at around 300 Ma.

During the early Permian, the exhumation and cooling of mid-crustal rocks in the Harlik region were achieved by extensional structures and associated magma emplacement (see Chapter 4). Permian magmatic rocks in the Bogda-Harlik-Dananhu and Kanggur-Yamansu regions were dominated by mafic and felsic rocks, with fewer intermediate rocks compared to the Carboniferous (see Chapter 5). A-type granitoids are widespread in the East Junggar and Bogda-Harlik-Dananhu regions, showing high zircon saturation temperatures throughout. Additionally, the mafic rocks are primarily distributed along or near major faults, indicating a close association with the transcurrent tectonics (Branquet et al., 2012; B. Wang et al., 2014). Previous studies show that the transcurrent faults (e.g., the Main Tianshan Shear Zone, Kanggur-Huangshan Shear Zone, and Irtysh Shear Zone) were active during ~290-245 Ma, and likely recorded an eastward escape of the Junggar Terrane (Laurent-Charvet et al., 2003; Y. Wang et al., 2008; Z. Y. He, et al., 2021; P. F. Li et al., 2021; W. W. Hu et al., 2023; Muhtar et al., 2023). Differential movements along these faults accommodated the rotation of the Junggar Terrane (B. Wang et al., 2007) and probably controlled localized crustal extension in a post-orogenic setting.

During the Triassic, the magmatism in the eastern Tianshan was more scattered compared to that of the late Paleozoic (see Chapter 6). Most Triassic magmatic intrusions are undeformed and typically cut through the folded or foliated pre-Triassic rocks, indicating post-kinematic characteristics. Additionally, the Triassic magmatic rocks are primarily felsic intrusions, with some mafic ones, contrasting with convergent margins. Geochemical and isotopic data suggest that the Triassic felsic rocks formed from the melting of ancient or juvenile crust at variable depths and temperatures. Furthermore, the absence of identified ophiolites younger than the early Permian (G. C. Wang et al., 2022) and the dominance of terrestrial environments during the Triassic (Fang et al., 2019; J. L. Wang et al., 2019), suggesting that the eastern Tianshan evolved into an intracontinental or intraplate setting during this period. The mafic rocks, originating from partial melting of the lithospheric or asthenospheric mantle due to mantle upwelling, likely provided additional heat for the crustal melting (S. Y. Liu et al., 2020; Feng & Zheng, 2021; Lei et al., 2021; Y. F. Wang et al., 2022). Triassic magmatic rocks from the Beishan Belt are interpreted to have formed due to asthenosphere upwelling in a post-orogenic or intraplate setting (S. Li et al., 2012; H.

R. Sun et al., 2020; R. Q. Liu et al., 2023), in agreement with our interpretations. The temporal correlation between mafic rocks and A-type granitoids with strike-slip faults, such as the Xingxingxia Fault, suggests that transcurrent tectonics, influenced by far-field effects from the Paleo-Tethys system, played a role in the Triassic evolution of the eastern Tianshan (Y. Wang et al., 2010; X. R. Zhang et al., 2017; Lei et al., 2021).

In summary, the new structural, metamorphic, and magmatic data from this thesis with existing research results suggest that the eastern Tianshan underwent an important transition from oceanic subduction to intraplate tectonics during the late Paleozoic to early Mesozoic. This evolution involved key processes such as arc-arc accretion, slab rollback and back-arc extension, post-orogenic development, and intraplate crustal reworking.

7.3 Magmatic fingerprints for the transition of tectonic regimes

As discussed above, a combination of structural, metamorphic, magmatic, paleomagnetic, and sedimentary data from this thesis and previous studies indicates that the eastern Tianshan transitioned from oceanic subduction in the Carboniferous to a post-orogenic setting in the Permian, and then to an intraplate setting in the Triassic. From the Carboniferous to the Triassic, the magmatism in the eastern Tianshan exhibits changes in type, volume, spatial distribution, and geochemical and isotopic compositions.

Carboniferous magmatic rocks are widespread in both the East Junggar, Bogda-Harlik-Dananhu, and Kanggur-Yamansu regions, characterized by varible rock types including arc-type mafic to intermediate rocks, I-type and A-type granitoids, and adakitic rocks (Chapter 5). These rocks exhibit a wide range of SiO_2 contents and K_2O/SiO_2, K_2O/Na_2O, and Th/La ratios, with averages similar to those of the bulk continental crust (Figure 7.2). Additionally, most of them display highly positive εNd(t) and zircon εHf(t) values, consistent with significant crustal growth related to the oceanic subduction. Some rocks from the Kanggur-Yamansu region have relatively enriched isotopic compositions, suggesting the involvement of the continental basement in this area. In the East Junggar, the magmatic rocks exhibit an increasing trend in SiO_2 contents and K_2O/SiO_2, K_2O/Na_2O, and Th/La ratios since ~330 Ma, following its accretion with the eastern Tianshan. Such changes coincide with the arc maturation by the incorporation of juvenile crustal rocks after arc-arc accretion (e.g., Y. Y. Zhang et al., 2022).

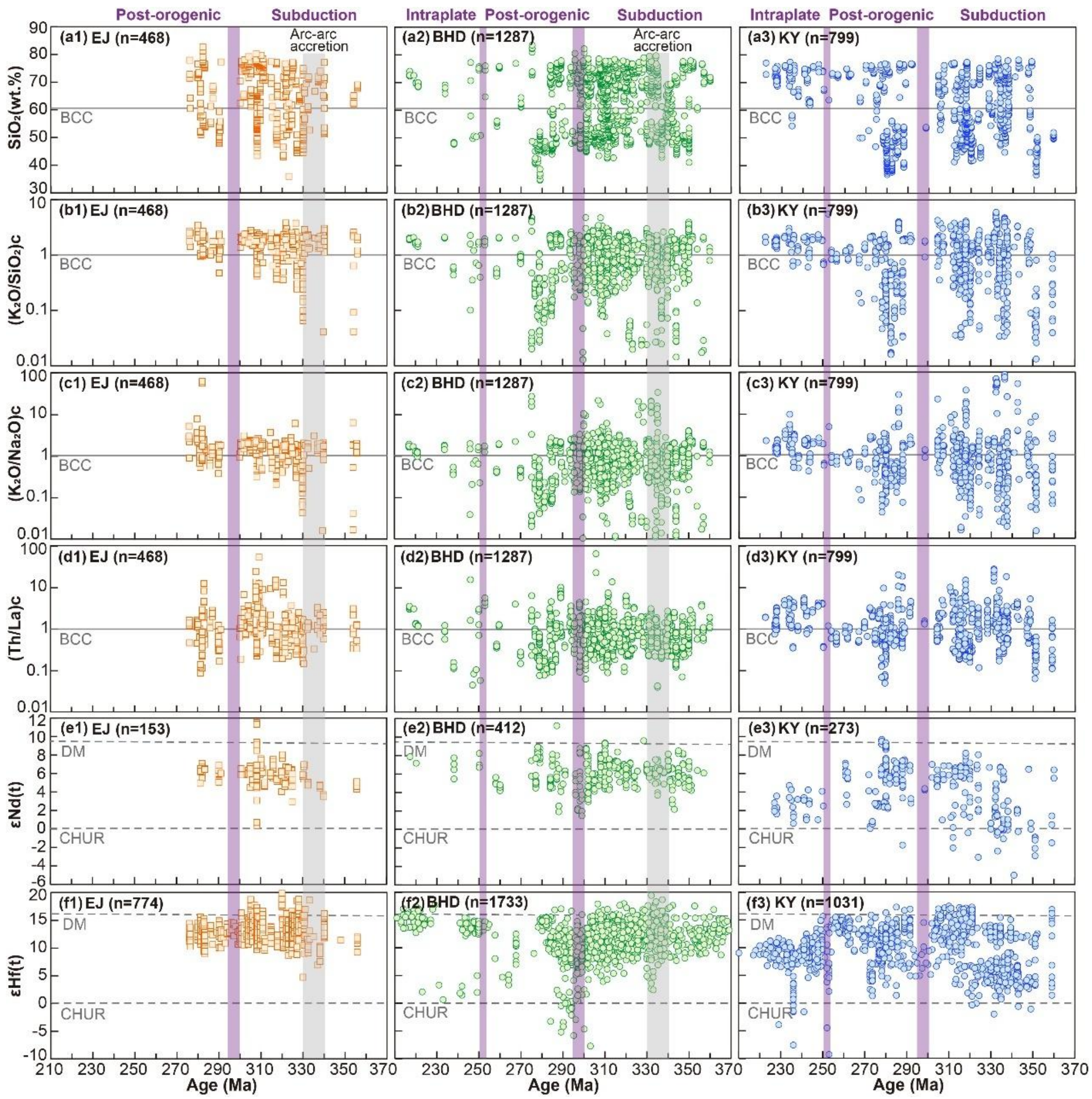

Figure 7.2. Evolving whole-rock geochemical and isotopic compositions of the magmatic rocks from the East Junggar (EJ), Bogda-Harlik-Dananhu (BHD), and Kanggur-Yamansu (KY) regions. K_2O/SiO_2, K_2O/Na_2O, and Th/La ratios are normalized by the bulk continental crust (BCC).

At the latest Caboniferous to earliest Permian (around 300 to 290 Ma), a magmatic lull can be observed in the East Junggar and Kanggur-Yamansu regions. Furthermore, the rock types in the Bogda-Harlik-Dananhu region suddenly changed with the reduction of intermediate rocks (Figure 7.2). These characteristics could be attributed to the final amalgamation and the cessation of oceanic subduction. Additionally, the incorporation of some ancient materails from the nearby continents (e.g., the Central Tianshan Block) resulted in the enriched isotopic compositions of some rocks from the Bogda-Harlik-Dananhu region.

Permian magmatic rocks in the East Junggar predominantly comprise intermediate to felsic rocks with high K_2O contents (Figure 7.2). Combined with their isotopic compositions similar to those of the Carboniferous rocks, this likely suggests that they were derived from the remelting of pre-existing arc crust (e.g., D. C. Zhu et al., 2022). In contrast, Permian magmatic rocks in the Bogda-Harlik-Dananhu and Kanggur-Yamansu regions mainly consist of mafic and felsic rocks, showing a bimodal affinity. Many mafic rocks in these regions show a correlation with the major strike-slip faults, suggesting the significant role of the transcurrent tectonics in their formation (Branquet et al., 2012). The presence of these mantle-derived rocks results in low K_2O/SiO_2, K_2O/Na_2O, and Th/La ratios (Figure 7.2). The felsic rocks mostly belong to A-type granitoids and are widespread in the eastern Tianshan, consistent with a post-orogenic setting (e.g., Han & Zhao et al., 2018).

Triassic magmatic rocks were identified in the Bogda-Harlik-Dananhu and Kanggur-Yamansu regions, but they are much more scattered than those from the Carboniferous to Permian periods (Figure 7.2). In the Bogda-Harlik-Dananhu region, Triassic magmatic rocks consist of small mafic and felsic intrusions. The mafic rocks were derived from partial melting of lithospheric or asthenospheric mantle due to mantle upwelling, while the felsic rocks have elevated K_2O and Th, with depleted Nd and zircon Hf isotopes, indicative of juvenile crust sources (cf. Chapter 6). In the Kanggur-Yamansu region, Triassic magmatic rocks are predominantly felsic.

Compared to the Permian rocks, they exhibit a significant increase in K_2O/SiO_2, K_2O/Na_2O, and Th/La ratios, as well as decerase in $\varepsilon_{Nd}(t)$ and zircon $\varepsilon_{Hf}(t)$ values (Figure 7.2), suggesting the remelting of pre-existing crustal rocks.

In summary, magmatism in the eastern Tianshan transitioned from subduction-related in the Carboniferous to bimodal in a post-orogenic setting during the Permian. In the Triassic, the magmatism weakened and was characterized by crustal remelting.

Chapter 8. Conclusions and perspectives

8.1 Conclusions

This thesis presents a multi-scale and multi-disciplinary study of the tectonic-metamorphic-magmatic evolution of the eastern Tianshan during the late Paleozoic to early Mesozoic. Integrating available results with the new data, the following main conclusions are summarized.

1. Late Paleozoic to early Mesozoic magmatic rocks in the East Junggar and the Bogda-Harlik-Dananhu region of the eastern North Tianshan mostly exhibit highly positive whole-rock εNd(t) and zircon εHf(t) values, with T_{DM2} ages ranging from 0.3 Ga to 1.0 Ga. In contrast, many magmatic rocks in the western Kanggur-Yamansu region show low to negative whole-rock εNd(t) and zircon εHf(t) values, with T_{DM2} ages older than 1.0 Ga, similar to contemporaneous magmatic rocks in the Central Tianshan Block. Therefore, the basement of the eastern North Tianshan and East Junggar regions primarily comprises Neoproterozoic to Phanerozoic juvenile crust, likely with the presence of a Mesoproterozoic continental basement similar to that of the Central Tianshan Block in the Kanggur-Yamansu area.
2. The eastern North Tianshan and East Junggar experienced compressional deformation and crustal thickening at around 340-330 Ma, which can be attributed to arc-arc accretion between these two tectonic units. From 330 to 310 Ma, extensional tectonics took place in the Bogda-Harlik region, accompanied by high temperature-low pressure (HT-LP) metamorphism, extension-related magmatism, and crustal thinning, likely indicating back-arc extension due to the rollback of the subducting Kanggur oceanic slab.
3. The final amalgamation of the eastern Tianshan occurred around 300 Ma, resulting in the crustal thickening in both the Bogda-Harlik-Dananhu and the Kanggur-Yamansu regions of the eastern North Tianshan. This was accompanied by a magmatic quiescence in the East Junggar and Kanggur-Yamansu regions, and a

sharp reduction in intermediate magmatic rocks in the Bogda-Harlik-Dananhu region.

4. Localized crustal extension occurred in the Harlik during the early Permian, resulting in the exhumation and cooling of the middle crust (i.e. the Xiaopu Metamorphic Complex). Combined with the formation of widespread bimodal magmatic rocks and A-type granitoids, it can be suggested that the eastern Tianshan and East Junggar evolved into a post-orogenic setting during the Permian. Regional transcurrent tectonics, including the Main Tianshan Shear Zone, Kanggur-Huangshan Shear Zone, and Irtysh Shear Zone, were activated in the Permian and show a spatial correlation with the magmatism, likely dominating the post-orogenic evolution of the eastern Tianshan and East Junggar.
5. Triassic magmatic rocks in the eastern Tianshan are more scattered than those of the late Paleozoic, exhibiting post-kinematic characteristics without strong deformation. The newly identified Triassic adakitic and low Sr/Y granitoids in the Bogda region were formed by the partial melting of juvenile crust at varying depths and temperatures. Integrating this with a compiled dataset, we conclude that the intraplate reworking of ancient and juvenile crust at variable conditions, along with the addition of some mantle-derived materials, is responsible for the Triassic magmatism in the eastern Tianshan.

8.2 Perspectives

Although the comprehensive investigations and insights presented in this thesis have enhanced our understanding of the tectonic evolution of the southwestern CAOB, many questions remain unresolved, and several intriguing questions have emerged.

1. This thesis indicates that the Xiaopu Metamorphic Complex, characterized by HT-LP metamorphism and migmatization, was formed by the emplacement of granitic batholiths in the middle crust. However, it is acknowledged that the relatively cold felsic intrusions could not provide sufficient heat to generate such a high thermal

gradient within several kilometers. Recently, Yamaoka et al. (2023) proposed a magma tapping and replenishment model for broad metamorphic aureoles around felsic plutons. More evidence is needed to determine whether this model can explain the formation of the Xiaopu Metamorphic Complex, or if alternative models are required.

2. At least two subduction systems, such as the Kalamaili and Kanggur oceanic subductions, played a role in shaping the Paleozoic tectonics of the eastern Tianshan. For instance, the crustal thickening in the Bogda-Harlik-Dananhu region may have resulted from both the accretion between the East Junggar and the eastern North Tianshan arcs, and the advancing subduction of the Kanggur Ocean (e.g., D. Li et al., 2020). However, whether and how these two systems interacted with each other remain unclear. Conducting numerical modeling could provide some significant insights into these issues.
3. Our statistical analysis of magmatic rocks in the eastern Tianshan and East Junggar regions provides valuable constraints on their tectonic evolution. Expanding our dataset to include the entire Tianshan and Junggar orogens, or even the broader Central Asian Orogenic Belt (CAOB), could further enhance our understanding of their tectonic evolution and the associated orogenic processes.

References

Alexeiev, D. V., Biske, Y. S., Wang, B., Djenchuraeva, A. V., Getman, O. F., Aristov, V. A., et al. (2015). Tectono-stratigraphic framework and Palaeozoic evolution of the Chinese South Tianshan. Geotectonics, 49, 93-122. https://doi.org/10.1134/S0016852115020028

Alexeiev, D. V., Biske, Y. S., Djenchuraeva, A. V., Wang, B., Kossovaya, O. L., Zhong, L. L., & Savitskiy, Y. V. (2019). Lower Moscovian limestones of the Bogdashan range (NW China) as an indicator of cessation of arc magmatism in the Junggar region. Stratigraphy and Geological Correlation, 27, 51-72.

An, R., Zhao, G., Liu, Q., & Han, Y. (2021). Early Palaeozoic subduction-accretion in East Junggar (NW China): Insights from age, geochemical, and Sr-Nd-Hf isotopic data of andesitic rocks in the northern Yemaquan Arc. Lithos, 380, 105892.

Andersen, T. (2002). Correction of common lead in U–Pb analyses that do not report 204Pb. Chemical geology, 192(1-2), 59-79. https://doi.org/10.1016/S0009-2541(02)00195-X

Ao, S., Mao, Q., Windley, B. F., Song, D., Zhang, Z., Zhang, J. E., et al. (2021). The youngest matrix of 234 Ma of the Kanggur accretionary mélange containing blocks of N-MORB basalts: constraints on the northward subduction of the Paleo-Asian Kanggur Ocean in the Eastern Tianshan of the Southern Altaids. International Journal of Earth Sciences, 110, 791-808. https://doi.org/10.1007/s00531-021-01990-5

Balé, P., & Brun, J. P. (1989). Late Precambrian thrust and wrench zones in northern Brittany (France). Journal of structural geology, 11(4), 391-405.

Beaudoin, A., Scaillet, S., Mora, N., Jolivet, L., & Augier, R. (2020). In situ and step-heating 40Ar/39Ar dating of white mica in low-temperature shear zones (Tenda massif, Alpine Corsica, France). Tectonics, 39(12), e2020TC006246. https://doi.org/10.1029/2020TC006246

Beaumont, C., Jamieson, R. A., Nguyen, M. H., & Lee, B. (2001). Himalayan tectonics explained by extrusion of a low-viscosity crustal channel coupled to focused surface denudation. Nature, 414(6865), 738-742. https://doi.org/10.1038/414738a

Belousova, E. A., Griffin, W. L., O'Reilly, S. Y., & Fisher, N. L. (2002). Igneous zircon: trace element composition as an indicator of source rock type. Contributions to mineralogy and petrology, 143, 602-622.

Belousova, E. A., Kostitsyn, Y. A., Griffin, W. L., Begg, G. C., O'reilly, S. Y., & Pearson, N. J. (2010). The growth of the continental crust: constraints from zircon Hf-isotope data. Lithos, 119(3-4), 457-466.

Bian, W., Hornung, J., Liu, Z., Wang, P., & Hinderer, M. (2010). Sedimentary and palaeoenvironmental evolution of the Junggar Basin, Xinjiang, northwest China. Palaeobiodiversity and Palaeoenvironments, 90, 175-186. https://doi.org/10.1007/s12549-010-0038-9

Biske, Y. S., Alexeiev, D. V., Ershova, V. B., Priyatkina, N. S., DuFrane, S. A., & Khudoley, A. K. (2019). Detrital zircon UPb geochronology of middle Paleozoic sandstones from the South Tianshan (Kyrgyzstan): Implications for provenance and tectonic evolution of the Turkestan Ocean. Gondwana Research, 75, 97-117. https://doi.org/10.1016/j.gr.2019.04.010

Biske, Y. S., & Seltmann, R. (2010). Paleozoic Tian-Shan as a transitional region between the Rheic and Urals-Turkestan oceans. Gondwana Research, 17(2-3), 602-613. https://doi.org/10.1016/j.gr.2009.11.014

Black, L. P., & Gulson, B.L. (1978). The age of the mud tank carbonatite, strangways range, northern territory. BMR Journal of Australian Geology and Geophysics, 3, 227-232.

Blichert-Toft, J., & Albarède, F. (1997). The Lu-Hf isotope geochemistry of chondrites and the evolution of the mantle-crust system. Earth and Planetary Science Letters, 148(1-2), 243-258. https://doi.org/10.1016/S0012-821X(97)00040-X

Bo, H. Z., Zhang, Z., Santosh, M., Cheng, Z., Xie, Q., Kong, W., ... & Li, B. (2021). Petrogenesis of an Early Permian bimodal intermediate-felsic suite in the East Junggar in Central Asian Orogenic Belt and tectonic implications. Geological Journal, 56(1), 547-571.

Branquet, Y., Gumiaux, C., Sizaret, S., Barbanson, L., Wang, B., Cluzel, D., et al. (2012). Synkinematic mafic/ultramafic sheeted intrusions: emplacement mechanism and strain restoration of the Permian Huangshan Ni-Cu ore belt (Eastern Tianshan, NW China). Journal of Asian Earth Sciences, 56, 240-257. https://doi.org/10.1016/j.jseaes.2012.05.021

Buick, I. S., Clark, C., Rubatto, D., Hermann, J., Pandit, M., & Hand, M. (2010). Constraints on the Proterozoic evolution of the Aravalli–Delhi Orogenic belt (NW India) from monazite geochronology and mineral trace element geochemistry.

Lithos, 120(3-4), 511-528. https://doi.org/10.1016/J.LITHOS.2010.09.011

Burg, J. P., Matte, P., Leyreloup, A., & Marchand, J. (1984). Inverted metamorphic zonation and large-scale thrusting in the Variscan Belt: an example in the French Massif Central. Geological Society, London, Special Publications, 14(1), 47-61. https://doi.org/10.1144/GSL.SP.1984.014.01.05

Carroll, A. R., Yunhai, L., Graham, S. A., Xuchang, X., Hendrix, M. S., Jinchi, C., & McKnight, C. L. (1990). Junggar basin, northwest China: trapped Late Paleozoic ocean. Tectonophysics, 181(1-4), 1-14.

Castillo, P. R., Janney, P. E., & Solidum, R. U. (1999). Petrology and geochemistry of Camiguin Island, southern Philippines: insights to the source of adakites and other lavas in a complex arc setting. Contributions to mineralogy and petrology, 134(1), 33-51. https://doi.org/10.1007/s004100050467

Cawood, P. A., Kröner, A., Collins, W. J., Kusky, T. M., Mooney, W. D., & Windley, B. F. (2009). Accretionary orogens through Earth history. Geological Society, London, Special Publications, 318(1), 1-36. https://doi.org/10.1144/SP318.1

Cesare, B., Ferrero, S., Salvioli-Mariani, E., Pedron, D., & Cavallo, A. (2009). "Nanogranite" and glassy inclusions: The anatectic melt in migmatites and granulites. Geology, 37(7), 627-630. https://doi.org/10.1130/G25759A.1

Chai, F. M., Zhang, Z., Li, W., Santosh, M., Wang, H., Wang, W., & Xu, Q. (2019). The early Paleozoic Huangtupo VMS Cu-Zn deposit in Kalatag, Eastern Tianshan: Implications from geochemistry and zircon U-Pb geochronology of volcanic host rocks. Lithos, 342, 97-113.

Chamberlain, K. R., & Bowring, S. A. (2001). Apatite-feldspar U-Pb thermochronometer: a reliable, mid-range (~ 450° C), diffusion-controlled system. Chemical Geology, 172(1-2), 173-200. https://doi.org/10.1016/S0009-2541(00)00242-4

Chapman, J. B., Ducea, M. N., DeCelles, P. G., & Profeta, L. (2015). Tracking changes in crustal thickness during orogenic evolution with Sr/Y: An example from the North American Cordillera. Geology, 43(10), 919-922.

Chapman, J. B., Ducea, M. N., Kapp, P., Gehrels, G. E., & DeCelles, P. G. (2017). Spatial and temporal radiogenic isotopic trends of magmatism in Cordilleran orogens. Gondwana Research, 48, 189-204.

Chappell, B. W. (1999). Aluminium saturation in I-and S-type granites and the characterization of fractionated haplogranites. Lithos, 46(3), 535-551. https://doi.org/10.1016/S0024-4937(98)00086-3

Chappell, B. W., & White, A. J. (2001). Two contrasting granite types: 25 years later. Australian journal of earth sciences, 48(4), 489-499. https://doi.org/10.1046/j.1440-0952.2001.00882.x

Chardon, D., Gapais, D., & Cagnard, F. (2009). Flow of ultra-hot orogens: a view from the Precambrian, clues for the Phanerozoic. Tectonophysics, 477(3-4), 105-118.

Charlton, T. R. (1991). Postcollision extension in arc-continent collision zones, eastern Indonesia. Geology, 19(1), 28-31.

Charvet, J., Shu, L. S., & Laurent-Charvet, S. (2007). Paleozoic structural and geodynamic evolution of eastern Tianshan (NW China): welding of the Tarim and Junggar plates. Episodes Journal of International Geoscience, 30(3), 162-186.

Charvet, J., Shu, L., Laurent-Charvet, S., Wang, B., Faure, M., Cluzel, D., et al. (2011). Palaeozoic tectonic evolution of the Tianshan belt, NW China. Science China Earth Sciences, 54, 166-184. https://doi.org/10.1007/s11430-010-4138-1

Chen, C., Lü, X., Wu, C., Jiang, X., & Mao, C. (2018). Origin and geodynamic implications of concealed granite in Shadong tungsten deposit, Xinjiang, China: Zircon U-Pb chronology, geochemistry, and Sr-Nd-Hf isotope constraint. Journal of Earth Science, 29, 114-129. https://doi.org/10.1007/s12583-017-0808-7

Chen, J. F., Han, B. F., Ji, J. Q., Zhang, L., Xu, Z., He, G. Q., & Wang, T. (2010). Zircon U–Pb ages and tectonic implications of Paleozoic plutons in northern West Junggar, North Xinjiang, China. Lithos, 115(1-4), 137-152. https://doi.org/10.1016/j.lithos.2009.11.014

Chen, X. J. & Shu, L. S. (2010). Features of the post-collisional tectono-magmatism and geochronological evidence in the Karlik Mt., Xinjiang. Acta Petrol. Sin. 26, 3057-3064 (in Chinese with English bstract).

Chen, X. J., Shu, L. S., & Santosh, M. (2011). Late Paleozoic post-collisional magmatism in the Eastern Tianshan Belt, Northwest China: new insights from geochemistry, geochronology and petrology of bimodal volcanic rocks. Lithos, 127(3-4), 581-598. https://doi.org/10.1016/j.lithos.2011.06.008

Chen, X. J, Shu, L. S., Santosh, M., & Zhao, X. (2013). Island arc-type bimodal magmatism in the eastern Tianshan Belt, Northwest China: geochemistry, zircon U–Pb geochronology and implications for the Paleozoic crustal evolution in Central

Asia. Lithos, 168, 48-66. https://doi.org/10.1016/j.lithos.2012.10.006
Chen, X. J., Shu, L. S., Santosh, M., & Xu, Z. (2014). The provenance and tectonic affinity of the Paleozoic meta-sedimentary rocks in the Chinese Tianshan belt: New insights from detrital zircon U–Pb geochronology and Hf–isotope analysis. Journal of Asian Earth Sciences, 94, 12-27. https://doi.org/10.1016/j.jseaes.2014.07.024
Chen, Z. Y., Xiao, W. J., Windley, B. F., Schulmann, K., Mao, Q. G., Zhang, Z., et al. (2019). Composition, provenance, and tectonic setting of the southern Kangurtag accretionary complex in the Eastern Tianshan, NW China: Implications for the late Paleozoic evolution of the North Tianshan Ocean. Tectonics, 38(8), 2779-2802. https://doi.org/10.1029/2018TC005385
Cheng, X. H., Yu, L., Ling, M., Geng, X., Yang, F., Zhang, Z., ... & Yun, L. (2023). Geochronological, mineralogical and geochemical studies of sulfide mineralization in the Yueyawan mafic intrusion in the East Tianshan orogenic Belt, NW China. Ore Geology Reviews, 152, 105257.
Chew, D. M., Petrus, J. A., & Kamber, B. S. (2014). U-Pb LA-ICPMS dating using accessory mineral standards with variable common Pb. Chemical Geology, 363, 185-199. https://doi.org/10.1016/j.chemgeo.2013.11.006
Chew, D. M., & Spikings, R. A. (2015). Geochronology and thermochronology using apatite: time and temperature, lower crust to surface. Elements, 11(3), 189-194. https://doi.org/10.2113/gselements.11.3.189
Choulet, F., Faure, M., Cluzel, D., Chen, Y., Lin, W., Wang, B., & Jahn, B. M. (2012). Architecture and evolution of accretionary orogens in the Altaids collage: The early Paleozoic West Junggar (NW China). American Journal of Science, 312(10), 1098-1145. https://doi.org/10.2475/10.2012.02
Chung, S. L., Liu, D., Ji, J., Chu, M. F., Lee, H. Y., Wen, D. J., ... & Zhang, Q. (2003). Adakites from continental collision zones: melting of thickened lower crust beneath southern Tibet. Geology, 31(11), 1021-1024. https://doi.org/10.1130/G19796.1
Coggon, R., & Holland, T. J. B. (2002). Mixing properties of phengitic micas and revised garnet-phengite thermobarometers. Journal of Metamorphic Geology, 20(7), 683-696. https://doi.org/10.1046/j.1525-1314.2002.00395.x
Collins, W. J. (2002). Hot orogens, tectonic switching, and creation of continental crust. Geology, 30(6), 535-538. https://doi.org/10.1130/0091-7613(2002)030%3C0535:HOTSAC%3E2.0.CO;2

Collins, W. J., Huang, H. Q., & Jiang, X. (2016). Water-fluxed crustal melting produces Cordilleran batholiths. Geology, 44(2), 143-146.

Connelly, J. N. (2001). Degree of preservation of igneous zonation in zircon as a signpost for concordancy in U/Pb geochronology. Chemical Geology, 172(1-2), 25-39.

Connolly, J. A. (2005). Computation of phase equilibria by linear programming: a tool for geodynamic modeling and its application to subduction zone decarbonation. Earth and Planetary Science Letters, 236(1-2), 524-541. https://doi.org/10.1016/j.epsl.2005.04.033

Connolly, J. A. D. (2009). The geodynamic equation of state: what and how. Geochemistry, geophysics, geosystems, 10(10), Q10014. https://doi.org/10.1029/2009GC002540

Corfu, F., Hanchar, J. M., Hoskin, P. W., & Kinny, P. (2003). Atlas of zircon textures. Reviews in mineralogy and geochemistry, 53(1), 469-500.

Cui, F. L., Xu, X. Y., Ma, Z. P., Wang, X. W., Zhu, X. H., & Sun, J. M. (2015). Confirmation of the late Devonian volcanic rocks from the northern Tuha basin in east Tianshan and its petrogenetic and tectonic significance. Acta Geologica Sinica, 89(8), 1402-1416 (in Chinese with English abstract).

Dai, J. F., Xue, C., Chi, G., Gao, R., Ming, H., Zhao, X., & Zhao, Y. (2020). Genesis of the Aqishan skarn Zn-Pb deposit in the Eastern Tianshan, NW China: Constraints from geology, geochronology and Hf-S-Pb isotopic geochemistry. Ore Geology Reviews, 123, 103608.

Defant, M.J., & Drummond, M.S. (1990). Derivation of some modern arc magmas by melting of young subducted lithosphere. Nature, 347, 662-665. https://doi.org/10.1038/347662a0

Deng, X. H., Chen, Y. J., Santosh, M., Wang, J. B., Li, C., Yue, S. W., et al. (2017). U–Pb zircon, Re–Os molybdenite geochronology and Rb–Sr geochemistry from the Xiaobaishitou W (–Mo) deposit: implications for Triassic tectonic setting in eastern Tianshan, NW China. Ore Geology Reviews, 80, 332-351. https://doi.org/10.1016/j.oregeorev.2016.05.013

Deng, X. H., Wang, J. B., Santosh, M., Li, Y. C., Wang, Y. W., Mao, Q. G., ... & Chen, X. (2018). New 40Ar/39Ar ages from the Kalatag district in the Eastern Tianshan, NW China: Constraints on the timing of Cu mineralization and stratigraphy. Ore

Geology Reviews, 100, 250-262.
Deng, Y. F., Yuan, F., Hollings, P., Song, X. Y., Zhou, T., Fu, B., et al. (2020). Magma generation and sulfide saturation of Permian mafic-ultramafic intrusions from the western part of the Northern Tianshan in NW China: implications for Ni-Cu mineralization. Mineralium Deposita, 55, 515-534. https://doi.org/10.1007/s00126-019-00890-8
Dhuime, B., Hawkesworth, C. J., Cawood, P. A., & Storey, C. D. (2012). A change in the geodynamics of continental growth 3 billion years ago. Science, 335(6074), 1334-1336. https://doi.org/10.1126/science.1216066
Ding, H., Kohn, M. J., & Zhang, Z. (2021). Long-lived (ca. 22-24 Myr) partial melts in the eastern Himalaya: Petrochronologic constraints and tectonic implications. Earth and Planetary Science Letters, 558, 116764. https://doi.org/10.1016/j.epsl.2021.116764
Dong, Y. P., Zhou, D., Zhang, G. W., Zhang, C. L., Xia, L. Q., Xu, X. Y., & Li, X. M. (2005). Tectonic setting of the Wuwamen ophiolite at the southern margin of Middle Tianshan belt. Acta Petrologica Sinica, 21(1), 37-44 (in Chinese with English abstract).
Dong, Y. P., Zhang, G., Neubauer, F., Liu, X., Hauzenberger, C., Zhou, D., & Li, W. (2011). Syn-and post-collisional granitoids in the Central Tianshan orogen: geochemistry, geochronology and implications for tectonic evolution. Gondwana Research, 20(2-3), 568-581. https://doi.org/10.1016/j.gr.2011.01.013
Du, L., Long, X., Yuan, C., Zhang, Y., Huang, Z., Sun, M., Zhao, G., & Xiao, W. (2018a). Early Paleozoic dioritic and granitic plutons in the Eastern Tianshan Orogenic Belt, NW China: Constraints on the initiation of a magmatic arc in the southern Central Asian Orogenic Belt. Journal of Asian Earth Sciences, 153, 139-153. https://doi.org/10.1016/j.jseaes.2017.03.026
Du, L., Long, X., Yuan, C., Zhang, Y., Huang, Z., Wang, X., & Yang, Y. (2018b). Mantle contribution and tectonic transition in the Aqishan-Yamansu Belt, Eastern Tianshan, NW China: Insights from geochronology and geochemistry of Early Carboniferous to Early Permian felsic intrusions. Lithos, 304, 230-244.
Du, L., Long, X., Yuan, C., Zhang, Y., Huang, Z., & Zhu, H. (2024). Tracing the subduction and accretion history of the trench-arc-basin system in the Chinese Eastern Tianshan: Insights from Paleozoic magmatic and crustal evolution. Earth-

Science Reviews, 104761. https://doi.org/10.1016/j.earscirev.2024.104761
Du, L., Zhang, Y., Huang, Z., Li, X. P., Yuan, C., Wu, B., & Long, X. (2019). Devonian to carboniferous tectonic evolution of the Kanggur Ocean in the Eastern Tianshan, NW China: Insights from three episodes of granitoids. Lithos, 350, 105243.
Ducea, M. N., Saleeby, J. B., & Bergantz, G. (2015). The architecture, chemistry, and evolution of continental magmatic arcs. Annual Review of Earth and Planetary Sciences, 43(1), 299-331. https://doi.org/10.1146/annurev-earth-060614-105049
Eby, G. N. (1992). Chemical subdivision of the A-type granitoids: petrogenetic and tectonic implications. Geology, 20(7), 641-644.
Fang, Y., Wu, C., Wang, Y., Hou, K., & Guo, Z. (2019). Topographic evolution of the Tianshan Mountains and their relation to the Junggar and Turpan Basins, Central Asia, from the Permian to the Neogene. Gondwana Research, 75, 47-67.
Feng, W., & Zheng, J. (2021). Triassic magmatism and tectonic setting of the eastern Tianshan, NW China: Constraints from the Weiya intrusive complex. Lithos, 394, 106171. https://doi.org/10.1016/j.lithos.2021.106171
Feng, Y., Coleman, R. G., Tilton, G., & Xiao, X. (1989). Tectonic evolution of the west Junggar region, Xinjiang, China. Tectonics, 8(4), 729-752. https://doi.org/10.1029/TC008i004p00729
Foster, G., Gibson, H. D., Parrish, R., Horstwood, M., Fraser, J., & Tindle, A. (2002). Textural, chemical and isotopic insights into the nature and behaviour of metamorphic monazite. Chemical Geology, 191(1-3), 183-207. https://doi.org/10.1016/S0009-2541(02)00156-0
Fuhrman, M. L., & Lindsley, D. H. (1988). Ternary-feldspar modeling and thermometry. American mineralogist, 73(3-4), 201-215.
Gao, J., Jiang, T., Wang, X. S., Li, J. L., Zhai, Q. G., Hu, P. Y., & Qian, Q. (2022). The Junggar, Tianshan and Beishan ophiolites: Constraint on the evolution of oceanic and continental framework along the southwestern margin of the Central-Asian Orogenic Belt. Chinese Journal of Geology, 57(1), 1-42 (in Chinese with English abstract).
Gao, J., & Klemd, R. (2003). Formation of HP–LT rocks and their tectonic implications in the western Tianshan Orogen, NW China: geochemical and age constraints. Lithos, 66(1-2), 1-22. https://doi.org/10.1016/S0024-4937(02)00153-6
Gao, J., Li, M. S., Xiao, X. C., Tang, Y. Q., & He, G. Q., (1998). Paleozoic tectonic

evolution of the Tianshan Orogen, northwestern China. Tectonophysics, 287(1-4), 213-231. https://doi.org/10.1016/S0040-1951(98)80070-X

Gao, J., Long, L., Klemd, R., Qian, Q., Liu, D., Xiong, X., et al. (2009). Tectonic evolution of the South Tianshan orogen and adjacent regions, NW China: geochemical and age constraints of granitoid rocks. International Journal of Earth Sciences, 98, 1221-1238. https://doi.org/10.1007/s00531-008-0370-8

Gao, R. Z., Xue, C., Chi, G., Dai, J., Dong, C., Zhao, X., & Man, R. (2020). Genesis of the giant Caixiashan Zn-Pb deposit in Eastern Tianshan, NW China: Constraints from geology, geochronology and S-Pb isotopic geochemistry. Ore Geology Reviews, 119, 103366.

Gao, Z. W., Lu, C. L., & Deng, M. G. (2021). Geochemical features and tectonic setting of the Mesozoic intrusions in eastern Tianshan. Earth Science, 46(7), 2287-2298 (in Chinese with English abstract).

Geng, H. Y., Sun, M., Yuan, C., Xiao, W., Xian, W., Zhao, G., ... & Wu, F. (2009). Geochemical, Sr–Nd and zircon U–Pb–Hf isotopic studies of Late Carboniferous magmatism in the West Junggar, Xinjiang: implications for ridge subduction?. Chemical Geology, 266(3-4), 364-389. https://doi.org/10.1016/j.chemgeo.2009.07.001

Gibson, H. D., Brown, R. L., & Parrish, R. R. (1999). Deformation-induced inverted metamorphic field gradients: an example from the southeastern Canadian Cordillera. Journal of Structural Geology, 21(7), 751-767. https://doi.org/10.1016/S0191-8141(99)00051-6

Göğüş, O. H., Pysklywec, R. N., & Faccenna, C. (2016). Postcollisional lithospheric evolution of the Southeast Carpathians: Comparison of geodynamical models and observations. Tectonics, 35(5), 1205-1224.

Gómez-Frutos, D., Castro, A., & Gutiérrez-Alonso, G. (2023). Post-collisional batholiths do contribute to continental growth. Earth and Planetary Science Letters, 603, 117978.

Gong, L., Chen, H., Wang, Q., Xiao, B., Zhang, S., & Tang, G. (2023). Multiple tectonic switches in the Eastern Tianshan, Central Asian Orogenic Belt: Implications for crustal growth and metallogenesis. Lithos, 107235. https://doi.org/10.1016/j.lithos.2023.107235

Graham, C. M., & England, P. C. (1976). Thermal regimes and regional metamorphism in the vicinity of overthrust faults: an example of shear heating and inverted metamorphic zonation from southern California. Earth and Planetary Science Letters, 31(1), 142-152. https://doi.org/10.1016/0012-821X(76)90105-9

Griffin, W. L., Wang, X., Jackson, S. E., Pearson, N. J., O'Reilly, S. Y., Xu, X., & Zhou, X. (2002). Zircon chemistry and magma mixing, SE China: in-situ analysis of Hf isotopes, Tonglu and Pingtan igneous complexes. Lithos, 61(3-4), 237-269. https://doi.org/10.1016/S0024-4937(02)00082-8

Grujic, D., Casey, M., Davidson, C., Hollister, L. S., Kündig, R., Pavlis, T., & Schmid, S. (1996). Ductile extrusion of the Higher Himalayan Crystalline in Bhutan: evidence from quartz microfabrics. Tectonophysics, 260(1-3), 21-43. https://doi.org/10.1016/0040-1951(96)00074-1

Gu, L. X., Hu, S. X., Chu, Q., Yu, C. S., & Xiao, X. J. (1999). Pre-collision granites and post-collision intrusive assemblage of the Kelameili-Harlik Orogenic Belt. Acta Petrologica Sinica-English Edition 73 (3), 316-329. https://doi.org/10.1111/j.1755-6724.1999.tb00840.x

Gu, L. X., Hu, S. X., Yu, C. S., Wu, C. Z., & Yan, Z. F. (2001). Initiation and evolution of the Bogda subduction-torn-type rift. Acta Petrologica Sinica, 17(4), 585-597 (in Chinese with English abstract).

Han, B. F., Ji, J. Q., Zhang, L., Song, B., & Chen, L. H. (2006). Late Paleozoic vertical growth of continental crust around the Junggar Basin, Xinjiang, China (Part I): timing of post-collisional plutonism. Acta Petrologica Sinica, 22(5), 1077-1086.

Han, B. F., He, G. Q., Wang, X. C., & Guo, Z. J. (2011). Late Carboniferous collision between the Tarim and Kazakhstan–Yili terranes in the western segment of the South Tian Shan Orogen, Central Asia, and implications for the Northern Xinjiang, western China. Earth-Science Reviews, 109(3-4), 74-93. https://doi.org/10.1016/j.earscirev.2011.09.001

Han, C. M., Xiao, W., Zhao, G., Mao, J., Yang, J., Wang, Z., ... & Mao, Q. (2006). Geological characteristics and genesis of the Tuwu porphyry copper deposit, Hami, Xinjiang, Central Asia. Ore Geology Reviews, 29(1), 77-94.

Han, C., Xiao, W., Zhao, G., Ao, S., Zhang, J., Qu, W., & Du, A. (2010). In-situ U–Pb, Hf and Re–Os isotopic analyses of the Xiangshan Ni–Cu–Co deposit in Eastern Tianshan (Xinjiang), Central Asia Orogenic Belt: constraints on the timing and genesis of the mineralization. Lithos, 120(3-4), 547-562.

Han, J. S., Chen, H., Jiang, H., Zhao, L., Zhang, W., & Lai, C. K. (2019). Genesis of the Paleozoic Aqishan-Yamansu arc-basin system and Fe (-Cu) mineralization in the Eastern Tianshan, NW China. Ore Geology Reviews, 105, 55-70.

Han, S., de Jong, K., & Yi, K. (2017). Detrital zircon ages in Korean mid-Paleozoic meta-sandstones (Imjingang Belt and Taean Formation): Constraints on tectonic and depositional setting, source regions and possible affinity with Chinese terranes. Journal of Asian Earth Sciences, 143, 191-217.

Han, S. J., Sang, S., Liang, J., Wang, W., Zhang, G., & Wang, S. (2019). Characteristics and genesis of diachronous Carboniferous volcano-sedimentary sequences: insights from geochemistry, petrology and U–Pb dating in the North Junggar basin, China. International Geology Review, 61(4), 404-423. https://doi.org/10.1080/00206814.2018.1428830

Han, Y. G, & Zhao, G. C. (2018). Final amalgamation of the Tianshan and Junggar orogenic collage in the southwestern Central Asian Orogenic Belt: Constraints on the closure of the Paleo-Asian Ocean. Earth-Science Reviews, 186, 129-152. https://doi.org/10.1016/j.earscirev.2017.09.012

Han, Y. G., Zhao, G., Cawood, P. A., Sun, M., Liu, Q., & Yao, J. (2019). Plume-modified collision orogeny: The Tarim–western Tianshan example in Central Asia. Geology, 47(10), 1001-1005.

Hanchar, J. M., & Watson, E. B. (2003). Zircon saturation thermometry. Reviews in mineralogy and geochemistry, 53(1), 89-112.

Harrison, T. M., Duncan, I. A. N., & Mcdougall, I. A. N. (1985). Diffusion of 40Ar in biotite: temperature, pressure and compositional effects. Geochimica et Cosmochimica Acta, 49(11), 2461-2468. https://doi.org/10.1016/0016-7037(85)90246-7

Harrison, T. M., Célérier, J., Aikman, A. B., Hermann, J., & Heizler, M. T. (2009). Diffusion of 40Ar in muscovite. Geochimica et Cosmochimica Acta, 73(4), 1039-1051. https://doi.org/10.1016/j.gca.2008.09.038

Hawkesworth, C. J., & Kemp, A. I. S. (2006). Evolution of the continental crust. Nature, 443(7113), 811-817.

Hawkesworth, C. J., Dhuime, B., Pietranik, A. B., Cawood, P. A., Kemp, A. I., & Storey, C. D. (2010). The generation and evolution of the continental crust. Journal of the Geological Society, 167(2), 229-248. https://doi.org/10.1144/0016-76492009-072

Hay, D. C., & Dempster, T. J. (2009). Zircon alteration, formation and preservation in sandstones. Sedimentology, 56(7), 2175-2191.

He, D. F., Li, D., Fan, C., & Yang, X. F. (2013). Geochronology, geochemistry and tectonostratigraphy of Carboniferous strata of the deepest Well Moshen-1 in the Junggar Basin, northwest China: Insights into the continental growth of Central Asia. Gondwana Research, 24(2), 560-577. https://doi.org/10.1016/j.gr.2012.10.015

He, X. H., Deng, X. H., Bagas, L., Zhang, J., Chen, S. B., Wu, L. N., ... & Shen, Y. (2021). The Silurian to devonian magmatic evolution of the Eastern Tianshan Terrane: New insights from geochemistry, geochronology, and Sr–Nd–Hf isotopes of new-discovered Sidingheishan porphyry Cu–Mo deposit, NW China. Ore Geology Reviews, 135, 104228.

Hegner, E., Klemd, R., Kröner, A., Corsini, M., Alexeiev, D. V., Iaccheri, L. M., ... & Windley, B. F. (2010). Mineral ages and PT conditions of Late Paleozoic high-pressure eclogite and provenance of mélange sediments from Atbashi in the south Tianshan orogen of Kyrgyzstan. American Journal of Science, 310(9), 916. https://doi.org/10.2475/09.2010.07.

Henry, D. J., Guidotti, C. V., & Thomson, J. A. (2005). The Ti-saturation surface for low-to-medium pressure metapelitic biotites: Implications for geothermometry and Ti-substitution mechanisms. American mineralogist, 90(2-3), 316-328. https://doi.org/10.2138/am.2005.1498

He, P. L., Huang, X. L., Yang, F., & Wang, X. (2020). Mineralogy constraints on magmatic processes controlling adakitic features of Early Permian high-magnesium diorites in the Western Tianshan orogenic belt. Journal of Petrology, 61(11-12), egaa114. https://doi.org/10.1093/petrology/egaa114

He, Z. Y., Zhang, Z. M., Zong, K. Q., Xiang, H., Chen, X. J., & Xia, M. J. (2014). Zircon U-Pb and Hf isotopic studies of the Xingxingxia Complex from Eastern Tianshan (NW China): significance to the reconstruction and tectonics of the southern Central Asian Orogenic Belt. Lithos, 190, 485-499. https://doi.org/10.1016/j.lithos.2013.12.023

He, Z. Y., Klemd, R., Zhang, Z. M., Zong, K. Q., Sun, L. X., Tian, Z. L., & Huang, B. T. (2015). Mesoproterozoic continental arc magmatism and crustal growth in the eastern Central Tianshan Arc Terrane of the southern Central Asian Orogenic Belt: geochronological and geochemical evidence. Lithos, 236, 74-89.

https://doi.org/10.1016/j.lithos.2015.08.009

He, Z. Y., Klemd, R., Lu, T. Y., Yan, L. L., & Xiang, H. (2024). Petrogenesis of the early Permian Hongliujing granite complex in the Chinese Eastern Tianshan orogen: Evidence for crustal growth in the Central Tianshan microcontinent. Bulletin, 136(7-8), 2845-2860. https://doi.org/10.1130/B36970.1

He, Z. Y., Wang, B., Ni, X., De Grave, J., Scaillet, S., Chen, Y., ... & Zhu, X. (2021). Structural and kinematic evolution of strike-slip shear zones around and in the Central Tianshan: Insights for eastward tectonic wedging in the southwest Central Asian Orogenic Belt. Journal of Structural Geology, 144, 104279. https://doi.org/10.1016/j.jsg.2021.104279

He, Z. Y., Wang, B., Glorie, S., Su, W. B., Ni, X. H., Jepson, G., et al. (2022). Mesozoic building of the Eastern Tianshan and East Junggar (NW China) revealed by low-temperature thermochronology. Gondwana Research, 103, 37-53. https://doi.org/10.1016/j.gr.2021.11.013

Holdaway, M. J. (2000). Application of new experimental and garnet Margules data to the garnet-biotite geothermometer. American mineralogist, 85(7-8), 881-892. https://doi.org/10.2138/am-2000-0701

Holland, T. J. B., & Powell, R. T. J. B. (1998). An internally consistent thermodynamic data set for phases of petrological interest. Journal of metamorphic Geology, 16(3), 309-343. https://doi.org/10.1111/j.1525-1314.1998.00140.x

Holland, T. J. B., & Powell, R. (2001). Calculation of phase relations involving haplogranitic melts using an internally consistent thermodynamic dataset. Journal of Petrology, 42(4), 673–683. https://doi.org/10.1093/petrology/42.4.673

Hopkins, M., Harrison, T. M., & Manning, C. E. (2008). Low heat flow inferred from > 4 Gyr zircons suggests Hadean plate boundary interactions. Nature, 456(7221), 493-496. https://doi.org/10.1038/nature07465

Hoskin, P. W., & Schaltegger, U. (2003). The composition of zircon and igneous and metamorphic petrogenesis. Reviews in mineralogy and geochemistry, 53(1), 27-62.

Hoskin, P. W. (2005). Trace-element composition of hydrothermal zircon and the alteration of Hadean zircon from the Jack Hills, Australia. Geochimica et cosmochimica acta, 69(3), 637-648.

Hou, Z. Q., Gao, Y. F., Qu, X. M., Rui, Z. Y., & Mo, X. X. (2004). Origin of adakitic intrusives generated during mid-Miocene east–west extension in southern Tibet.

Earth and Planetary Science Letters, 220(1-2), 139-155. https://doi.org/10.1016/S0012-821X(04)00007-X

Hu, A., Jahn, B. M., Zhang, G., Chen, Y., & Zhang, Q. (2000). Crustal evolution and Phanerozoic crustal growth in northern Xinjiang: Nd isotopic evidence. Part I. Isotopic characterization of basement rocks. Tectonophysics, 328(1-2), 15-51. https://doi.org/10.1016/S0040-1951(00)00176-1

Hu, W. W., Li, P. F., Yuan, C., Sun, M., Jiang, Y. D., Cai, K. D., & Zhang, C. (2023). Structural and Geochronological Constraints on the Collision Between the Chinese Altai and the West Junggar in Central Asia: Implication for Deformation Response and Geodynamic Evolution of Arc-Arc Collision in 4D. Tectonics, 42(9), e2023TC007770. https://doi.org/10.1029/2023TC007770

Huang, B., Fu, D., Kusky, T., Ruan, K., Zhou, W., & Zhang, X. (2018). Sedimentary provenance in response to Carboniferous arc-basin evolution of East Junggar and North Tianshan belts in the southwestern Central Asian Orogenic Belt. Tectonophysics, 722, 324-341. https://doi.org/10.1016/j.tecto.2017.11.015

Huang, G., Niu, G. Z., Wang, X. L., Guo, J., & Yu, F. (2012). Formation and emplacement age of Karamaili ophiolite: LA-ICP-MS zircon U-Pb age evidence from the diabase and tuff in eastern Junggar, Xinjiang. Geological Bulletin of China, 31(8), 1267-1278 (in Chinese with English abstract).

Huang, H., Wang, T., Tong, Y., Qin, Q., Ma, X., & Yin, J. (2020). Rejuvenation of ancient micro-continents during accretionary orogenesis: Insights from the Yili Block and adjacent regions of the SW Central Asian Orogenic Belt. Earth-Science Reviews, 208, 103255. https://doi.org/10.1016/j.earscirev.2020.103255

Huang, H., Wang, T., Guo, L., Tong, Y., He, Z. Y., Yin, J., & Wu, H. H. (2024). Crustal modification influenced by multiple convergent systems: Insights from Mesozoic magmatism in northeastern China. Earth-Science Reviews, 104737.

Huang, Z. Y., Long, X., Yuan, C., Sun, M., Wang, Y., Zhang, Y., & Chen, B. (2016). Detrital zircons from Neoproterozoic sedimentary rocks in the Yili Block: Constraints on the affinity of microcontinents in the southern Central Asian Orogenic Belt. Gondwana Research, 37, 39-52. https://doi.org/10.1016/j.gr.2016.05.009

Huang, Z. Y., Long, X., Wang, X. C., Zhang, Y., Du, L., Yuan, C., & Xiao, W. (2017). Precambrian evolution of the Chinese Central Tianshan Block: Constraints on its tectonic affinity to the Tarim Craton and responses to supercontinental cycles. Precambrian Research, 295, 24-37.

Huang, Z. Y., Yuan, C., Long, X. P., Zhang, Y. Y., & Du, L. (2019). From breakup of Nuna to assembly of Rodinia: a link between the Chinese Central Tianshan Block and Fennoscandia. Tectonics, 38(12), 4378-4398. https://doi.org/10.1029/2018TC005471

Jackson, S. E., Pearson, N. J., Griffin, W. L., & Belousova, E. A. (2004). The application of laser ablation-inductively coupled plasma-mass spectrometry to in situ U–Pb zircon geochronology. Chemical geology, 211(1-2), 47-69. https://doi.org/10.1016/j.chemgeo.2004.06.017

Jahn, B. M. (2004). The Central Asian Orogenic Belt and growth of the continental crust in the Phanerozoic. Geological Society, London, Special Publications, 226(1), 73-100.

Jahn, B. M., Wu, F., & Chen, B. (2000). Granitoids of the Central Asian Orogenic Belt and continental growth in the Phanerozoic. Earth and Environmental Science Transactions of the Royal Society of Edinburgh, 91(1-2), 181-193. https://doi.org/10.1017/S0263593300007367

Jamieson, R. A., Beaumont, C., Hamilton, J., & Fullsack, P. (1996). Tectonic assembly of inverted metamorphic sequences. Geology, 24(9), 839-842. https://doi.org/10.1130/0091-7613(1996)024%3C0839:TAOIMS%3E2.3.CO;2

Jamieson, R. A., Beaumont, C., Medvedev, S., & Nguyen, M. H. (2004). Crustal channel flows: 2. Numerical models with implications for metamorphism in the Himalayan-Tibetan orogen. Journal of Geophysical Research: Solid Earth, 109(B6). https://doi.org/10.1029/2003JB002811

Jian, P. (2003). SHRIMP dating of ophiolite and leucocratic rocks within ophiolite. Earth Science Frontiers, 10(4), 439-456 (in Chinese with English abstract).

Jiang, H. J., Han, J., Chen, H., Zheng, Y., Lu, W., Deng, G., & Tan, Z. (2017). Intra-continental back-arc basin inversion and Late Carboniferous magmatism in Eastern Tianshan, NW China: Constraints from the Shaquanzi magmatic suite. Geoscience Frontiers, 8(6), 1447-1467.

Jiang, T., Gao, J., Klemd, R., Qian, Q., Zhang, X., Xiong, X., ... & Chen, B. (2014). Paleozoic ophiolitic mélanges from the South Tianshan Orogen, NW China: Geological, geochemical and geochronological implications for the geodynamic setting. Tectonophysics, 612, 106-127. https://doi.org/10.1016/j.tecto.2013.11.038

Jiang, Y., Sun, M., Zhao, G., Yuan, C., Xiao, W., Xia, X., ... & Wu, F. (2011). Precambrian detrital zircons in the Early Paleozoic Chinese Altai: their provenance and implications for the crustal growth of central Asia. Precambrian Research, 189(1-2), 140-154.

Jolivet, M., 2017. Mesozoic tectonic and topographic evolution of Central Asia and Tibet: a preliminary synthesis. Geological Society, London, Special Publications, 427, 19-55.

Kang, H., Chen, Y. L., Li, D. P., Zhang, H. H., Yang, Y., Xue, G. L., & Liu, W. (2022). Late Triassic Mg andesite of Juluotage, eastern Tianshan: Identification and tectonic implications. Earth Science Frontiers, 29(4), 358.

Kelsey, D. E., Clark, C., & Hand, M. (2008). Thermobarometric modelling of zircon and monazite growth in melt-bearing systems: Examples using model metapelitic and metapsammitic granulites. Journal of Metamorphic Geology, 26(2), 199-212. https://doi.org/10.1111/j.1525-1314.2007.00757.x

Kelemen, P. B., Hanghøj, K., & Greene, A. R. (2014). One view of the geochemistry of subduction-related magmatic arcs, with an emphasis on primitive andesite and lower crust. Treatise on Geochemistry, 4, 749-806. https://doi.org/10.1016/B978-0-08-095975-7.00323-5

Kemp, A. I. S., Hawkesworth, C. J., Paterson, B. A., & Kinny, P. D. (2006). Episodic growth of the Gondwana supercontinent from hafnium and oxygen isotopes in zircon. Nature, 439(7076), 580-583.

Kemp, A. I. S., Hawkesworth, C. J., Collins, W. J., Gray, C. M., & Blevin, P. L. (2009). Isotopic evidence for rapid continental growth in an extensional accretionary orogen: The Tasmanides, eastern Australia. Earth and Planetary Science Letters, 284(3-4), 455-466.

Keto, L. S., & Jacobsen, S. B. (1987). Nd and Sr isotopic variations of Early Paleozoic oceans. Earth and Planetary Science Letters, 84(1), 27-41. https://doi.org/10.1016/0012-821X(87)90173-7

Kidder, S., & Ducea, M. N. (2006). High temperatures and inverted metamorphism in the schist of Sierra de Salinas, California. Earth and Planetary Science Letters, 241(3-4), 422-437. https://doi.org/10.1016/j.epsl.2005.11.037

Kohn, M. J. (2014). Himalayan metamorphism and its tectonic implications. Annual

Review of Earth and Planetary Sciences, 42, 381-419. https://doi.org/10.1146/annurev-earth-060313-055005

Lanari, P., Vidal, O., De Andrade, V., Dubacq, B., Lewin, E., Grosch, E. G., & Schwartz, S. (2014). XMapTools: A MATLAB©-based program for electron microprobe X-ray image processing and geothermobarometry. Computers & Geosciences, 62, 227-240. https://doi.org/10.1016/j.cageo.2013.08.010

Lanari, P., & Engi, M. (2017). Local bulk composition effects on metamorphic mineral assemblages. Reviews in Mineralogy and Geochemistry, 83(1), 55-102. https://doi.org/10.2138/rmg.2017.83.3

Lanari, P., Vho, A., Bovay, T., Airaghi, L., & Centrella, S. (2019). Quantitative compositional mapping of mineral phases by electron probe micro-analyser. Geological Society, London, Special Publications, 478(1), 39-63. https://doi.org/10.1144/SP478.4

Le Fort, P. (1975). Himalayas: the collided range. Present knowledge of the continental arc. American Journal of Science, 275(1), 1-44.

Lei, R. X., Brzozowski, M. J., Feng, Y. G., Zhang, K., Muhtar, M. N., Luo, X., & Wu, C. Z. (2021). Triassic crust–mantle interaction in the Eastern Tianshan, southern Altaids: Insights from microgranular enclaves and their host Tianhu granitoids. Lithos, 402, 105879. https://doi.org/10.1016/j.lithos.2020.105879

Lei, R. X., Wu, C. Z., Gu, L. X., Zhang, Z. Z., Chi, G. X., & Jiang, Y. H. (2011). Zircon U–Pb chronology and Hf isotope of the Xingxingxia granodiorite from the Central Tianshan zone (NW China): implications for the tectonic evolution of the southern Altaids. Gondwana Research, 20(2-3), 582-593. https://doi.org/10.1016/j.gr.2011.02.010

Lei, W. S., Guo, J., Chen, D., Chu, J., & Li, Y. (2018). Ductile shearing and LA-ICP MS zircon U-Pb dating of Sa'erqiaoke ductile shear belt in the Bogda orogen: Constraints on the process of mountain building of eastern Tianshan. Geological Journal, 53, 206-222. https://doi.org/10.1002/gj.3196

Li, D., He, D., Santosh, M., Ma, D., & Tang, J. (2015). Tectonic framework of the northern Junggar Basin part I: The eastern Luliang Uplift and its link with the East Junggar terrane. Gondwana Research, 27(3), 1089-1109. https://doi.org/10.1016/j.gr.2014.08.015

Li, D., He, D., & Tang, Y. (2016). Reconstructing multiple arc-basin systems in the

Altai–Junggar area (NW China): implications for the architecture and evolution of the western Central Asian Orogenic Belt. Journal of Asian Earth Sciences, 121, 84-107. https://doi.org/10.1016/j.jseaes.2016.02.010

Li, D., He, D., Sun, M., & Zhang, L. (2020). The Role of Arc-Arc Collision in Accretionary Orogenesis: Insights From ~320 Ma Tectono-sedimentary Transition in the Karamaili Area, NW China. Tectonics, 39(1), e2019TC005623. https://doi.org/10.1029/2019TC005623

Li, D., He, D., Lu, Y., Fan, D., Zhen, Y., & Hou, S. (2021). Diverse origins of late Paleozoic calc-alkaline magmatic rocks from the Bogda tectonic belt: Implications for the geodynamic evolution of the eastern Tianshan, NW China. Lithos, 404, 106442. https://doi.org/10.1016/j.lithos.2021.106442

Li, D., Han, Y., He, D., Hou, S., Zhen, Y., & Yang, H. (2024). Arc-arc amalgamation during accretionary orogenesis: Insights from mid-Paleozoic tectono-magmatic records in eastern Junggar, NW China. Geosphere, 20(2), 407-420. https://doi.org/10.1130/GES02694.1

Li, D. D., Wang, Y., Shi, Y., Xie, H., Wang, J., & Lai, C. (2019). Age and geochemistry of the Carboniferous-Permian magmatism and Fe-Ti-V oxide metallogeny in the Eastern Tianshan Orogen, NW China: evidence from the Yaxi mafic-ultramafic complex. International Geology Review, 61(7), 853-867.

Liu, H. Q., Xu, Y. G., Wei, G. J., Wei, J. X., Yang, F., Chen, X. Y., et al. (2016). B isotopes of Carboniferous-Permian volcanic rocks in the Tuha basin mirror a transition from subduction to intraplate setting in Central Asian Orogenic Belt. Journal of Geophysical Research: Solid Earth, 121(11), 7946-7964. https://doi.org/10.1002/2016JB013288

Li, J. T., He, X. F., Liu, L., Yang, P. T., Liang, B., Su, H., et al. (2017). Ordovician tectonic evolution of Harlik in Eastern Tianshan of Xinjiang: Constraints from LA-ICP-MS zircon U-Pb geochronology and geochemistry of volcanic rocks. Geoscience 31 (3), 460-473 (in Chinese with English abstract).

Li, J. Y., Yang, T. N., Li, Y. P., & Zhu, Z. X., 2009. Geological features of the Karamaili faulting belt, eastern Junggar region, Xinjiang, China and its constraints on the reconstruction of Late Paleozoic ocean-continental framework of the Central Asian region. Geological Bulletin of China 28(12), 1817-1826 (in Chinese with English abstract).

Li, L., Xiao, W., Windley, B. F., Mao, Q., Jia, X., Yang, H., ... & Abuduxun, N. (2021). Contrasting Early Palaeozoic provenance of the Yemaquan and Harlik arcs in the SW Altaids (NW China): identification of cryptic sutures in accretionary orogens. International Geology Review, 63(17), 2192-2214. https://doi.org/10.1080/00206814.2021.1992302

Li, L., Xiao, W., Windley, B. F., Yang, H., Jia, X., Sang, M., ... & Liu, Y. (2022). Early Carboniferous rifting of the Harlik arc in the Eastern Tianshan (NW China): Response to rollback in the southern Altaids?. American Journal of Science, 322(2), 313-350. http://dx.doi.org/10.2475/02.2022.07

Li, L., Xiao, W., Windley, B. F., Zhao, G., Yang, H., Sang, M., & Jia, X. (2023). An early Paleozoic accumulation-foundering cycle of ultramafic cumulates in the Harlik arc and its implications for continental crustal growth in the Altaids. Lithos, 462, 107404. https://doi.org/10.1016/j.lithos.2023.107404

Li, N., Yang, F., Zhang, Z., & Yang, C. (2019). Geochemistry and chronology of the biotite granite in the Xiaobaishitou W-(Mo) deposit, eastern Tianshan, China: Petrogenesis and tectonic implications. Ore Geology Reviews, 107, 999-1019. https://doi.org/10.1016/j.oregeorev.2019.03.027

Li, N., Yang, F., Zhang, Z., & Li, C. (2020). Dating the Xiaobaishitou skarn W–(Mo) deposit, Eastern Tianshan, NW China: constraints from zircon U–Pb, muscovite 40Ar-39Ar, and molybdenite Re–Os system. Ore Geology Reviews, 124, 103637. https://doi.org/10.1016/j.oregeorev.2020.103637

Li, P. F., Sun, M., Yuan, C., Jourdan, F., Hu, W., & Jiang, Y. (2021). Late Paleozoic tectonic transition from subduction to collision in the Chinese Altai and Tianshan (Central Asia): New geochronological constraints. American Journal of Science, 321(1–2), 178–205. https://doi.org/10.2475/01.2021.05

Li, S., Wang, T., Wilde, S. A., Tong, Y., Hong, D., & Guo, Q. (2012). Geochronology, petrogenesis and tectonic implications of Triassic granitoids from Beishan, NW China. Lithos, 134, 123-145. https://doi.org/10.1016/j.lithos.2011.12.005

Li, W., Chen, Y., Yuan, X., Xiao, W., & Windley, B. F. (2022). Intracontinental deformation of the Tianshan Orogen in response to India-Asia collision. Nature Communications, 13(1), 3738.

Li, X., Tang, G., Gong, B., Yang, Y., Hou, K., Hu, Z., et al. (2013). Qinghu zircon: A working reference for microbeam analysis of U-Pb age and Hf and O isotopes.

Chinese Science Bulletin, 58, 4647-4654. https://doi.org/10.1007/s11434-013-5932-x

Li, Y. L., Shan, X., Gelwick, K. D., Yu, X., Jin, L., Yao, Z., ... & Yang, S. (2022). Permian mountain building in the bogda mountains of NW China. International Geology Review, 64(22), 3260-3274.

Li, Z. L., Yang, J. S., & Liu, Z. (2011). LA-ICP-MS zircon U-Pb dating of the volcanic rocks in the middle section of the eastern Tianshan, and its geological significance. Acta Petrologica Sinica, 27(1), 181-192 (in Chinese with English abstract).

Liang, P., Chen, H., Hollings, P., Wu, C., Xiao, B., Bao, Z., & Xu, D. (2016). Geochronology and geochemistry of igneous rocks from the Laoshankou district, North Xinjiang: Implications for the Late Paleozoic tectonic evolution and metallogenesis of East Junggar. Lithos, 266, 115-132.

Lin, W., Faure, M., Shi, Y., Wang, Q., & Li, Z. (2009). Palaeozoic tectonics of the south-western Chinese Tianshan: new insights from a structural study of the high-pressure/low-temperature metamorphic belt. International Journal of Earth Sciences, 98, 1259-1274. https://doi.org/10.1007/s00531-008-0371-7

Liu, D. D., Kong, X., Zhang, C., Wang, J., Yang, D., Liu, X., ... & Song, Y. (2018). Provenance and geochemistry of Lower to Middle Permian strata in the southern Junggar and Turpan basins: A terrestrial record from mid-latitude NE Pangea. Palaeogeography, Palaeoclimatology, Palaeoecology, 495, 259-277.

Liu, D. D., Zhang, C., Li, C., Guo, J., Zhang, Z., Huang, Z., & Pan, Z. (2021). Slab roll-back and crustal growth in the Eastern Junggar terrane, NW China: evidence from Carboniferous A-type granitoids and adakitic rocks. International Geology Review, 63(6), 748-768.

Liu, F., Chai, F., Li, Q., & Yang, F. (2019). Constraints on the timing of Fe–(Cu) metallogenesis in the eastern Aqishan–Yamansu–Shaquanzi metallogenic belt, Eastern Tianshan, NW China. Ore Geology Reviews, 113, 103089.

Liu, H. S., Wang, B., Shu, L., Jahn, B. M., & Lizuka, Y. (2014). Detrital zircon ages of Proterozoic meta-sedimentary rocks and Paleozoic sedimentary cover of the northern Yili Block: Implications for the tectonics of microcontinents in the Central Asian Orogenic Belt. Precambrian Research, 252, 209-222. https://doi.org/10.1016/j.precamres.2014.07.018

Li, J. H., Zhao, G. C., Johnston, S. T., Dong, S., Zhang, Y., Liu, Q., et al. (2020).

Contributions of triassic tectonism to build the northern tibetan plateau: Insights from tectonic evolution of the Jinhongshan Range, central altyn tagh fault system. Tectonics, 39(12), e2020TC006438. https://doi.org/10.1029/2020TC006438

Liu, J. S., Wang, B., Ni, X. H., Song, F., Sun, Z. C., Deng, J., & Li, Y. Y. (2022). Late Devonian transition from advancing to retreating subduction in the SW Central Asian Orogenic Belt: Insights from multiple deformation and magmatic events in the southern Yili Block, NW China. Gondwana Research, 105, 468-487. https://doi.org/10.1016/j.gr.2021.10.001

Liu, L., Li, J. T., Ma, Y. C., Li, S. H.., Wang, L. & Wang, F. J. (2020). Geochemical characteristics and zircon U-Pb dating of the Omltag Massif in the Eastern Tianshan, Xinjiang. Mineralogy and Petrology, 40 (4), 20-29 (in Chinese with English abstract).

Liu, R. Q, Chen, C., Lv, X., Zhang, Z., Ruan, B., Zhang, S., & Hu, E. (2023). Petrogenesis and geological implications of the qiyishan triassic granitoids in east Beishan orogen, inner Mongolia, NW China: evidence from geochronology, geochemistry and Nd-Hf isotopes. Frontiers in Earth Science, 11, 1260852. https://doi.org/10.3389/feart.2023.1260852

Liu, S. B., Dou, H., Li, H. B., & Wen, Z. G. (2019). Geological significance of the discovery of Late Jurassic intermediate-acidic intrusive rock in Bogeda area of East Tianshan, Xinjiang, and its U-Pb zircon age. Geological Bulletin of China, 38(2/3), 288-294 (in Chinese with English abstract).

Liu, S. W., Guo, Z. J., Zhang, Z. C., Li, Q. G., & Zheng, H. F. (2004). Nature of the Precambrian metamorphic blocks in the eastern segment of Central Tianshan: Constraint from geochronology and Nd isotopic geochemistry. Science in China Series D: Earth Sciences, 47, 1085-1094. https://doi.org/10.1360/03yd0177

Liu, S. Y., Wang, R., Jeon, H., Hou, Z., Xue, Q., Zhou, L., et al. (2020). Indosinian magmatism and rare metal mineralization in East Tianshan orogenic belt: An example study of Jingerquan Li-Be-Nb-Ta pegmatite deposit. Ore Geology Reviews, 116, 103265. https://doi.org/10.1016/j.oregeorev.2019.103265

Liu, W., Liu, X. J., & Liu, L. J. (2013). Underplating generated A-and I-type granitoids of the East Junggar from the lower and the upper oceanic crust with mixing of mafic magma: Insights from integrated zircon U–Pb ages, petrography, geochemistry and Nd–Sr–Hf isotopes. Lithos, 179, 293-319.

https://doi.org/10.1016/j.lithos.2013.08.009

Liu, W., Si, C., & Liu, X. (2021). Middle-crust accumulation of hornblendite and pyroxenes from slab-and mantle wedge-derived magmas and recharge of high-18O felsic magma collectively generated the Hadanxun arc magmas, northern East Junggar. Lithos, 386, 105986. https://doi.org/10.1016/j.lithos.2021.105986

Liu, Y., Wang, X., Wu, K., Chen, S., Shi, Z., & Yao, W. (2019). Late Carboniferous seismic and volcanic record in the northwestern margin of the Junggar Basin: Implication for the tectonic setting of the West Junggar. Gondwana Research, 71, 49-75. https://doi.org/10.1016/j.gr.2019.01.013

Liu, Y. S., Hu, Z. C., Gao, S., Günther, D., Xu, J., Gao, C. G., & Chen, H. H. (2008). In situ analysis of major and trace elements of anhydrous minerals by LA-ICP-MS without applying an internal standard. Chemical Geology, 257(1-2), 34-43. https://doi.org/10.1016/j.chemgeo.2008.08.004

Lister, G., & Forster, M. (2009). Tectonic mode switches and the nature of orogenesis. Lithos, 113(1-2), 274-291.

Long, D. H. (2021). Geochemistry, Zircon U-Pb dating and tectonic significance of basitein the middle section of Bogda Orogenic Belt, Xinjiang. Northwestern Geology, 54(1), 15-29 (in Chinese with English abstract). https://link.oversea.cnki.net/doi/10.19751/j.cnki.61-1149/p.2021.01.002

Long, L. L., Gao, J., Xiong, X. M., & Qian, Q. (2006). The geochemical characteristics and the age of the Kole Lake ophiolite in the southern Tianshan. Acta Petrologica Sinica, 22(1), 65-73 (in Chinese with English abstract).

Long, X. P., Yuan, C., Sun, M., Safonova, I., Xiao, W. J., & Wang, Y. J. (2012). Geochemistry and U–Pb detrital zircon dating of Paleozoic graywackes in East Junggar, NW China: Insights into subduction–accretion processes in the southern Central Asian Orogenic Belt. Gondwana Research, 21, 637-653. https://doi.org/10.1016/j.gr.2011.05.015

Long, X. P., Wilde, S. A., Wang, Q., Yuan, C., Wang, X. C., Li, J., et al. (2015). Partial melting of thickened continental crust in central Tibet: Evidence from geochemistry and geochronology of Eocene adakitic rhyolites in the northern Qiangtang Terrane. Earth and Planetary Science Letters, 414, 30-44. https://doi.org/10.1016/j.epsl.2015.01.007

Long, X. P., Wu, B., Sun, M., Yuan, C., Xiao, W., & Zuo, R. (2020). Geochronology and geochemistry of Late Carboniferous dykes in the Aqishan–Yamansu belt, eastern Tianshan: Evidence for a post-collisional slab breakoff. Geoscience Frontiers, 11(1), 347-362.

Ludwig, K. R. (2011). Isoplot/Ex version4.15, Berkeley Geochronology Center, Special Publication.

Luo, J., Xiao, W., Wakabayashi, J., Han, C., Zhang, J. E., Wan, B., ... & Chen, Y. (2017). The Zhaheba ophiolite complex in Eastern Junggar (NW China): Long lived supra-subduction zone ocean crust formation and its implications for the tectonic evolution in southern Altaids. Gondwana Research, 43, 17-40.

Luo, T., Liao, Q. A., Zhang, X. H., Chen, J. P., Wang, G. C., & Huang, X. (2016). Geochronology and geochemistry of Carboniferous metabasalts in eastern Tianshan, Central Asia: evidence of a back-arc basin. International Geology Review, 58(6), 756-772.

Ma, H. D., He, W. D., Tu, Q. J., Chen, J., Cao, F. G., & Ren, Y. (2008). Characteristics of the Tashuihe ductile shear zone, eastern Tianshan, Xinjiang. Geotectonica et Metallogenia, 32(01), 1-10 (in Chinese with English abstract).

Ma, Q., Zheng, J. P., Xu, Y. G., Griffin, W. L., & Zhang, R. S. (2015). Are continental "adakites" derived from thickened or foundered lower crust?. Earth and Planetary Science Letters, 419, 125-133. https://doi.org/10.1016/j.epsl.2015.02.036

Ma, X. H., Chen, B., Wang, C., & Yan, X. L. (2015). Early Paleozoic subduction of the Paleo-Asian Ocean: Zircon U-Pb geochronological, geochemical and Sr-Nd isotopic evidence from the Harlik pluton, Xinjiang. Acta Petrologica Sinica, 31 (1), 89-104 (in Chinese with English abstract).

Ma, X. X., Shu, L., Meert, J. G., & Li, J. (2014). The Paleozoic evolution of Central Tianshan: Geochemical and geochronological evidence. Gondwana Research, 25(2), 797-819. https://doi.org/10.1016/j.gr.2013.05.015

Macpherson, C. G., Dreher, S. T., & Thirlwall, M. F. (2006). Adakites without slab melting: high pressure differentiation of island arc magma, Mindanao, the Philippines. Earth and Planetary Science Letters, 243(3-4), 581-593. https://doi.org/10.1016/j.epsl.2005.12.034

Maniar, P. D., & Piccoli, P. M. (1989). Tectonic discrimination of granitoids. Geological Society of America Bulletin, 101(5), 635-643. https://doi.org/10.1130/0016-7606(1989)101<0635:TDOG>2.3.CO;2

Mao, J. W., Goldfarb, R. J., Wang, Y., Hart, C. J., Wang, Z., & Yang, J. (2005). Late Paleozoic base and precious metal deposits, East Tianshan, Xinjiang, China: characteristics and geodynamic setting. Episodes Journal of International Geoscience, 28(1), 23-36.

Mao, L. J., He, Z. Y., Zhang, Z. M., Klemd, R., Xiang, H., Tian, Z. L., & Zong, K. Q. (2015). Origin and geodynamic significance of the early Mesozoic Weiya LP and HT granulites from the Chinese Eastern Tianshan. Lithos, 239, 142-156. https://doi.org/10.1016/j.lithos.2015.10.016

Mao, Q. G., Ao, S., Windley, B. F., Song, D., Sang, M., Tan, Z., ... & Xiao, W. (2022a). Late Paleozoic southward migration of the Dananhu arc in the Eastern Tianshan (NW China). Earth and Space Science, 9(3), e2021EA002027.

Mao, Q. G., Ao, S. J., Windley, B. F., Zhang, Z., Sang, M., Tan, Z., et al. (2022b). Middle-Late Triassic southward-younging granitoids: Tectonic transition from subduction to collision in the Eastern Tianshan-Beishan Orogen, NW China. GSA Bulletin, 134(9-10), 2206-2224. https://doi.org/10.1130/B36172.1

Mao, Q. G., Wang, J., Yu, M., Ao, S., Deng, X., Lü, X., & Li, Y. (2020b). Re-Os and U-Pb geochronology for the Xiaorequanzi VMS deposit in the Eastern Tianshan, NW China: Constraints on the timing of mineralization and stratigraphy. Ore Geology Reviews, 122, 103473.

Mao, Q. G., Wang, J., Xiao, W., Windley, B. F., Schulmann, K., Ao, S., ... & Fang, T. (2021). From Ordovician nascent to early Permian mature arc in the southern Altaids: Insights from the Kalatage inlier in the Eastern Tianshan, NW China. Geosphere, 17(2), 647-683.

Mao, Q. G., Xiao, W., Windley, B. F., Yu, M., Sun, M., Ao, S., & Zhang, J. E. (2021). Early Permian subduction-related transtension in the Turpan Basin, East Tianshan (NW China): implications for accretionary tectonics of the southern Altaids. Geological Magazine, 158(1), 175-198.

Mao, Q., Yu, M., Xiao, W., Windley, B. F., Li, Y., Wei, X., ... & Lü, X. (2018). Skarn-mineralized porphyry adakites in the Harlik arc at Kalatage, E. Tianshan (NW China): Slab melting in the Devonian-early Carboniferous in the southern Central Asian Orogenic Belt. Journal of Asian Earth Sciences, 153, 365-378.

Martin, H., Smithies, R. H., Rapp, R., Moyen, J. F., & Champion, D. (2005). An overview of adakite, tonalite–trondhjemite–granodiorite (TTG), and sanukitoid:

relationships and some implications for crustal evolution. Lithos, 79(1-2), 1-24. https://doi.org/10.1016/j.lithos.2004.04.048

Memtimin, M., Pe-Piper, G., Piper, D. J., Guo, Z., & Zhang, Y. (2020). Carboniferous arc-related volcanism in SW Bogda Mountain, Northwest China, and its implications for regional tectonics. Lithos, 360, 105413.

Middlemost, E. A. (1994). Naming materials in the magma/igneous rock system. Earth-science reviews, 37(3-4), 215-224. https://doi.org/10.1016/0012-8252(94)90029-9

Miller, C. F., McDowell, S. M., & Mapes, R. W. (2003). Hot and cold granites? Implications of zircon saturation temperatures and preservation of inheritance. Geology, 31(6), 529-532.

Mohan, A., Windley, B. F., & Searle, M. P. (1989). Geothermobarometry and development of inverted metamorphism in the Darjeeling-Sikkim region of the eastern Himalayan. Journal of Metamorphic Geology, 7(1), 95-110. https://doi.org/10.1111/j.1525-1314.1989.tb00577.x

Mole, D. R., Fiorentini, M. L., Thebaud, N., Cassidy, K. F., McCuaig, T. C., Kirkland, C. L., ... & Miller, J. (2014). Archean komatiite volcanism controlled by the evolution of early continents. Proceedings of the National Academy of Sciences, 111(28), 10083-10088.

Mottram, C. M., Warren, C. J., Regis, D., Roberts, N. M., Harris, N. B., Argles, T. W., & Parrish, R. R. (2014). Developing an inverted Barrovian sequence; insights from monazite petrochronology. Earth and Planetary Science Letters, 403, 418-431. http://dx.doi.org/10.1016/j.epsl.2014.07.006

Moyen, J. F., Janoušek, V., Laurent, O., Bachmann, O., Jacob, J. B., Farina, F., ... & Villaros, A. (2021). Crustal melting vs. fractionation of basaltic magmas: Part 1, granites and paradigms. Lithos, 402, 106291. https://doi.org/10.1016/j.lithos.2021.106291

Muhtar, M. N., Wu, C. Z., Santosh, M., Lei, R. X., Gu, L. X., Wang, S. M., & Gan, K. (2020). Late Paleozoic tectonic transition from subduction to post-collisional extension in Eastern Tianshan, Central Asian Orogenic Belt. GSA Bulletin, 132(7-8), 1756-1774. https://doi.org/10.1130/B35432.1

Muhtar, M. N., Wu, C. Z., Brzozowski, M. J., Zhang, W. F., Chen, B. Y., Lei, R. X., & Xiao, W. J. (2022). Age and genesis of the Jinshan gold deposit in the Chinese North Tianshan: A link to large-scale strike–slip shearing events. Ore Geology

Reviews, 142, 104734.

Muhtar, M. N., Wu, C. Z., Brzozowski, M. J., Santosh, M., Tian, R. S., Xie, G. A., et al. (2023). Timing and spatial variation of deformation along the Kanggur-Huangshan shear zone in the Chinese Tianshan: Implications for regional differential uplift and mineralization. GSA Bulletin, 135(5-6), 1429-1448. https://doi.org/10.1130/B36221.1

Muhtar, M. N., Xiao, W. J, Brzozowski, M. J., Mao, Q., Yang, H., & Wu, C. (2024). Permian-Triassic magmatism above a slab window in the Eastern Tianshan: Implications for the evolution of the southern Altaids. GSA Bulletin. https://doi.org/10.1130/B37133.1

Käßner, A., Ratschbacher, L., Pfänder, J. A., Hacker, B. R., Zack, G., Sonntag, B. L., & Oimahmadov, I. (2017). Proterozoic-Mesozoic history of the Central Asian orogenic belt in the Tajik and southwestern Kyrgyz Tian Shan: U-Pb, 40Ar/39Ar, and fission-track geochronology and geochemistry of granitoids. GSA Bulletin, 129(3-4), 281-303. https://doi.org/10.1130/B31466.1

Karsli, O., Dokuz, A., Kandemir, R., Aydin, F., Schmitt, A. K., Ersoy, E. Y., & Alyıldız, C. (2019). Adakite-like parental melt generation by partial fusion of juvenile lower crust, Sakarya Zone, NE Turkey: a far-field response to break-off of the southern Neotethyan oceanic lithosphere. Lithos, 338, 58-72. https://doi.org/10.1016/j.lithos.2019.03.029

Klemd, R., Gao, J., Li, J. L., & Meyer, M. (2015). Metamorphic evolution of (ultra)-high-pressure subduction-related transient crust in the South Tianshan Orogen (Central Asian Orogenic Belt): Geodynamic implications. Gondwana Research, 28(1), 1-25. https://doi.org/10.1016/j.gr.2014.11.008

Kröner, A., Alexeiev, D. V., Rojas-Agramonte, Y., Hegner, E., Wong, J., Xia, X., ... & Kiselev, V. V. (2013). Mesoproterozoic (Grenville-age) terranes in the Kyrgyz North Tianshan: zircon ages and Nd-Hf isotopic constraints on the origin and evolution of basement blocks in the southern Central Asian Orogen. Gondwana Research, 23(1), 272-295. https://doi.org/10.1016/j.gr.2012.05.004

Odlum, M. L., & Stockli, D. F. (2020). Geochronologic constraints on deformation and metasomatism along an exhumed mylonitic shear zone using apatite U-Pb, geochemistry, and microtextural analysis. Earth and Planetary Science Letters, 538, 116177. https://doi.org/10.1016/j.epsl.2020.116177

O'Sullivan, G., Chew, D., Kenny, G., Henrichs, I., & Mulligan, D. (2020). The trace element composition of apatite and its application to detrital provenance studies. Earth-Science Reviews, 201, 103044. https://doi.org/10.1016/j.earscirev.2019.103044

Passchier, C. W., & Trouw, R. A. (2005). Microtectonics. Springer Science & Business Media.

Paton, C., Hellstrom, J., Paul, B., Woodhead, J., & Hergt, J. (2011). Iolite: Freeware for the visualisation and processing of mass spectrometric data. Journal of Analytical Atomic Spectrometry, 26(12), 2508-2518. https://doi.org/10.1039/C1JA10172B

Peccerillo, A., & Taylor, S. R. (1976). Geochemistry of Eocene calc-alkaline volcanic rocks from the Kastamonu area, northern Turkey. Contributions to Mineralogy and Petrology, 58(1), 63–81. https://doi.org/10.1007/BF00384745

Penniston-Dorland, S. C., Kohn, M. J., & Manning, C. E. (2015). The global range of subduction zone thermal structures from exhumed blueschists and eclogites: Rocks are hotter than models. Earth and Planetary Science Letters, 428, 243-254. https://doi.org/10.1016/j.epsl.2015.07.031

Pearce, J. A., & Peate, D. W. (1995). Tectonic implications of the composition of volcanic arc magmas. Annual Review of Earth and Planetary Sciences, 23, 251-286.

Pitra, P., Ballevre, M., & Ruffet, G. (2010). Inverted metamorphic field gradient towards a Variscan suture zone (Champtoceaux Complex, Armorican Massif, France). Journal of metamorphic Geology, 28(2), 183-208. https://doi.org/10.1111/j.1525-1314.2009.00862.x

Profeta, L., Ducea, M. N., Chapman, J. B., Paterson, S. R., Gonzales, S. M. H., Kirsch, M., ... & DeCelles, P. G. (2015). Quantifying crustal thickness over time in magmatic arcs. Scientific reports, 5(1), 17786.

Qin, J. Y., Zhang, Z., Hou, T., Cheng, Z., Xie, Q., Kong, W., ... & Santosh, M. (2022). Petrogenesis of Early Permian basalts in the Turpan-Hami basin, NW China: Implications for the spatial limits of the Tarim mantle plume. Journal of Asian Earth Sciences, 226, 105097.

Qin, K. Z., Su, B. X., Sakyi, P. A., Tang, D. M., Li, X. H., Sun, H., ... & Liu, P. P. (2011). SIMS zircon U-Pb geochronology and Sr-Nd isotopes of Ni-Cu-Bearing Mafic-Ultramafic Intrusions in Eastern Tianshan and Beishan in correlation with flood basalts in Tarim Basin (NW China): Constraints on a ca. 280 Ma mantle plume.

American Journal of Science, 311(3), 237-260.

Qiu, K. F., Deng, J., He, D. Y., Rosenbaum, G., Zheng, X., Williams-Jones, A. E., ... & Balen, D. (2023). Evidence of vertical slab tearing in the Late Triassic Qinling Orogen (central China) from multiproxy geochemical and isotopic imaging. Journal of Geophysical Research: Solid Earth, 128(4), e2022JB025514.

Rapp, R. P., Shimizu, N., Norman, M. D., & Applegate, G. S. (1999). Reaction between slab-derived melts and peridotite in the mantle wedge: experimental constraints at 3.8 GPa. chemical Geology, 160(4), 335-356. https://doi.org/10.1016/S0009-2541(99)00106-0

Reimink, J. R., Davies, J. H., Moyen, J. F., & Pearson, D. G. (2023). A whole-lithosphere view of continental growth. Geochemical Perspectives Letters, 26. https://doi.org/10.7185/geochemlet.2324

Ribeiro, B. V., Mulder, J. A., Faleiros, F. M., Kirkland, C. L., Cawood, P. A., O'Sullivan, G., et al. (2020). Using apatite to resolve the age and protoliths of mid-crustal shear zones: A case study from the Taxaquara Shear Zone, SE Brazil. Lithos, 378, 105817. https://doi.org/10.1016/j.lithos.2020.105817

Richards, J. P., & Kerrich, R. (2007). Special paper: adakite-like rocks: their diverse origins and questionable role in metallogenesis. Economic geology, 102(4), 537-576. https://doi.org/10.2113/gsecongeo.102.4.537

Royden, L. H. (1993). Evolution of retreating subduction boundaries formed during continental collision. Tectonics, 12(3), 629-638.

Rubatto, D., Hermann, J., & Buick, I. S. (2006). Temperature and bulk composition control on the growth of monazite and zircon during low-pressure anatexis (Mount Stafford, central Australia). Journal of Petrology, 47(10), 1973-1996. https://doi.org/10.1093/petrology/egl033

Rubatto, D., Chakraborty, S., & Dasgupta, S. (2013). Timescales of crustal melting in the higher Himalayan Crystallines (Sikkim, Eastern Himalaya) inferred from trace element-constrained monazite and zircon chronology. Contributions to Mineralogy and Petrology, 165(2), 349–372. https://doi.org/10.1007/s00410-012-0812-y

Rubatto, D. (2017). Zircon: The metamorphic mineral. Reviews in mineralogy and geochemistry, 83(1), 261-295.

Rudnick, R. L. (1995). Making continental crust. Nature, 378(6557), 571-578. https://doi.org/10.1038/378571a0

Rudnick, R. L., & Gao, S. (2014). The composition of the continental crust. Treatise on Geochemistry, 4, 1-51. https://doi.org/10.1016/B978-0-08-095975-7.00301-6

Sandiford, M., & Powell, R. (1986). Deep crustal metamorphism during continental extension: Modern and ancient examples. Earth and Planetary Science Letters, 79, 151-158. https://doi.org/10.1016/0012-821X(86)90048-8

Scaillet, S. (2000). Numerical error analysis in 40Ar/39Ar dating. Chemical Geology, 162(3-4), 269-298. https://doi.org/10.1016/S0009-2541(99)00149-7

Schärer, U. (1984). The effect of initial 230Th disequilibrium on young U-Pb ages: the Makalu case, Himalaya. Earth and Planetary Science Letters, 67(2), 191-204. https://doi.org/10.1016/0012-821X(84)90114-6

Seltmann, R., Konopelko, D., Biske, G., Divaev, F., & Sergeev, S. (2011). Hercynian post-collisional magmatism in the context of Paleozoic magmatic evolution of the Tien Shan orogenic belt. Journal of Asian Earth Sciences, 42(5), 821-838. https://doi.org/10.1016/j.jseaes.2010.08.016

Şengör, A.M.C., Natal'in, B.A., & Burtman, V.S., 1993. Evolution of the Altaid tectonic collage and Paleozoic crustal growth in Eurasia. Nature 364, 209-304. https://doi.org/10.1038/364299a0

Shen, X. P., Zhang, H., Wang, Q., Wyman, D. A., & Yang, Y. (2011). Late Devonian–Early Permian A-type granites in the southern Altay Range, Northwest China: petrogenesis and implications for tectonic setting of "A2-type" granites. Journal of Asian Earth Sciences, 42(5), 986-1007.

Shi, Y., Wang, Y., Wang, J., Zhou, G., Xie, H., Li, D., et al. (2021). Formation of the Weiya magmatic Fe–Ti oxide deposit and its ore-hosting layered gabbro intrusion, Eastern Tianshan (Xinjiang, NW China). Ore Geology Reviews, 132, 104003. https://doi.org/10.1016/j.oregeorev.2021.104003

Shu, L. S., Charvet, J., Guo, L., Lu, H., & Laurent-Charvet, S. (1999). A Large-Scale Palaeozoic Dextral Ductile Strike-Slip Zone: the Aqqikkudug-Weiya Zone along the Northern Margin of the Central Tianshan Belt, Xinjiang, NW China. Acta Geologica Sinica, 73(2), 148-162. https://doi.org/10.1111/j.1755-6724.1999.tb00822.x

Shu, L. S., Zhu, W. B., Wang, B., Faure, M., Charvet, J., & Cluzel, D. (2005). The post-collision intracontinental rifting and olistostrome on the southern slope of Bogda Mountains, Xinjiang. Acta Petrologica Sinica, 21(1), 25-36 (in Chinese with

English abstract).

Shu, L. S., Wang, B., Zhu, W. B., Guo, Z. J., Charvet, J., & Zhang, Y. (2011). Timing of initiation of extension in the Tianshan, based on structural, geochemical and geochronological analyses of bimodal volcanism and olistostrome in the Bogda Shan (NW China). International Journal of Earth Sciences, 100, 1647-1663. https://doi.org/10.1007/s00531-010-0575-5

Song, F., Wang, B., Ni, X., Anbar, M. A., Chen, Y., Faure, M., et al. (2024). From early Paleozoic subduction to end-Carboniferous post-orogenic collapse: New constraints on the tectonic evolution of the Central and South Tianshan (NW China). Gondwana Research, 129, 305-331. https://doi.org/10.1016/j.gr.2024.01.001

Song, P., Wang, T., Tong, Y., Zhang, J., Huang, H., & Qin, Q. (2019). Contrasting deep crustal compositions between the Altai and East Junggar orogens, SW Central Asian Orogenic Belt: Evidence from zircon Hf isotopic mapping. Lithos, 328, 297-311.

Song, P., Wang, T., Tong, Y., Zhang, J., & Huang, H. (2023). Late Carboniferous intrusions along the Kalamaili suture zone, southwestern Central Asian Orogenic Belt (CAOB): Implications for a tectonic switch from subduction to collision. International Geology Review, 65(10), 1601-1621. https://doi.org/10.1080/00206814.2022.2098834

Soret, M., Agard, P., Dubacq, B., Plunder, A., & Yamato, P. (2017). Petrological evidence for stepwise accretion of metamorphic soles during subduction infancy (Semail ophiolite, Oman and UAE). Journal of Metamorphic Geology, 35(9), 1051-1080.

Soret, M., Larson, K. P., Cottle, J. M., Smit, M., Johnson, A., Shrestha, S., et al. (2019). Mesozoic to Cenozoic tectono-metamorphic history of the South Pamir–Hindu Kush (Chitral, NW Pakistan): Insights from phase equilibria modelling, and garnet–monazite petrochronology. Journal of Metamorphic Geology, 37(5), 633-666. https://doi.org/10.1111/jmg.12479

Soret, M., Bonnet, G., Agard, P., Larson, K. P., Cottle, J. M., Dubacq, B., et al. (2022). Timescales of subduction initiation and evolution of subduction thermal regimes. Earth and Planetary Science Letters, 584, 117521. https://doi.org/10.1016/j.epsl.2022.117521

Spencer, C. J., Kirkland, C. L., & Taylor, R. J. (2016). Strategies towards statistically robust interpretations of in situ U–Pb zircon geochronology. Geoscience Frontiers, 7(4), 581-589. https://doi.org/10.1016/j.gsf.2015.11.006

Spencer, C. J., Roberts, N. M. W., & Santosh, M. (2017). Growth, destruction, and preservation of Earth's continental crust. Earth-Science Reviews, 172, 87-106.

Stipp, M., StuÈnitz, H., Heilbronner, R., & Schmid, S. M. (2002). The eastern Tonale fault zone: a 'natural laboratory' for crystal plastic deformation of quartz over a temperature range from 250 to 700 °C. Journal of structural geology, 24(12), 1861-1884. https://doi.org/10.1016/S0191-8141(02)00035-4

Sun, G. H. (2007). Structural deformation and tectonic evolution of Harlik Mountain. Xinjiang since the Paleozoic. Dissertation, Chinese Academy of Geological Sciences (in Chinese with English abstract).

Sun, H. R., Lv, Z. C., Yu, X. F., Li, Y. S., Du, Z. Z., Lv, X., et al. (2020). Early Mesozoic tectonic evolution of Beishan Orogenic Belt: Constraints from chronology and geochemistry of the Late Triassic diabase dyke in Liuyuan area, Gansu Province. Acta Petrologica Sinica, 36(6), 1755-1768. https://doi.org/10.18654/1000-0569/2020.06.07

Sun, H. S., Li, H., Danišík, M., Xia, Q., Jiang, C., Wu, P., et al. (2017). U–Pb and Re–Os geochronology and geochemistry of the Donggebi Mo deposit, Eastern Tianshan, NW China: Insights into mineralization and tectonic setting. Ore Geology Reviews, 86, 584-599. https://doi.org/10.1016/j.oregeorev.2017.03.020

Sun, Y., Wang, J., Lv, X., Yu, M., Li, Y., Mao, Q., ... & Long, L. (2019). Geochronology, petrogenesis and tectonic implications of the newly discovered Cu–Ni sulfide-mineralized Yueyawan gabbroic complex, Kalatag district, northwestern Eastern Tianshan, NW China. Ore Geology Reviews, 109, 598-614.

Sun, Y., Wang, J., Wang, Y., Long, L., Mao, Q., & Yu, M. (2019). Ages and origins of granitoids from the Kalatag Cu cluster in Eastern Tianshan, NW China: Constraints on Ordovician–Devonian arc evolution and porphyry Cu fertility in the Southern Central Asian orogenic belt. Lithos, 330, 55-73.

Sun, Z. C., Wang, B., Liu, J., Ni, X., & Song, F. (2021). Age and tectonic setting of Neoproterozoic gneissic granites in the southern Yili Block (NW China) and implications for the origins of the continental blocks in SW Central Asian Orogenic Belt. Geological Journal, 56(10), 5027-5045. https://doi.org/10.1002/gj.4218

Sun, Z. Y., Long, L. L., Wang, Y. W., Luo, Z. H., Hu, Q. T., & Wang, M. L. (2019).

Geology, chronology, fluid inclusions, and H–o–s isotopic compositions of the Hongyuntan magnetite deposit, Eastern Tianshan, NW China. Journal of Asian Earth Sciences, 172, 328-345.

Sun, Z. Y., Wang, J., Wang, Y., Long, L., Luo, Z., Deng, X., ... & Wang, M. (2020). Sodium-rich volcanic rocks and their relationships with iron deposits in the Aqishan–Yamansu belt of Eastern Tianshan, NW China. Geoscience Frontiers, 11(2), 697-713.

Sundell, K. E., Laskowski, A. K., Kapp, P. A., Ducea, M. N., & Chapman, J. B. (2021). Jurassic to Neogene quantitative crustal thickness estimates in southern Tibet. GSA Today, 31(6), 4-10.

Sylvester, P. J. (1998). Post-collisional strongly peraluminous granites. Lithos, 45(1-4), 29-44. https://doi.org/10.1016/S0024-4937(98)00024-3

Tan, Z., Agard, P., Monie, P., Gao, J., John, T., Bayet, L., ... & Caron, B. (2019). Architecture and PT-deformation-time evolution of the Chinese SW-Tianshan HP/UHP complex: Implications for subduction dynamics. Earth-Science Reviews, 197, 102894. https://doi.org/10.1016/j.earscirev.2019.102894

Taira, A. (2001). Tectonic evolution of the Japanese island arc system. Annual Review of Earth and Planetary Sciences, 29(1), 109-134. https://doi.org/10.1146/annurev.earth.29.1.109

Tang, G. J., Wang, Q., Wyman, D. A., & Dan, W. (2019). Crustal maturation through chemical weathering and crustal recycling revealed by Hf–O–B isotopes. Earth and Planetary Science Letters, 524, 115709.

Tang, M., Chen, K., & Rudnick, R. L. (2016). Archean upper crust transition from mafic to felsic marks the onset of plate tectonics. Science, 351(6271), 372-375.

Tang, Y. W., Chen, L., Zhao, Z. F., & Zheng, Y. F. (2020). Geochemical evidence for the production of granitoids through reworking of the juvenile mafic arc crust in the Gangdese orogen, southern Tibet. GSA Bulletin, 132(7-8), 1347-1364. https://doi.org/10.1130/B35304.1

Teng, L. S. (1990). Geotectonic evolution of late Cenozoic arc-continent collision in Taiwan. Tectonophysics, 183(1-4), 57-76. https://doi.org/10.1016/0040-1951(90)90188-E

Thomson, S. N., Gehrels, G. E., Ruiz, J., & Buchwaldt, R. (2012). Routine low-damage apatite U-Pb dating using laser ablation-multicollector-ICPMS. Geochemistry, Geophysics, Geosystems, 13(2). https://doi.org/10.1029/2011GC003928

Tomascak, P. B., Krogstad, E. J., & Walker, R. J. (1996). U-Pb monazite geochronology of granitic rocks from Maine: implications for late Paleozoic tectonics in the Northern Appalachians. The Journal of Geology, 104(2), 185-195. https://doi.org/10.1086/629813

Wali, G., Wang, B., Cluzel, D., & Zhong, L. (2018). Carboniferous–Early Permian magmatic evolution of the Bogda Range (Xinjiang, NW China): Implications for the late Paleozoic accretionary tectonics of the SW Central Asian orogenic belt. Journal of Asian Earth Sciences, 153, 238-251.

Wan, Y., Xie, H., Williams, I. S., Dong, C., & Liu, D. (2021). Dating Metamorphism. In Alderton, D., and Elias, S.A., eds., 2nd, Encyclopedia of Geology, 2, 569-583. https://doi.org/10.1016/B978-0-08-102908-4.00141-7.

Wang, B., Faure, M., Cluzel, D., Shu, L. S., Charvet, J., Meffre, S., & Ma, Q. (2006). Late Paleozoic tectonic evolution of the northern West Chinese Tianshan belt. Geodinamica Acta, 19(3-4), 237-247. https://doi.org/10.3166/ga.19.237-247

Wang, B., Chen, Y., Zhan, S., Shu, L., Faure, M., Cluzel, D., ... & Laurent-Charvet, S. (2007). Primary Carboniferous and Permian paleomagnetic results from the Yili Block (NW China) and their implications on the geodynamic evolution of Chinese Tianshan Belt. Earth and Planetary Science Letters, 263(3-4), 288-308. https://doi.org/10.1016/j.epsl.2007.08.037

Wang, B., Faure, M., Shu, L. S., Cluzel, D., Charvet, J., De Jong, K., & Chen, Y. (2008). Paleozoic tectonic evolution of the Yili Block, western Chinese Tianshan. Bulletin de la Société Géologique de France, 179(5), 483-490. https://doi.org/10.2113/gssgfbull.179.5.483

Wang, B., Cluzel, D., Shu, L. S, Faure, M., Charvet, J., Chen, Y., et al. (2009). Evolution of calc-alkaline to alkaline magmatism through Carboniferous convergence to Permian transcurrent tectonics, western Chinese Tianshan. International Journal of Earth Sciences, 98, 1275-1298. https://doi.org/10.1007/s00531-008-0408-y

Wang, B., Shu, L. S., Faure, M., Jahn, B. M., Cluzel, D., Charvet, J., et al. (2011). Paleozoic tectonics of the southern Chinese Tianshan: Insights from structural, chronological and geochemical studies of the Heiyingshan ophiolitic mélange (NW China). Tectonophysics, 497(1-4), 85-104. https://doi.org/10.1016/j.tecto.2010.11.004

Wang, B., Liu, H., Shu, L., Jahn, B. M., Chung, S. L., Zhai, Y., & Liu, D. (2014). Early Neoproterozoic crustal evolution in northern Yili Block: insights from migmatite, orthogneiss and leucogranite of the Wenquan metamorphic complex in the NW Chinese Tianshan. Precambrian Research, 242, 58-81. https://doi.org/10.1016/j.precamres.2013.12.006

Wang, B., Song, F., Ni, X. H., Cao, T. T., Liu, J. S., Zhong, L. L., et al. (2022). Paleozoic accretionary orogenesis and major transitional tectonic events of the Tianshan orogen. Acta Geologica Sinica, 96(10), 3514-3540 (in Chinese with English abstract).

Wang, B., Zhai, Y., Kapp, P., de Jong, K., Zhong, L., Liu, H., et al. (2018). Accretionary tectonics of back-arc oceanic basins in the South Tianshan: Insights from structural, geochronological, and geochemical studies of the Wuwamen ophiolite mélange. GSA Bulletin, 130(1-2), 284-306. https://doi.org/10.1130/B31397.1

Wang, C. S., Gu, L. X., Zhang, Z. Z., Wu, C. Z., Tang, J. H., & Tang, X. Q. (2009a). Petrogenesis and geological implications of the Permian high-k calc-alkaline granites in Harlik Mountains of eastern Tianshan, NW China. Acta Petrologica Sinica, 25(6), 1499-1511 (in Chinese with English abstract).

Wang, C. S., Gu, L. X., Zhang, Z. Z., Wu, C. Z., Tang, J. H., San, J. Z., et al. (2009b). Petrogenesis and tectonic implications of the Permian alkaline granite and quartzsyenite assemblage in Harlik Mountains, Xinjiang. Acta Petrologica Sinica, 3182-3196 (in Chinese with English abstract).

Wang, F. J., Luo, M., He, Z., Ge, R., Cao, Y., Grave, J. D., & Zhu, W. (2022). Late Mesozoic intracontinental deformation and magmatism in the Chinese Tianshan and adjacent areas, Central Asia. Bulletin, 134(11-12), 3003-3021.

Wang, F. J., He, Z. Y., Ge, R. F., Luo, M., Zheng, B., Zhang, Z., et al. (2024). First identification of late Mesozoic intraplate magmatism in the Chinese north Tianshan: implications for the orogenic architecture and crustal evolution. Journal of the Geological Society, 181(4), jgs2023-176. https://doi.org/10.1144/jgs2023-176

Wang, G. C, Zhang, M., Zhang, X. H., Liao Q. A., Wang, W., Tian, J. M., & Xuan, Z. Y. (2019). Significant Paleozoic tectonic events in the northern part of the East Tianshan Mountains, Xinjiang and their implications for the evolution of CAOB: New evidence from 1∶50000 geological survey of Banfanggou and Xiaoliugou sheets. Geology in China, 46(5): 954-976 (in Chinese with English abstract).

https://doi.org/10.12029/gc20190502

Wang, G. C., Zhang, M., Zhang, X. H., Kang, L., Liao, Q. A., Guo, R. L., Wang, W. (2022). Re-understanding on the tectonic implication and evolutional model of the "North Tianshan Ocean" from the eastern Tianshan area, Xinjiang, NW China. Acta Geologica Sinica, 96(10): 3494-3513 (in Chinese with English abstract). https://doi.org/10.19762/j.cnki.dizhixuebao.2022080

Wang, J., Su, Y., Zheng, J., Belousova, E. A., Chen, M., Dai, H., & Zhou, X. (2021). Petrogenesis of early Carboniferous bimodal-type volcanic rocks from the Junggar Basin (NW China) with implications for Phanerozoic crustal growth in Central Asian Orogenic Belt. Gondwana Research, 89, 220-237. https://doi.org/10.1016/j.gr.2020.10.008

Wang, J., Su, Y., Zheng, J., Belousova, E. A., Chen, M., Dai, H., & Zhou, L. (2022). Rapid transition from oceanic subduction to postcollisional extension revealed by Carboniferous magmatism in East Junggar (NW China), southwestern Central Asian orogenic belt. GSA Bulletin, 134(3-4), 1018-1042. https://doi.org/10.1130/B36074.1

Wang, J. L., Wu, C., Li, Z., Zhu, W. E. N., Zhou, T., Wu, J. U. N., & Wang, J. U. N. (2018). The tectonic evolution of the Bogda region from Late Carboniferous to Triassic time: evidence from detrital zircon U–Pb geochronology and sandstone petrography. Geological Magazine, 155(5), 1063-1088.

Wang, J. L., Wu, C., Zhou, T., Zhu, W., Zhou, Y., Jiang, X., & Yang, D. (2019). Source-to-sink analysis of a transtensional rift basin from syn-rift to uplift stages. Journal of Sedimentary Research, 89(4), 335-352. https://doi.org/10.2110/jsr.2019.19

Wang, J. L., Wu, C. D., Li, Z., Zhou, T. Q., Zhou, Y. X., Feng, G., et al. (2020). The Pennsylvanian composite volcanism in the Bogda Mountains, NW China: Evidence for postcollisional rift basins. Lithosphere, 2020(1). https://doi.org/10.2113/2020/8852440

Wang, L. Y., Liao, Q. A., Xiao, D., Luo, T., Zhao, H., Liu, H. F., & Wang, G. C. (2016). Petrogenesis and tectonic significance of Early Carboniferous A-type grainte in Harlik, Xinjiang. Journal of Geomechanics, 22(4), 1032-1048 (in Chinese with English abstract).

Wang, K., Xiao, W., Mao, Q., Yang, H., Ji, W., Abuduxun, N., ... & Li, Y. (2024). Retreat and advance subduction processes in the Yamansu–Central Tianshan arc (NW

China): insights into the long-lasting accretionary orogenesis and final closure of the Palaeo-Asian Ocean in the southern Altaids. Journal of the Geological Society, 181(3), jgs2022-184.

Wang, Q., Xu, J. F., Jian, P., Bao, Z. W., Zhao, Z. H., Li, C. F., et al. (2006). Petrogenesis of adakitic porphyries in an extensional tectonic setting, Dexing, South China: implications for the genesis of porphyry copper mineralization. Journal of Petrology, 47(1), 119-144. https://doi.org/10.1093/petrology/egi070

Wang, Q., Wyman, D. A., Xu, J., Dong, Y., Vasconcelos, P. M., Pearson, N., et al. (2008). Eocene melting of subducting continental crust and early uplifting of central Tibet: evidence from central-western Qiangtang high-K calc-alkaline andesites, dacites and rhyolites. Earth and Planetary Science Letters, 272(1-2), 158-171. https://doi.org/10.1016/j.epsl.2008.04.034

Wang, Q., Hawkesworth, C. J., Wyman, D., Chung, S. L., Wu, F. Y., Li, X. H., et al. (2016). Pliocene-Quaternary crustal melting in central and northern Tibet and insights into crustal flow. Nature Communications, 7(1), 11888. https://doi.org/10.1038/ncomms11888

Wang, T., Xiao, W. J, Collins, W. J., Tong, Y., Hou, Z., Huang, H., Han, B. et al. (2023). Quantitative characterization of orogens through isotopic mapping. Communications Earth & Environment, 4(1), 110. https://doi.org/10.1038/s43247-023-00779-5

Wang, W., Wang, G., Zhang, M., Polat, A., Guo, R., Zhang, P., ... & Wang, Z. (2024). Structural anatomy of the newly recognized Paleozoic Dacaotan composite mélange belt: Implications for the subduction-accretion processes in the North Tianshan Ocean, southwestern Central Asian Orogenic belt. Gondwana Research.

Wang, X. S., Gao, J., Klemd, R., Jiang, T., Li, J. L., Zhang, X., & Xue, S. C. (2017). The Central Tianshan Block: A microcontinent with a Neoarchean-Paleoproterozoic basement in the southwestern Central Asian orogenic belt. Precambrian Research, 295, 130-150. https://doi.org/10.1016/j.precamres.2017.03.030

Wang, X. S., Klemd, R., Gao, J., Jiang, T., Li, J. L., & Xue, S. C. (2018). Final assembly of the southwestern Central Asian Orogenic Belt as constrained by the evolution of the South Tianshan Orogen: Links with Gondwana and Pangea. Journal of Geophysical Research: Solid Earth, 123(9), 7361-7388. https://doi.org/10.1029/2018JB015689

Wang, X. S., Klemd, R., Li, J. L., Gao, J., Jiang, T., Zong, K. Q., & Xue, S. C. (2022a). Paleozoic Subduction-Accretion in the Southern Central Asian Orogenic Belt: Insights From the Wuwamen Accretionary Complex of the Chinese South Tianshan. Tectonics, 41(2), e2021TC006965. https://doi.org/10.1029/2021TC006965

Wang, X. S., Sun, M., Weinberg, R. F., Cai, K., Zhao, G., Xia, X., et al. (2022b). Adakite generation as a result of fluid-fluxed melting at normal lower crustal pressures. Earth and Planetary Science Letters, 594, 117744. https://doi.org/10.1016/j.epsl.2022.117744

Wang, Y., Li, J., & Sun, G. (2008). Postcollisional eastward extrusion and tectonic exhumation along the Eastern Tianshan orogen, Central Asia: Constraints from dextral strike-slip motion and 40Ar/39Ar geochronological evidence. The Journal of Geology, 116(6), 599-618. https://doi.org/10.1086/591993

Wang, Y. F., Chen, H., Falloon, T. J., & Han, J. (2022). The Paleozoic-Mesozoic magmatic evolution of the Eastern Tianshan, NW China: Constraints from geochronology and geochemistry of the Sanchakou intrusive complex. Gondwana Research, 103, 1-22. https://doi.org/10.1016/j.gr.2021.11.002

Wang, Y. H., Xue, C. J., Liu, J. J., & Zhang, F. F. (2016). Geological, geochronological, geochemical, and Sr–Nd–O–Hf isotopic constraints on origins of intrusions associated with the Baishan porphyry Mo deposit in eastern Tianshan, NW China. Mineralium Deposita, 51, 953-969. https://doi.org/10.1007/s00126-016-0646-z

Wang, Y. J., Jia, D., Pan, J., Wei, D., Tang, Y., Wang, G., ... & Ma, D. (2018). Multiple-phase tectonic superposition and reworking in the Junggar Basin of northwestern China-Implications for deep-seated petroleum exploration. AAPG Bulletin, 102(8), 1489-1521. https://doi.org/10.1306/10181716518

Wang, Y. J., Zhu, D. C., Lin, C., Hu, F., & Liu, J. (2022). Quantifying the growth of continental crust through crustal thickness and zircon Hf-O isotopic signatures: A case study from the southern Central Asian Orogenic Belt. GSA Bulletin, 134(7-8), 2072-2084. https://doi.org/10.1130/B36046.1

Wang, Z. H, Sun, S., Li, J., Hou, Q., Qin, K., Xiao, W., & Hao, J. (2003). Paleozoic tectonic evolution of the northern Xinjiang, China: geochemical and geochronological constraints from the ophiolites. Tectonics, 22(2). https://doi.org/10.1029/2002TC001396

Wasserburg, G. J., Jacobsen, S. B., DePaolo, D. J., McCulloch, M. T., & Wen, T. (1981).

Precise determination of SmNd ratios, Sm and Nd isotopic abundances in standard solutions. Geochimica et Cosmochimica Acta, 45(12), 2311-2323. https://doi.org/10.1016/0016-7037(81)90085-5

Watson, E. B., & Harrison, T. M. (1983). Zircon saturation revisited: temperature and composition effects in a variety of crustal magma types. Earth and Planetary Science Letters, 64(2), 295-304. https://doi.org/10.1016/0012-821X(83)90211-X

Wei, R. Z., Dong, A. G., Li, S., Wang, R. J., & Chai, J. Z. (2011). Discovery and significance of Early Devonian fossils in the Mayileshan area, western Junggar, Xinjiang, China. Geological Bulletin of China, 30(1), 101-105 (in Chinese with English abstract).

Weis, D., Kieffer, B., Maerschalk, C., Barling, J., De Jong, J., Williams, G. A., et al. (2006). High-precision isotopic characterization of USGS reference materials by TIMS and MC-ICP-MS. Geochemistry, Geophysics, Geosystems, 7(8). https://doi.org/10.1029/2006GC001283

Whalen, J. B., & Hildebrand, R. S. (2019). Trace element discrimination of arc, slab failure, and A-type granitic rocks. Lithos, 348, 105179.

White, R.W., Powell, R., Holland, T.J.B. & Worley, B.A. (2000). The effect of TiO2 and Fe2O3 on metapelitic assemblages at greenschist and amphibolite facies conditions: mineral equilibria calculations in the system K2O-FeO-MgO-Al2O3-SiO2-H2O-TiO2-Fe2O3. Journal of Metamorphic Geology, 18(5), 497-511. https://doi.org/10.1046/j.1525-1314.2000.00269.x

Whitney, D. L., & Evans, B. W. (2010). Abbreviations for names of rock-forming minerals. American mineralogist, 95(1), 185-187. https://doi.org/10.2138/am.2010.3371

Winchester, J. A., & Floyd, P. A. (1977). Geochemical discrimination of different magma series and their differentiation products using immobile elements. Chemical geology, 20, 325-343. https://doi.org/10.1016/0009-2541(77)90057-2.

Windley, B. F., Alexeiev, D., Xiao, W., Kröner, A., & Badarch, G. (2007). Tectonic models for accretion of the Central Asian Orogenic Belt. Journal of the Geological Society, 164(1), 31-47. https://doi.org/10.1144/0016-76492006-022

Wood, D. A. (1980). The application of a Th-Hf-Ta diagram to problems of tectonomagmatic classification and to establishing the nature of crustal contamination of basaltic lavas of the British Tertiary Volcanic Province. Earth and planetary science letters, 50(1), 11-30. https://doi.org/10.1016/0012-821X(80)90116-8

Woodhead, J. D., & Hergt, J. M. (2005). A preliminary appraisal of seven natural zircon reference materials for in situ Hf isotope determination. Geostandards and Geoanalytical Research, 29(2), 183-195. https://doi.org/10.1111/j.1751-908X.2005.tb00891.x

Wu, B., Long, X., Zhang, S., Zhang, Y., Huang, Z., & Du, L. (2023). Carboniferous variation of crustal thickness and subduction angles in Eastern Tianshan, NW China: evidence from the petrogenesis of the magmatic rocks in the Aqishan–Yamansu Belt. International Geology Review, 65(5), 682-705.

Wu, C., Chiaradia, M., Tang, G., & Chen, H. (2023). Crustal control on the petrogenesis of adakite-like rocks. Chemical Geology, 632, 121548. https://doi.org/10.1016/j.chemgeo.2023.121548

Wu, C. M., Zhang, J., & Ren, L. D. (2004). Empirical garnet-biotite-plagioclase-quartz (GBPQ) geobarometry in medium-to high-grade metapelites. Journal of Petrology, 45(9), 1907-1921. https://doi.org/10.1093/petrology/egh038

Wu, C. M. (2017). Calibration of the garnet-biotite-Al2SiO5-quartz geobarometer for metapelites. Journal of Metamorphic geology, 35(9), 983-998. https://doi.org/10.1111/jmg.12264

Wu, C. Z., Zhang, Z. Z., Gu, L. X., Tang, J. H., & Lei, R. X. (2010). Sr, Nd and O isotopic characters of quartz syenite in the Weiya magmatic complex from eastern Tianshan in NW China: Melting of the thickened juvenile lower crust. Geochemical Journal, 44(4), 285-298. https://doi.org/10.2343/geochemj.1.0072

Wu, C. Z., Xie, S. W., Gu, L. X., Samson, I. M., Yang, T., Lei, R. X., ... & Dang, B. (2018). Shear zone-controlled post-magmatic ore formation in the Huangshandong Ni–Cu sulfide deposit, NW China. Ore Geology Reviews, 100, 545-560.

Wu, F. Y., Li, X. H., Zheng, Y. F., & Gao, S. (2007). Lu-Hf isotopic systematics and their applications in petrology. Acta Petrologica Sinica, 23(2): 185-220 (in Chinese with English abstract).

Wu, S. C., Huang, R., Xu, Y., Yang, Y., Jiang, X., & Zhu, L. (2018). Seismological evidence for a remnant oceanic slab in the western Junggar, Northwest China. Journal of Geophysical Research: Solid Earth, 123(5), 4157-4170.

Wu, S. C., Yang, Y., Xu, Y., Afonso, J. C., & Zhang, A. (2023). A fossil oceanic lithosphere preserved inside a continent. Geology, 51(2), 204-208.

Wu, Y. S., Zhou, K. F., Li, N., & Chen, Y. J. (2017). Zircon U–Pb dating and Sr–Nd–Pb–Hf isotopes of the ore-associated porphyry at the giant Donggebi Mo deposit, Eastern Tianshan, NW China. Ore Geology Reviews, 81, 794-807. https://doi.org/10.1016/j.oregeorev.2016.02.007

XBGMR (Xinjiang Bureau of Geology and Mineral Resources). (1993). Regional Geology of Xinjiang Uygur Autonomy Region. Geology Publishing House, Beijing, 1-841 (in Chinese).

Xiao, D., Zhao, X., Liao, Q. A., Zhao, H., & Zeng, Z. (2020). Early Palaeozoic arc-related gabbro-diorite suite in East Junggar, southern Central Asian Orogenic Belt: petrogenesis and tectonic implications. International Geology Review, 62(9), 1205-1223. https://doi.org/10.1080/00206814.2019.1641852

Xiao, W. J., Zhang, L. C., Qin, K. Z., Sun, S. H. U., & Li, J. L. (2004). Paleozoic accretionary and collisional tectonics of the Eastern Tianshan (China): implications for the continental growth of central Asia. American Journal of Science, 304(4), 370-395. https://doi.org/10.2475/ajs.304.4.370

Xiao, W. J., Windley, B. F., Yan, Q. R., Qin, K. Z., Chen, H. L., Yuan, C., Sun, M., et al. (2006). SHRIMP zircon age of the Aermantai ophiolite in the North Xinjiang area, China and its tectonic implications. Acta Geologica Sinica, 80, 32-37 (in Chinese with English abstract).

Xiao, W. J., Windley, B. F., Yuan, C., Sun, M., Han, C. M., Lin, S. F., ... & Sun, S. (2009). Paleozoic multiple subduction-accretion processes of the southern Altaids. American Journal of Science, 309(3), 221-270.

Xiao, W. J., Windley, B. F., Allen, M. B., & Han, C. (2013). Paleozoic multiple accretionary and collisional tectonics of the Chinese Tianshan orogenic collage. Gondwana Research, 23(4), 1316-1341. https://doi.org/10.1016/j.gr.2012.01.012

Xiao, W. J., & Santosh, M. (2014). The western Central Asian Orogenic Belt: a window to accretionary orogenesis and continental growth. Gondwana Research, 25(4), 1429-1444.

Xiao, W. J., Windley, B. F., Sun, S., Li, J., Huang, B., Han, C., et al. (2015). A tale of amalgamation of three Permo-Triassic collage systems in Central Asia: Oroclines, sutures, and terminal accretion. Annual review of earth and planetary sciences, 43,

477-507. https://doi.org/10.1146/annurev-earth-060614-105254
Xiao, X. C., Tang, Y. Q., Feng, Y. M., Zhu, B. Q., Li, J. Y., & Zhao, M. (1992). Tectonic Evolution of the Northern Xinjiang and its Adjacent Regions. Geology Publishing House, Beijing (in Chinese with English abstract).
Xie, W., Xu, Y. G., Chen, Y. B., Luo, Z. Y., Hong, L. B., Ma, L., & Liu, H. Q. (2016). High-alumina basalts from the Bogda Mountains suggest an arc setting for Chinese Northern Tianshan during the Late Carboniferous. Lithos, 256, 165-181. https://doi.org/10.1016/j.lithos.2016.04.005
Xie, W., Lu, Y., Song, X. Y., Deng, Y. F., Liang, Q. L., & Yi, J. N. (2022). A late Carboniferous bimodal volcanic suite before closure of the North Tianshan Ocean at the southwestern margin of the Central Asian Orogenic Belt. Journal of Asian Earth Sciences, 226, 105090. https://doi.org/10.1016/j.jseaes.2022.105090
Xu, J. F., Shinjo, R., Defant, M. J., Wang, Q., & Rapp, R. P. (2002). Origin of Mesozoic adakitic intrusive rocks in the Ningzhen area of east China: partial melting of delaminated lower continental crust?. Geology, 30(12), 1111-1114. https://doi.org/10.1130/0091-7613(2002)030%3C1111:OOMAIR%3E2.0.CO;2
Xu, Q. Q., Zhao, L., Niu, B., Zheng, R., Yang, Y., & Liu, J. (2020). Early Paleozoic arc magmatism in the Kalamaili orogenic belt, Northern Xinjiang, NW China: Implications for the tectonic evolution of the East Junggar terrane. Journal of Asian Earth Sciences, 194, 104072.
Xu, W., Song, B., Wang, B., Shi, J., Zhao, Y., Zhang, H., et al. (2023). New paleomagnetic and geochronologic results from late Paleozoic rocks in the Turfan-Hami block (NW China) and implications for the geodynamic evolution of the western Altaids. Geological Society of America Bulletin. https://doi.org/10.1130/B37055.1
Xu, X. W., Ma, T. L., Sun, L. Q., & Cai, X. P. (2003). Characteristics and dynamic origin of the large-scale Jiaoluotage ductile compressional zone in the eastern Tianshan Mountains, China. Journal of Structural Geology, 25(11), 1901-1915.
Xu, X. W., Jiang, N., Li, X. H., Qu, X., Yang, Y. H., Mao, Q., ... & Dong, L. H. (2013). Tectonic evolution of the East Junggar terrane: Evidence from the Taheir tectonic window, Xinjiang, China. Gondwana Research, 24(2), 578-600.
Xu, X. Y., Li, X. M., Ma, Z. P., Xia, L. Q., Xia, Z. C., & Peng, S. X. (2006). LA-ICPMS zircon U-Pb dating of gabbro from the Bayingou ophiolite in the northern Tianshan

Mountains. Acta Geol. Sin. 80, 1168–1176 (in Chinese with English abstract).
Xu, Z., Han, B. F., Ren, R., Zhou, Y. Z., Zhang, L., Chen, J. F., ... & Liu, D. Y. (2012). Ultramafic–mafic mélange, island arc and post-collisional intrusions in the Mayile Mountain, West Junggar, China: implications for Paleozoic intra-oceanic subduction-accretion process. Lithos, 132, 141-161. https://doi.org/10.1016/j.lithos.2011.11.016
Yakymchuk, C., & Brown, M. (2014). Behaviour of zircon and monazite during crustal melting. Journal of the Geological Society, 171(4), 465-479. https://doi.org/10.1144/jgs2013-115
Yang, G. X., Li, Y., Wu, H., Zhong, X., Yang, B., Yan, C., ... & Si, G. (2011). Geochronological and geochemical constrains on petrogenesis of the Huangyangshan A-type granite from the East Junggar, Xinjiang, NW China. Journal of Asian Earth Sciences, 40(3), 722-736.
Yang, W. B., Niu, H. C., Shan, Q., Sun, W. D., Zhang, H., Li, N. B., ... & Yu, X. Y. (2014). Geochemistry of magmatic and hydrothermal zircon from the highly evolved Baerzhe alkaline granite: implications for Zr–REE–Nb mineralization. Mineralium Deposita, 49, 451-470.
Yang, Y. T., Guo, Z. X., & Luo, Y. J. (2017). Middle-Late Jurassic tectonostratigraphic evolution of Central Asia, implications for the collision of the Karakoram-Lhasa Block with Asia. Earth-Science Reviews, 166, 83-110.
Yao, Y., Xing, W. W., Jia, H. X., Wang, Y. G., Zhao, Z. N., Ma, M. L., & Guo, S. E. (2020). Geochronology, geochemistry and tectonic significance of Southern Xiamaya granite in Harlik area, Dongtianshan Mountain. Mineralogy and Petrology, 40, 30-43 (in Chinese with English abstract).
Yuan, C., Sun, M., Wilde, S., Xiao, W., Xu, Y., Long, X., & Zhao, G. (2010). Post-collisional plutons in the Balikun area, East Chinese Tianshan: evolving magmatism in response to extension and slab break-off. Lithos, 119(3-4), 269-288. https://doi.org/10.1016/j.lithos.2010.07.004
Yuan, J. G., Tong, Y., Zhang, H. F., & Geng, X. X. (2023). Partial melting of thickened lower crust in the intraplate setting: constraints from triassic postectonic baishandong granitic pluton in Eastern Tianshan. International Geology Review, 65(2), 253-277. https://doi.org/10.1080/00206814.2022.2042861
Zeng, L. J., Niu, H., Bao, Z., Shan, Q., Li, H., Li, N., & Yang, W. (2015). Petrogenesis

and tectonic significance of the plagiogranites in the Zhaheba ophiolite, Eastern Junggar orogen, Xinjiang, China. Journal of Asian Earth Sciences, 113, 137-150.

Zha, Y., Wang, G., Shen, T., Cao, T., & Zhang, P. Geochronology and Deformation Stages of Koumenzi Ductile Shear Zone in Harlik Mountain, Xinjiang. Geotectonica et Metallogenia, 2020(2), 297-310 (in Chinese with English abstract).

Zhang, D. Y., Zhou, T. F., Yuan, F., Fiorentini, M. L., Said, N., Lu, Y., & Pirajno, F. (2013). Geochemical and isotopic constraints on the genesis of the Jueluotage native copper mineralized basalt, Eastern Tianshan, Northwest China. Journal of Asian Earth Sciences, 73, 317-333. https://doi.org/10.1016/j.jseaes.2013.04.043

Zhang, F. F., Wang, Y., Liu, J., & Wang, J. (2015). Zircon U–Pb and molybdenite Re–Os geochronology, Hf isotope analyses, and whole-rock geochemistry of the Donggebi Mo deposit, eastern Tianshan, Northwest China, and their geological significance. International Geology Review, 57(4), 446-462. https://doi.org/10.1080/00206814.2015.1013067

Zhang, J. E., Chen, Y., Xiao, W., Wakabayashi, J., Windley, B. F., & Yin, J. (2021). Sub-parallel ridge-trench interaction and an alternative model for the Silurian-Devonian archipelago in Western Junggar and North-Central Tianshan in NW China. Earth-Science Reviews, 217, 103648. https://doi.org/10.1016/j.earscirev.2021.103648

Zhang, J. E., Xiao, W., Luo, J., Chen, Y., Windley, B. F., Song, D., ... & Safonova, I. (2018). Collision of the Tacheng block with the Mayile-Barleik-Tangbale accretionary complex in Western Junggar, NW China: Implication for Early-Middle Paleozoic architecture of the western Altaids. Journal of Asian Earth Sciences, 159, 259-278. https://doi.org/10.1016/j.jseaes.2017.03.023

Zhang, J. J., Wang, T., Tong, Y., Zhang, Z., Song, P., Zhang, L., ... & Hou, Z. (2017). Tracking deep ancient crustal components by xenocrystic/inherited zircons of Palaeozoic felsic igneous rocks from the Altai–East Junggar terrane and adjacent regions, western Central Asian Orogenic Belt and its tectonic significance. International Geology Review, 59(16), 2021-2040. https://doi.org/10.1080/00206814.2017.1308841

Zhang, L. C., Xiao, W., Qin, K., & Zhang, Q. (2006). The adakite connection of the Tuwu–Yandong copper porphyry belt, eastern Tianshan, NW China: trace element and Sr-Nd-Pb isotope geochemistry. Mineralium Deposita, 41, 188-200.

Zhang, L. F., Ai, Y., Song, S., Liou, J., & Wei, C. (2007). A brief review of UHP meta-ophiolitic rocks, Southwestern Tianshan, Western China. International Geology Review, 49(9), 811-823.

Zhang, M., Wang, G. C., Zhang, X., Wang, W., Guo, R., & Zhang, P. (2021). Reconstruction of the Silurian to Devonian stratigraphic succession along the northeastern margin of the Junggar block, Xinjiang, NW China, and its tectono-paleogeographic implications for the southwestern Central Asian Orogenic Belt. Sedimentary Geology, 411, 105780. https://doi.org/10.1016/j.sedgeo.2020.105780

Zhang, S. L., Chen, H., Hollings, P., Zhao, L., & Gong, L. (2021). Tectonic and magmatic evolution of the Aqishan-Yamansu belt: A Paleozoic arc-related basin in the Eastern Tianshan (NW China). Bulletin, 133(5-6), 1320-1344.

Zhang, W. F., Chen, H., Han, J., Zhao, L., Huang, J., Yang, J., & Yan, X. (2016). Geochronology and geochemistry of igneous rocks in the Bailingshan area: Implications for the tectonic setting of late Paleozoic magmatism and iron skarn mineralization in the eastern Tianshan, NW China. Gondwana Research, 38, 40-59.

Zhang, X. R., Zhao, G., Eizenhöfer, P. R., Sun, M., Han, Y., Hou, W., ... & Xu, B. (2015). Latest Carboniferous closure of the Junggar Ocean constrained by geochemical and zircon U–Pb–Hf isotopic data of granitic gneisses from the Central Tianshan block, NW China. Lithos, 238, 26-36.

Zhang, X. R., Zhao, G. C., Sun, M., Eizenhöfer, P. R., Han, Y. G., Hou, W., et al. (2016a). Tectonic evolution from subduction to arc-continent collision of the Junggar ocean: Constraints from U-Pb dating and Hf isotopes of detrital zircons from the North Tianshan belt, NW China. GSA Bulletin, 128(3-4), 644-660. https://doi.org/10.1130/B31230.1

Zhang, X. R, Zhao, G., Eizenhöfer, P. R., Sun, M., Han, Y., Hou, W., ... & Xu, B. (2016b). Late Ordovician adakitic rocks in the Central Tianshan block, NW China: Partial melting of lower continental arc crust during back-arc basin opening. Bulletin, 128(9-10), 1367-1382.

Zhang, X. R., Zhao, G., Sun, M., Han, Y., & Liu, Q. (2017). Triassic magmatic reactivation in Eastern Tianshan, NW China: Evidence from geochemistry and zircon U-Pb-Hf isotopes of granites. Journal of Asian Earth Sciences, 145, 446-

459.
Zhang, Y. Y., Guo, Z., Pe-Piper, G., & Piper, D. J. (2015). Geochemistry and petrogenesis of Early Carboniferous volcanic rocks in East Junggar, North Xinjiang: Implications for post-collisional magmatism and geodynamic process. Gondwana Research, 28(4), 1466-1481. https://doi.org/10.1016/j.gr.2014.08.018
Zhang, Y. Y., Yuan, C., Long, X. P., Sun, M., Huang, Z. Y., Du, L., & Wang, X. (2017). Carboniferous bimodal volcanic rocks in the Eastern Tianshan, NW China: evidence for arc rifting. Gondwana Research, 43, 92-106. https://doi.org/10.1016/j.gr.2016.02.004
Zhang, Y. Y., Sun, M., Yin, J., Yuan, C., Sun, Z., & Xia, X. (2022). Maturation of East Junggar oceanic arc related to supracrustal recycling driven by arc–arc collision: perspectives from zircon Hf–O isotopes. International Journal of Earth Sciences, 111(8), 2519-2533.
Zhang, Z. C., Zhou, G., Kusky, T. M., Yan, S., Chen, B., & Zhao, L. (2009). Late Paleozoic volcanic record of the Eastern Junggar terrane, Xinjiang, Northwestern China: major and trace element characteristics, Sr–Nd isotopic systematics and implications for tectonic evolution. Gondwana Research, 16(2), 201-215.
Zhang, Z. Z., Gu, L. X., Wu, C. Z., Li, W. Q., Xi, A. H., & Wang, S. (2005). Zircon SHRIMP dating for the Weiya pluton, eastern Tianshan: its geological implications. Acta Geologica Sinica (English edition) 79, 481-490. https://doi.org/10.1111/j.1755-6724.2005.tb00914.x
Zhang, Z. Z., Gu, L. X., Wu, C. Z., Zhai, J. P., Li, W. Q., & Tang, J. H. (2007). Early Indosinian Weiya Gabbro in Eastern Tianshan, China: Elemental and Sr-Nd-O Isotopic Geochemistry, and Its Tectonic Implications. Acta Geologica Sinica-English Edition, 81(3), 424-432. https://doi.org/10.1111/j.1755-6724.2007.tb00965.x
Zhao, H., Liao, Q., Li, S., Xiao, D., Wang, G., Guo, R., ... & Li, X. (2022). Early Paleozoic tectonic evolution and magmatism in the Eastern Tianshan, NW China: Evidence from geochronology and geochemistry of volcanic rocks. Gondwana Research, 102, 354-371. https://doi.org/10.1016/j.gr.2019.12.016
Zhao, L. D., Chen, H., Hollings, P., & Han, J. (2019a). Late Paleozoic magmatism and metallogenesis in the Aqishan-Yamansu belt, Eastern Tianshan: Constraints from the Bailingshan intrusive complex. Gondwana Research, 65, 68-85.

Zhao, L.D., Chen, H., Hollings, P., & Han, J. (2019b). Tectonic transition in the Aqishan-Yamansu belt, Eastern Tianshan: Constraints from the geochronology and geochemistry of Carboniferous and Triassic igneous rocks. Lithos, 344, 247-264.

Zhao, M., Shu, L. S., & Wang, C. Y. (1997). Characteristics of metamorphism in the Harlik Metamorphic Belt, east Xinjiang, and its tectonic envorionment. Geological Journal of China Universities, 3 (1), 40-50 (in Chinese with English abstract).

Zhao, X., Seltmann, R., Xue, C., & Sun, Q. (2024). Orogenic cyclicity and episodic tectono-magmatic processes in the formation of the Paleozoic northern Yili magmatic arc, Central Asian Orogenic Belt. GSA Bulletin, 136(5-6), 2137-2156. https://doi.org/10.1130/B37192.1

Zheng, J. P., Sun, M., Zhao, G., Robinson, P. T., & Wang, F. (2007). Elemental and Sr–Nd–Pb isotopic geochemistry of Late Paleozoic volcanic rocks beneath the Junggar basin, NW China: implications for the formation and evolution of the basin basement. Journal of Asian Earth Sciences, 29(5-6), 778-794.

Zheng, Y. F., & Chen, Y. X. (2016). Continental versus oceanic subduction zones. National Science Review, 3(4), 495-519. https://doi.org/10.1093/nsr/nww049

Zheng, Y. F., & Gao, P. (2021). The production of granitic magmas through crustal anatexis at convergent plate boundaries. Lithos, 402, 106232. https://doi.org/10.1016/j.lithos.2021.106232

Zhong, L. L, Wang, B., de Jong, K., Zhai, Y. Z, & Liu, H. (2019). Deformed continental arc sequences in the South Tianshan: New constraints on the Early Paleozoic accretionary tectonics of the Central Asian Orogenic Belt. Tectonophysics, 768, 228169. https://doi.org/10.1016/j.tecto.2019.228169

Zhou, M. F., Lesher, C. M., Yang, Z., Li, J., & Sun, M. (2004). Geochemistry and petrogenesis of 270 Ma Ni–Cu–(PGE) sulfide-bearing mafic intrusions in the Huangshan district, Eastern Xinjiang, Northwest China: implications for the tectonic evolution of the Central Asian orogenic belt. Chemical Geology, 209(3-4), 233-257.

Zhou, T. F., Yuan, F., Fan, Y., Zhang, D., Cooke, D., & Zhao, G. (2008). Granites in the Sawuer region of the west Junggar, Xinjiang Province, China: geochronological and geochemical characteristics and their geodynamic significance. Lithos, 106(3-4), 191-206. https://doi.org/10.1016/j.lithos.2008.06.014

Zhu, D. C., Wang, Q., Weinberg, R. F., Cawood, P. A., Chung, S. L., Zheng, Y. F., ... & Mo, X. X. (2022). Interplay between oceanic subduction and continental collision in building continental crust. Nature Communications, 13(1), 7141.

Zhu, R., Zhao, G., Xiao, W., Chen, L., & Tang, Y. (2021). Origin, accretion, and reworking of continents. Reviews of Geophysics, 59(3), e2019RG000689.

Zhu, X., Wang, B., Chen, Y., & Liu, H. (2019). Constraining the Intracontinental Tectonics of the SW Central Asian Orogenic Belt by the Early Permian Paleomagnetic Pole for the Turfan-Hami Block. Journal of Geophysical Research: Solid Earth, 124(12), 12366-12387. https://doi.org/10.1029/2019JB017680

Zhu, X. H., Zhu, T., Zhang, X., Xi, R. G., Meng, Y., Wang, K. (2018). Petrogenesis and geological implications of late Carboniferous leucogranites in Harlik aera, eastern Xinjiang. Earth Science, 43, 179-194 (in Chinese with English abstract).

Zhu, X. Y., Wang, B., Cluzel, D., He, Z., Zhou, Y., & Zhong, L. (2019). Early Neoproterozoic gneissic granitoids in the southern Yili Block (NW China): Constraints on microcontinent provenance and assembly in the SW Central Asian Orogenic Belt. Precambrian Research, 325, 111-131. https://doi.org/10.1016/j.precamres.2019.02.019

Zhu, X. Y, Wang, B., Sun, Z., Liu, J., He, Z., & Zhong, L. (2020). Detrital zircon ages of the Mesoproterozoic metasedimentary rocks in the southern Yili Block: Implications for tectonic affinities of the microcontinents in SW Central Asian Orogenic Belt. Precambrian Research, 350, 105926. https://doi.org/10.1016/j.precamres.2020.105926

Appendices

Table A1. Compilation of the late Paleozoic magmatic rocks in the eastern Tianshan and East Junggar.

Tectonic unit	Localty	Sample No.	Rock type		E	N	Mineral	Method	Age	2s	Ref. Author	Ref. Year
BHD	Baiyanggou	640	Basalt	Arc-type	88° 1'00"	43°40'0"	Zircon	LA-ICP-MS	296	3	Chen XJ et al.	2011
BHD	Baiyanggou	641	Rhyolite	A-type	88° 1'00"	43°40'0"	Zircon	LA-ICP-MS	293	2	Chen XJ et al.	2011
BHD	Qijiaojing	647	Rhyolite	A-type	91° 30'00"	43°35'0"	Zircon	LA-ICP-MS	294	2	Chen XJ et al.	2011
BHD	Hongshankou	650	Rhyolite	A-type	91° 44'00"	43°23'00"	Zircon	LA-ICP-MS	294	2	Chen XJ et al.	2011
BHD	Cheguluquan	652	Rhyolite	A-type	92° 06'00"	43°28'00"	Zircon	LA-ICP-MS	294	2	Chen XJ et al.	2011
BHD	Cheguluquan	653	Basalt	Arc-type	92° 06'05"	43°28'00"	Zircon	LA-ICP-MS	295	4	Chen XJ et al.	2011
BHD	Hongshankou	648-1	Rhyolite	A-type	91°30'00"	43°24'00"	Zircon	LA-ICP-MS	344	2	Chen XJ et al.	2013
BHD	Hongshankou	648-2	Rhyolite	A-type	91°30'01"	43°24'01"	Zircon	LA-ICP-MS	345	2	Chen XJ et al.	2013
BHD	Hongshankou	648	Basalt	Arc-type	91°30'02"	43°24'02"	Zircon	LA-ICP-MS	347	4	Chen XJ et al.	2013

BHD	Sepikou	SP-RZ1	Quartz keratophyre	Arc-type	91°21'00"	43°49'00"	Zircon	LA-ICP-MS	315	1	Gao J et al.	2018
BHD	Sepikou	SE-RZ2	Rhyolite	A-type	91°18'00"	43°48'00"	Zircon	LA-ICP-MS	314	1	Gao J et al.	2018
BHD	Dalonggou	JL23-5	Andesite	Arc-type	89°06'00"	43°44'00"	Zircon	LA-ICP-MS	310	3	Li D et al.	2021
BHD	Dalonggou	JL23-10	Granite porphyry	I-type	89°06'10"	43°44'00"	Zircon	LA-ICP-MS	289	3	Li D et al.	2021
BHD	Dalonggou	JL23-15	MME	Arc-type	89°06'10"	43°44'01"	Zircon	LA-ICP-MS	290	4	Li D et al.	2021
BHD	Liushugou	18LS08	Diabase dike	Arc-type	87°55'00"	43°41'30"	Zircon	LA-ICP-MS	308	5	Memtimin M et al.	2020
BHD	Haxionggou	16HXG-12	Rhyolite	A-type	87°57'22"	43°49'36"	Zircon	LA-ICP-MS	310	2	Wang J et al.	2020
BHD	Haxionggou	16HXG-13	Rhyolite	A-type	87°57'15"	43°49'41"	Zircon	LA-ICP-MS	301	3	Wang J et al.	2020
BHD	Qijiaojing	16QJJ-15	Rhyolite	A-type	91°38'56"	43°40'59"	Zircon	LA-ICP-MS	309	3	Wang J et al.	2020
BHD	Baiyanggou	BYG-14	Dacite ignimbrite	Arc-type	88°03'00"	43°41'00"	Zircon	SHRIMP	311	2	Xie W et al.	2016a
BHD	Dashitou	DST-02	Trachyte ignimbrite	Arc-type	91°10'00"	43°44'00"	Zircon	SHRIMP	319	3	Xie W et al.	2016 b
BHD	Tianchi	TC-23	Trachyte ignimbrite	Arc-type	88°07'00"	43°54'30"	Zircon	SHRIMP	315	2	Xie W et al.	2016 b
BHD	Daheyan	D01	syenogranite	A-type	88°52'00"	43°22'30"	Zircon	LA-ICP-MS	308	1	Zhang XB et al.	2020
BHD	Daheyan	D02	Diorite	Arc-type	88°50'00"	43°22'00"	Zircon	LA-ICP-MS	311	2	Zhang XB et al.	2020
BHD	Daheyan	D03	Granodiorite	I-type	88°38'00"	43°20'00"	Zircon	LA-ICP-MS	303	1	Zhang XB et al.	2020
BHD	Daheyan	D04	Monzonite	I-type	88°37'00"	43°19'00"	Zircon	LA-ICP-MS	304	2	Zhang XB et al.	2020

BHD	Dashitou	ET4QJ22	Rhyolite	A-type	91°30'00"	43°52'00"	Zircon	LA-ICP-MS	330	3	Zhang YY et al.	2017
BHD	Hongshankou	ET4QJ30	dolerite	Arc-type	91°42'00"	43°22'00"	Zircon	LA-ICP-MS	302	3	Zhang YY et al.	2020
BHD	Hongshankou	ET4QJ31	dolerite	Arc-type	91°42'01"	43°22'01"	Zircon	LA-ICP-MS	305	2	Zhang YY et al.	2020
BHD	Sepikou	SP-RZ3	Diabase	Arc-type	91°29'00"	43°37'00"	Zircon	LA-ICP-MS	301	2	Gao JG et al.	2013
BHD	Sangeshan	TS101	Quartz diorite	Arc-type	88°32'00"	43°39'00"	Zircon	SHRIMP	335	2	Li P et al.	2013
BHD	Sangechagou	SGCG-23	Gabbro	Arc-type	88°34'25.4"	43°45'8.6"	Zircon	LA-ICP-MS	305	2	Liu L et al.	2020
BHD	Mulei	PM12-25	Diabase	Arc-type	90°16'00"	43°42'00"	Zircon	LA-ICP-MS	306	3	Long DH	2021
BHD	Xidi		Basalt	Arc-type	91°22'00"	43°53'00"	Whole rock	Rb-Sr isochron	322	3	Tian LP et al.	2010
BHD	Balikun	10XJ-121	Diorite	Arc-type	93°03'00"	43°34'00"	Zircon	LA-ICP-MS	332	4	Wang C et al.	2018
BHD	Balikun	10XJ-93	Diorite	Arc-type	92°32'00"	44°02'00"	Zircon	LA-ICP-MS	327	3	Wang C et al.	2018
BHD	Saerqiaok	BD86	Dacite	A-type	92°30'00"	43°57'00"	Zircon	LA-ICP-MS	320	1	Wang XW et al.	2015
BHD	Kezikuduk	BD07	Basalt	Arc-type	91°49'10"	43°48'10"	Zircon	LA-ICP-MS	331	3	Wang XW et al.	2015
BHD	Jijitaizi	BD117	Rhyolite	A-type	91°50'30"	43°45'40"	Zircon	LA-ICP-MS	312	1	Wang XW et al.	2015
BHD	Shagoukuduk		Diorite	Arc-type	92°29'16.0"	43°48'0.10"	Zircon	LA-ICP-MS	342	3	Wang XW et al.	2015
BHD	Qijiaojing		Basalt	Arc-type	92°27'00"	43°46'00"	Whole rock	Rb-Sr isochron	342	3	Wang YX et al.	2006

BHD	Qijiaojing		Rhyolite	Unclassified	92°27'01"	43°46'01"	Whole rock	Rb-Sr isochron	340	3	Wang YX et al.	2006
BHD	Qijiaojing	XN16-A1	Rhyolite	A-type	91°44'0"	43°22'60"	Zircon	SHRIMP	296	2	Zhu JJ et al.	2020
BHD	Dabancheng	753	Diorite	Arc-type	88°28'13"	43°11'53"	Zircon	LA-ICP-MS	283	3	Ma XX et al.	2015
BHD	Dabancheng	753-4	Granite	A-type	88°28'13"	43°11'53"	Zircon	LA-ICP-MS	279	5	Ma XX et al.	2015
BHD	Heicaotan	X3ET372	Porphyritic granite	I-type	92°27'11"	42°28'15"	Zircon	LA-ICP-MS	357	3	Du L et al.	2019
BHD	Heicaotan	X3ET459	K-feldspar granite	I-type	93°19'5"	42°15'52"	Zircon	LA-ICP-MS	311	3	Du L et al.	2019
BHD	Nanbeidagou	X3ET-239	Porphyritic granite	I-type	92°25'00"	42°06'00"	Zircon	LA-ICP-MS	360	3	Du L et al.	2019
BHD	Nanbeidagou	X3ET-282	Granite	I-type	92°29'00"	42°07'00"	Zircon	LA-ICP-MS	348	2	Du L et al.	2019
BHD	Nanbeidagou	X3ET-232	Porphyritic granite	Adakitic	92°15'00"	42°06'50"	Zircon	LA-ICP-MS	317	5	Du L et al.	2019
BHD	Nanbeidagou	X3ET-222	Granodiorite porphyry	Adakitic	92°15'00"	42°06'00"	Zircon	LA-ICP-MS	310	2	Du L et al.	2019
BHD	Nanbeidagou	X3ET-223	Granodiorite	Adakitic	92°15'00"	42°06'30"	Zircon	LA-ICP-MS	302	4	Du L et al.	2019
BHD	Tuwu	TW	Plagiogranite porphyry	Adakitic	92°37'00"	42°07'00"	Zircon	LA-ICP-MS	339	1	Han ZK et al.	2013
BHD	Yandong	YD	Plagiogranite porphyry	Adakitic	92°31'00"	42°06'00"	Zircon	LA-ICP-MS	338	1	Han ZK et al.	2013
BHD	Nanbeidagou	ETS1910	Granite	Unclassified	92°17'00"	42°06'50"	Zircon	LA-ICP-MS	314	3	Hu J et al.	2021
BHD	Dananhu	d1-11	Andesite	Arc-type	92°55'00"	42°30'00"	Feldspar	Ar-Ar	321	10	Liu HQ et al.	2016
BHD	Dananhu	d16-1	Basalt	Arc-type	92°55'10"	42°30'10"	Feldspar	Ar-Ar	279	4	Liu HQ et al.	2016
BHD	Kalatage	10SF02	Rhyolite	A-type	91°49'00"	42°29'00"	Zircon	SIMS	287	2	Mao QG et al.	2014
BHD	Kalatage	10SF01	Gabbro	Arc-type	91°49'10"	42°29'10"	Zircon	SIMS	287	2	Mao QG et al.	2014

BHD	Xiaorequanzi	12XR09	Porphyritic granite	Unclassified	89°33'45"	42°14'40"	Zircon	LA-ICP-MS	355	3	Mao QG et al.	2020
BHD	Xiaorequanzi	12XR04	Porphyritic dacite	Unclassified	89°33'50"	42°14'30"	Zircon	LA-ICP-MS	360	3	Mao QG et al.	2020
BHD	Kalatage	13TH03	Basaltic andesite	Arc-type	91°41'10"	42°34'10"	Zircon	SHRIMP	285	6	Mao QG et al.	2021
BHD	Kalatage	11TH04	Rhyolite	A-type	91°41'20"	42°34'00"	Zircon	LA-ICP-MS	275	2	Mao QG et al.	2021
BHD	Kalatage	12KL19	Rhyolite	I-type	91°54'22"	42°38'31"	Zircon	LA-ICP-MS	299	2	Mao QG et al.	2021
BHD	Kalatage	12KL18	Rhyolite	I-type	91°49'0.5"	42°39'36"	Zircon	LA-ICP-MS	301	2	Mao QG et al.	2021
BHD	Kalatage	12KL20	Dacite	I-type	91°54'28"	42°38'26"	Zircon	LA-ICP-MS	301	1	Mao QG et al.	2021
BHD	Kalatage	09HSB01	Dacite	I-type	91°48'0"	42°40'57"	Zircon	SIMS	351	4	Mao QG et al.	2021
BHD	Kalatage	08KL03-10	Dacite	I-type	91°48'0.1"	42°40'57"	Zircon	SIMS	354	4	Mao QG et al.	2021
BHD	Kalatage	13KL02	Granodiorite	I-type	91°53'32"	42°39'32"	Zircon	LA-ICP-MS	334	5	Mao QG et al.	2021
BHD	Kalatage	13KL05	Granite	I-type	91°54'8"	42°38'30"	Zircon	LA-ICP-MS	323	4	Mao QG et al.	2021
BHD	Kalatage	10ZB46	Granite	I-type	91°54'18"	42°38'19"	Zircon	LA-ICP-MS	314	2	Mao QG et al.	2021

BHD	Kalatage	13KL10	Granite	I-type	91°53'23"	42°40'18"	Zircon	LA-ICP-MS	323	4	Mao QG et al.	2021
BHD	Tuwu	FX01	Granitic porphyry	Adakitic	92°20'20"	42°4'56"	Zircon	LA-ICP-MS	335	2	Mao QG et al.	2021
BHD	Kezier	KZ03	Granodiorite	Adakitic	91°43'3"	42°11'33"	Zircon	LA-ICP-MS	313	2	Mao QG et al.	2021
BHD	Dananhu	D01	Granodiorite	Adakitic	92°53'54"	42°27'20"	Zircon	LA-ICP-MS	311	7	Mao QG et al.	2021
BHD	Kezier	K3	Granite	I-type	92°4'12"	42°19'51"	Zircon	LA-ICP-MS	357	2	Mao QG et al.	2022
BHD	Kezier	K6	Monzoniticgranite	I-type	92°9'18"	42°16'5"	Zircon	LA-ICP-MS	335	3	Mao QG et al.	2022
BHD	Kezier	K7	Monzoniticgranite	A-type	92°7'12"	42°15'50"	Zircon	LA-ICP-MS	356	4	Mao QG et al.	2022
BHD	Tuwu	Y1	Granidiorite	I-type	92°33'7"	42°6'47"	Zircon	LA-ICP-MS	322	3	Mao QG et al.	2022
BHD	Tuwu	Y2	Granite porphyry	S-type	92°31'22"	42°5'26"	Zircon	LA-ICP-MS	322	2	Mao QG et al.	2022
BHD	Tuwu	Y4	Granite porphyry	S-type	92°31'12"	42°5'8"	Zircon	LA-ICP-MS	315	3	Mao QG et al.	2022
BHD	Tuwu	Y6	Granite porphyry	S-type	92°34'8"	42°4'59"	Zircon	LA-ICP-MS	323	3	Mao QG et al.	2022
BHD	Tuwu	Y7	Granite porphyry	S-type	92°37'23"	42°6'36"	Zircon	LA-ICP-MS	334	4	Mao QG et al.	2022

BHD	Tuwu	Y9	Biotite granite	I-type	92°20'13"	42°5'8"	Zircon	LA-ICP-MS	328	3	Mao QG et al.	2022
BHD	Tuwu	TW201	Dacite	I-type	92°26'00"	42°04'00"	Zircon	LA-ICP-MS	344	4	Mao QG et al.	2022
BHD	Tudunbei	19KH-168	Basaltic tuff	Arc-type	92°09'30"	42°16'25"	Zircon	LA-ICP-MS	337	4	Muhtar et al.	2023
BHD	Tudunbei	19KH-137	K-feldspar granite	I-type	92°09'35"	42°16'20"	Zircon	LA-ICP-MS	335	2	Muhtar et al.	2023
BHD	Tudunbei	19KH-155	Quartz diorite	Arc-type	92°09'30"	42°16'23"	Zircon	LA-ICP-MS	316	2	Muhtar et al.	2023
BHD	Tudunbei	19KH-148	Gabbroic diorite	Arc-type	92°09'32"	42°16'23"	Zircon	LA-ICP-MS	318	2	Muhtar et al.	2023
BHD	Tudunbei	19KH-163	Gabbro	Arc-type	92°09'30"	42°16'20"	Zircon	LA-ICP-MS	314	2	Muhtar et al.	2023
BHD	Kalatage	TH12-1	Tuff	Unclassified	91°43'20"	42°34'00"	Zircon	LA-ICP-MS	298	2	Qin JY et al.	2022
BHD	Yandong	YZK6303-291	Diorite porphyry	Arc-type	92°30'30"	42°06'30"	Zircon	SIMS	340	3	Shen P et al.	2014
BHD	Yandong	YZK6307-610	Plagiogranite porphyry	Adakitic	92°30'30"	42°06'21"	Zircon	SIMS	332	2	Shen P et al.	2014
BHD	Tuwu	TZK705-530	Plagiogranite porphyry	Adakitic	92°36'15"	42°06'50"	Zircon	SIMS	333	3	Shen P et al.	2014
BHD	Linglong	L1201-1	Quartz albite porphyry	I-type	92°47'57"	42°07'46"	Zircon	SIMS	319	3	Sun M et al.	2020
BHD	Kalatage	D6600-1	Rhyolite	I-type	91°39'21"	42°46'09"	Zircon	LA-ICP-MS	299	2	Sun XH et al.	2018
BHD	Kalatage	14XF-1	Hornblende gabbro	Arc-type	91°35'30"	42°40'20"	Zircon	LA-ICP-MS	281	1	Sun Y et al.	2019
BHD	Kalatage	14XF-2	Hornblende gabbro	Arc-type	91°35'30"	42°40'10"	Zircon	LA-ICP-MS	282	1	Sun Y et al.	2019
BHD	Kalatage	14XF-3	Olivine gabbro	Arc-type	91°35'30"	42°40'00"	Zircon	LA-ICP-MS	281	2	Sun Y et al.	2019

BHD	Kalatage	14XF-4	Gabbro	Arc-type	91°35'20"	42°40'20"	Zircon	LA-ICP-MS	281	1	Sun Y et al.	2019
BHD	Yuhai	YH15-001	Granite	I-type	94°37'50"	42°20'50"	Zircon	LA-ICP-MS	325	3	Wang YF et al.	2018
BHD	Yuhai	YH15-99	Pyroxene diorite	Arc-type	94°38'00"	42°22'00"	Zircon	LA-ICP-MS	291	3	Wang YF et al.	2018
BHD	Sanchakou	SCK15-15	Granodiorite	I-type	94°47'30"	42°23'00"	Zircon	LA-ICP-MS	319	3	Wang YF et al.	2022
BHD	Sanchakou	SCK16-14	Granodiorite	I-type	94°47'30"	42°22'50"	Zircon	LA-ICP-MS	312	5	Wang YF et al.	2022
BHD	Sanchakou	SCK16-7	Diorite porphyry	Arc-type	94°47'10"	42°22'40"	Zircon	LA-ICP-MS	259	5	Wang YF et al.	2022
BHD	Tuwu	TW702-59	Tonalite	Adakitic	92°36'15"	42°06'57"	Zircon	SHRIMP	332	6	Wang YH et al.	2015
BHD	Yandong	YD-10	Tonalite	Adakitic	92°31'29"	42°06'23"	Zircon	SHRIMP	335	4	Wang YH et al.	2015
BHD	Fuxing	FX-1	Plagiogranite porphyry	Adakitic	92°19'40"	42°05'05"	Zircon	SIMS	332	2	Wang YH et al.	2016
BHD	Fuxing	FX-3	Monzogranite	Adakitic	92°20'40"	42°05'00"	Zircon	SIMS	328	3	Wang YH et al.	2016
BHD	Yandong	YD1501-29	Diorite porphyry	Arc-type	92°31'30"	42°06'30"	Zircon	SIMS	339	3	Wang YH et al.	2018
BHD	Yandong	YD2-4703-10	Tonalite	Adakitic	92°31'31"	42°06'31"	Zircon	SIMS	335	3	Wang YH et al.	2018
BHD	Yandong	YD2-004-1	Quartz porphyry	I-type	92°31'32"	42°06'32"	Zircon	SIMS	328	3	Wang YH et al.	2018

BHD	Yandong	YD2-004-3	Quartz porphyry	I-type	92°31'33"	42°06'33"	Zircon	SIMS	326	3	Wang YH et al.	2018
BHD	Tuwu-Yandong	YD13-91	Diorite	Arc-type	92°31'36"	42°06'26"	Zircon	LA-ICP-MS	348	6	Xiao B et al.	2017
BHD	Tuwu-Yandong	YD13-1	Albite quartz porphyry	I-type	92°31'33"	42°06'23"	Zircon	LA-ICP-MS	324	3	Xiao B et al.	2017
BHD	Tuwu-Yandong	YD13-114	Plagiogranite porphyry	Adakitic	92°31'31"	42°06'21"	Zircon	LA-ICP-MS	339	2	Xiao B et al.	2017
BHD	Tuwu-Yandong	YD13-165	Quartz porphyry	I-type	92°31'32"	42°06'22"	Zircon	LA-ICP-MS	324	2	Xiao B et al.	2017
BHD	Baixintan	BXT	Ol-gabbro	Arc-type	92°31'30"	42°8'50"	Zircon	SHRIMP	277	1	You MX et al.	2021
BHD	Chihu	CH-9	Granodiorite	I-type	92°59'50"	42°09'50"	Zircon	SIMS	320	2	Zhang FF et al.	2016
BHD	Chihu	CH001-12	Porphyritic granodiorite	I-type	92°59'10"	42°09'55"	Zircon	SIMS	315	3	Zhang FF et al.	2016
BHD	Xiaorequanzi	XRQZ19-44	Tuff	Unclassified	89°33'40"	42°14'45"	Zircon	LA-ICP-MS	355	4	Zhang ZX et al.	2021
BHD	Xiaorequanzi	XRQZ19-40	Dacite porphyry	Unclassified	89°33'41"	42°14'46"	Zircon	LA-ICP-MS	342	3	Zhang ZX et al.	2021
BHD	Tuwu	TW-6-1	Andesite	Arc-type	92°36'30"	42°06'00"	Zircon	SHRIMP	337	7	Hou GS et al.	2006
BHD	Yudai	H14-5	Rhyolite	I-type	91°44'1.32"	42°41'9.02"	Zircon	LA-ICP-MS	300	2	Ma ZJ et al.	2021
BHD	Kalatage	H11	Gabbro	N-MORB	91°43'56"	42°40'02"	Zircon	LA-ICP-MS	285	3	Ma ZJ et al.	2021
BHD	Kalatage	H10	Quartz diorite	A-type	91°43'54"	42°40'00"	Zircon	LA-ICP-MS	270	3	Ma ZJ et al.	2021
BHD	Dacaotan	DT05	Gabbro	Arc-type	92°09'00"	42°12'00"	Zircon	SIMS	279	2	Ren MH et al.	2013

BHD	Dacaotan	DT01	Gabbro	Arc-type	92°14'02"	42°11'00"	Zircon	SIMS	278	2	Ren MH et al.	2013
BHD	Kalatage	KLT-04	Dacite	I-type	91°42'00"	42°37'00"	Zircon	LA-ICP-MS	268	2	Zhang X et al.	2021
BHD	Kalatage	KLT-05	Dacite	I-type	91°42'01"	42°37'01"	Zircon	LA-ICP-MS	297	2	Zhang X et al.	2021
BHD	Caixiashan	G425	Granite	I-type	91°45'20"	42°10'00"	Zircon	SHRIMP	316	4	Li WQ et al.	2006
BHD	Shichengzi	H13911-7.1	K-feldspar granite	A-type	93°42'56.51"	43°2'30.15"	Zircon	LA-ICP-MS	310	1.4	Huang W	2014
BHD	Qinchengnan	H13917-1.1	K-feldspar granite	A-type	94°27'55.1"	42°42'32.1"	Zircon	LA-ICP-MS	320	0.9	Huang W	2014
BHD	Balikun	T90912-2.2	K-feldspar granite	A-type	93°09'04.6"	43°54'49.8"	Zircon	LA-ICP-MS	289	0.6	Huang W	2014
BHD	Aomortag	H13916-1.1	K-feldspar granite	A-type	95°19'32.0"	43°01'09.8"	Zircon	LA-ICP-MS	312	0.8	Huang W	2014
BHD	Nanshankou	PM41-16-2	K-feldspar granite	A-type	93°41'30"	43°11'00"	Zircon	LA-ICP-MS	352	2.0	Liu HF et al.	2021
BHD	Nanshankou	PM41-20-3	K-feldspar granite	A-type	93°41'35"	43°11'05"	Zircon	LA-ICP-MS	351	2.0	Liu HF et al.	2021
BHD	Xiaopu	XP10	Monzogranite	I-type	94°42'30"	42°51'50"	Zircon	LA-ICP-MS	312	2.2	Liu L et al.	2020
BHD	Qinchengnan	14TS53	Granite porphyry	Unclassified	94°26'47"	42°43'15"	Zircon	LA-ICP-MS	314	1.5	Pang BC et al.	2020
BHD	Qinchengnan	14TS56	Diorite	Unclassified	94°34'08"	42°41'10"	Zircon	LA-ICP-MS	309	2.3	Pang BC et al.	2020
BHD	Balikun	EJ16909-1	Monzogranite	I-type	92°31'00"	44°03'00"	Zircon	LA-ICP-MS	332	3.0	Song P et al.	2019
BHD	Balikun	EJ16910-1	Monzogranite	I-type	92°58'00"	44°03'30"	Zircon	LA-ICP-MS	305	3.0	Song P et al.	2019
BHD	Balikun	EJ16912-3	Monzogranite	I-type	92°41'00"	43°36'00"	Zircon	LA-ICP-MS	307	6.0	Song P et al.	2019
BHD	Balikun	EJ16910-3	Porphyritic monzogranite	I-type	92°44'00"	43°48'00"	Zircon	LA-ICP-MS	298	3.0	Song P et al.	2019
BHD	Qincheng	T12716-1.2	Monzogranite	I-type	94°42'30"	42°51'45"	Zircon	LA-ICP-MS	316	4.0	Song P et al.	2018

BHD	Qinchengnan	T12716-8.4	Monzogranite	A-type	94°35'20"	42°42'30"	Zircon	LA-ICP-MS	320	3.0	Song P et al.	2018
BHD	Tianshanmiao	D75-1	Diorite	Unclassified	93°49'53"	43°14'20"	Zircon	SHRIMP	316	3.0	Sun GH et al.	2005
BHD	Qincheng	D05072-1	Gneissic granite	Unclassified	94°41'00"	42°50'00"	Zircon	SHRIMP	311	9.0	Sun GH et al.	2007
BHD	Badashi	X603	Dioritc enclave	Arc-type	94°07'00"	42°58'20"	Zircon	LA-ICP-MS	301	1.0	Wang CS et al.	2009
BHD	Badashi	X604	Monzogranite	I-type	94°06'35"	42°58'30"	Zircon	LA-ICP-MS	298	2.0	Wang CS et al.	2009a
BHD	Aomortag	X614	Alkaline granite	A-type	95°21'58"	43° 1'17"	Zircon	LA-ICP-MS	288	2.1	Wang CS et al.	2009 b
BHD	Nanshankou	HK-9	Andesite	Arc-type	93°54'30"	43°11'30"	Zircon	LA-ICP-MS	302	1.6	Wang C et al.	2017
BHD	Nanshankou	PM44-4-2	Granite	A-type	93°39'32"	43°10'52"	Zircon	LA-ICP-MS	331	1.9	Wang LY et al.	2016
BHD	Xiaopu	14XP-03	Leucogranite	S-type	94°42'13"	42°50'55"	Zircon	LA-ICP-MS	309	2.2	Zhu XH et al.	2018
BHD	Xiaopu	14XP-04	Leucogranite	S-type	94°42'13"	42°50'55"	Zircon	LA-ICP-MS	308	2.3	Zhu XH et al.	2018
BHD	Balikunbei	K18	Gabbro	Arc-type	92°02'10"	43°49'40"	Zircon	LA-ICP-MS	301	6.0	Yuan C et al.	2010
BHD	Dajiashan	K16	K-feldspar granite	A-type	92°35'10"	43°51'30"	Zircon	LA-ICP-MS	287	2.0	Yuan C et al.	2010
BHD	Balikunshan	K10	Monzogranite	A-type	92°22'10"	43°29'30"	Zircon	LA-ICP-MS	284	5.0	Yuan C et al.	2010
BHD	Daliugou	K09	Monzogranite	A-type	93°42'10"	43°35'30"	Zircon	LA-ICP-MS	288	3.0	Yuan C et al.	2010
BHD	Aomortag	TS8-1	Alkaline granite	A-type	95°18'00"	43° 02'10"	Zircon	LA-ICP-MS	289	1.6	Chen XJ et al.	2016
BHD	Nanshankou	TS28	Granite	I-type	93°41'21"	43°12'31"	Zircon	LA-ICP-MS	294	2.7	Chen XJ et al.	2016
BHD	Nanshankou	TS29	Dioritic enclave	Arc-type	93°41'20"	43°12'30"	Zircon	LA-ICP-MS	298	2.0	Chen XJ et al.	2016

BHD	Xiaopu	621	Gneissic granite	I-type	94°43'10"	42°51'36"	Zircon	LA-ICP-MS	297	2.0	Chen XJ and Shu LS	2010
BHD	Xiaopu	622	Gneissic granite	I-type	94°40'57"	42°48'36"	Zircon	LA-ICP-MS	295	2.0	Chen XJ and Shu LS	2010
BHD	Shichengzi	SCZ-2	Granite porphyry	A-type	93°42'33.9"	43°06'58.5"	Zircon	LA-ICP-MS	260	4.5	Nan Y et al.	2018
BHD	Aomortag	PM15TW1	K-feldspar granite	A-type	95°16'10"	43°1'50"	Zircon	LA-ICP-MS	295	2.4	Yao Y et al.	2020
BHD	Xiaopu	T12716-6.3	Monzogranite	I-type	94°43'26.2"	42°51'8.7"	Zircon	LA-ICP-MS	317	4.0	Song P et al.	2023
BHD	Qinchengnan	T12716-3.5	Gabbro	Arc-type	94°45'2.3"	42°41'0.3"	Zircon	LA-ICP-MS	311	4.0	Song P et al.	2023
BHD	Yiwuxi	EJ16913-1	Granodiorite	I-type	94°20'2"	43°23'29"	Zircon	LA-ICP-MS	303	2.0	Song P et al.	2023
BHD	Wuzunbulak	T15709-2	Diorite	Arc-type	94°3'21.6"	43°31'53.8"	Zircon	LA-ICP-MS	301	3.0	Song P et al.	2023
BHD	Daliugou	19KL65-5	Granodioritic enclave	A-type	93°37'24.9"	43°36'4.2"	Zircon	LA-ICP-MS	299	2.0	Wang Q et al.	2021
BHD	Daliugou	19KL65-1	Monzogranite	A-type	93°37'24.9"	43°36'4.2"	Zircon	LA-ICP-MS	297	1.0	Wang Q et al.	2021
BHD	Mawangmiao	19KL67	Monzonite	A-type	93°03'54.3"	43°51'26.2"	Zircon	LA-ICP-MS	284	2.0	Wang Q et al.	2021
BHD	Xiaopu	18TS80B	Gneissic granodiorite	I-type	94°41'04"	42°50'24"	Zircon	LA-ICP-MS	341	3.4	Ni XH et al.	2021
BHD	Xiaopu	18TS82A	Granodiorite dike	I-type	94°41'49"	42°50'02"	Zircon	LA-ICP-MS	330	2.7	Ni XH et al.	2021
BHD	Xiaopu	18TS82B	Granodiorite dike	I-type	94°41'49"	42°50'02"	Zircon	LA-ICP-MS	332	2.8	Ni XH et al.	2021
BHD	Xiaopu	18TS82D	Granodiorite dike	I-type	94°41'49"	42°50'02"	Zircon	LA-ICP-MS	332	2.7	Ni XH et al.	2021
BHD	Xiaopu	18TS82F	Granodiorite dike	I-type	94°41'49"	42°50'02"	Zircon	LA-ICP-MS	332	2.3	Ni XH et al.	2021
BHD	Xiaopu	18TS82H	Granodiorite dike	I-type	94°41'49"	42°50'02"	Zircon	LA-ICP-MS	331	2.2	Ni XH et al.	2021
BHD	Xiaopu	12TS119G	Leucogranite	S-type	94°41'44"	42°49'56"	Zircon	LA-ICP-MS	297	2.1	Ni XH et al.	2021
BHD	Xiaopu	12TS119H	Leucogranite	S-type	94°41'44"	42°49'56"	Zircon	LA-ICP-MS	297	2.7	Ni XH et al.	2021

BHD	Badashi	18HAM008A	Granite	I-type	94°05'14"	43°00'39"	Zircon	LA-ICP-MS	343	4.7	Li L et al.	2022
BHD	Nanshankou	18HAM015A	Gabbro	Arc-type	93°37'32"	43°12'57"	Zircon	LA-ICP-MS	334	3.2	Li L et al.	2022
BHD	Nanshankou	18HAM083A	Gabbro	Arc-type	93°37'16"	43°12'53"	Zircon	LA-ICP-MS	348	3.6	Li L et al.	2022
BHD	Nanshankou	18HAM085A	Diorite	Arc-type	93°36'58"	43°13'54"	Zircon	LA-ICP-MS	342	3.2	Li L et al.	2022
BHD	Xishan	XS03-6	Rhyolite	A-type	93°05'00"	43°23'00"	Zircon	LA-ICP-MS	311	1.7	Wang WJ et al.	2023
BHD	Sujishan	T	Gabbro	Arc-type	92°39'07"	43°36'07"	Zircon	LA-ICP-MS	308	1.1	Lei WS et al.	2016
BHD	Sujishan	D431	K-feldspar granite	A-type	92°39'36"	43°35'33"	Zircon	LA-ICP-MS	302	2.4	Lei WS et al.	2016
BHD	Hongliuxia	QJ-3-1	Mylonitic granite	Unclassified	92°22'00"	44°04'00"	Zircon	LA-ICP-MS	343	2.6	Wu Q et al.	2012
BHD	Hongliuxia	QJ-3-3	Mylonitic granite	Unclassified	92°22'00"	44°04'10"	Zircon	LA-ICP-MS	348	2.8	Wu Q et al.	2012
BHD	Xiaopu	18TS86A	Diorite	Arc-type	94°41'45"	42°49'52"	Zircon	LA-ICP-MS	303	2.6	This study	
BHD	Xiaopu	18TS86E	Diorite	Arc-type	94°41'45"	42°49'52"	Zircon	LA-ICP-MS	305	2.5	This study	
BHD	Nanshankou	22TS16E	Rhyolite	A-type	93°44'56.169''	43°8'32.829"	Zircon	LA-ICP-MS	303	3.0	This study	
BHD	Qincheng	22TS51C	Diorite	Arc-type	94°54'8.468"	42°46'27.658''	Zircon	LA-ICP-MS	301	3.0	This study	
BHD	D1	13D1-6	Basalt	Arc-type	89°35'00"	44°35'00"	Zircon	SIMS	353	2.5	Li D et al.	2020
BHD	T3	13T3-3	Andesite	Arc-type	90°40'00"	44°10'00"	Zircon	LA-ICP-MS	331	2.3	Li D et al.	2020
BHD	XQ10	XQ10-5	Dacite	A-type	88°35'6.26"	44°17'30.30"	Zircon	LA-ICP-MS	325	3.4	Chen CY et al.	2018

BHD	XQ1	XQ1-1	Dacite	A-type	88°34'15.63"	44°14'42.82"	Zircon	LA-ICP-MS	310	3.1	Chen CY et al.	2018
BHD	Shuangjingzi	BS-9	Trachyandesite	Arc-type	90°25'03"	44°50'03"	Zircon	LA-ICP-MS	342	6.0	Du Q et al.	2018
BHD	Shuangjingzi	BS-20	Basalt	Arc-type	90°25'05"	44°50'05"	Zircon	LA-ICP-MS	338	6.0	Du Q et al.	2018
BHD	Shuangjingzi	BS-18	Andesite	Arc-type	90°23'03"	44°50'33"	Zircon	LA-ICP-MS	324	11.0	Du Q et al.	2018
BHD	Shuangjingzi	BS-17	Andesite	Arc-type	90°23'02"	44°50'32"	Zircon	LA-ICP-MS	317	6.9	Du Q et al.	2018
BHD	Shuangjingzi	BS-11	Rhyolite	A-type	90°23'00"	44°50'30"	Zircon	LA-ICP-MS	305	3.7	Du Q et al.	2018
BHD	Shuangjingzi	BS-14	Andesite	Arc-type	90°23'01"	44°50'31"	Zircon	LA-ICP-MS	307	18.0	Du Q et al.	2018
BHD	Shuangjingzi	BS-16	Rhyolite	A-type	90°23'04"	44°50'34"	Zircon	LA-ICP-MS	304	3.0	Du Q et al.	2018
BHD	Shuangjingzi	SJ-2	Andesite	Unclassified	90°25'19"	44°48'17"	Zircon	SIMS	351	2.6	Li D et al.	2020
BHD	Shuangjingzi	SJ-26	Dacite	Unclassified	90°21'06"	44°50'58"	Zircon	SIMS	335	2.5	Li D et al.	2020
BHD	Wuzunbulake	T15709-2	Diorite	Arc-type	94°3'21.6"	43°31'53.8"	Zircon	LA-ICP-MS	301	3.0	Song P et al.	2019
BHD	Kalamaili	09LSG-6	Rhyolite	A-type	89°18'00"	44°58'00"	Zircon	LA-ICP-MS	314	1.9	Su YP et al.	2012
BHD	Kalamaili	09BJE-79	Rhyolite	A-type	89°03'00"	45°02'00"	Zircon	LA-ICP-MS	307	1.5	Su YP et al.	2012
BHD	Baijiandong	BJE-8	Diabase dyke	Arc-type	89°02'00"	45°02'00"	Whole rock	Ar-Ar	320	1.6	Wang J et al.	2022
BHD	Zhifang	19KL93	Gneissic granite	I-type	91°55'09.0"	44°16'25.2"	Zircon	LA-ICP-MS	324	1.0	Wang Q et al.	2021
BHD	Baijiangou	BJG02	Syenite porphyry	Unclassified	89°0'00"	45°05'00"	Zircon	LA-ICP-MS	312	3.0	Xiao Y et al.	2011
BHD	Baijiangou	BJG07	Syenite porphyry	Unclassified	89°0'01"	45°05'01"	Zircon	LA-ICP-MS	307	5.0	Xiao Y et al.	2011
BHD	Baijiangou	BJG14	Rhyolite	I-type	89°0'02"	45°05'02"	Zircon	LA-ICP-MS	315	4.0	Xiao Y et al.	2011
BHD	Baijiangou	BJG15	Rhyolite	I-type	89°0'03"	45°05'03"	Zircon	LA-ICP-MS	323	5.0	Xiao Y et al.	2011
BHD	Zhangpenggou	ZPG-3	Rhyolite	I-type	89°15'01"	44°55'01"	Zircon	LA-ICP-MS	332	9.0	Xiao Y et al.	2011

BHD	Zhangpenggou	ZPG-5	Keratophyre	I-type	89°15'00"	44°55'00"	Zircon	LA-ICP-MS	336	4.0	Xiao Y et al.	2011
BHD	Zhifang	ZF2	Quartz diorite	Arc-type	91°44'9.6"	44°23'8.3"	Zircon	SIMS	348	4.3	Xu XW et al.	2015
BHD	Zhifang	ZF3	Andesitic tuff	Arc-type	91°43'46.6"	44°23'7.4"	Zircon	SIMS	342	1.2	Xu XW et al.	2015
BHD	Zhifang	ZF16	Granodiorite	I-type	91°15'43.6"	44°31'48.5"	Zircon	SIMS	332	1.4	Xu XW et al.	2015
BHD	Zhifang	ZF20	Granitic porphyry	A-type	91°15'14.7"	44°32'27.3"	Zircon	SIMS	314	2.4	Xu XW et al.	2015
BHD	Kalamaili	008-15	Basalt	Arc-type	89°04'00"	45°04'00"	Zircon	LA-ICP-MS	321	4.2	Luo T et al.	2016
BHD	Kalamaili	056-5	Rhyolite	A-type	89°02'00"	45°02'00"	Zircon	LA-ICP-MS	309	3.0	Luo T et al.	2016
BHD	Balikun	8687-2	Basalt	Arc-type	93°38'12"	43°45'05"	Zircon	LA-ICP-MS	312	4.0	Luo T et al.	2018
BHD	Balikun	12-11-1	Trachyandesite	Arc-type	93°32'07"	43°46'57"	Zircon	LA-ICP-MS	312	2.9	Luo T et al.	2018
BHD	Balikun	9481	Rhyolite	A-type	93°32'02"	43°46'56"	Zircon	LA-ICP-MS	308	3.1	Luo T et al.	2018
BHD	Balikun	12-8-1	Rhyolite	A-type	93°32'10"	43°47'05"	Zircon	LA-ICP-MS	309	3.1	Luo T et al.	2018
BHD	Shuangjingzi	SHJ-8-4	Trachyandesite	Unclassified	90°26'57"	44°52'06"	Zircon	SHRIMP	350	6.3	Tan JY et al.	2009
BHD	Wucaicheng	022-7	K-feldspar granite	I-type	89°03'00"	45°09'00"	Zircon	LA-ICP-MS	341	5.1	Tian J et al.	2015
BHD	Wucaicheng	025-5	K-feldspar granite	I-type	89°06'00"	45°11'00"	Zircon	LA-ICP-MS	341	4.0	Tian J et al.	2015
BHD	Wucaicheng	021-2-1	K-feldspar granite	A-type	88°56'00"	45°16'00"	Zircon	LA-ICP-MS	321	2.0	Tian J et al.	2016
BHD	Wucaicheng	021-17-1	Gabbro	Arc-type	88°56'00"	45°15'00"	Zircon	LA-ICP-MS	319	3.0	Tian J et al.	2016
BHD	Dishuiquan	01-55	Basalt	Arc-type	88°53'00"	45°14'00"	Zircon	LA-ICP-MS	338	5.2	Wang FM et al.	2013
BHD	Dishuiquan	02-12	Basaltic andesite	Arc-type	88°54'00"	45°16'00"	Zircon	LA-ICP-MS	337	3.7	Wang FM et al.	2013
BHD	Yiwu	X-623	Monzogranite	A-type	94°49'03"	43°18'10"	Zircon	LA-ICP-MS	285	1.4	Wang CS et al.	2010
BHD	Yiwu	X-627	K-feldspar granite	I-type	94°47'08"	43°14'59"	Zircon	LA-ICP-MS	284	1.1	Wang CS et al.	2010

KY	Nanbeidagou	10H32A	K-feldspar granite	I-type	92°19'37"	42°05'40"	Zircon	LA-ICP-MS	347	2	Wang B et al.	2014
KY	Nanbeidagou	10H32B	Gabbroic dike	E-MORB	92°19'38"	42°05'40"	Zircon	LA-ICP-MS	275	6	Wang B et al.	2014
KY	Lubei	LB16-19	Hornblende gabbro	Arc-type	90°21'00"	42°10'00"	Zircon	LA-ICP-MS	288	1.6	Chen BY et al.	2018
KY	Lubei	B17-81	Diorite	Arc-type	90°21'07"	42°10'20"	Zircon	LA-ICP-MS	283	4.0	Chen BY et al.	2019
KY	Bailiangshan	B17-13	Diorite	Arc-type	90°50'39"	42°14'28"	Zircon	SHRIMP	281	3.1	Chen BY et al.	2019
KY	Lubei	LB	Hornblende gabbro	Arc-type	90°21'00"	42°10'15"	Zircon	LA-ICP-MS	278	3.4	Deng YF et al.	2020
KY	Lubei	16LBD-01	lherzolite	Arc-type	90°21'00"	42°10'10"	Zircon	ID-TIMS	280	0.2	Deng YF et al.	2020
KY	Hulu	HL	Gabbro	Arc-type	95°42'00"	42°31'00"	Zircon	LA-ICP-MS	282	1.2	Han ZK et al.	2013
KY	Xiangshan	XS	Gabbro	Arc-type	94°33'00"	42°18'00"	Zircon	SIMS	280	1.1	Han ZK et al.	2013
KY	Huangshandong	HSD-16	Gabbrodiorite	Arc-type	94°43'48"	42°16'20"	Zircon	LA-ICP-MS	280	1.6	He YP et al.	2019
KY	Huangshandong	HSD-15	Bojite	Arc-type	94°43'48"	42°16'21"	Zircon	LA-ICP-MS	278	1.9	He YP et al.	2019
KY	Huangshandong	HSD-37	Olivine gabbro	Arc-type	94°46'02"	42°16'57"	Zircon	LA-ICP-MS	279	2.1	He YP et al.	2019
KY	Jingerquan	ETS1922	Diorite	Unclassified	95°57'00"	42°33'00"	Zircon	LA-ICP-MS	287	2.9	Hu J et al.	2021
KY	Huangshandong	ETS1904	Diorite	Unclassified	94°43'40"	42°16'25"	Zircon	LA-ICP-MS	279	2.9	Hu J et al.	2021
KY	Huangshanxi	ETS1906	Granite	Unclassified	94°38'50"	42°16'00"	Zircon	LA-ICP-MS	280	1.9	Hu J et al.	2021
KY	Jingxia	ETS1923	Granite	Unclassified	95°06'45"	42°19'25"	Zircon	LA-ICP-MS	258	1.8	Hu J et al.	2021
KY	Jingxia	ETS1820	Granite	Unclassified	95°03'00"	42°18'00"	Zircon	LA-ICP-MS	258	2.3	Hu J et al.	2021
KY	Yanmansubei	ETS1914	Granite	Unclassified	93°27'00"	42°08'00"	Zircon	LA-ICP-MS	273	1.6	Hu J et al.	2021
KY	Huangshandong	HSG	Granite	I-type	95°05'00"	42°18'30"	Zircon	LA-ICP-MS	257	2.1	Li P et al.	2022

KY	Huludong	HDG	Deformed granite	I-type	95°45'00"	42°32'10"	Zircon	LA-ICP-MS	347	2.5	Li P et al.	2022
KY	Aqishan	YM-80	Mylonized granite porphyry	I-type	90°58'32"	42°01'26"	Zircon	LA-ICP-MS	336	3.3	Liu B et al.	2021
KY	Aqishan	KG-22	Two-mica granite	S-type	91°00'43"	42°02'58"	Zircon	LA-ICP-MS	332	6.1	Liu B et al.	2021
KY	Aqishan	YM-50	Quartz porphyry	S-type	91°03'51"	42°01'18"	Zircon	LA-ICP-MS	333	1.7	Liu B et al.	2021
KY	Shidong	SD-19	Syenite porphyry	S-type	90°55'00"	42°03'00"	Zircon	SIMS	332	2.6	Liu YH et al.	2022
KY	Kanggur	Y5	Monzoniticgranite	S-type	92°32'33"	42°3'58"	Zircon	LA-ICP-MS	280	2.7	Mao QG et al.,	2022
KY	Hancaohu	N3	Biotite granite	I-type	93°45'27"	42°6'59"	Zircon	LA-ICP-MS	279	2.7	Mao QG et al.,	2022
KY	Hancaohu	N8	Granite	Adakitic	95°5'3"	42°18'39"	Zircon	LA-ICP-MS	254	27.0	Mao QG et al.,	2022
KY	Hancaohu	N10	Granodiorite	I-type	95°7'36"	42°14'25"	Zircon	LA-ICP-MS	270	2.4	Mao QG et al.,	2022
KY	Hancaohu	N14	Biotite granite	I-type	94°50'56"	42°12'26"	Zircon	LA-ICP-MS	278	2.1	Mao QG et al.,	2022
KY	Qiziltag	18SZ-17	Boitite granite	I-type	91°39'00"	42°06'00"	Zircon	LA-ICP-MS	289	1.9	Muhtar et al.	2020
KY	Qiziltag	18SZ-21	Boitite monzogranite	I-type	91°39'50"	42°04'45"	Zircon	LA-ICP-MS	292	1.7	Muhtar et al.	2020
KY	Qiziltag	18SZ-01	K-feldspar granite	I-type	91°40'00"	42°04'00"	Zircon	LA-ICP-MS	288	3.1	Muhtar et al.	2020
KY	Qiziltag	18SZ-34	Boitite monzogranite	I-type	91°38'10"	42°06'20"	Zircon	LA-ICP-MS	279	1.8	Muhtar et al.	2020
KY	Qiziltag	18SZ-06	Gabbro	N-MORB	91°39'50"	42°04'25"	Zircon	LA-ICP-MS	278	2.3	Muhtar et al.	2020
KY	Kanggur	18K-16	Andesite	Arc-type	91°03'10"	41°59'30"	Zircon	LA-ICP-MS	338	1.7	Muhtar et al.	2020

KY	Kanggur	18K-32	Rhyolite	I-type	91°03'05"	41°59'30"	Zircon	LA-ICP-MS	332	2.8	Muhtar et al.	2020
KY	Kanggur	19K-94	Dacite	I-type	91°03'20"	41°59'00"	Zircon	LA-ICP-MS	338	3.2	Muhtar et al.	2020
KY	Kanggur	18K-43	Granite porphyry	I-type	91°03'00"	41°59'30"	Zircon	LA-ICP-MS	343	1.9	Muhtar et al.	2020
KY	Jinshan	18KH-56	Diorite	Arc-type	94°38'55"	42°18'30"	Zircon	LA-ICP-MS	335	4.7	Muhtar et al.	2022
KY	Shuangchagoubei	18KH-68	Two-mica granite	I-type	95°06'02.00"	42°18'40.38"	Zircon	LA-ICP-MS	261	2.0	Muhtar et al.	2023a
KY	Shuangchagoubei	18KH-75	Gneissic biotite granite	Adakitic	95°04'57.15"	42°18'41.17"	Zircon	LA-ICP-MS	262	1.5	Muhtar et al.	2023a
KY	Shuangchagoubei	18KH-83	Two-mica granite	I-type	95°06'30.00"	42°17'23.00"	Zircon	LA-ICP-MS	263	5.0	Muhtar et al.	2023a
KY	Shuangchagoubei	20KH-15	Mylonized granite dyke	Unclassified	95°07'51.08"	42°18'50.59"	Zircon	LA-ICP-MS	257	2.9	Muhtar et al.	2023a
KY	Longdong	19KH-91	Granodiorite	I-type	93°11'12.72"	42°01'08.00"	Zircon	LA-ICP-MS	277	2.6	Muhtar et al.	2023a
KY	Longdong	19KH-109	Biotite monzogranite	I-type	93°17'26.96"	42°00'28.58"	Zircon	LA-ICP-MS	279	3.0	Muhtar et al.	2023a
KY	Longdong	19KH-114	K-feldspar granite	I-type	93°19'22.33"	41°59'32.03"	Zircon	LA-ICP-MS	277	1.9	Muhtar et al.	2023a
KY	Hongshi	18K-83	Biotite granite	I-type	90°50'08.99"	42°09'13.73"	Zircon	LA-ICP-MS	273	2.2	Muhtar et al.	2023a
KY	Hongshi	18K-91	Biotite granite	I-type	90°53'12.58"	42°08'56.77"	Zircon	LA-ICP-MS	274	2.1	Muhtar et al.	2023a
KY	Huangshandong	HSD-01	Gabbro	Arc-type	94°45'46.14"	42°16'26.48"	Zircon	LA-ICP-MS	278	1.4	Muhtar et al.	2023b
KY	Shuangchagou	18KH-216	Gneiss	S-type	94°47'53.60"	42°12'50.73"	Zircon	LA-ICP-MS	289	4.1	Muhtar et al.	2023b
KY	Shuangchagou	18KH-94	Gneissic biotite granite	I-type	94°53'49.04"	42°14'02.39"	Zircon	LA-ICP-MS	272	1.4	Muhtar et al.	2023b

KY	Shuangchagou	18KH-231	Biotite granite	I-type	94°50'48.22"	42°12'31.34"	Zircon	LA-ICP-MS	282	1.5	Muhtar et al.	2023 b
KY	Shuangchagou	19KH-22	Biotite granite	I-type	95°06'44.61"	42°16'09.43"	Zircon	LA-ICP-MS	283	1.7	Muhtar et al.	2023 b
KY	Shuangchagou	19KH-66	Two-mica granite	I-type	94°48'19.71"	42°11'37.13"	Zircon	LA-ICP-MS	277	2.5	Muhtar et al.	2023 b
KY	Shuangchagou	18KH-81	Muscovite granite	I-type	95°06'30.00"	42°17'23.00"	Zircon	LA-ICP-MS	261	1.6	Muhtar et al.	2023 b
KY	Huangshan	HS-V	Gabbro	Unclassified	94°43'50"	42°16'20"	Zircon	SIMS	284	3.4	Qin KZ et al.	2011
KY	Xiangshang	XSTiFe-V	Gabbro	Unclassified	94°33'00"	42°18'00"	Zircon	SIMS	279	1.8	Qin KZ et al.	2011
KY	Huangshanxi	DHS17-24	Gabbronorite	Unclassified	94°36'00"	42°15'40"	Zircon	SHRIMP	283	2.0	Song XY et al.	2021
KY	Huangshanxi	HSX1	Lherzolite	Unclassified	94°36'00"	42°15'45"	Zircon	SHRIMP	281	1.9	Song XY et al.	2021
KY	Huangshandong	HSDD-02	Lherzolite	Unclassified	94°44'15"	42°16'23"	Zircon	LA-ICP-MS	284	2.0	Song XY et al.	2021
KY	Huangshandong	16HSDD-02	Gabbronorite	Unclassified	94°45'15"	42°16'45"	Zircon	SHRIMP	283	3.0	Song XY et al.	2021
KY	Huangshandong	HSDD-01	Gabbronorite	Unclassified	94°43'50"	42°16'21"	Zircon	LA-ICP-MS	283	1.4	Song XY et al.	2021
KY	Tudun	17TD-112	Lherzolite	Unclassified	94°06'45"	42°13'33"	Zircon	SHRIMP	283	1.7	Song XY et al.	2021
KY	Huangshannan	HSN1	Lherzolite	Unclassified	94°39'30"	42°11'41"	Zircon	SHRIMP	279	2.6	Song XY et al.	2021

KY	Erhongwa	17E-111	Lherzolite	Unclassified	94°16'00"	42°07'50"	Zircon	SHRIMP	281	3.5	Song XY et al.	2021
KY	Hongliugou	HLG-1	Norite	Unclassified	95°57'10"	42°29'30"	Zircon	SHRIMP	281	3.4	Song XY et al.	2021
KY	Tulaergen	TLD19-1B	Lherzolite	Unclassified	95°54'10"	42°35'20"	Zircon	SHRIMP	281	2.2	Song XY et al.	2021
KY	Mati	MT18A	Lherzolite	Unclassified	95°47'20"	42°32'50"	Zircon	SHRIMP	282	2.2	Song XY et al.	2021
KY	Jingerquanbei	JEB-1	Lherzolite	Unclassified	95°35'00"	42°34'50"	Zircon	SHRIMP	282	2.5	Song XY et al.	2021
KY	Jingerquanbei	JEB-2	Gabbro	Unclassified	95°35'02"	42°34'50"	Zircon	SHRIMP	316	3.2	Song XY et al.	2021
KY	Hulu	HL18-A	Websterite	Unclassified	95°41'40"	42°31'05"	Zircon	SHRIMP	283	1.8	Song XY et al.	2021
KY	Sidingheishan	SDHS	Ol-gabbro	Arc-type	96°13'10"	42°38'30"	Zircon	SHRIMP	351	5.8	Sun T et al.	2018
KY	Sidingheishan	SDGB	Gabbro	Arc-type	96°13'00"	42°38'20"	Zircon	LA-ICP-MS	359	6.4	Sun T et al.	2018
KY	Huangshandong	01H04A	Biotite granite	I-type	94°45'42"	42°17'13"	Zircon	LA-ICP-MS	338	3.8	Wang B et al.	2014
KY	Huangshandong	01H07A	Gabbro	N-MORB	94°45'02"	42°16'20"	Zircon	LA-ICP-MS	268	2.1	Wang B et al.	2014
KY	Huangshandong	01H07B	Gabbro	E-MORB	94°45'02"	42°16'20"	Zircon	LA-ICP-MS	275	3.6	Wang B et al.	2014
KY	Huangshandong	10H13	Pyroxene diorite	E-MORB	94°43'42"	42°16'16"	Zircon	LA-ICP-MS	271	3.8	Wang B et al.	2014
KY	Huangshandong	10H16	Granitic dike	Unclassified	94°43'33"	42°16'16"	Zircon	LA-ICP-MS	290	1.3	Wang B et al.	2014
KY	Huangshandong	10H21A-1	Gabbro	E-MORB	94°45'04"	42°16'44"	Zircon	LA-ICP-MS	267	2.1	Wang B et al.	2014
KY	Huangshanxi	HSW30	Diorite	Arc-type	94°37'3.3"	42°15'59.5"	Zircon	SHRIMP	269	2.0	Zhou MF et al..	2004

KY	Kushui	17BY-TW-8	Gabbro	N-MORB	94°23'00"	42°06'00"	Zircon	LA-ICP-MS	336	2.3	Jiang YX et al.	2019
KY	Sidingheishan	25-50	Gabbro	Arc-type	96°06'00"	42°36'05"	Zircon	LA-ICP-MS	352	1.9	Li QX et al.	2010
KY	Tugemantashi	15TS11	Diorite	Unclassified	90°21'54"	42°05'05"	Zircon	LA-ICP-MS	282	2.4	Pang BC et al.	2020
KY	Tugemantashi	15TS12	Monzogranite	Unclassified	90°21'55"	42°05'05"	Zircon	LA-ICP-MS	269	1.9	Pang BC et al.	2020
KY	Huangshanxi	14TS33	Monzogranite	Unclassified	94°35'01"	42°15'14"	Zircon	LA-ICP-MS	328	1.7	Pang BC et al.	2020
KY	Tuwuxi	15TS29	Monzogranite	Unclassified	92°14'45"	42°03'51"	Zircon	LA-ICP-MS	272	2.0	Pang BC et al.	2020
KY	Aqishan	AQ-01	Granodiorite porphyry	Unclassified	90°51'00"	41°49'00"	Zircon	LA-ICP-MS	306	2.8	Da JF et al.	2020
KY	Aqishan	X3SS-1	Granodiorite	I-type	90°38'00"	41°57'30"	Zircon	LA-ICP-MS	336	3.0	Du L et al.	2018
KY	Aqishan	X3SS-8	Diorite enclave	Arc-type	90°38'05"	41°57'30"	Zircon	LA-ICP-MS	335	2.0	Du L et al.	2018
KY	Aqishan	X3SS-14	Albitophyre	I-type	90°38'10"	41°57'30"	Zircon	LA-ICP-MS	333	3.0	Du L et al.	2018
KY	Aqishan	X3SS-34	K-feldspar granite	A-type	90°38'00"	41°57'20"	Zircon	LA-ICP-MS	292	3.0	Du L et al.	2018
KY	Aqishan	X3SS-32	Monzonitic granite	I-type	90°38'00"	41°57'25"	Zircon	LA-ICP-MS	281	2.0	Du L et al.	2018
KY	Yamansu	YMS44	Basalt	Arc-type	93°52'00"	41°54'30"	Zircon	LA-ICP-MS	324	0.9	Hou T et al.	2014
KY	Shaquanzi	Y-12	Andesite	Arc-type	94°45'00"	41°55'00"	Zircon	LA-ICP-MS	315	3.0	Jiang HJ et al.	2017
KY	Shaquanzi	ZK1-112	Andesitic tuff	Arc-type	94°45'30"	41°55'00"	Zircon	LA-ICP-MS	305	3.5	Jiang HJ et al.	2017

KY	Shaquanzi	ZK2	Diorite	Arc-type	94°46'00"	41°56'00"	Zircon	LA-ICP-MS	299	5.1	Jiang HJ et al.	2017
KY	Tieling	20TL	Moyite	I-type	91°05'30"	41°47'30"	Zircon	LA-ICP-MS	305	2.4	Li P et al.	2022
KY	Shaquanzi	SQZ75	Rhyolite	Unclassified	94°45'00"	41°55'30"	Zircon	LA-ICP-MS	328	2.6	Liu F et al.	2019
KY	Shaquanzi	SQZ81	Rhyolite	Unclassified	94°45'00"	41°55'35"	Zircon	LA-ICP-MS	328	1.4	Liu F et al.	2019
KY	Shaquanzi	SQZ82	Diorite	Unclassified	94°45'00"	41°55'50"	Zircon	LA-ICP-MS	276	1.4	Liu F et al.	2019
KY	Shaquanzi	SQZ19	Basaltic andesite	Unclassified	94°45'00"	41°55'40"	Zircon	LA-ICP-MS	286	2.0	Liu F et al.	2019
KY	Yanmansu	YMS37	Basaltic andesite	Unclassified	93°53'00"	41°54'30"	Zircon	LA-ICP-MS	328	6.4	Liu F et al.	2019
KY	Bailingshan	16CXS29	Diorite porphyry	Adakitic	91°21'20.8"	41°50'31.9"	Zircon	LA-ICP-MS	315	1.0	Long XP et al.	2020
KY	Bailingshan	16CXS40	Granite dyke	I-type	91°21'25"	41°50'31.9"	Zircon	LA-ICP-MS	312	3.0	Long XP et al.	2020
KY	Jueleuotage	1050-2	Basaltic andesite	Arc-type	92°15'00"	41°52'00"	Zircon	LA-ICP-MS	336	2.0	Luo T et al.	2016
KY	Jueleuotage	CN02-55	Basaltic andesite	Arc-type	92°15'00"	41°46'00"	Zircon	LA-ICP-MS	321	2.0	Luo T et al.	2016
KY	Jueleuotage	CN03-39	Basaltic andesite	MORB	92°15'00"	41°46'10"	Zircon	LA-ICP-MS	320	2.0	Luo T et al.	2016
KY	Shilipo	B6916-11	Dacite	I-type	91°15'00"	41°54'30"	Zircon	SHRIMP	313	3.3	Sun ZY et al.	2020
KY	Aqishan	A5830-7	Tuff	I-type	91°45'00"	41°54'30"	Zircon	SHRIMP	338	2.3	Sun ZY et al.	2020
KY	Hongyuntan	H-3	Dacite	Unclassified	90°46'00"	41°48'00"	Zircon	SHRIMP	334	5.3	Sun ZY et al.	2020
KY	Hongyuntan	H-12	Diabase	Unclassified	90°46'01"	41°48'00"	Zircon	SHRIMP	308	2.8	Sun ZY et al.	2020
KY	Bailingshan	16CXS13	Andesite	Arc-type	91°0'27.5"	41°58'35.4"	Zircon	LA-ICP-MS	330	3.0	Wu B et al.	2023
KY	Bailingshan	16CXS44	Granite	I-type	91°20'52.5"	41°50'5.3"	Zircon	LA-ICP-MS	321	2.0	Wu B et al.	2023
KY	Yamansu	16YN-01	Rhyolite	I-type	93°22'30"	41°47'00"	Zircon	SHRIMP	318	3.1	Xie W et al.	2022
KY	Yamansu	16YN-03	Rhyolite	I-type	93°23'00"	41°47'30"	Zircon	SHRIMP	311	2.4	Xie W et al.	2022
KY	Yamansu	16XDG-B10	Andesite	Unclassified	93°44'30"	41°56'00"	Zircon	LA-ICP-MS	313	3.2	Xu W et al.	2021

KY	Shuanglong	SL17-20	Rhyolite	S-type	91°51'30"	41°52'40"	Zircon	LA-ICP-MS	341	1.9	Zhang SL et al.	2021
KY	Shuanglong	SL17-225	Rhyolitic tuff	S-type	91°51'30"	41°52'00"	Zircon	LA-ICP-MS	333	2.0	Zhang SL et al.	2021
KY	Shuanglong	SL17-29	Andesite	Arc-type	91°50'40"	41°50'10"	Zircon	LA-ICP-MS	319	1.9	Zhang SL et al.	2021
KY	Shuanglong	SL17-250	Andesite tuff	Arc-type	91°51'50"	41°45'05"	Zircon	LA-ICP-MS	312	1.7	Zhang SL et al.	2021
KY	Shuanglong	SL17-45	Rhyolitic ignimbrite	I-type	91°51'10"	41°46'50"	Zircon	LA-ICP-MS	312	2.5	Zhang SL et al.	2021
KY	Shuanglong	SL17-37	Andesite tuff	Arc-type	91°49'15"	41°45'00"	Zircon	LA-ICP-MS	305	1.6	Zhang SL et al.	2021
KY	Shuanglong	SL17-31	Diorite	Arc-type	91°50'40"	41°50'08"	Zircon	LA-ICP-MS	317	3.3	Zhang SL et al.	2021
KY	Shuanglong	SL17-193	Monzogranite	I-type	91°51'10"	41°46'58"	Zircon	LA-ICP-MS	311	1.4	Zhang SL et al.	2021
KY	Shuanglong	SL17-8	Granite porphyry	I-type	91°51'10"	41°46'56"	Zircon	LA-ICP-MS	307	1.7	Zhang SL et al.	2021
KY	Shuanglong	SL17-220	Quartz diorite	Adakitic	91°50'23"	41°47'20"	Zircon	LA-ICP-MS	267	1.3	Zhang SL et al.	2021
KY	Shuanglong	SL17-192	Quartz diorite	Adakitic	91°51'10"	41°46'52"	Zircon	LA-ICP-MS	276	2.3	Zhang SL et al.	2021
KY	Shuanglong	SL17-30	Diorite porphyry	Adakitic	91°50'40"	41°50'06"	Zircon	LA-ICP-MS	275	1.5	Zhang SL et al.	2021

KY	Shuanglong	SL17-14	Diorite porphyry	Adakitic	91°51'50"	41°46'46"	Zircon	LA-ICP-MS	275	2.1	Zhang SL et al.	2021
KY	Bailingshan	BL-004	Tuffaceous dacite	I-type	91°18'30"	41°50'00"	Zircon	LA-ICP-MS	324	2.1	Zhang WF et al.	2016
KY	Bailingshan	BL-065	Granodiorite	I-type	91°20'30"	41°50'30"	Zircon	LA-ICP-MS	318	1.8	Zhang WF et al.	2016
KY	Bailingshan	BL-058	Monzogranite	I-type	91°21'00"	41°50'00"	Zircon	LA-ICP-MS	314	1.8	Zhang WF et al.	2016
KY	Bailingshan	BL-050	Granite	I-type	91°20'50"	41°50'00"	Zircon	LA-ICP-MS	307	2.3	Zhang WF et al.	2016
KY	Chilongfeng	CL13-009	Diorite	Arc-type	91°40'00"	41°48'10"	Zircon	LA-ICP-MS	317	1.4	Zhao LD et al.	2018
KY	Chilongfeng	HJ13-007	Felsic tuff	I-type	91°33'00"	41°47'00"	Zircon	LA-ICP-MS	316	2.6	Zhao LD et al.	2018
KY	Chilongfeng	CL13-010	Granodiorite	I-type	91°40'00"	41°48'00"	Zircon	LA-ICP-MS	306	1.9	Zhao LD et al.	2018
KY	Hongshanliang	HSL14-002	Rhyolite	I-type	91°35'55"	41°55'48"	Zircon	LA-ICP-MS	349	2.1	Zhao LD et al.	2019
KY	Hongshanliang	HSL14-004	Granite porphyry	I-type	91°35'41"	41°55'36"	Zircon	LA-ICP-MS	343	2.3	Zhao LD et al.	2019
KY	Shuanglong	SL14-016	Diorite enclave	Arc-type	91°52'10"	41°46'30"	Zircon	LA-ICP-MS	329	2.1	Zhao LD et al.	2019
KY	Shuanglong	SL14-001-1	Diorite	Arc-type	91°52'06.38"	41°46'26.93"	Zircon	LA-ICP-MS	323	2.6	Zhao LD et al.	2019

KY	Shuanglong	SL14-012	Andesitic tuff	Arc-type	91°51'59.92"	41°46'06.36"	Zircon	LA-ICP-MS	318	2.0	Zhao LD et al.	2019
KY	Shuanglong	SL14-004-1	Monzogranite	I-type	91°52'03.66"	41°46'27.55"	Zircon	LA-ICP-MS	313	2.0	Zhao LD et al.	2019
KY	Shuanglong	SL14-017	Granodiorite	I-type	91°51'29.14"	41°46'58.06"	Zircon	LA-ICP-MS	308	1.7	Zhao LD et al.	2019
KY	Tieling	20TL	K-feldspar granite	I-type	91°05'40"	41°47'30"	Zircon	LA-ICP-MS	286	1.9	Chen BX et al.	2022
KY	Shaquanzi	SQ1-1	Dacite	I-type	94°48'10"	42°01'45"	Zircon	LA-ICP-MS	348	1.7	Luo T et al.	2012
KY	Liangtoubao	1050-1	Dacite	I-type	92°42'30"	41°48'17"	Zircon	LA-ICP-MS	336	2.4	Luo T et al.	2012
KY	Heijianshan	HJS1-1	Rhyolite	I-type	91°40'00"	41°46'30"	Zircon	LA-ICP-MS	334	2.5	Luo T et al.	2012
KY	Tongyuliang	J4723-10	Diorite porphyry	Arc-type	94°26'15"	41°51'40"	Zircon	SHRIMP	318	2.4	Sun ZY et al.	2018
KY	Zhaibeishan	Z5827-3	Basaltic andesite	Arc-type	95°39'12"	42°10'17"	Zircon	SHRIMP	338	3.3	Sun ZY et al.	2018
KY	Hongyuntan	X356	Granodiorite	I-type	90°40'00"	41°49'30"	Zircon	LA-ICP-MS	329	9.3	Wu CZ et al.	2006
EJ	Zhaheba	K28-16-1	Rhyolite	A-type	89°15'10"	46°27'00"	Zircon	SHRIMP	276	3.0	Li D et al.	2014
EJ	Zhaheba	K28-18-1	Rhyolite	A-type	89°15'20"	46°27'00"	Zircon	SHRIMP	276	3.1	Li D et al.	2014
EJ	Kouan	11QH02	Syenite	A-type	90°53'21"	46°03'16"	Zircon	SIMS	279	2.6	Tang GJ et al.	2019
EJ	Kouan	11QH06	Syenite	A-type	90°54'18"	46°03'21"	Zircon	SIMS	279	2.4	Tang GJ et al.	2019
EJ	Zhaheba	K28-5-1	Rhyolite	A-type	89°15'00"	46°27'00"	Zircon	SHRIMP	280	2.5	Li D et al.	2014
EJ	Kalatongke	ZK07	Leucogabbro	Arc-type	89°45'00"	46°42'19"	Zircon	SHRIMP	281	1.5	Duan J et al.	2017
EJ	Hadanxun	HDX106	Quartz monzonite	I-type	90°10'40"	46°22'00"	Zircon	SHRIMP	281	0.9	Li W et al.	2021
EJ	Santanghu	ZK2-8	Rhyolite	A-type	95°30'00"	43°52'00"	Zircon	LA-ICP-MS	282	1.8	Bo HZ et al.	2021

EJ	Hadanxun	BL7	K-feldspar granite	A-type	90°11'20"	46°23'30"	Zircon	SHRIMP	283	2.2	Li W et al.	2021
EJ	Beilekuduke	IV-1-1	Granite	A-type	90°01'30"	45°11'06"	Zircon	LA-ICP-MS	283	2.0	Yang GX et al.	2010
EJ	Kalatongke	ZK7503	Norite	Arc-type	89°42'40.15"	46°44'40"	Zircon	SHRIMP	283	1.3	Duan J et al.	2017
EJ	Kubusunan	IV-25-2	Diorite enclave	I-type	90°04'37"	45°15'43"	Zircon	LA-ICP-MS	286	3.0	Yang GX et al.	2010
EJ	Kubusunan	IV-25-1	Granodiorite	I-type	90°05'08"	45°15'36"	Zircon	LA-ICP-MS	287	2.0	Yang GX et al.	2010
EJ	Hadanxun	A15703-2	Monzonite	Unclassified	90°10'20"	46°23'30"	Zircon	LA-ICP-MS	290	3.0	Song P et al.	2019
EJ	Hadanxun	HDX103	Dioritic porphyry	Arc-type	90°10'10"	46°22'00"	Zircon	SHRIMP	290	1.2	Li W et al.	2021
EJ	Kalatongke	ZK8302	Diotite	Arc-type	89°42'21"	46°44'32"	Zircon	SHRIMP	290	1.5	Qian Z et al.	2018
EJ	Qiakuerte	08WLG-07	K-feldspar granite	A-type	89°25'00"	46°15'00"	Zircon	LA-ICP-MS	291	7.0	Shen XM et al.	2011
EJ	Yemaquan	XH08-11	Granodiorite	I-type	90°26'50"	45°19'0"	Zircon	LA-ICP-MS	297	6.0	Gan L et al.	2010
EJ	Yemaquan	XH08-3	Monzogranite	A-type	90°24'00"	45°26'10"	Zircon	LA-ICP-MS	298	2.0	Gan L et al.	2010
EJ	Huangyangshan	D1191	Enclave	A-type	90°25'00"	45°3'00"	Zircon	LA-ICP-MS	300	6.0	Yang GX et al.	2011
EJ	Yemaquan	XH08-09-1	Monzogranite	A-type	90°22'0"	45°19'0"	Zircon	LA-ICP-MS	300	2.0	Gan L et al.	2010
EJ	Laoyaquan	LY8	K-feldspar granite	A-type	89°45'01"	45°18'01"	Zircon	LA-ICP-MS	300	5.0	Han YJ et al.	2012
EJ	Sareshenke	SR01	Peralkaline granite	A-type	90°18'43"	45°08'23"	Zircon	SIMS	301	2.4	Liu W et al.	2013
EJ	Wuzunbulake	A15709-2	Diorite	Unclassified	94°3'21.6"	43°31'53.8"	Zircon	LA-ICP-MS	301	3.0	Song P et al.	2019
EJ	Laoyaquan	LY6	K-feldspar granite	A-type	89°45'00"	45°18'00"	Zircon	LA-ICP-MS	301	2.0	Han YJ et al.	2012
EJ	Beilekudouke	BL02	Granodiorite	I-type	90°06'56"	45°11'30"	Zircon	SIMS	302	2.0	Liu W et al.	2013
EJ	Huangyangshan	HY13	K-feldspar granite	A-type	90°17'00"	45°06'00"	Zircon	LA-ICP-MS	302	2.0	Su YP et al.	2008

EJ	Guersi	A15703-1	Tonalite	Unclassified	90°9'47.5"	46°11'3.2"	Zircon	LA-ICP-MS	303	3.0	Song P et al.	2019
EJ	Sujiquan	SJ02	K-feldspar granite	A-type	90°20'04"	45°01'47"	Zircon	SIMS	304	1.9	Liu W et al.	2013
EJ	Yemaquan	XH08-1	K-feldspar granite	A-type	90°25'50"	45°26'10"	Zircon	LA-ICP-MS	304	3.0	Gan L et al.	2010
EJ	Sujiquan	SJ39	Biotite granite	A-type	90°28'00"	45°02'30"	Zircon	LA-ICP-MS	304	2.0	Su YP et al.	2006
EJ	Bashan	BS-13	Rhyolite	A-type	90°57'00"	44°48'00"	Zircon	LA-ICP-MS	305	2.0	Wang J et al.	2022
EJ	Hongliugou	19KL19	Granodiorite	I-type	90°07'43.3"	45°13'15.7"	Zircon	LA-ICP-MS	306	1.0	Wang Q et al.	2021
EJ	Sabei	HY19	K-feldspar granite	A-type	90°24'00"	45°12'00"	Zircon	LA-ICP-MS	306	3.0	Tang HF et al.	2007
EJ	Baijiangou	BJG07	Syenite porphyry	Unclassified	89°0'01"	45°05'01"	Zircon	LA-ICP-MS	307	5.0	Xiao Y et al.	2011
EJ	Kalatongke	KTG39	Diorite	Arc-type	89°42'01"	46°44'01"	Zircon	LA-ICP-MS	308	7.0	Gao JF and Zhou MF	2013
EJ	Kalasayi	023-3-1	K-feldspar granite	A-type	89°26'00"	45°21'00"	Zircon	LA-ICP-MS	308	3.2	Wu WW et al.	2015
EJ	Aketas	Aketas-19	Quartz monzonite	Adakitic	89°40'7"	46°48'22"	Zircon	LA-ICP-MS	308	3.5	Zhang C et al.	2018
EJ	Qiakuerte	08WLG-16	K-feldspar granite	A-type	89°12'00"	46°19'00"	Zircon	LA-ICP-MS	308	6.0	Shen XM et al.	2011
EJ	Kalatongke	KTGO7	Ferrodiorite	Arc-type	89°42'00"	46°44'00"	Zircon	LA-ICP-MS	308	3.6	Gao JF and Zhou MF	2013
EJ	N. Kurankazigan	G133	Granodiorite	I-type	90°20'59.4"	45°25'03.9"	Zircon	SIMS	309	2.1	Liu W et al.	2013
EJ	Kalasayi	052-7-1	K-feldspar granite	A-type	89°26'01"	45°21'01"	Zircon	LA-ICP-MS	309	2.0	Wu WW et al.	2015
EJ	N. Balebagayi	OT03	Granodiorite	I-type	90°18'45"	45°11'45"	Zircon	SIMS	310	2.0	Liu W et al.	2013
EJ	Huangyangshan	HY32	K-feldspar granite	A-type	90°16'00"	45°07'00"	Zircon	LA-ICP-MS	310	4.0	Su YP et al.	2008

EJ	Balebagayi	G167	K-feldspar granite	A-type	90°17'30.7"	45°09'34.8"	Zircon	SIMS	311	2.1	Liu W et al.	2013
EJ	Kalatongke	18KL57	Granitic porphyry	I-type	89°41'03"	46°44'03"	Zircon	LA-ICP-MS	311	2.5	Wang XH et al.	2021
EJ	Huangyangshan	X-29-1	Granite	A-type	90°19'00"	45°4'00"	Zircon	LA-ICP-MS	311	5.0	Yang GX et al.	2011
EJ	Shigela-N	Shigela-N01	Monzogranite	A-type	89°15'00"	46°45'00"	Zircon	LA-ICP-MS	312	6.3	Liu DD et al.	2021
EJ	Baijiangou	BJG02	Syenite porphyry	Unclassified	89°0'00"	45°05'00"	Zircon	LA-ICP-MS	312	3.0	Xiao Y et al.	2011
EJ	Sabei	S2	Granite	Unclassified	90°23'00"	45°12'00"	Zircon	SHRIMP	313	2.0	Lin JF et al.	2007
EJ	Sabei	S4	Granite	Unclassified	90°23'10"	45°12'10"	Zircon	SHRIMP	314	5.0	Lin JF et al.	2007
EJ	Ulungur	08AET68	Gabbro	Arc-type	89°10'38"	46°18'03"	Zircon	SIMS	314	4.2	Tang GJ et al.	2019
EJ	Kurankazigan	KLP03	Granodiorite	I-type	90°18'55"	45°18'44"	Zircon	SIMS	315	4.2	Liu W et al.	2013
EJ	Baijiangou	BJG14	Rhyolite	Unclassified	89°0'02"	45°05'02"	Zircon	LA-ICP-MS	315	4.0	Xiao Y et al.	2011
EJ	Zhaheba	K17-34	Dacite	A-type	89°14'00"	46°33'00"	Zircon	LA-ICP-MS	315	1.6	Li D et al.	2014
EJ	Zhaheba	K17-19	Basaltic andesite	Arc-type	89°14'01"	46°33'01"	Zircon	LA-ICP-MS	317	2.1	Li D et al.	2014
EJ	Ulungur	08AET99	Granodiorite	I-type	89°28'22"	46°12'46"	Zircon	SIMS	318	5.8	Tang GJ et al.	2019
EJ	Wulungu-W	Wulungu-W01	Monzogranite	A-type	90°12'00"	46°10'00"	Zircon	LA-ICP-MS	318	5.4	Liu DD et al.	2021
EJ	Kezier	Kezier01	Quartz monzogranite	Adakitic	90°04'00"	46°30'00"	Zircon	LA-ICP-MS	320	4.7	Liu DD et al.	2021
EJ	Kalatongke	ZK2012-3-2	Diotite	Arc-type	89°42'46"	46°44'37"	Zircon	SHRIMP	320	2.0	Qian Z et al.	2018
EJ	Kalatongke	ZK906-1	Gabbro	Arc-type	89°42'40"	46°44'38"	Zircon	SHRIMP	321	2.5	Qian Z et al.	2018

EJ	Wulungu-E	Wulungu-E01	Monzogranite	A-type	90°40'00"	45°57'00"	Zircon	LA-ICP-MS	321	4.6	Liu DD et al.	2021
EJ	Zhaheba	Pt-48	Syenogranite	A-type	88°50'00"	46°28'00"	Zircon	LA-ICP-MS	322	4.8	Tang HJ et al.	2021
EJ	Zhaheba	H-06-18	K-feldspar granite	A-type	88°55'00"	46°35'00"	Zircon	LA-ICP-MS	322	0.6	Tang HJ et al.	2021
EJ	N. Tasigake	G23	Monzogranite	I-type	89°33'04.9"	46°08'45.6"	Zircon	SIMS	322	2.0	Liu W et al.	2013
EJ	Saertielieke	G71	Peralkaline granite	A-type	89°12'18.1"	46°17'50.4"	Zircon	SIMS	322	2.0	Liu W et al.	2013
EJ	Baijiangou	BJG15	Rhyolite	Unclassified	89°0'03"	45°05'03"	Zircon	LA-ICP-MS	323	5.0	Xiao Y et al.	2011
EJ	Zhalate	ZLG08	Quartz monzonite	I-type	89°10'00"	46°40'00"	Zircon	SIMS	323	2.2	Liu XJ et al.	2019
EJ	Hadanxun	HDX74	Diorite	Arc-type	90°11'00"	46°21'30"	Zircon	LA-ICP-MS	323	1.1	Liu W et al.	2021
EJ	Hadanxun	HDX97	Monzodiorite	Adakitic	90°10'40"	46°21'00"	Zircon	LA-ICP-MS	325	1.0	Liu W et al.	2021
EJ	Hadanxun	HDX53	Monzogranite	Adakitic	90°10'00"	46°24'00"	Zircon	LA-ICP-MS	325	2.5	Liu W et al.	2021
EJ	S. Tasigake	G44	Peralkaline granite	A-type	89°27'08.7"	46°08'33.3"	Zircon	SIMS	325	2.0	Liu W et al.	2013
EJ	Kalatongke	18KL17	Granitic porphyry	S-type	89°41'02"	46°44'02"	Zircon	LA-ICP-MS	325	2.6	Wang XH et al.	2021
EJ	Xilekuduke	XKQP-BP	Granite porphyry	I-type	89°06'20"	46°42'30"	Zircon	LA-ICP-MS	326	2.0	Aibai et al.	2019
EJ	Xinyuan	XY1-13	Ol Gabbro	Arc-type	95°02'00"	44°00'15"	Zircon	SIMS	327	1.1	Mao YJ et al.	2017
EJ	Xilekuduke	ZK7-BD	Monzogranite	I-type	89°06'30"	46°42'30"	Zircon	LA-ICP-MS	328	1.8	Aibai et al.	2019
EJ	Santanghu	DH103	Andesite	Arc-type	94°14'14.5"	43°39'41"	Zircon	LA-ICP-MS	329	1.9	Li W et al.	2013
EJ	Kamste	KM-1	Dacite	Arc-type	89°25'00"	46°02'00"	Zircon	LA-ICP-MS	329	4.0	Wang J et al.	2022
EJ	Ulungur	08AET72	Monzogranite	I-type	89°31'50"	46°11'13"	Zircon	LA-ICPMS	329	4.0	Tang GJ et al.	2019
EJ	Kala'an	KLG08	Granodiorite	I-type	89°15'00"	46°50'00"	Zircon	SIMS	331	2.7	Liu XJ et al.	2019

EJ	Qiaoxiahala	QX-055-1	Aplite	A-type	89°39'48.45"	46°48'20.51"	Zircon	LA-ICP-MS	331	3.1	Liang P et al.	2016
EJ	Santanghu	ML05	Andesite	Arc-type	94°15'24.5"	43°44'7.2"	Zircon	LA-ICP-MS	331	2.3	Li W et al.	2013
EJ	Zhangpenggou	ZPG-3	Rhyolite	Unclassified	89°15'01"	44°55'01"	Zircon	LA-ICP-MS	332	9.0	Xiao Y et al.	2011
EJ	Shigela-S	Shigela-S01	Monzogranite	A-type	88°50'00"	46°40'00"	Zircon	LA-ICP-MS	333	4.4	Liu DD et al.	2021
EJ	Kamste	KM-6	Basaltic andesite	Arc-type	89°25'00"	45°55'00"	Zircon	LA-ICP-MS	333	4.0	Wang J et al.	2022
EJ	Kalatongke	18KL55	Granitic porphyry	I-type	89°41'01"	46°44'01"	Zircon	LA-ICP-MS	336	0.8	Wang XH et al.	2021
EJ	Zhangpenggou	ZPG-5	Keratophyre	Unclassified	89°15'00"	44°55'00"	Zircon	LA-ICP-MS	336	4.0	Xiao Y et al.	2011
EJ	Daheishan	DHS07N	Tuff	Unclassified	94°09'37.6"	43°35'23.6"	Zircon	LA-ICP-MS	336	2.6	Fan TT et al.	2011
EJ	Wulungu	Wulungu01	Monzogranite	A-type	90°20'00"	45°57'00"	Zircon	LA-ICP-MS	338	4.8	Liu DD et al.	2021
EJ	Daheishan	DHS04N	Tuff	Unclassified	94°09'35.7"	43°35'20.8"	Zircon	LA-ICP-MS	339	1.9	Fan TT et al.	2011
EJ	Kalatongke	18KL54	Granitic porphyry	I-type	89°41'00"	46°44'00"	Zircon	LA-ICP-MS	340	0.9	Wang XH et al.	2021
EJ	Qiakuerte	QK-7	Andesite	Arc-type	89°21'00"	46°26'00"	Zircon	LA-ICP-MS	340	8.0	Wang J et al.	2022
EJ	Qiakuerte	QK-8	Dacite	Arc-type	89°21'01"	46°26'01"	Zircon	LA-ICP-MS	340	4.0	Wang J et al.	2022
EJ	Shuangjingzi	SHJ-8-4	Trachyandesite	Unclassified	90°26'57"	44°52'06"	Zircon	SHRIMP	350	6.3	Tan JY et al.	2009
EJ	Lvshigou	H703-06-8.2	Monzogranite	I-type	95°02'32"	44°4'32"	Zircon	LA-ICP-MS	354	1.0	Zhao JX et al.	2017
EJ	Shigela	Shigela01	Monzogranite	A-type	89°00'00"	46°43'00"	Zircon	LA-ICP-MS	356	4.6	Liu DD et al.	2021

Publications

[1] **Ni, X.**, Wang, B., Cluzel, D., Liu, J., & He, Z. (2021). Late Paleozoic tectonic evolution of the North Tianshan Belt: New structural and geochronological constraints from meta-sedimentary rocks and migmatites in the Harlik Range (NW China). *Journal of Asian Earth Sciences*, 210, 104711.

[2] **Ni, X.**, Wang, B., Soret, M., Cluzel, D., Chen, Y., Jia, C., Jia, D., Faure, M., Liu, J., Li, Y., Anbar, M. A. 2024. Late Paleozoic tectonic evolution of the North Tianshan (NW China): Insights from an inverted HT-LP metamorphic sequence in the Harlik Range. *Journal of Metamorphic Geology*, under review.

[3] **Ni, X.**, Wang, B., Cluzel, D., Chen, Y., Jia, C., Jia, D., Faure, M., Cao, T., Li, Y., Sun, Y., Chen, Y., Anbar, M. A. 2024. Late Triassic Adakitic and Low Sr/Y Granitoids from the Bogda Belt: Insights into Intraplate Crustal Reworking of the Chinese Eastern Tianshan. *Geochemistry, Geophysics, Geosystems*, in preparation.

[4] Song, F., Wang, B., **Ni, X.**, Anbar, M. A., Chen, Y., Faure, M., ... & Liu, H. (2024). From early Paleozoic subduction to end-Carboniferous post-orogenic collapse: New constraints on the tectonic evolution of the Central and South Tianshan (NW China). *Gondwana Research*, 129, 305-331.

[5] Liu, J., Wang, B., **Ni, X.**, Song, F., Sun, Z., Deng, J., & Li, Y. (2022). Late Devonian transition from advancing to retreating subduction in the SW Central Asian Orogenic Belt: Insights from multiple deformation and magmatic events in the southern Yili Block, NW China. *Gondwana Research*, 105, 468-487.

[6] He, Z., Wang, B., **Ni, X.**, De Grave, J., Scaillet, S., Chen, Y., ... & Zhu, X. (2021). Structural and kinematic evolution of strike-slip shear zones around and in the Central Tianshan: Insights for eastward tectonic wedging in the southwest Central Asian Orogenic Belt. *Journal of Structural Geology*, 144, 104279.

[7] Sun, Z., Wang, B., Liu, J., **Ni, X.**, & Song, F. (2021). Age and tectonic setting of Neoproterozoic gneissic granites in the southern Yili Block (NW China) and

implications for the origins of the continental blocks in SW Central Asian Orogenic Belt. *Geological Journal*, 56(10), 5027-5045.

[8] He, Z., Wang, B., Glorie, S., Su, W., **Ni, X.**, Jepson, G., ... & De Grave, J. (2022). Mesozoic building of the Eastern Tianshan and East Junggar (NW China) revealed by low-temperature thermochronology. *Gondwana Research*, 103, 37-53.

[9] He, Z., Wang, B., Nachtergaele, S., Glorie, S., Ni, X., Su, W., ... & De Grave, J. (2021). Long-term topographic evolution of the Central Tianshan (NW China) constrained by low-temperature thermochronology. *Tectonophysics*, 817, 229066.

[10] He, Z., Wang, B., Su, W., Glorie, S., **Ni, X**., Liu, J., ... & De Grave, J. (2022). Meso-Cenozoic thermo-tectonic evolution of the Yili block within the Central Asian Orogenic Belt (NW China): Insights from apatite fission track thermochronology. *Tectonophysics*, *823*, 229194.

[11] Zhu, X., Chen, Y., Wang, B., Dong, Y., Scaillet, S., Faure, M., **Ni, X.**, & Duval, F. (2023). Paleomagnetic study on the Early Permian Gubaoquan doleritic dike swarm in the southern Beishan area, NW China: Implications for the tectonic and paleogeographic reconstructions of the southern Central Asian Orogenic Belt. *Journal of Asian Earth Sciences*, 256, 105832.

[12] Wang, Y., Wang, B., Li, M., Cao, S., Wang, H., Pan, S., ... & Ni, X. (2022). New constraints on volcanism during Ordovician-Silurian transition: Insights from marine bentonites in northern Yili Block (NW China). *Palaeogeography, Palaeoclimatology, Palaeoecology*, 600, 111073.

Conferences

[1] EGU General Assembly 2024, 2024.04, Vienna, Austria

[2] RST Conference 2023, 2023.10, Rennes, France

Xinghua NI

Évolution tectonique du Sud-Ouest de la Ceinture Orogénique de l'Asie Centrale du Paléozoïque supérieur au Mésozoïque inférieur: évidences structurale, métamorphique et magmatique de Tianshan oriental

Les orogènes d'accrétion formées le long de marges convergentes se caractérisent par une longue évolution et sont les principaux sites de croissance continentale sur la Terre. La Ceinture Orogénique d'Asie Centrale (COAC) en Eurasie est un vaste système orogénique d'accrétion constituant une croûte juvénile, et offre un laboratoire naturel pour examiner la croissance continentale et les processus d'orogénèse. Le Tianshan oriental, situé au Sud-Ouest de la COAC, préserve des enregistrements de la subduction de la plaque océanique, de l'accrétion arc-arc/continent et de l'évolution post-collisionnelle. Des débats entravent notre compréhension de son évolution tectonique, y compris des questions liées aux socles crustaux, aux processus tectoniques, à la chronologie de l'amalgamation finale, et à l'évolution magmatique. Cette thèse présente une étude multi-échelle et multidisciplinaire de l'évolution tectono-métamorphique-magmatique du Tianshan oriental du Paléozoïque supérieur au Mésozoïque inférieur. Les principaux résultats sont les suivants : (1) le socle du Tianshan nord-est et de l'Est de Junggar se compose principalement de croûte juvénile du Néoprotérozoïque au Phanérozoïque, probablement avec la présence d'un socle continental d'âge Méso-protérozoïque ; (2) l'accrétion arc-arc entre le Tianshan nord-est et l'Est de Junggar autour de 340-330 Ma a entraîné un raccourcissement et un épaississement crustal. Le retrait de la plaque océanique de Kangguer entre 330 et 310 Ma a provoqué une extension rétro-arc et un amincissement crustal dans la région de Bogda-Harlik, ainsi qu'un magmatisme lié à l'extension et un métamorphisme à haute température et basse pression. (3) l'amalgamation finale du Tianshan oriental a eu lieu vers 300 Ma, entraînant un épaississement crustal dans le Tianshan nord-est et une accalmie magmatique dans les régions de l'Est de Junggar et de Kangguer-Yamansu, ainsi qu'une forte réduction de roches magmatiques intermédiaires dans la région de Bogda-Harlik-Dananhu. (4) après l'amalgamation, le Tianshan nord-est et l'Est de Junggar ont évolué vers un environnement post-orogénique pendant le Permien. L'extension et l'exhumation localisées, ainsi que la formation de roches magmatiques bimodales et de granitoïdes de type A généralisés, se sont produites en association avec la tectonique transcurrente régionale. (5) pendant le Trias, le magmatisme diversifié dans le Tianshan oriental résulte du remaniement de croûtes anciennes et juvéniles à des profondeurs et des températures variées, avec un apport du manteau dans un contexte intraplaque.

Mots clés : Sud-Ouest de la Ceinture Orogénique de l'Asie Centrale, Paléozoïque supérieur, Mésozoïque inférieur, Structures et métamorphisme, Magmatisme, Processus tectoniques.

Late Paleozoic - Early Mesozoic tectonic evolution of the southwestern Central Asian Orogenic Belt: Structural, metamorphic and magmatic evidence from the eastern Tianshan

Accretionary orogens forming along convergent margins are characterized by long-lived evolution and are the primary sites of continental growth on Earth. The Central Asian Orogenic Belt (CAOB) within Eurasia is a vast accretionary orogenic system containing significant juvenile crust, and offers a natural laboratory to examine continental growth and orogenic processes. The eastern Tianshan in the southwestern CAOB preserves crucial records of subduction, arc-arc/continent accretion and post-collisional evolution, providing unique insights into orogenic tectonics. Nonetheless, several debates still hinder our understanding of its tectonic evolution, including issues related to the crustal basement, detailed tectonic processes, timing of the final amalgamation, and magmatic evolution. This thesis presents a multi-scale and multi-disciplinary study of the tectonic-metamorphic-magmatic evolution of the eastern Tianshan during the late Paleozoic to early Mesozoic. The main results lead to the following conclusions: (1) the basement of the eastern North Tianshan and East Junggar regions primarily comprises Neoproterozoic to Phanerozoic juvenile crust, likely with a presence of a Mesoproterozoic continental basement similar to that of the Central Tianshan Block in the Kangguer-Yamansu area; (2) arc-arc accretion between the eastern North Tianshan and East Junggar around 340-330 Ma resulted in crustal shortening and thickening. The roll-back of the Kangguer oceanic slab between 330 and 310 Ma caused back-arc extension and crustal thinning in the Bogda-Harlik region, along with extension-related magmatism and high temperature and low pressure (HT-LP) metamorphism; (3) the final amalgamation of the eastern Tianshan occurred around 300 Ma, leading to crustal thickening in the eastern North Tianshan and a magmatic lull in the East Junggar and Kangguer-Yamansu belts, as well as a sharp reduction in intermediate magmatic rocks in the Bogda-Harlik-Dananhu region; (4) following the amalgamation, the eastern North Tianshan and East Junggar evolved into a post-orogenic setting during the Permian. Localized crustal extension and exhumation, along with the formation of bimodal magmatic rocks and widespread A-type granitoids, likely occurred in association with regional transcurrent tectonics; (5) during the Triassic, the magmatism diversity in the eastern Tianshan resulted from the reworking of both ancient and juvenile crust at varying depths and temperatures, with some mantle input in an intraplate setting.

Keywords: Southwestern Central Asian Orogenic Belt (CAOB), Late Paleozoic, Early Mesozoic, Structures and metamorphism, Magmatism, Tectonic processes

Institut des Sciences de la Terre d'Orléans

Univ Orléans, SNRS, BRGM, OSUC, F-45071 Orléans, France